UNIVERSITÉ DE LIÈGE
INTERACTIONS FONDAMENTALES EN PHYSIQUE ET ASTROPHYSIQUE
FACULTÉ DES SCIENCES

YEAR 2010

Quasi-Elastic Production at Hadronic Colliders

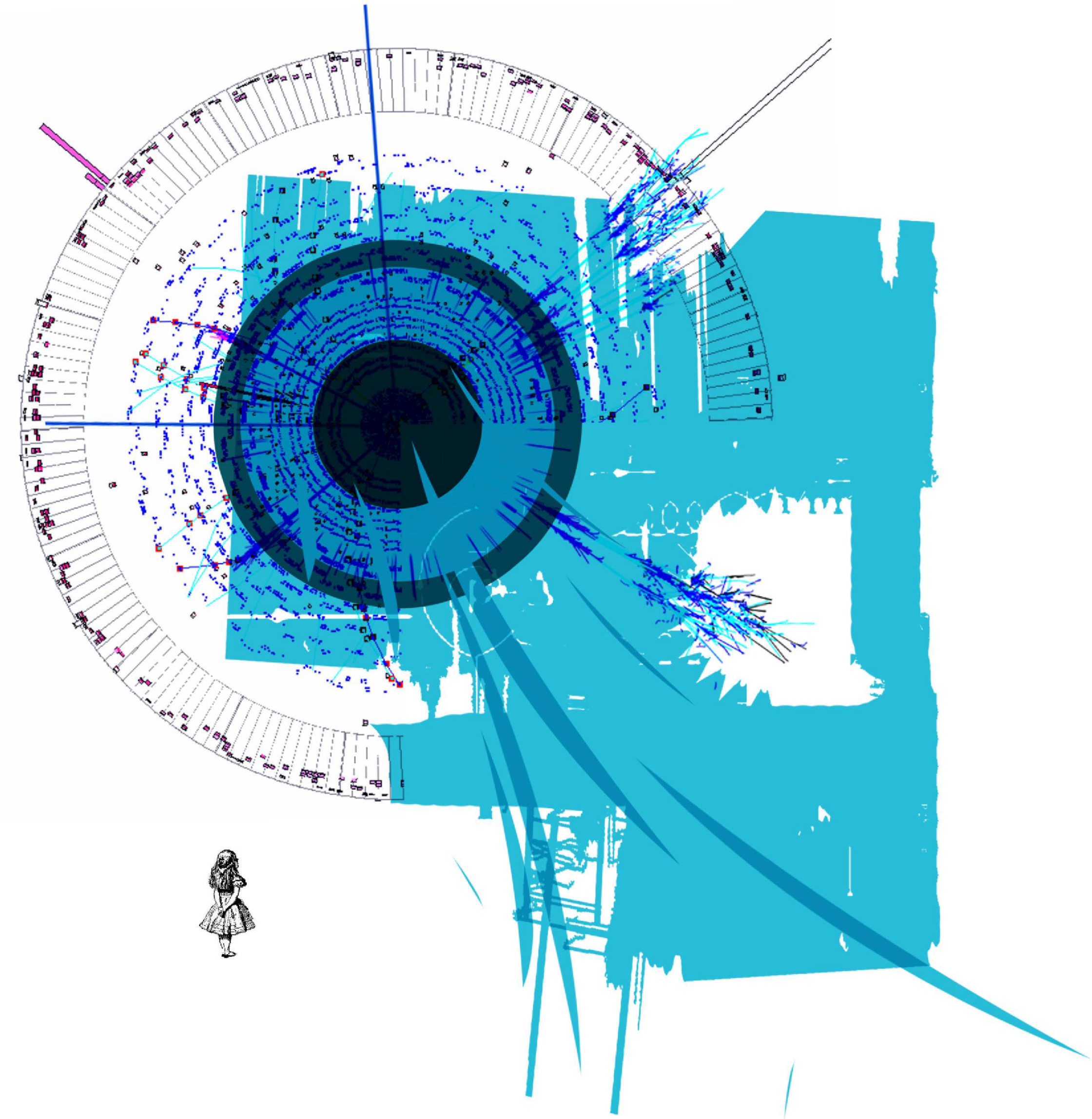

THESIS PRESENTED IN FULFILLMENT OF
THE REQUIREMENTS FOR THE DEGREE OF DOCTOR IN SCIENCE

Dechambre Alice

Université de Liège
Interactions Fondamentales en Physique et Astrophysique
Faculté des Sciences

Year 2010

Quasi-Elastic Production at Hadronic Colliders

Advisor: : J.R Cudell

Member of the jury:

Prof. Joseph Cugnon
Igor P. Ivanov
Christophe Royon
Prof. Jeff Forshaw

President of the jury: Pierre Dauby

Thesis presented in fulfillment of
the requirements for the Degree of Doctor in Science

15 of July 2010

Abstract: Quasi-elastic production is usually viewed as a golden signal for the detection of objects such as the Higgs boson(s) or exotic particles and this is due to the very clean final state and the lack of hadronic remnants after the interaction. In view of the recent data from CDF Run II, we critically re-evaluated the standard approach to the calculation of quasi-elastic cross sections in the high-energy limit and evaluated the uncertainties that affect this kind of process. The main idea of this work was to understand the various ingredients that enter the calculation and the uncertainties coming from each of them. We studied and narrowed down these uncertainties using available data on dijets quasi-elastic event at the TeVatron. All the arguments developed apply to high-mass central systems and lead to a prediction of the Higgs quasi-elastic cross section at the LHC energies.

Résumé: La production quasi-élastique est souvent considerée comme une méthode pouvant conduire à d'importantes découvertes lors de colisions hadron-hadron, en particulier pour la recherche du(des) boson(s) de Higgs ou de particules exotiques. Cela est du à l'absence de pollution hadronique qui rend l'état final de l'interaction très simple. En nous basant sur les données récentes de CDF Run II, nous avons ré-évalué de facon critique l'approche standard pour le calcul de la section efficace quasi-élastique dans la limite à haute énergie. Les incertitudes théoriques qui affectent ce genre de calcul ont également été étudiées en détails. Ce travail a consisté en l'étude des différents éléments qui composent le calcul et à comprendre l'origine des incertitudes provenant de chacun d'entre eux. Nous avons alors pu dégager une méthode d'analyse qui a permis de les réduire en utilisant les données de production quasi-elastique de dijet au TeVatron. Comme tout les arguments développés sont identiques quelque soit le type d'objet massif produit, cela nous a permis de donner une estimation de la section efficace quasi-élastique pour la production du boson de Higgs aux énergies du LHC.

Acknowledgments:

First of all, I want to thank Jean-René. I'm really proud that he was my "third daddy" during my whole PhD-hood, with constant kindness and support in my scientific or day-to-day life. Without even noticing, I had grown up from the shy student I was to a woman ready to fight for her work. I have really appreciated his advice and I hope to be able to honour the knowledge he gave me. I also want to emphasize his courage and abnegation during the corrections to this thesis, especially when dealing with my mistakes.
I particularly thank all the members of the jury and especially Jeff Forshaw for the careful reading of the manuscript and the numerous corrections he made.

I have also learned a lot from Prof. Joseph Cugnon who first believed that I could became a particle physicist one day and who has supported me all these years. I thank all the members of the IFPA group including the numerous visitors. In particular, I thank Igor who started in an impressive way the work presented in this thesis, Mrs Stancu and Oscar for their friendship. A special thank to all the members (permanent or not) of the lunch and coffee breaks on the fourth floor©, for the useful discussions... or not. Davide, the Local Linux Guru© and Alex shall inherit my chair, be worth of it. I would also like to add a thought for all people in the B5 building and across the world but always behind their computers, Aurore and Angeliki who understand exactly what it means to teach physics to physicians and other stuff.
Not so far from Liège, I would like to thank Christophe Ochando, my personal TeVatron advisor and all the people from Saclay. I would also like to thanks Cyrille who introduced me at the IPhT, I really owe him a room in that group. He introduced me to Roby and Christophe that showed me a new direction for my work in addition to their trust and kindness when I was trying to walk by myself in the real world. Thank you for the warm welcome and the 5 o'clock tea. I particularly thank Rafal for all our discussions. When trying to find a solution we were both learning from our experimental-theoretical points of view.
Now I want to thank my family and my parents, my brothers and sisters. Amélie, you are not actually here but I know that you were concerned and followed all my steps, you were there each time I needed, even from the end of the earth. Thanks also to Psoman who made the wonderful cover picture which will add value to my thesis in the future. Méline, you are my soul mate of studies, as you know what scientific studies mean. Be careful with the spiders. You can rely on me all along your way to be a great biologist. Clément, because each time I see you I totally forget about all that scientific stuff. I'm your number one fan! And finally Arthur, "mon petit doudou", I know that growing up is a long and tough process but I totally believe in you. You are maybe the only not physicist to have read the whole thesis, thank you for the corrections and sorry for the sunburn.

My last word is for Vincent. As you were writing your own PhD thesis you said that one day we shall stop giving money to Thalys and it is now time to do so. After long years far away, in which you took care of me regardless of the distance, now I know what I want.

Contents

Introduction **13**

1 Quasi-Elastic Production in High-Energy Physics **15**
- 1.1 Definitions and Variables . . . 15
- 1.2 Standard Scheme of the Calculation . . . 17
- 1.3 Theory of Quasi-Elastic Processes: A QCD Laboratory . . . 19
  - 1.3.1 The Analytic-S-Matrix Description . . . 20
  - 1.3.2 Perturbative QCD Path . . . 22
  - 1.3.3 Unsolved Problems in Diffractive QCD . . . 22
- 1.4 Detectors for Quasi-Elastic Events . . . 25
  - 1.4.1 The TeVatron . . . 25
  - 1.4.2 The Large Hadron Collider . . . 26
  - 1.4.3 Missing-Mass Measurement . . . 30

I Dijet Quasi-Elastic Production **33**

2 Perturbative QCD Calculation **37**
- 2.1 Two-Gluon Amplitude . . . 37
  - 2.1.1 Tools: Contour Integration . . . 38
  - 2.1.2 Toy Calculation . . . 39
- 2.2 The Longitudinal Integral . . . 46
- 2.3 The Overall Picture . . . 48
- 2.4 Two-Gluon Production . . . 49
- 2.5 Gluon Elastic Scattering . . . 53
- 2.6 The Parton-Level Cross Section . . . 57
- 2.7 Comments . . . 57
  - 2.7.1 The Second Diagram . . . 59

3 The Impact Factor **63**
- 3.1 General Properties of Impact Factors . . . 63
- 3.2 Impact Factor from a Quark Model . . . 64
  - 3.2.1 Finding the Parameters of the Model . . . 67
- 3.3 The Unintegrated Gluon Density . . . 68
  - 3.3.1 Impact Factor from the Unintegrated Gluon Density . . . 71
- 3.4 Results and Conclusion . . . 73

4 The Sudakov Form Factor **75**
- 4.1 General Definition of the Resummation . . . 75
- 4.2 Arbitrariness of the Sudakov Form Factor . . . 78
  - 4.2.1 Scales . . . 78

4.2.2 The Logarithmic Contribution and the Constant Terms 80
4.2.3 Sensitivity to the Sudakov Parametrization 83
4.2.4 The Role of the Screening Gluon 86
4.3 Summary of the Uncertainties 88

5 Additional Soft Corrections 93
5.1 Gap-Survival Probability 93
5.1.1 Definition and Method of Estimation 93
5.1.2 Beyond the Gap 96
5.2 The Splash-Out 97
5.2.1 From Partons to Jets 97
5.2.2 Simple Parametrisation of the Splash-Out 100

6 Results and Conclusion 105
6.1 Back-of-the-Envelope Calculation 105
6.2 Numerical Implementation 108
6.3 Presentation of the Numerical Results 109
6.3.1 CDF Run II Data 110
6.3.2 Choice of Parametrisation 111
6.3.3 Uncertainties 115
6.4 Extrapolation to the LHC 115
6.5 Conclusion 118

II Higgs Boson Quasi-Elastic Production 119

7 Searching for the Higgs Boson 125
7.1 Overview 125
7.1.1 Higgs-Boson Production in the Standard Model 125
7.1.2 The Quasi-Elastic Mode 127
7.2 The Durham Model 128

8 Calculation 131
8.1 Higgs Boson Production at the Parton Level 131
8.1.1 Higgs Boson Effective Vertex 132
8.1.2 Phase Space 134
8.2 Higher-Order Corrections 136

9 Estimation of the Higgs-Boson Quasi-elastic Cross Section 139
9.1 Results 139
9.2 Strategy Analysis of Early Data 143
9.3 Summary 144

A Master Formulae and FORTRAN code 149
A.1 Dijet Production 149

B Dijet: Details of the Calculation 153
B.1 Integration by Residue 153
B.2 Lowest-Order Two-Gluon Production in Quasi-Multi-Regge Kinematics 154
B.2.1 s_1u_2 and u_1s_2 Diagrams 154
B.2.2 Single-Crossed Diagram u_1s_2 156
B.2.3 u_1u_2 Diagram 158
B.2.4 Comparison of the Two Main Diagrams 160

B.2.5 The Second Diagram . . . 161
B.2.6 Kinematics . . . 161
B.2.7 Contraction with the First Lipatov Vertex . . . 163
B.3 Sudakov Form Factor . . . 166
B.3.1 The DDT Prescription . . . 166
B.3.2 The Cut-Off Prescription . . . 167
B.3.3 The Sudakov Form Factor with Two Scales . . . 168
B.3.4 Estimation of the Sudakov Suppression . . . 169
B.4 Model of the Splash-Out: LHE files . . . 171
B.5 Parametrisation of the Curves . . . 172

C Higgs: Details of the Calculation **173**
C.1 Some Kinematics . . . 173
C.2 Contribution of W_2 . . . 174

So she was considering in her own mind (as well as she could, for the hot day made her fell very sleepy and stupid), whether the pleasure of making a daisy-chain would be worth the trouble of getting up and picking the daisies, when suddenly a White Rabbit with pink eyes ran close by her.

There was nothing so *very* remarkable in that; nor did Alice think it so *very* much out of the way to hear the Rabbit say to itself, “Oh dear! Oh dear! I shall be too late!” (when she thought it over after-wards, it occurred to her that she ought to have wondered at this, but at the time it all seemed quite natural); but when the Rabbit actually *took a watch out of its waistcoat-pocket*, and looked at it, and then hurried on, Alice started to her feet, for it flashed across her mind that she had never before seen a rabbit with either a waistcoat-pocket, or a watch to take out of it, and burning with curiosity, she ran across the field after it, and fortunately was just in time to see it pop down a large rabbit-hole under the hedge.

In another moment down went Alice after it, never once considering how in the world she was to get out again.

Alice’s Adventures in Wonderland,
Lewis Carrol

Introduction

Quasi-elastic production in proton-proton collisions is a process in which the protons do not break despite the appearance of a high-mass system. This kind of production has two major interests: firstly, the centrally-produced system is within a rapidity gap and clean of hadronic remnants, secondly there is the possibility to measure the energy-momentum lost by the two initials protons and to reconstruct the mass of the centrally produced system without detecting it or its decay products. According to these properties, quasi-elastic processes are viewed as a "superb" channel for exotic particle production [1].
The first evidence for the existence of this kind of events with the production of a high-mass system in hadronic collisions was discovered at the TeVatron and published in 2008 by the CDF collaboration. The data, *i.e.* the cross section of exclusive dijet production, can be used in order to compare the different quasi-elastic models on the market and to constrain the different calculations. In addition, calculations of various quasi-elastic processes are based on the same ingredients, hence when the parameters are fixed using the dijet data one can use them to make a prediction on other processes, as for instance Higgs boson(s) quasi-elastic production.

This family of processes has small cross sections but their final state is simple and free of hadronic pollution (except from pile-up). This characteristics can be important at the dawn of the LHC era. The energy in the center-of-mass frame of the CERN proton-proton collider should reach 14 TeV and will cross 1.15×10^{11} protons every 25 nanoseconds at its nominal operating condition. This means that a huge number of particles should be produced every 25 nanoseconds and the four main detectors will have to handle very complex final states. For that reason, even if the cross sections of quasi-elastic processes are small, their identification and the identification of the produced particles is simplified by the possibility to search for gaps in the central detector and for protons in forward detectors. At the LHC, quasi-elastic processes are competitive and as I write these lines[1], the very first proton collision has been observed by the ATLAS and CMS experiments, so that, the hunt is opened.

From the phenomenologist point of view, the calculation of quasi-elastic processes at high-energy is one of the most complete and open topics as it involves many aspects of QCD, from perturbative tree-level calculations to non-perturbative corrections. Theoretically, high-energy diffractive calculations lead to relatively good predictions especially in the domain of hard interactions but their richest interest is the possibility to improve and constrain the model using data. This duality, to learn from both theory and data, to request theoretical knowledge for the basis and data for the details or the other way around, always leads to an interesting interplay between experimentalists and theorists as one needs an understanding of the process from the paper to the detector. Because Nature will always surprise physicists and give them new phenomena to explain, high energy quasi-elastic calculations are a fascinating playground for phenomenologists and experimentalists alike.

---

[1] November 24, 2009 in the SPP Building at Saclay.

Chapter 1

Quasi-Elastic Production in High-Energy Physics

A quasi-elastic process is possible from the exchange of a colour singlet and these quasi-elastic events are part of a wider class, the diffractive events, which are characterized by a rapidity gap in the final state, between the centrally produced system and the remaining hadrons. This was suggested by Bjorken [1] as a means of detecting new physics in hadron-hadron collisions because of the very simple final state in which rare particles can be produced and decay without background.

In this chapter, we define quasi-elastic processes and related quantities before explaining their interest from both theoretical and experimental points of view. In the second section, we give the standard scheme of the calculation and each ingredient is introduced before being studied in details. Because diffractive physics is often synonym of pomeron physics, we briefly introduce present issues about the pomeron and diffraction in Quantum Chromo-Dynamics (QCD) and finally, we describe two machines able to study quasi-elastic processes in hadronic collision, the TeVatron and the LHC as well as their dedicated detectors.

1.1 Definitions and Variables

Events with a large rapidity gap between the produced particles and the nucleons in the final state have several names. Diffraction is the generic term and the first authors to give a description of hadronic diffraction in modern terms were Good and Walker [2] who wrote in 1960:

A phenomenon is predicted in which a high energy particle beam undergoing diffraction scattering from a nucleus will acquire components corresponding to various products of the virtual dissociations of the incident particle [...] *These diffraction-produced systems would have a characteristic extremely narrow distribution in transverse momentum and would have the same quantum numbers of the initial particle.*

A hadronic diffractive event is then an elastic event or an event with a rapidity gap but where the initial particles break, giving rise to a bunch of final particles which carry the same quantum numbers as the initial state. In the present work, we are studying a particular case of diffraction with corresponds to the production of particles within a rapidity gap that we shall call quasi-elastic, considering the fact that it keeps initial hadrons intact as in an elastic collision. In the literature, the same phenomenon is sometimes called exclusive production because all final state objects, be they particles or jets, are detected. However, we think that this can be confusing as the term is used to describe events where all particles in the final state were detected, *i.e.* centrally produced particles and the remains of the colliding one. In the following, we shall exclusively talk about quasi-elastic production and let us start with a reminder of the vocabulary and pertinent variables.

In a detector, particles can be located using two variables, the azimuthal angle ϕ and the pseudo-rapidity η defined as

$$\eta = -\log\left(\tan\frac{\theta}{2}\right), \tag{1.1}$$

where θ is the usual polar angle and so a measurement of θ leads to a measurement of η. Note that particles or jets with a large pseudo-rapidity are called forward. For high-energy particles, pseudo-rapidity tends to rapidity defined as

$$y = \frac{1}{2}\log\frac{E+p_z}{E-p_z}, \tag{1.2}$$

where E and p_z are respectively the energy of the particle and the component of its four-momentum along the z axis. Rapidity is the key variable in diffractive processes because the large non-exponentially suppressed rapidity gap in the final state makes it easily recognizable from central inelastic hadronic scattering. Indeed, the latter has a flat distribution of particle rapidity due to soft interactions between the two colliding particles as shown in Fig. 1.1. If there is any particle production during the process, the centrally-produced system is within the gap. Actually, there are three different types of event that can give this particular final state, namely:

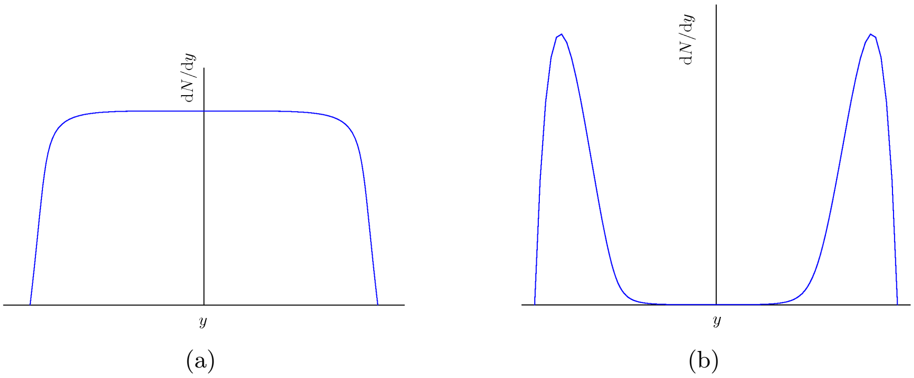

(a) (b)

Figure 1.1: Schematic picture of the rapidity distribution of the products of (a) a central hadronic scattering and (b) a diffractive hadronic scattering.

Quasi-elastic production: Both incoming hadrons emerge intact in the final state, see Fig. 1.2.a.

Single-diffractive production: Only one of the incoming hadrons emerges intact, the second breaks but the final system has the same quantum numbers as the initial one, see Fig. 1.2.b.

Double-diffractive production: Both initial hadrons break, see Fig. 1.2.c.

The corresponding rapidity picture of these processes is also drawn in Fig. 1.2. The coloured area represents the rapidity region where particles can be detected while the white, the lack of hadronic remnants that corresponds to the gap. In diffraction, the final hadrons are broken but for quasi-elastic processes, the kinematics is constrained in the region where the energy lost by the initial hadrons, Δ_i is small in order to keep them forward. In high-energy physics, the quantity Δ_i is one of the essential variables directly related to the fraction of energy lost by

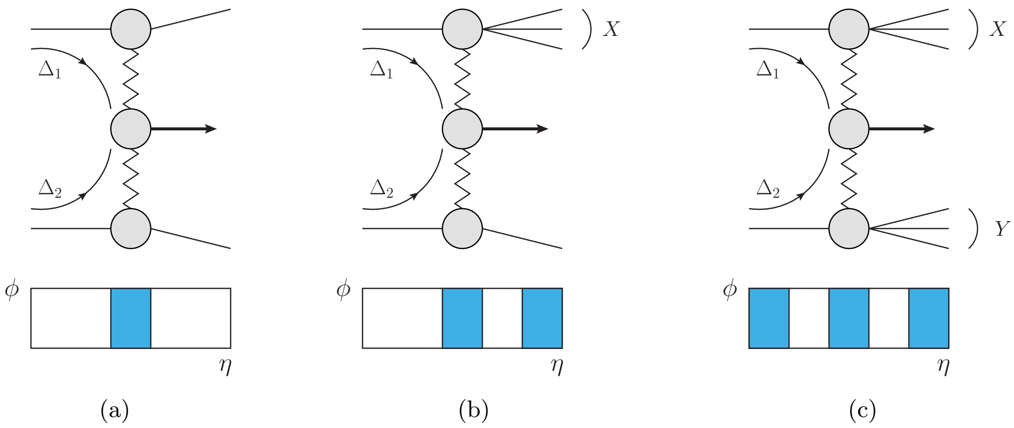

(a) (b) (c)

Figure 1.2: The three types of diffractive production and the resulting picture of the final state in rapidity in the central detector. The zigzag line denotes the exchange of a colour singlet and Δ_i is the energy lost by the initial hadrons.

the proton (antiproton). If p is the four-momentum of one of the incoming hadrons and ξ_i the longitudinal fraction lost by the same hadron then, in the approximation of negligible transferred transverse momentum, one has

$$\Delta_i \simeq \xi_i p, \tag{1.3}$$

and one can show that the relation between the mass of the centrally produced system and the energy in the center-of-mass frame of the collision s reads,

$$M^2 \simeq \xi_1 \xi_2 s \ll s. \tag{1.4}$$

The advantage of a quasi-elastic process is then a distinctive final state. In addition, this kind of process allows one to reconstruct the mass of the central system from the measurement of the fraction of momentum lost by the initial hadrons. We shall see that this is the event topology that is really interesting for current detectors and when one has the correct ingredients, the theoretical calculation of the cross section gives relatively good agreement with available data.

1.2 Standard Scheme of the Calculation

Quasi-elastic processes have been studied from various points of view and within different models [3–16]. The basis of all calculations is the set of tree-level diagrams involving quarks and gluons, upon which one has to add virtual and soft corrections in order to reproduce the full process, from the hadron collision to the final state. The first group who put together most of the necessary ingredients was the Durham group [16, 17]. In this thesis, we present a model made of five ingredients, related to the Durham scheme, but somewhat different. The various parts of our model are as follows.

The parton-level calculation: The first ingredient is the analytic computation of all Feynman diagrams that describe the production of a colour-singlet and keep the colour of initial particles. It is schematically shown in Fig. 1.3.a, the calculation is under theoretical control. It can be done using cutting rules or direct integration within the kinematical regime where the momentum lost by the initial particles is small. In particular, we made efforts to keep an exact transverse kinematics all along the calculation. The lowest-order cross section is presented in Chapter 2. We discuss there the details of the calculation, the effect of approximations used in [16, 17] and the contribution of diagrams in which the screening gluon participates to the hard sub-process, diagrams that were neglected in previous works.

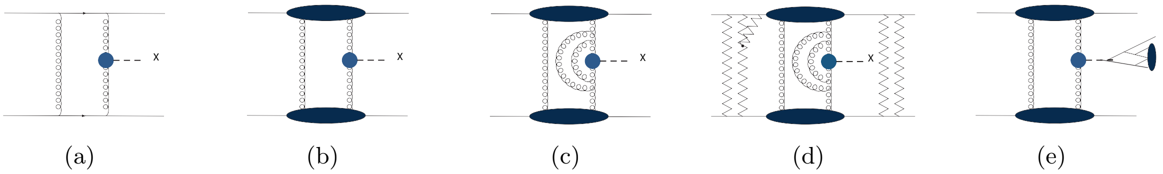

Figure 1.3: Standard scheme of a quasi-elastic cross section calculation with its various steps.

The impact factor: To describe a collision at the LHC or at the TeVatron, one needs protons (anti-protons) in the initial state. Therefore, the first correction is the introduction of an impact factor that models the behavior of real protons and embeds the quarks as represented in Fig. 1.3.b. The model of the proton includes soft physics and relies on a phenomenological description. Following references [14] and [18], we use theoretical models for the impact factor based on the composition in quarks, light-cone wave-functions, dipole form factor, ... and tuned to different data (elastic cross section, gluons density, ...). The impact factor is described in Chapter 3 where we consider two ways to embed the perturbative calculation into the proton. The uncertainties coming from the fits will be carefully evaluated.

The Sudakov form factor: One of the most important ingredients of the calculation is the Sudakov form factor, *i.e.* large double-logarithmic terms that suppress the cross section by a factor of the order of 100 to 1000. It corresponds to virtual vertex corrections and in the Higgs case, it is calculated to subleading-log accuracy [19–21]. However, in the dijet case the single-log contributions have to be evaluated completely and several questions remain. In particular, the dijet vertex cannot be considered point-like at all scales and consequently, we claim that the hard scale of the process is not anymore related to the invariant mass of the dijet system. Moreover, we have found that leading and subleading logs that are resummed to give the Sudakov form factor are not dominant for the whole momentum range, *i.e.* the constant terms are numerically important. This topic and related issues are developed in Chapter 4.

The gap-survival probability: This is the probability that the gap survives after the first interaction. The initial protons that stay intact may re-interact and possibly produce particles that might fill the gap created at the parton level as schematically shown in Fig. 1.3.d. The gap-survival probability is also the probability to have no inelastic interactions between the two remaining protons. It is treated as a factor that multiplies the cross section and is discussed in Chapter 5.

The splash-out: The last piece of the calculation is at the very border between theory and experiment. Before its introduction, one is left with a cross section for partons in the final state. To go from partons to real hadrons or jets observed by experimentalists, there are several steps, *i.e.* parton showering, hadronization, jet reconstruction algorithms and tagging. This last step is tricky: as there is no perfect matching between the reconstructed jet and the parton that gives birth to it, one can loose some energy from parton to jet and this loss of energy is the splash-out. It is usually treated as a factor and even if reference [22] considered it, its effect was not really studied in details. In Chapter 5, we shall show how it is possible to use Pythia and a Monte-Carlo study to approximate the probability to have a jet of transverse energy $E_\perp^{\text{jet}}$ from a parton of energy $E_\perp^{\text{parton}}$.

Each piece of the calculation can be investigated separately, the theoretical approaches developed and the uncertainties evaluated. The phenomenological description of quasi-elastic processes is thus based on the assumption that each ingredient can be studied separately as they matter at different scales, typically two well separated hard and soft scales. The important point is that some of the corrections are identical in all quasi-elastic processes so that they can be studied in one particular process then used in another. Consequently, the main idea of the present thesis is to use available data to constrain the different prescriptions for the corrections, *i.e.* impact factor, Sudakov form factor, gap survival, splash-out, and this should lead to a more precise prediction of quasi-elastic cross sections for non-yet observed processes as well as improve our knowledge in different aspects of QCD. In particular, we focus on the uncertainties and show how it is possible to use the TeVatron data to reduce some of them. Using that knowledge, we shall extrapolate the model to predict the cross section for dijet and Higgs boson quasi-elastic production at the LHC.

The plan of the thesis is then the following. The first part is devoted to the dijet quasi-elastic cross section [23]. All ingredients described above are studied in details and the uncertainties that affect the calculation are evaluated at each step. The second part treats the Higgs boson quasi-elastic production [24] in the same way and explains how uncertainties are narrowed down using the dijet study. All results will be presented for both the TeVatron and the LHC.
Nevertheless, before coming to the effective calculation, we shall say a few words about the theory behind quasi-elastic scattering and about the detectors built to study this kind of processes in high-energy physics.

1.3 Theory of Quasi-Elastic Processes: A QCD Laboratory

Quasi-elastic processes provide a laboratory where several aspects of QCD can be investigated: soft and hard interactions, exotic particle production, non-perturbative effects or high-energy behavior of the cross section. The present section focuses on the interest from the theoretical side and we start with the history of diffraction. We continue with two different philosophies of the theory behind quasi-elastic scattering while the last section is dedicated to some of the related unsolved problems of QCD.

With the first high-energy hadron accelerators, one needed to describe the dynamics of the produced events and the observed slow increase of the total cross section with the center-of-mass frame energy [25, 26]. The first success of elastic scattering theory, and consequently of diffraction, was to find a mechanism that explained the behavior of the total cross section at high-energy by the exchange of an object with the quantum numbers of the vacuum called the pomeron [27]. It was the pre-QCD epoch of Regge theory where physicists tried to describe strong interactions within a robust mathematical model of the scattering matrix [28–30]. They focused first on the study of elastic and exclusive processes, *i.e.* reactions where the kinematics of the final state is fully reconstructed. Ten years later, the theory of quarks and gluons was born [31, 32] and a lot of people chose to turn to inclusive processes where one considers only total rates of production. In the new framework of QCD, the theorem of factorisation [33] allows to separate the hard interaction, that produced the leading particles and can be calculated perturbatively, from the soft ones. Unfortunately no such theorem exists for the diffractive case. In the last two decades, diffractive processes made a come back with the observation of rapidity gap events at HERA [34], followed by the diffraction program of TeVatron. The presence of the rapidity gap was then identified by Bjorken [1] as an interesting signature and the interest

in diffraction started slowly to be reborn. It quickly appeared from HERA that this kind of events has properties from soft and hard physics at the same time. The idea of hard diffraction was born in 1984 from Donnachie and Landshoff [35] and developed later by Ingelman and Schlein [36], who tried to factorise the soft and hard interactions so that QCD would formulate the hard collision in terms of quarks and gluons. One would have the possibility from this basis to extend the calculation to the non-perturbative region where soft exchanges occur. It was rapidly confirmed by the H1 and ZEUS collaboration in 1993 that hard diffraction exists and few years later, by the UA8 experiment at CERN $p\bar{p}$ collider [37] but also by the CDF and $D\emptyset$ collaborations at the TeVatron [38]. Unfortunately, it also appeared the the Ingelman-Schlein factorisation did not work.
One can show that colour-singlet exchange between high-energy protons is a very common event, about 25% of the cross section at TeVatron[1] is from elastic scattering $p\bar{p} \to p\bar{p}$ and another 20% is due to single-diffractive or double-diffractive scattering. Hence, this aspect of QCD is important and will be even more so at the LHC where the center-of-mass frame energy should be equal to $\sqrt{s} = 14$ TeV[2]. This energy will increase the rate of elastic scattering to about 30% of the total cross section [39] and may allow the production of heavy particles as for example, the wanted Higgs boson(s).

At present, quasi-elastic production is considered as a rich topic of hadronic physics. The signature of events is one of the cleanest and the mathematical basis are defined even if important questions and issues subsist. We shall now describe the basic concepts of quasi-elastic scattering from two points of view. The first is a description from the analytic-S-matrix theory as soft exchanges with an additional hard interaction, the second starts with the hard inclusive process and introduced afterward soft corrections to make it quasi-elastic.

1.3.1 The Analytic-S-Matrix Description

Before the rise of QCD, the first attempt to describe strong interactions relied on the properties of the scattering matrix S. In this framework, all scattering processes are described by their singularities in the complex-J plane. In the simplest case, these singularities are poles and represent the exchange of an infinite number of bound states with the same quantum numbers, except for the spin. The theory predicts the asymptotic behavior of the cross section, *i.e.* its behavior in the limit where the center-of-mass frame energy is much larger than the exchange momentum $|t|$ and than all masses. Note that is exactly what we requested for quasi-elastic events in Eq. (1.3).

Without going into much detail, the phenomenological description of scatterings using the analytic S-matrix gives the s-channel high-energy behavior of the amplitude due to the exchange of a family of resonances in the crossed channel. The ensemble of resonances with the same quantum numbers[3] lies on a "Regge trajectory" that is a function of t and reads

$$\alpha(t) = \alpha(0) + \alpha' t. \tag{1.5}$$

The constant $\alpha(0)$ is called the "intercept" and α' is the "slope". There exists different trajectories characterized by the quantum numbers of their resonances and by their slope and intercept. In the S-matrix phenomenology, the amplitude of a given elastic-scattering process is proportional to a power of s

---

[1] From the Particle Data Group.

[2] Up to now, it appears that due to technical reasons, the LHC should run between $\sqrt{s} = 7$ TeV and $\sqrt{s} = 10$ TeV.

[3] Parity, charge conjugation, G-parity, isospin, strangeness, etc. apart for their spin.

$$\mathcal{A} \propto s^{\alpha(t)}. \tag{1.6}$$

Here $\alpha(t)$ is the Regge trajectory corresponding to the quantum numbers of the exchange. The total cross section is related by the optical theorem to

$$\sigma_{tot} \simeq \frac{1}{s}\mathrm{Im}\left(\mathcal{A}(0)\right) \sim s^{\alpha(0)-1}. \tag{1.7}$$

At high energy only the highest-spin trajectory contributes and the others are suppressed by a power of s, but if more than one pole are exchanged then the cross section is given by a sum over all contributions

$$\sigma_{tot} \propto \sum \mathcal{A}_i s^{\alpha_i(0)-1}. \tag{1.8}$$

The values of the slope and the intercept for a given trajectory can be obtained by a fit to total cross-section data for different processes or center-of-mass frame energies. The important point is that the S-matrix description leads to a parametrisation of high-energy scatterings for a large set of data but only in the limit of small momentum transfer. This means that one has here a representation of soft exchanges between colliding particles. Note that the exchange of a Regge trajectory (or reggeon) is usually represented as in Fig. 1.4.a. To explain the growth of the cross section, the pomeron trajectory was introduced, see for instance Sec. 1.3.3. High-energy elastic scattering is thus described by the exchange of a trajectory with the quantum numbers of the vacuum[4] and with an intercept of the order of 1. One of the remaining problems is the description of multiple pomeron exchanges, this in turn will lead to an uncertainty in the gap-survival probability.

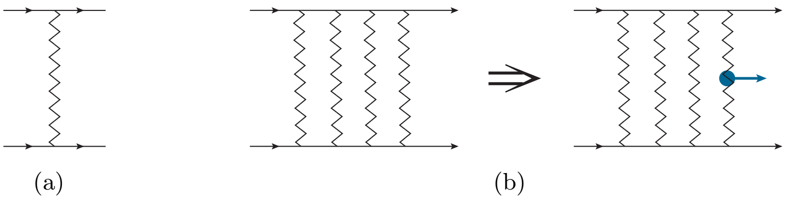

Figure 1.4: (a) Exchange of a Regge trajectory or reggeon. (b) Inclusion of a hard scattering into the soft exchange. The hard subprocess can be attached to any of the exchanged pomerons.

In the framework of the analytic scattering matrix, one can see quasi-elastic production as the embedding of a hard interaction into the above soft exchange schematically pictured in Fig. 1.4.b. Two pomerons emitted from the incoming hadrons collide at very short distances and this collision can be treated separately from the rest of the exchange due to the presence of a hard scale. The argument is essential and allows to treat separately the hard and the soft interaction, the former can be calculated perturbatively and the latter parametrised, *e.g.* by its slope and intercept, using Eq. (1.7) and elastic cross section data. The quasi-elastic production of any particles is then written in a factorised form

$$\sigma = \mathcal{F}_{\mathbb{P}}(|t|, s) \times \hat{\sigma}, \tag{1.9}$$

where $\hat{\sigma}$ is the hard scattering and $\mathcal{F}_{\mathbb{P}}$ is either a pomeron flux or a phenomenological soft pomeron that includes, in both cases the dependence in s of the cross section. This picture of pomeron flux is used by the Durham group and in Chap. 7 and can be also found in Chap. 3,

---

[4] P=+1, C=+1, I=0.

where we shall use a Regge factor to take into account the dependence of the quasi-elastic cross section on the center-of-mass frame energy.

1.3.2 Perturbative QCD Path

Quasi-elastic production with gluon fusion can be analysed from the point of view of standard perturbative QCD (pQCD), provided several modifications are made. If one starts with the usual gluon fusion schematically presented in Fig. 1.5, quasi-elastic production can be obtained by the addition of a gluon in the t-channel in order to have a colour-singlet exchange.

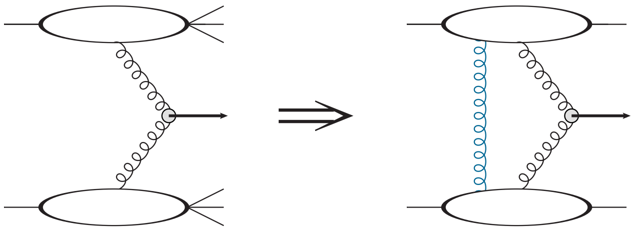

Figure 1.5: Production by gluon fusion.

What seems easy at first sight is not in fact. The hard subprocess producing the final particle is identical in both inclusive and quasi-elastic cases but, in the inclusive case, the cross section is summed over all possible final states. In particular, the additional soft exchanges between final particles disappear in the sum and the calculation is perturbative. Furthermore, at the cross-section level the proton structure functions are well defined in the framework of QCD and can be measured in different experiments. Three decades of data taking over several ranges of energy in the center-of-mass frame and transferred momentum have led to a precise knowledge of these quantities.

In the quasi-elastic case, the addition of the soft screening gluon that prevents colour flow in the t-channel and the exclusivity of the event definitively change the picture. The factorisation theorem doesn't hold and the proton structure functions, that needs to be defined here for very small transferred momenta, cannot be used anymore. Furthermore, as the final state is now specified, all soft interactions between the different particles of the system should be added. This includes in fact, higher-order and soft corrections in the form of a Sudakov form factor and gap-survival probability, that cannot be fully computed using pQCD and consequently have to be modeled or fitted to data, bringing in the same time large uncertainties on the final result.

1.3.3 Unsolved Problems in Diffractive QCD

Diffraction and consequently quasi-elastic production seems to have reached a level where one knows which elements of the cross section are needed to reproduce the data. Moreover, the relatively good agreement between calculations and data suggests that diffraction might be described by the theory of strong interactions [40]. However, diffraction is at the border of our understanding of QCD and this leads to results affected by large theoretical uncertainties. We stress that the analysis presented here, with the help of recent CDF data, may lead to an improvement in our knowledge of the deep details of quasi-elastic production. Hence, we briefly discuss two different issues to give a general idea of the problems one has to deal with when working on diffractive physics: the nature of the pomeron and the non-perturbative regime of QCD.

The Nature of the Pomeron

The pomeron exchange is responsible for the slow rise of the total cross section with s and is called after its inventor Pomeranchuk [27]. In the present section, we shall remind the reader of the outstanding issues connected with the pomeron $\mathbb{P}$ in QCD.

In the theory of the analytic S-matrix, and as explained in Sec. 1.3.1, a two-body scattering process is described in terms of an exchange of Regge trajectories in the t-channel. The asymptotic behavior of the total cross section with s is related to the intercept $\alpha(0)$ of the leading trajectory by

$$\sigma_{\text{tot}} \underset{s\to\infty}{\sim} \frac{1}{s}\text{Im}A(s,t=0) \underset{s\to\infty}{\sim} s^{\alpha(0)-1}. \tag{1.10}$$

The known mesonic trajectories have intercepts smaller than 1 and thus, their exchange leads to a decrease of the total cross section with s. Nevertheless, the total cross section increases with energy and this unexpected behavior can be explained by the introduction of an additional trajectory, dominant at high energy and with a intercept slightly larger than one [29, 30]. The bound states corresponding to the pole are not related to any known particles but it is usually admitted that they should be bound states of gluons called glueballs[5].

The parameters, slope and intercept, of the pomeron trajectory can be extracted from a fit to elastic scattering data. This was done by Donnachie and Landshoff in [42] and recently refitted to

$$\alpha_{\mathbb{P}}(t) = 1.09 + 0.3\,t, \tag{1.11}$$

in the region 0.5 GeV$^2 < |t| < 0.1$ GeV^2 and 6 GeV $< \sqrt{s} <$ 63 GeV [43]. It can be argued that an intercept larger than one would eventually violate the Froissard-Martin bound but multiple-pomeron exchanges should prevent the breakdown of unitarity at higher energy.

The difficulty with the pomeron is that, besides an ad-hoc description of the data, its exact nature is not well known considering that QCD is unable to predict the value of the intercept. Actually, there exists in the literature two main, but rather different, physical pictures of the pomeron sometimes called the soft and the hard pomeron. The former is a simple but accurate parametrisation of Regge theory in a large region of data that leads to a small intercept $\alpha_{\mathbb{P}}^{\text{soft}} \simeq 1.1$, in the limit of small momentum transfer. The latter derives from the huge efforts made in the calculation of the exchange of a gluon ladder between two interacting quarks in the framework of pQCD. The pomeron amplitude is then the result of the summation of leading and subleading $\log(s)$ contributions from a number of diagrams and is summarised by the BFKL equation developed by Balitsky, Fadin, Kuraev and Lipatov [44–47]. The equation includes all transverse momenta, from soft contributions to hard ones, so that all scales are mixed. This hard pomeron is sometimes called the BFKL pomeron and has an intercept of $\alpha_{\mathbb{P}}^{\text{hard}} \simeq 1.5$ at the leading-log level. Nevertheless, the BFKL approach may reproduce the data only with huge non-leading corrections [47] and in addition, the calculation is very sensitive to details of the IR region where one has to include non-perturbative corrections that complicate the solution [48, 49]. Up to now, the pomeron is just something that makes the cross section increase with energy and a lot of questions still remain open.

The attempts to describe the nature of the pomeron raise several interesting questions about the scales one is studying in QCD. Experimentalists are left with a huge amount of data from processes that include hard scales and soft scales. Each of the kinematical regimes are described using different parametrisation but also different regions of QCD since the soft pomeron is

---

[5] Glueballs are expected to be the bound state of at least two gluons, there is now a 2^{++} candidate and one can find more details about them in reference [41].

highly non-perturbative whereas the hard one is a perturbative object. It is clearly important to understand what happens between these two regions and this is why processes at the border, such as hard diffraction and quasi-elastic processes, are still a laboratory where QCD dynamics at different scales can be studied.

Non-Perturbative Aspects of Diffraction

After the discovery of QCD, the idea of a pomeron pictured as a two-gluon exchange was proposed by Low and Nussinov [50, 51] as the simplest way to model a colour-singlet with the quantum numbers of the vacuum. At the Born level, these gluons couple to quarks inside the incoming hadron as shown in Fig. 1.6. Rapidly, it appeared that this simple perturbative picture wasn't sufficient to explain data due to the IR sensitivity of QCD as a non-abelian gauge theory with confinement. We shall see in Chap. 2 and Chap. 4 that results strongly depend on the details of this regime.

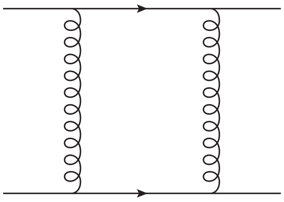

Figure 1.6: Elastic scattering via pomeron exchange modeled at the Born level through the exchange of two gluons in the t-channel. The crossed diagrams are not represented here.

Non-perturbative effects naturally appear in the soft corrections to the calculation, *i.e.* in the impact factor and in the gap-survival probability. As they cannot be calculated in pQCD, one has to use instead fits to data or phenomenological models. Hence, those parametrisations are automatically and irremediably plagued by large uncertainties. One has to allow this introduction of non-perturbative effects in the calculation and try to learn as much information as possible from the data in order to build models and reach a reasonable precision on the cross section. This is what we shall do for the quasi-elastic case in Chap. 5 and Chap. 6.

Another interesting manifestation of the non-perturbative regime in the calculation is the softness of exchanged gluon momenta. Consequently, if one wants to go beyond the usual perturbative assumption, the gluon propagator can be modified and this technique is sometimes used to remove the IR divergence of the parton-level amplitude as the IR sensitivity of QCD comes in part from the gluon propagator itself. One expects the perturbative propagator to be different from the exact propagator of QCD. In particular, one can only trust its shape when the coupling of QCD becomes small, *i.e* above twice the mass of the charm quark m_c [52]. Purely perturbative calculations in QCD use the gluon propagator

$$D_{\mu\nu}(k^2) = \frac{-ig_{\mu\nu}\delta^{ab}}{k^2 + i\epsilon}, \tag{1.12}$$

in the Feynman gauge where a and b are colour indices [53]. The IR problem largely comes from the pole at $k^2 = 0$ since poles on the real axis correspond to real particles that propagate far away in space, such a pole is not permitted because gluons are confined. In order to model the non-perturbative dynamics of QCD that cannot be calculated exactly in the absence of a hard scale, some authors proposed to derive phenomenologically a new gluon propagator. Landshoff and Nachtmann [48] proposed a propagator in the form of a falling exponential

$$D_{\mu\nu}(k^2) = C\, e^{k^2/\Lambda^2}, \tag{1.13}$$

that is finite for $k^2 = 0$ and where Λ is a constant related to the scale at which non-perturbative effects begin to appear. According to Gribov, it is also possible to improve the quantization of non-abelian gauge fields and this leads to a gluon propagator of the form [54],

$$D_{\mu\nu}(k^2) = \frac{-ig_{\mu\nu}\delta^{ab}}{k^2 + \frac{\Lambda^4}{k^2}}. \tag{1.14}$$

The divergence vanishes because the propagator is null at $k = 0$ and the consequences of the use of such a propagator in two-gluon exchange was previously studied in [55]. There also exists several other possibilities, *e.g.* adding directly an effective mass μ_g for the gluon. All these attempts to include the contribution of the non-perturbative region into the calculation constitute an important step towards the full description of diffractive processes and more generally of QCD processes. However, these corrections are tentative at best as if one wants to be complete, the vertices should also be modified and this is even more complicated. The understanding of the non-perturbative contributions implies a larger treatment, that is up to now far from our present capabilities.

We shall show that the non-perturbative aspects of the calculation are important and that results are sensitive to the details of this regime of QCD but the present knowledge and methods don't allow to derive those parts reliably, so that one has to use models or fits.

1.4 Detectors for Quasi-Elastic Events

The identification of diffractive events can be done through the particular pattern of the final state and is improved by the presence of dedicated forward detectors. In this section, we shall give a short overview of the present and future detectors able to study details of diffraction at the TeVatron or the LHC. In the second section, we shall describe the experimental method that can be used to reconstruct the mass of the centrally produced system in a quasi-elastic collision.

1.4.1 The TeVatron

The TeVatron is named after the energy −of the order of 1 TeV− of the proton and antiproton beams that circulate at the Fermi National Accelerator Laboratory in Illinois. Due to several successful upgrades since its start in 1983, the energy in the center-of-mass frame is exactly 1.960 TeV for the Run II events. The TeVatron has been the highest-energy particle collider in the world for a long time and its success was the discovery by CDF and D∅, of the top quarks in 1995. Up until now, the TeVatron collaborations are still trying to find the Higgs boson before the LHC.

The particularity of the TeVatron is that it collides protons and antiprotons, and as they have opposite charges, beams travel through the same beam pipe in opposite directions. There are two interaction points positioned at opposite sides of the ring as shown in Fig. 1.7. The two detectors, CDF for Collider Detector at Fermilab [56, 57] and D∅ [58, 59] are built differently, but both are classical devices for particle physics in which the different sensitive layers are placed in a concentric way around the beam axis. First a tracker system, then a electromagnetic calorimeter, then an hadronic calorimeter and finally a muon detector. In addition, both CDF and D∅ are equipped with forward detectors that extend the rapidity coverage beyond 3.6 and those detectors can be used to study diffraction during the low-luminosity phases as they principally collect particles scattered at small angles.

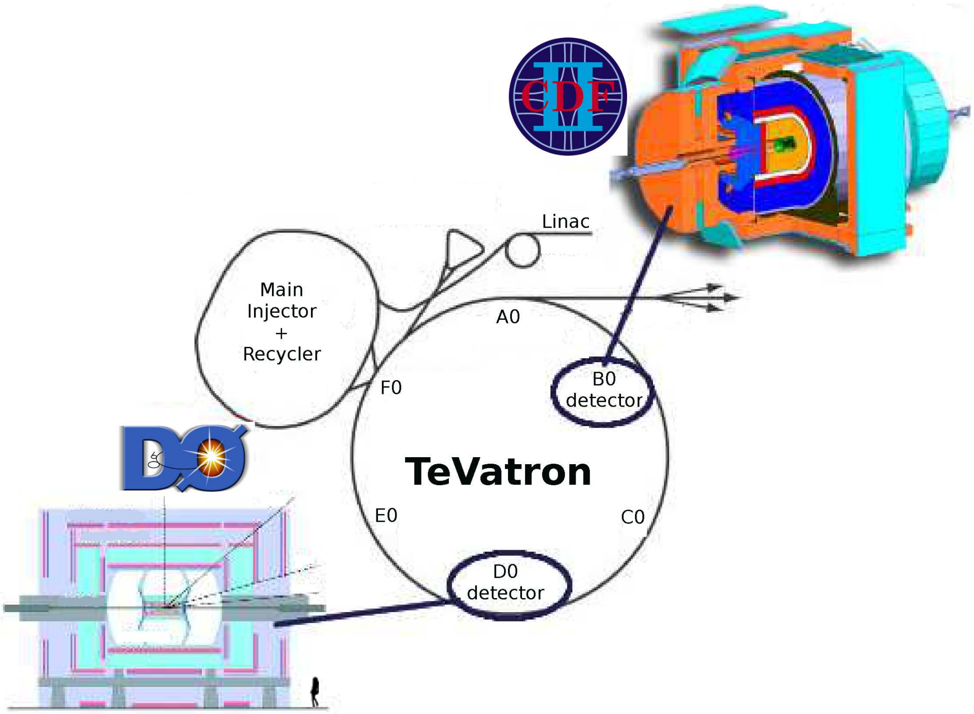

Figure 1.7: Map of the TeVatron. Adapted from [58, 60].

In CDF, which published in 2008 the dijet quasi-elastic cross section measurement, the very forward instrumentation is composed of three Roman pot stations located about 57 m downstream in the antiproton beam direction. Each contains a scintillation counter used for triggering on the final anti-proton of quasi-elastic or elastic collisions. Note that there is no very forward detector on the proton side that hence is not detected.

1.4.2 The Large Hadron Collider

The Large Hadron Collider (LHC) was approved in December 1994 but the construction started only at the beginning of 2004 in the old LEP tunnel. Since March 2010, the circulation of the beams and the first collisions have been achieved and the data taking started at an energy of $\sqrt{s} = 7$ TeV. During the recent Workshop on LHC Performance held in Chamonix in January 2010, it was decided to run at this energy until summer or autumn 2011 and by the end of the year, one hopes to achieve a luminosity of 3.1 10^{31} $\text{cm}^{-2}\text{s}^{-1}$ [61, 62]. This should be followed by a long shutdown to allow the necessary works to reach the LHC design energy of $\sqrt{s} = 14$ TeV.

The LHC has a circumference of 27 km dug at 175 m underneath two countries, France and Switzerland. Along the tunnel, two beams of protons run in opposite directions inside two beam pipes and their rotation are controlled by over 1600 superconducting magnets cooled at -271.25 °C. This allows engineers to circulate bunches of protons close to the speed of light and with an energy of several TeV per protons. The nominal commissioned energy of the beam is 7 TeV, leading to collision of 14 TeV in the center-of-mass frame. However, the recent issues with the supra-conducting magnets have been followed by an early stage of run at 3.5 TeV per beam that should allow interesting high-energy studies. The two beams can be collided in the four points of Fig. 1.8, named interaction points (IP), where are built detectors that collect the particles produced during the interaction.

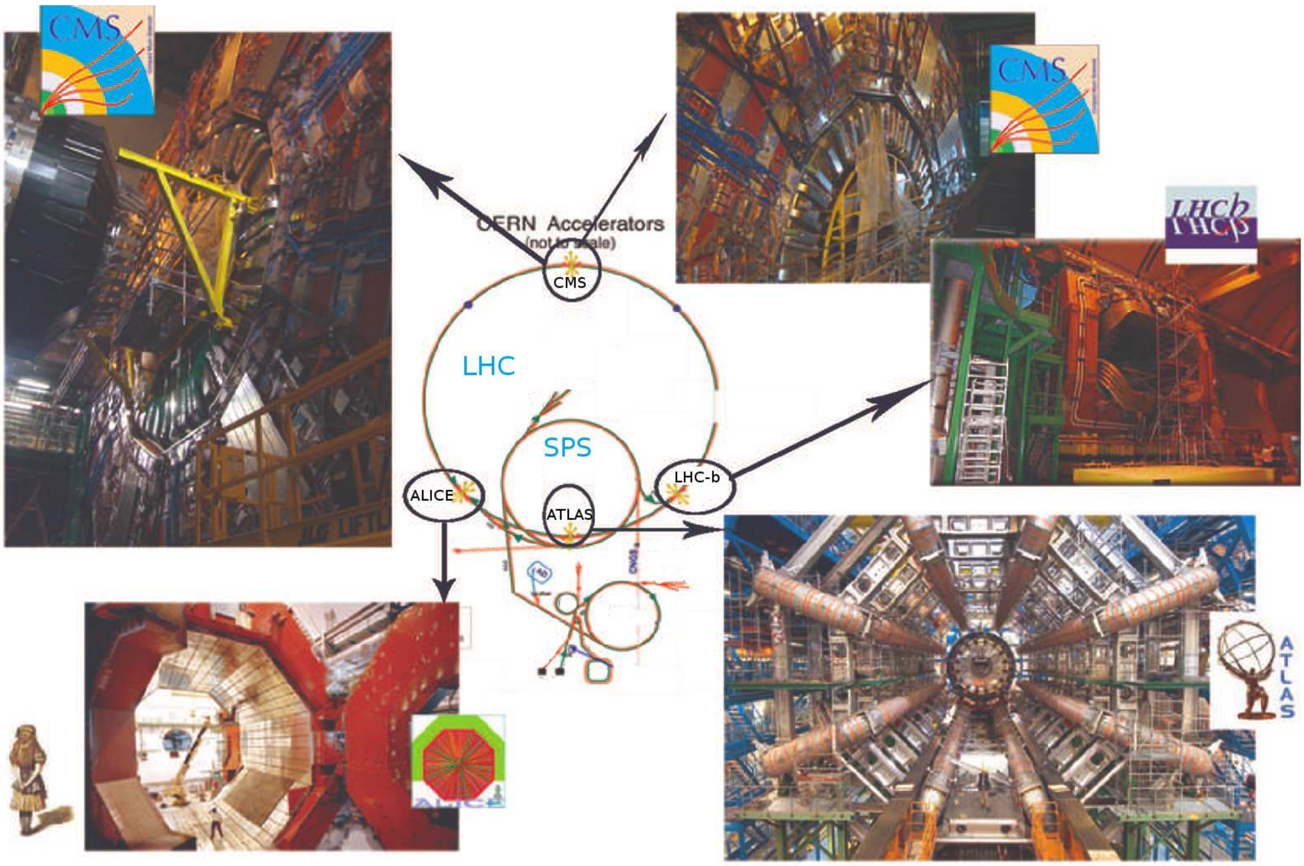

Figure 1.8: Map of the LHC and its four interaction points with pictures [63–65] of their detector: ATLAS (IP1), ALICE (IP2), CMS (IP5) and LHCb (IP8). The top of the remaining octants are occupied by beam maintenance devices, beam cleaning and collimation, acceleration cavities and beam dump system [66, 67].

ATLAS and CMS are multi-purpose detectors able to study almost any kind of physics that can pop up. LHCb is dedicated to the study of CP-violation in the production of b-quarks and anti-quarks, looking for an asymmetry in their decays and ALICE is designed to study the physics of strongly interacting matter and of the quark-gluon plasma during the heavy-ion collision phase[6]. From here on, we shall focus on ATLAS and CMS as their design is more adapted to the study of quasi-elastic events and diffraction.

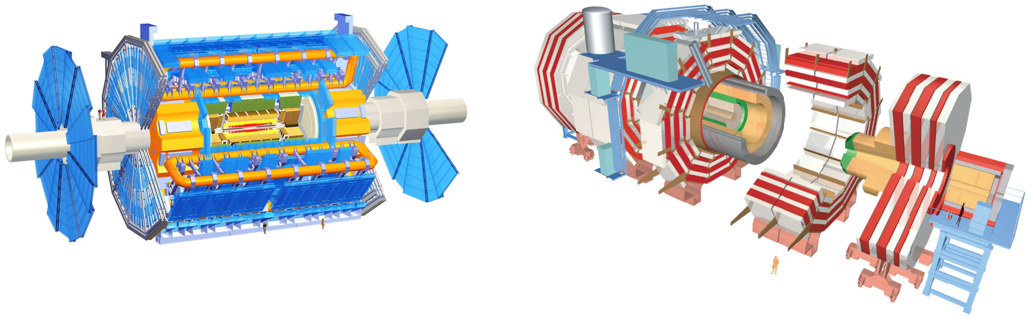
(a) (b)

Figure 1.9: ATLAS and CMS detectors at the LHC. The two pictures come from the official websites [63].

Like most of the detectors, they are constituted by a central inner tracking system, a high resolution electromagnetic calorimeter, a hadronic calorimeter and a muon detector shown in Fig. 1.9. If one includes all the central parts then the rapidity coverage of ATLAS and CMS extends from zero to 3 as shown in Fig. 1.10. The forward calorimeters FCal in ATLAS and the CMS hadronic calorimeters HF increase the rapidity range to $|\eta| < 5$ and are considered as part of the central detector. Particles with higher rapidity are detected in forward detectors, *i.e.* close to the beam pipe and far away from the interaction point. Those detectors are on the trajectory of

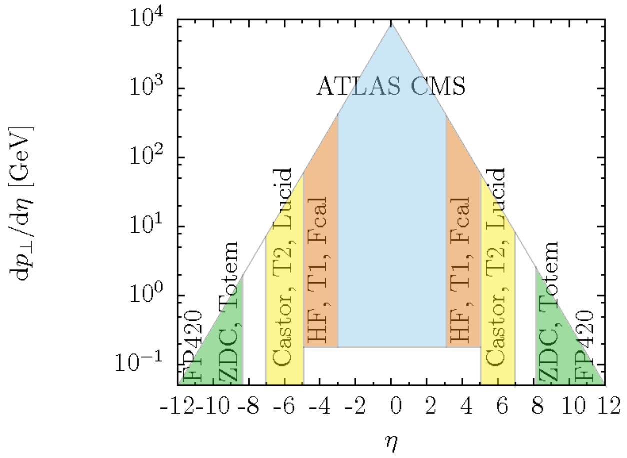

Figure 1.10: Approximate transverse momentum and rapidity coverage of ATLAS and CMS. Adapted from [68].

---

[6] The four acronyms stand for A Toroidal Lhc ApparatuS, Compact Muon Solenoid, Large Hadron Collider Beauty and A Large Ion Collider Experiment.

particles scattered at small angle. Both ATLAS and CMS are completed by Roman pots (RP) designed to measure these particles in the rapidity region of 6.5, their are the T1 and T2 trackers for CMS and LUCID for ATLAS, measuring the luminosity by counting charge particle tracks[7]. Both should be used as a trigger for forward detectors TOTEM and ALPHA [69, 70] located respectively at 150 m and 240 m on each sides of the central detector and able to detect protons elastically scattered at angles of the order of 100 μrad. Finally, and this would be the first time at a hadronic collider, there is a proposal for very forward detectors using Roman Pot techniques at 220 m and 420 m of the interaction point. They are called respectively RP220 and FP420[8]. At such distances, they could be hit by protons that have lost a tiny fraction of their initial momentum and the inclusion of those detectors would make the rapidity coverage reach $|\eta| \sim 12$.

Even without RP220 and FP420, the two multi-purpose detectors of the LHC should be able to observe diffractive events by triggering on rapidity gaps in the final state. However, it was shown in the technical reports of the two experiments that a good acceptance and resolution on elastic and quasi-elastic events will be only achieved by the introduction of these very forward detectors. In particular, at high luminosity they are useful to reject background.

Forward Detectors

In order to tag the remaining protons of a quasi-elastic scattering event, one has to place a detector close to the beam itself as the protons loose only a tiny part of their momenta and hence stay around their initial bunch. However, it is impossible to put a detector so close to the beam, as it would be rapidly destroyed by radiation and particle collisions. Thus, one can use the fact that after about a hundred meters, the final proton is now separated by few millimeters from the beam and can hit a strategically placed detector.

The FP420 detector would be located in a small space left on the beam line of LHC and to protect its sensors during the injection phases it is co-moving with the pipe[9]. After injection and when the beam is stable, FP420 can get closer and would be able to collect protons flying at 10 to 5 mm from the beam. With the addition of these two forward detectors on the right and on the left of the central detector, CMS is represented in Fig. 1.11 and if one considers the addition of both RP220 and FP420, it should be possible to detect protons that have lost a

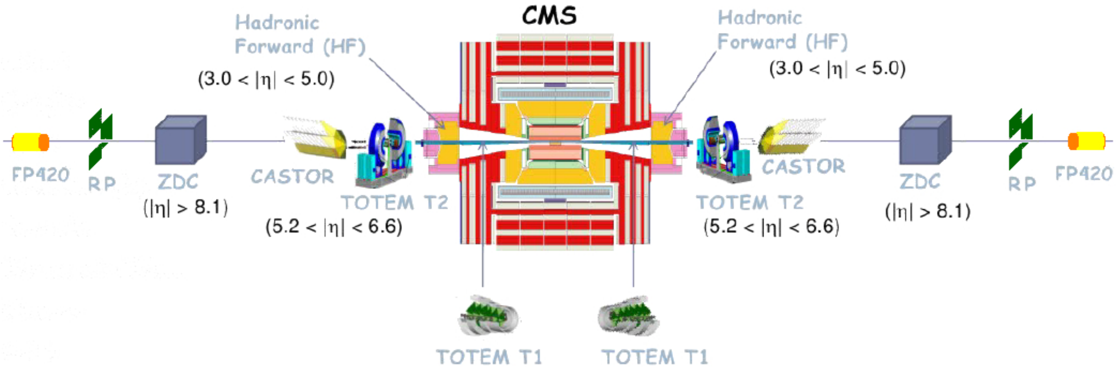

Figure 1.11: Drawing of the CMS and surrounding detectors at the LHC [71].

---

[7] T1 and T2 stands for Telescope 1 and 2, LUCID means LUminosity measurement using Čerenkov Integrating Detector.

[8] Recently, they were gathered under the name of ATLAS Forward Physics (AFP) in the ATLAS collaboration and High Precision Spectrometers (HPS) in the CMS collaboration.

[9] The technique is called the “Hamburg pipe” in reference to a similar setup at HERA.

fraction $0.002 < \xi < 0.2$ of their momentum with an acceptance close to 100%. However, the proton tagging has to be related to the central collision. This can be done by measuring the time of flight from the vertex to the forward detectors. This measurement should also allow the reduction of background by associating the information from both the central and the forward detectors. The technique allows a clear identification of quasi-elastic events and seems perfect, apart from the fact that the distance between the central detector and FP420 is too large to admit any communication, *i.e* FP420 cannot be used as a Level 1 trigger. Hence, the matching requests an exact knowledge of the timing, underlying the importance of high-precision fast detectors. In particular, the uncertainty on the vertex position is small if the time resolution is good and it is then possible to match the detection of remaining protons in the right and left forward detectors with the vertex observed in the central part. If there is no correspondence, the event is rejected as well as most of background events. The time measurement should be achieved by two types of time-of-flight (ToF) detectors, GASTOF and QUARTIC[10], that should reach a precision of less than 10 ps after a final upgrade [72].

The amazing energy available at the LHC could produce a huge number of particles at each collision and the different detectors have to be able to handle that. In the case of quasi-elastic processes, pile-up will be a major issue for the analysis but tagging both remaining protons in addition with the production vertex in the central detector should help to manage some of it. Moreover, the precise measurement of the momentum of the final protons can be used to determine the momentum loss and consequently the mass of the system centrally produced.

1.4.3 Missing-Mass Measurement

If the proposal for very forward detectors at both CMS and ATLAS is accepted, the LHC will be ready to study diffractive physics with a high precision. In particular, a part of the program should be devoted to quasi-elastic processes for which the unique and clear final state is a real asset.

The three methods of identification of diffractive events are [73]:

1. The presence of a leading proton in the forward region, *i.e* the region close to the beam and at large rapidity, carrying almost all of the momentum of the initial particle. It corresponds to a peak around one in the distribution of the ratio between the final and initial proton momentum.
2. The presence, in the central detector, of an hadronic system well separated in rapidity from the final protons. The rapidity distribution of the event should look like that of Fig. 1.2.c.
3. The presence of an important forward peak in the differential cross section in $|t|$, *i.e* a large cross section at $|t|$ close to zero that exhibits a rapid fall when $|t|$ increases.

Hence, the characteristics of a quasi-elastic event are a lack of hadronic activity in given regions of the detector and the presence of protons in forward detectors. However, it should be noted that several collisions can happen simultaneously due to the presence of a high number of protons in the same bunch. Actually, the average number of inelastic interactions per bunch crossing is given by

$$\mu = \frac{\sigma_{in}\mathcal{L}}{f_B}, \tag{1.15}$$

where σ_{in} is the inelastic cross section estimated to be close to 80 mb at the LHC, $\mathcal{L}$ is the luminosity and f_B is the effective bunch crossing frequency of the order of 31.5 MHz. This means

---

[10] Gaz Time Of Flight and QUARtz TIming Čerenkov.

that, for a luminosity of 10^{-34} cm^{-2}s^{-1}, the average number of interactions will be around 25 per bunch [67]. All collisions are close in time and space and their final products should be observed together in the detectors. In particular, some of the products of the additional collisions can be detected in the gap region that is then not empty and the event would be rejected after triggering. This effect is sometimes called pile-up but the real origin of the name comes from the technical effect that is the pileup of several events in the same calorimeter tower. At the TeVatron, but also at the LHC, the time between each bunch crossing is smaller that the time of reaction of the acquisition system and consequently data accumulate in the same part of the detector disturbing the measurement of the energy. In both cases, the result is that the centrally-produced system or its decay products could be completely hidden in the background, especially at high luminosity.
Because of pile-up in the central detector, the mass of the produced system is not easily obtained but quasi-elastic production has the interesting feature to allow mass reconstruction from the measurement of the momentum lost by the initial protons tagged in very forward detectors.

Using the notation of Sec. 1.1 where ξ_1, ξ_2 are the momentum fractions lost by the protons and $\sqrt{s}$ the energy in the center-of-mass frame, one indeed has

$$M^2 \sim \xi_1 \xi_2 s, \tag{1.16}$$

in the approximation of small proton transverse momentum. The uncertainty on mass depends on the precision of the measurement of ξ_i, itself related to the knowledge of the magnetic field, on the momentum spread of the incoming beams and on the position of the interaction point. According to reference [72, 74], the precision is of the order of 250 MeV at the TeVatron and 2-3 GeV at the LHC, independently of the measured mass. Moreover, the technique allows for a good signal-over-background separation as the resonance peak should appear clearly in the momentum distribution of the final proton. The method is then accurate to measure the mass of any object produced in the central region through a quasi-elastic process.

At low luminosity, it should be possible to detect simultaneously the decay products of the particle(s) and/or the presence of a rapidity gap in addition to the two intact protons in the forward detectors. In this particular case, all particles in the final state are detected and the kinematics fully reconstructed. At high luminosity however, it seems that only the detection of forward protons is relevant and should be used as a filter to measurements in the central detector. This would be possible only if one can deal with the time measurement issues described in the previous section.

Part I

Dijet Quasi-Elastic Production

The study of dijet quasi-elastic production is particularly interesting in view of the recent data published by the CDF RunII collaboration [57] and presented in Fig. 1.12, note that data will be described in more details in Chap. 6. The cross section is rather small from 1 nb to 1 pb depending on the minimum transverse energy of the jet. Nevertheless, it corresponds to 2.10^5 high-energy dijet events at the TeVatron luminosity[11] and one can note that the data include high-mass central systems of about 100 GeV. Therefore, the mechanism lies in the kinematical region relevant for Higgs boson production for a Higgs boson mass of an hundred GeV and that corresponds exactly to the mass range we are interested in, as explained in Chap. 7. In addition, and this is the main point of the present work, data can be used to tune the standard calculation of quasi-elastic cross sections and to narrow down the uncertainties. One can select accurate parametrisations of the soft physics entering the process and use them in other quasi-elastic processes taking into account that soft corrections are similar. Thus, one should be able to give a better prediction for dijet and Higgs boson production at the LHC in the quasi-elastic regime. We shall show that the cross section is significant at the LHC, which could provide a large set of new data and those data should help reduce even more the uncertainties affecting the calculation.

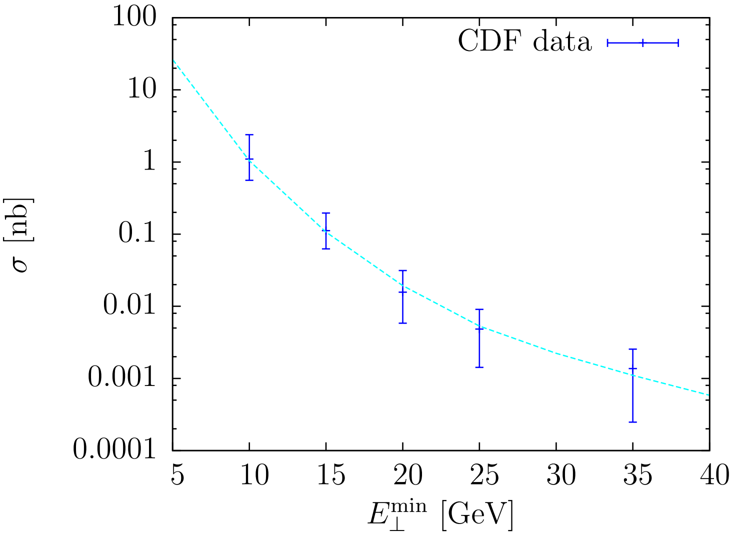

Figure 1.12: Cross section of quasi-elastic production of two jets as a function of the jet minimum transverse energy. Data from [57].

The aim of this part is to describe in detail the calculation of the cross section for quasi-elastic gluon dijet production. The structure is as follows: first a calculation of the parton-level cross section (Eq. (2.91) Chap. 2)

$$\mathcal{M}_{qq} = \mathcal{M}(qq \to q^* + gg + q^*), \tag{1.17}$$

---

[11] This number is calculated for a luminosity of 200 fb^{-1} according to reference [57].

followed by the inclusion of the impact factor (Eq. (3.25) Chap. 3)

$$\mathcal{M}(p_1p_2 \to p_1^* + gg + p_2^*) = \mathcal{M}_{qq} \otimes \Phi(p_1)\Phi(p_2), \tag{1.18}$$

of the Sudakov form factor (Eq. (4.1) Chap. 4)

$$\mathcal{M}(p_1p_2 \to p_1^* + gg + p_2^*) = \mathcal{M}_{qq} \otimes \Phi(p_1)\sqrt{T(\mu^2, \ell_1^2)}\; \Phi(p_2)\sqrt{T(\mu^2, \ell_2^2)}, \tag{1.19}$$

of the gap-survival probability (Eq. (5.3) Chap. 5)

$$\mathcal{M}(p_1p_2 \to p_1^* + gg + p_2^*) = \sqrt{S^2}\,\mathcal{M}_{qq} \otimes \Phi(p_1)\sqrt{T(\mu^2, \ell_1^2)}\; \Phi(p_2)\sqrt{T(\mu^2, \ell_2^2)}, \tag{1.20}$$

and of the splash-out (Eq. (5.16) and Eq. (5.17) Chap. 5). Each ingredient is studied in different chapters and in order to show the uncertainty, each chapter ends on a small discussion. Throughout this study, we select a reference curve shown in Fig. 1.12, coming from a given model that we shall progressively build and given explicitly in Appendix A. We warn the reader that this curve is not a prediction but rather specific choice that goes through the data. At each step of the calculation, *i.e.* in each chapter detailing a particular piece of the calculation, this curve is the reference for a change in the parametrisation of the corresponding ingredients.
The last chapter summarises everything, presents the results and discussions, including the prediction for dijet cross section at different LHC energy.

Chapter 2

Lowest Order: Perturbative QCD Calculation

The backbone of the quasi-elastic dijet production is the partonic subprocess

$$qq \to q + gg + q. \tag{2.1}$$

The central gluon system is in a colour-singlet state and is separated by a large rapidity gap from the two scattering quarks. This chapter presents the details of the QCD calculation of the amplitude at the parton level. The first section reminds the reader of integration by residue and other tools that will be used, the second part is the computation of the loop integral and is divided in two sections. The first one shows how to compute the longitudinal part of the integral but in a simpler case, the one-particle production for which the kinematics is similar to the dijet case but less complex. The idea is to identify clearly the different contributions and the structure of the calculation in order to use this knowledge in the two-particle production case. After that we focus on the hard subprocess, namely the gluon elastic scattering and present the imaginary part of the amplitude. The final section is devoted to the study of the theoretical uncertainties where we critically re-evaluate the effect of the usual approximations used in literature.

2.1 Two-Gluon Amplitude

One first has to compute the imaginary part of the diagrams of Fig. 2.1 that is

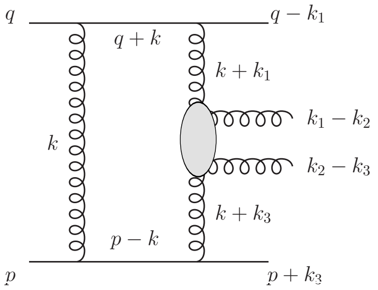

Figure 2.1: Leading diagram for the process $qq \to q + gg + q$. The central blob corresponds to the gluon-gluon scattering subprocess.

$$\mathrm{Im}\,\mathcal{M} = C\,g^4 \int \frac{\mathrm{d}^4 k}{(2\pi^4)} \frac{a(g^* g^* \to gg)}{[(q+k)^2 + i\epsilon][(p-k)^2 + i\epsilon][(k+k_1)^2 + i\epsilon][(k+k_3)^2 + i\epsilon][k^2 + i\epsilon]} \tag{2.2}$$

where g is the quark-gluon coupling constant and C is the colour factor while $a(g^* g^* \to gg)$ corresponds to the numerator and the amplitude of the hard subprocess.
We assume the quarks massless and consider the collision in a frame where the incoming quarks have no transverse momenta. We introduce the light-cone momenta q^μ and p^μ that correspond to the direction of the initial quarks with

$$s = 2\, q^\mu p_\mu, \tag{2.3}$$

the energy in the center-of-mass frame of the parton-parton collision. The other momenta of the problem are written using a Sudakov decomposition. The idea is to project the four-momenta upon the incoming particle directions and the transverse plane. In this particular decomposition,

$$\begin{aligned} k^\mu &= y p^\mu + z q^\mu + \mathbf{k}^\mu, \\ k_i^\mu &= y_i p^\mu + z_i q^\mu + \mathbf{k}_i^\mu, \end{aligned} \tag{2.4}$$

where transverse vectors are in bold. Note that the notation defined here will be used in the whole thesis and that

$$\begin{aligned} \mathbf{k}^2 &= -\mathbf{k}^\mu\, \mathbf{k}_\mu, \\ (\mathbf{k} + \mathbf{k}_i)^2 &= -(\mathbf{k} + \mathbf{k}_i)^\mu (\mathbf{k} + \mathbf{k}_i)_\mu, \end{aligned} \tag{2.5}$$

where the square of transverse momenta are positive quantities. The integration over the four-momentum k is also written in terms of the Sudakov variables,

$$\int \frac{\mathrm{d}^4 k}{(2\pi)^4} \quad \to \quad \frac{s}{2(2\pi)^2} \int \frac{\mathrm{d}^2 \mathbf{k}}{(2\pi)^2} \mathrm{d}y \mathrm{d}z. \tag{2.6}$$

The use of the Sudakov parametrisation leads to a clear physical interpretation of variables y_i, z_i and $\mathbf{k}_i$ besides a good intuition for what happens during the scattering. One can understand $\mathbf{k}_i$ as the part of the momentum in the perpendicular direction, y_i (resp. z_i) as the part of the four-momentum in the p^μ (resp. q^μ) direction and $y_i \ll z_i$ indicates that the intermediate particle is more in the direction of the ingoing particle q^μ than in the opposite. In addition to these advantages, we have the covariance of k_i, *i.e.* a longitudinal Lorentz boost simply changes the four-vectors p^μ and q^μ and keeps y_i and z_i unchanged.

Here we shall keep an exact transverse kinematics, that is to say, the momenta transferred from the hadrons, noted k_i, are not neglected with respect to the momentum in the loop k.

2.1.1 Tools: Contour Integration

In the calculation of the imaginary part of the amplitude, most integrals in this work are performed using contour integration and the Cauchy theorem. Hence, we describe the method.

We would like to compute the integral of $f(z)$ that is an analytic function with a finite number of poles z_i

$$\int_{-\infty}^{\infty} f(z) \mathrm{d}z. \tag{2.7}$$

In the calculation of Feynman diagram, these poles come from the propagators. Using the Cauchy residue theorem, one can perform the integration along the contour in the complex plane shown in Fig. 2.2 and one obtains

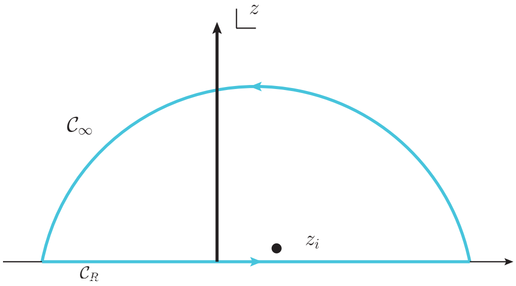

Figure 2.2: Closed contour $\mathcal{C} = \mathcal{C}_\infty + \mathcal{C}_R$ in the complex plane and the singularity z_i.

$$\begin{aligned}\oint_{\mathcal{C}} f(z)\mathrm{d}z &= \int_{\mathcal{C}_R} f(z)dz + \int_{\mathcal{C}_\infty} f(z)\mathrm{d}z \\ &= (2i\pi)\sum_i \mathrm{Res}_{z_i}[f(z)],\end{aligned} \tag{2.8}$$

as if $f(z)$ vanishes quickly at infinity, *i.e.* faster than $1/z$, the integration over the half semi-circle is zero and the integral along the z axis is the sum of the pole contributions or residues $\mathrm{Res}_{z_i}[f(z)]$. Note that when the contour is closed below the z axis, there is an extra-minus sign in front of the residue for which the definition depends of the multiplicity of the poles. The residue for simple poles is

$$Res_{z_i}[f(z)] = \lim_{z\longrightarrow z_i}(z - z_i)f(z), \tag{2.9}$$

and the formal statement of the Cauchy theorem is given in Appendix. B.1. In the following, we shall make an explicit calculation of the different integrals and it corresponds to the application of Cutkosky rules or cutting rules proved by Cutkosky in 1960 [75]. By analogy to them and to compute the residue, we shall use the prescription to substitute

$$\int f(z)\,\mathrm{d}z \rightarrow \int \delta\left(\frac{1}{f(z)}\right)\,\mathrm{d}z, \tag{2.10}$$

and the propagator corresponding to the pole z_i will be designed as a cut propagator.

Now, we are ready to evaluate the amplitude of the two-gluon quasi-elastic production at the parton level by computing the integral over k and k' in Eq. (2.2). In particular, one can start by the integral over the longitudinal components of the Sudakov decomposition y and z.

2.1.2 Toy Calculation

We shall first pave the way by computing a similar but simpler case, the production of a massless particle as represented with its kinematics in Fig. 2.3.

The momenta transferred from the first and second quarks are k_1 and $-k_3$ so that, the four-momentum of the produced particle is

$$(k_1 - k_3)^\mu = \alpha p^\mu + \beta q^\mu + (\mathbf{k}_1 - \mathbf{k}_3)^\mu, \tag{2.11}$$

with

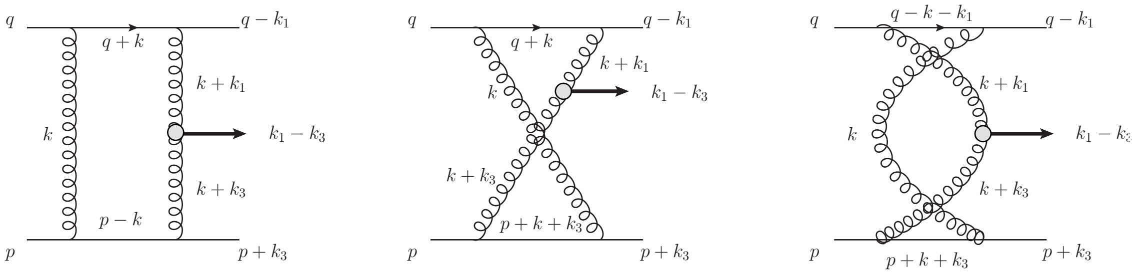

Figure 2.3: Kinematical conventions for the central one-particle production. One has in turn diagram $s_1 s_2$, diagram $s_1 u_2$ and diagram $u_1 u_2$.

$$\begin{aligned}\alpha &= y_1 - y_3, \\ \beta &= z_1 - z_3.\end{aligned} \tag{2.12}$$

The central production of a colourless object by pomeron exchange is an example of one-loop particle production in multi-Regge kinematics and at this order it is known that the amplitude is dominated by its imaginary part. The leading behavior of the cross section comes from the region where one has an ordering of the longitudinal momentum fractions [40]

$$\frac{|\mathbf{k}_i^2|}{s} \ll \beta, \alpha \ll 1, \tag{2.13}$$

while the transverse momenta are of the same order

$$|\mathbf{k}^2|,\ |\mathbf{k}_1^2|,\ |\mathbf{k}_3^2| \ll s. \tag{2.14}$$

The first step is to use the on-shell condition for the produced particle:

$$\begin{aligned}(k_1 - k_3)^2 &= 0 \\ &= \alpha\beta s - (\mathbf{k}_1 - \mathbf{k}_3)^2 \\ &\rightarrow \alpha\beta s = (\mathbf{k}_1 - \mathbf{k}_3)^2,\end{aligned} \tag{2.15}$$

and the same for the final quarks

$$\begin{aligned}(q - k_1)^2 &= 0 \\ &= -y_1(1 - z_1)s - \mathbf{k}_1^2 \\ &\rightarrow y_1 = \frac{-\mathbf{k}_1^2}{(1 - z_1)s}, \\ (p + k_3)^2 &= 0 \\ &= z_3(1 + y_3)s - \mathbf{k}_3^2 \\ &\rightarrow z_3 = \frac{\mathbf{k}_3^2}{(1 + y_3)s}.\end{aligned} \tag{2.16}$$

The last identities also give information about the other longitudinal components considering the fact that

$$\begin{aligned} y_1 - y_3 &= \alpha \quad &\to y_3 \simeq -\alpha, \\ z_1 - z_3 &= \beta \quad &\to z_1 \simeq \beta. \end{aligned} \tag{2.17}$$

The imaginary part of the amplitude can now be evaluated and we first focus on the s_1s_2 diagram. As the origin of the singularities is in the propagators only, one can first forget about the numerator and study the integral

$$\int \frac{\mathrm{d}^4k}{(2\pi)^4} \frac{1}{[(q+k)^2+i\epsilon][(p-k)^2+i\epsilon][(k+k_1)^2+i\epsilon][(k+k_3)^2+i\epsilon][k^2+i\epsilon]}, \tag{2.18}$$

where k is the momentum inside the loop. This can be translated to an integral over the Sudakov variables using Eq. (2.6) and in this section, we are interested in the integral over y and z that amounts to the evaluation of

$$\mathcal{I}_{s_1s_2} = \int \mathrm{d}y\mathrm{d}z \frac{1}{[(q+k)^2+i\epsilon][(p-k)^2+i\epsilon][(k+k_1)^2+i\epsilon][(k+k_3)^2+i\epsilon][k^2+i\epsilon]}. \tag{2.19}$$

The five propagators are written using Sudakov variables:

$$\begin{aligned} P_1 &= (q+k)^2 + i\epsilon \\ &= y(1+z)s - \mathbf{k}^2 + i\epsilon, \\ P_2 &= (p-k)^2 + i\epsilon \\ &= -z(1-y)s - \mathbf{k}^2 + i\epsilon, \\ P_3 &= (k+k_1)^2 + i\epsilon \\ &= (y+y_1)(z+z_1)s - (\mathbf{k}+\mathbf{k}_1)^2 + i\epsilon, \\ P_4 &= (k+k_3)^2 + i\epsilon \\ &= (y+y_3)(z+z_3)s - (\mathbf{k}+\mathbf{k}_3)^2 + i\epsilon, \\ P_5 &= k^2 + i\epsilon \\ &= yzs - \mathbf{k}^2 + i\epsilon. \end{aligned} \tag{2.20}$$

In order to perform the y integral, we first identify the position of the five y poles

$$\begin{aligned} y_{P_1} &= \frac{\mathbf{k}^2 - i\epsilon}{(1+z)s}, \\ y_{P_2} &= \frac{\mathbf{k}^2 - i\epsilon}{zs} + 1, \\ y_{P_3} &= \frac{(\mathbf{k}+\mathbf{k}_1)^2 - i\epsilon}{(z+z_1)s} - y_1, \\ y_{P_4} &= \frac{(\mathbf{k}+\mathbf{k}_3)^2 - i\epsilon}{(z+z_3)s} - y_3, \\ y_{P_5} &= \frac{\mathbf{k}^2 - i\epsilon}{zs}, \end{aligned} \tag{2.21}$$

as a function of z and we draw their positions in the upper or in the lower half-plan of the z axis in Fig. 2.4. If one closes the contour below the real axis, there are only three poles that can contribute simultaneously for specific values of z and as the integrated function quickly vanishes

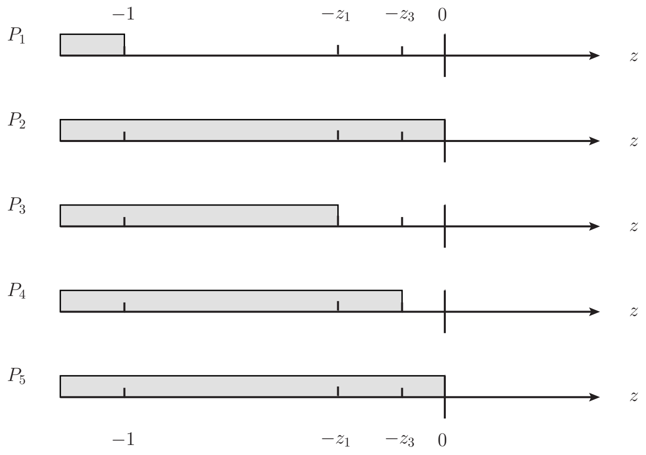

Figure 2.4: Diagram $s_1 s_2$: Positions of the y poles of the different propagators as functions of z. The shaded regions correspond to poles above the real axis while the unshaded ones to poles below the real axis.

at infinity, one can use Eq. (2.10). The longitudinal part of the integral is the sum of the three residues

$$\begin{aligned}\mathcal{I}_{s_1 s_2} &= \int_{-1}^{0} \mathrm{d}z \int \mathrm{d}y(-2\pi i)\delta\left[y(1+z)s - \mathbf{k}^2\right]\frac{1}{P_2P_3P_4P_5} \\ &+ \int_{-z_1}^{0} \mathrm{d}z \int \mathrm{d}y(-2\pi i)\delta\left[(y+y_1)(z+z_1)s - (\mathbf{k}+\mathbf{k}_1)^2\right]\frac{1}{P_1P_2P_4P_5} \\ &+ \int_{-z_3}^{0} \mathrm{d}z \int \mathrm{d}y(-2\pi i)\delta\left[(y+y_3)(z+z_3)s - (\mathbf{k}+\mathbf{k}_3)^2\right]\frac{1}{P_1P_2P_3P_5}.\end{aligned} \tag{2.22}$$

One can directly see that the z variable is always negative so that we change it to $-|z|$ and calculate separately each of the integrals.

Contribution 1

Let us start with the evaluation of the first term of Eq. (2.22). Using the delta function, one is left with an integral over z

$$\begin{aligned}\mathcal{I}_1 &= \int_{-1}^{0} \mathrm{d}z \int \mathrm{d}y(-2\pi i)\delta\left[y(1-|z|)s - \mathbf{k}^2\right]\frac{1}{P_2P_3P_4P_5} \\ &= \int_{-1}^{0} \mathrm{d}z \int \mathrm{d}y\frac{(-2\pi i)}{(1-|z|)s}\delta\left[y - \frac{\mathbf{k}^2}{(1-|z|)s}\right]\frac{1}{P_2P_3P_4P_5} \\ &= \int_{-1}^{0} \mathrm{d}z\frac{(-2\pi i)}{(1-|z|)s}\frac{1}{P_2P_3P_4P_5}\bigg|_{y=\frac{\mathbf{k}^2}{(1-|z|)s}}.\end{aligned} \tag{2.23}$$

This second integral is performed using the same technique, we evaluate the position of the z poles for each of the remaining propagator. P_5 now gives

$$\begin{aligned}k^2 &= -y|z|s - \mathbf{k}^2\Big|_{y=\frac{\mathbf{k}^2}{(1-|z|)s}} \\ &= -\frac{\mathbf{k}^2}{(1-|z|)s} < 0,\end{aligned} \tag{2.24}$$

and is negative-definite due to the kinematics, as well as P_3:

$$\begin{aligned}(k+k_1)^2 &= (y+y_1)(z_1-|z|)s - (\mathbf{k}+\mathbf{k}_1)^2\Big|_{y=\frac{\mathbf{k}^2}{(1-|z|)s}} \\ &= -\frac{[\mathbf{k}(1-\beta)+\mathbf{k}_1(1-|z|)]^2}{(1-|z|)(1-\beta)} < 0,\end{aligned} \tag{2.25}$$

using for the second line the conditions from Eq. (2.16) and Eq. (2.17). Consequently, both don't have poles that can contribute to the imaginary part of the amplitude and one has to check only propagators P_2 and P_4. The former is

$$\begin{aligned}(p-k)^2 &= (1-y)|z|s - \mathbf{k}^2\Big|_{y=\frac{\mathbf{k}^2}{(1-|z|)s}} \\ &= |z|s - \frac{\mathbf{k}^2}{1-|z|},\end{aligned} \tag{2.26}$$

which changes sign at $|z| \simeq \mathbf{k}^2/s$. The imaginary part of the integral is

$$\begin{aligned}\mathcal{I}_1^{c_1} &= \int_{-1}^{0} \mathrm{d}z \frac{(-2\pi i)}{(1-|z|)^2 s}\frac{(-i\pi)}{s}\delta\left[|z| - \frac{\mathbf{k}^2}{(1-|z|)s}\right]\frac{1}{P_3P_4P_5}\Big|_{y=\frac{\mathbf{k}^2}{(1-|z|)s}} \\ &= -\frac{2\pi^2}{s^2}\frac{1}{[-\mathbf{k}^2]\left[\alpha\mathbf{k}^2-\alpha\mathbf{k}_3^2-(\mathbf{k}+\mathbf{k}_3)^2\right][-(\mathbf{k}+\mathbf{k}_1)^2]},\end{aligned} \tag{2.27}$$

where one has taken the large-s limit and where the index c_1 indicates that this is the first possible cut. Due to the multi-Regge-kinematics regime, the terms $\alpha\mathbf{k}^2$ and $\alpha\mathbf{k}_3^2$ are negligible in front of $\mathbf{k}_i^2$, thus the first contribution yields

$$\mathcal{I}_1^{c_1} = +\frac{2\pi^2}{s^2}\frac{1}{\mathbf{k}^2(\mathbf{k}+\mathbf{k}_3)^2(\mathbf{k}+\mathbf{k}_1)^2}. \tag{2.28}$$

Putting both propagators P_1 and P_2 on-shell corresponds to the cut of diagram (a) in Fig. 2.5 and we shall call it the usual cut contribution. According to [76, 77], the contribution of this cut gives the imaginary part of the full amplitude and other cut contributions cancel or are negligible. This can be checked by a direct calculation as shown here.

Actually, there is also the possibility to use propagator P_4. In this case, we substitute $y = y_{P_1}$ and find

$$\begin{aligned}(k+k_3)^2 &= (y+y_3)(z_3-|z|)s - (\mathbf{k}+\mathbf{k}_3)^2\Big|_{y=\frac{\mathbf{k}^2}{(1-|z|)s}} \\ &= \left(\frac{\mathbf{k}^2}{1-|z|}-\alpha s\right)\left(\frac{\mathbf{k}_3^2}{(1-\alpha)s}-|z|\right) - (\mathbf{k}+\mathbf{k}_3)^2,\end{aligned} \tag{2.29}$$

using again Eq. (2.16) and Eq. (2.17). One can consider two different z regions, namely $|z|$ close to 1 and $|z| \sim \beta \ll 1$. In the former case, the propagator P_4 becomes

$$\begin{aligned}(k+k_3)^2 &\simeq \frac{\mathbf{k}^2}{1-|z|} - \alpha s \\ &\to |z| = \frac{-\mathbf{k}^2}{\alpha s} + 1,\end{aligned} \tag{2.30}$$

that is the value at which $|z|$ changes sign and one has to evaluate the integral

$$\begin{aligned} \mathcal{I}_1^{c_2} &= \frac{-2\pi^2}{\alpha s^2} \frac{1}{P_2 P_3 P_5} \Big|_{y=\frac{\mathbf{k}^2}{(1-|z|)s}, |z|=\frac{-\mathbf{k}^2}{\alpha s}+1} \\ &\simeq -\frac{-2\pi^2}{\alpha s^2} \frac{1}{[s][-\alpha s][-\alpha s]}. \end{aligned} \tag{2.31}$$

This case leads to a very large y, of the order of α, and to the suppression of the cross section by order of s^5 due to the other propagators. Thus, the kinematical region of large $|z|$ doesn't contribute to the amplitude in the large s-limit. One only has to consider the $|z| \sim \beta$ situation for which propagator P_4 simplifies to

$$\begin{aligned} (k+k_3)^2 &\simeq \alpha |z| s - (\mathbf{k}+\mathbf{k}_3)^2 \\ \rightarrow |z| &= \frac{(\mathbf{k}+\mathbf{k}_3)^2}{\alpha s}. \end{aligned} \tag{2.32}$$

The integral yields

$$\begin{aligned} \mathcal{I}_1^{c_3} &= \int_{-1}^{0} \mathrm{d}z \frac{-2\pi^2}{(1-|z|)\alpha s^2} \delta \left[|z| - \frac{(\mathbf{k}+\mathbf{k}_3)^2}{\alpha s} \right] \frac{1}{P_2 P_3 P_5} \Big|_{y=\frac{\mathbf{k}^2}{(1-|z|)s}} \\ &\simeq \frac{-2\pi^2}{s^2} \frac{1}{\mathbf{k}^2 (\mathbf{k}+\mathbf{k}_1)^2 (\mathbf{k}+\mathbf{k}_3)^2}. \end{aligned} \tag{2.33}$$

The contribution corresponds to the cut of diagram (c) of Fig. 2.5 which is actually equal, apart from the sign, to the usual contribution of Eq. (2.28).

Contribution 2

The second term of Eq. (2.22) is evaluated in exactly the same way, this time propagator P_3 is on-shell and the integral reads

$$\begin{aligned} \mathcal{I}_2 &= \int_{-z_1}^{0} \mathrm{d}z \int \mathrm{d}y \frac{(-2\pi i)}{(\beta-|z|)s} \delta \left[y + y_1 - \frac{(\mathbf{k}+\mathbf{k}_1)^2}{(\beta-|z|)s} \right] \frac{1}{P_1 P_2 P_4 P_5} \\ &= \int_{-z_1}^{0} \mathrm{d}z \frac{(-2\pi i)}{(\beta-|z|)s} \frac{1}{P_1 P_2 P_4 P_5} \Big|_{y=\frac{(\mathbf{k}+\mathbf{k}_1)^2}{(\beta-|z|)s}+\frac{\mathbf{k}_1^2}{(1-\beta)s}}. \end{aligned} \tag{2.34}$$

Due to kinematics, propagators P_1 and P_5 cannot be on-shell and one only has to compute the possible contribution of P_2 and P_4. We start with P_2 and once again, the large $|z|$ region doesn't contribute as it is suppressed by a power of s in other propagators. The result is different if one considers the small $|z|$ case for which one has a pole at

$$\begin{aligned} (p-k)^2 &= \left(1 - \frac{(\mathbf{k}+\mathbf{k}_1)^2}{(z+\beta)s} - \frac{\mathbf{k}_1^2}{(1-\beta)s} \right) |z| s - \mathbf{k}^2 \\ &\simeq |z| s - \mathbf{k}^2 \\ \rightarrow |z| &= \frac{\mathbf{k}^2}{s}. \end{aligned} \tag{2.35}$$

Note that due to the assumption of multi-Regge-kinematics $|z| = \mathbf{k}^2/s \ll \alpha$. The evaluation of the remaining propagators at the pole leads to

$$\begin{aligned}
\mathcal{I}_2^{c_1} &= \int_{-z_1}^{0} \mathrm{d}z \frac{(-2\pi i)}{(\beta-|z|)s}\frac{(-i\pi)}{s}\delta\left[|z|-\frac{\mathbf{k}^2}{s}\right]\frac{1}{P_1P_4P_5}\Big|_{y=\frac{(\mathbf{k}+\mathbf{k}_1)^2}{(\beta-|z|)s}+\frac{\mathbf{k}_1^2}{(1-\beta)s}} \\
&\simeq \frac{-2\pi^2}{\beta s^2}\frac{\beta}{[(\mathbf{k}+\mathbf{k}_1)^2]}\frac{1}{[-(\mathbf{k}+\mathbf{k}_3)^2]\,[-\mathbf{k}^2]} \\
&\simeq \frac{-2\pi^2}{s^2}\frac{1}{\mathbf{k}^2(\mathbf{k}+\mathbf{k}_3)^2(\mathbf{k}+\mathbf{k}_1)^2}.
\end{aligned} \tag{2.36}$$

This cut corresponds to the one shown in Fig. 2.5.b and is, once again, equal and opposite in sign to the usual cut contribution. One is now left with the last piece that comes from the pole of propagator P_4. The result is straightforward if the produced particle is massless because P_4 cannot be put on-shell together with P_2 and P_3, so that the contribution is zero. This is demonstrated by the negative definiteness of

$$(k+k_3)^2 \simeq -\left(\frac{(\mathbf{k}+\mathbf{k}_1)^2}{(\beta-|z|)s}-\alpha s\right)|z|-(\mathbf{k}+\mathbf{k}_3)^2 < 0. \tag{2.37}$$

Nevertheless, in the case of the production of massive particles such the Higgs boson, the contribution of the pole is non-zero and the cut corresponds to the diagram (d) of Fig. 2.5. One can estimate the contribution of the pole, starting from Eq. (2.15) that becomes

$$\alpha\beta s = (\mathbf{k}_1-\mathbf{k}_3)^2+m^2, \tag{2.38}$$

where m is the mass of the produced particle. Hence,

$$\begin{aligned}
\alpha &= \frac{\mathbf{k}_1-\mathbf{k}_3}{\beta s}+\frac{m^2}{\beta s}, \\
\beta &= z_1-z_3,
\end{aligned} \tag{2.39}$$

and after a little bit of algebra, one can write the propagator P_4 without any approximation as

$$(k+k_3)^2 = -\frac{1}{\rho}\left[(\mathbf{k}+\mathbf{k}_1)(1-\rho)+(\mathbf{k}+\mathbf{k}_3)\rho\right]^2+m^2(1-\rho), \tag{2.40}$$

with

$$\rho = \frac{z_1+z}{z_1-z_2}. \tag{2.41}$$

One can show that Eq. (2.40) changes sign at

$$m^2 = \frac{\left[(\mathbf{k}+\mathbf{k}_1)(1-\rho)+(\mathbf{k}+\mathbf{k}_3)\rho\right]^2}{\rho(1-\rho)}, \tag{2.42}$$

leading to a non-zero contribution to the amplitude. In the general case, *i.e* arbitrary value of $\mathbf{k}_i$ and $\mathbf{k}$, the solution is non-trivial and different from the usual cut contribution. We do not intend to calculate it explicitly, so we simply denote it by

$$\mathcal{I}_2^{c_2} = \frac{2\pi^2}{s^2}\frac{1}{\mathbf{k}^2(\mathbf{k}+\mathbf{k}_1)^2(\mathbf{k}+\mathbf{k}_3)^2}\times\Delta, \tag{2.43}$$

where Δ is a complicated function of $\mathbf{k}_i$, $\mathbf{k}$ and ρ.

Contribution 3

Finally, we come to the contribution of the third term of Eq. (2.22) that takes into account the y pole due to the on-shellness of propagator P_4. One has to calculate the integral over z

$$\mathcal{I}_3 = \int_{-z_3}^{0} \mathrm{d}z \frac{(-2\pi i)}{(z_3 - |z|)s} \frac{1}{P_1 P_2 P_3 P_5}\Big|_{y=\frac{(\mathbf{k}+\mathbf{k}_3)^2}{(z_3-|z|)s}+\alpha}. \tag{2.44}$$

According to the same argument than in the previous subsection, propagators P_2 and P_5 cannot be put on-shell and because P_1 and P_3 are both positive definite at the pole, this contribution is zero.

Summary

We compile now the results from the different contributions to the $s_1 s_2$ diagram, the integral is the sum

$$\begin{aligned}\mathcal{I}_{s_1 s_2} &= \mathcal{I}_1^{c_1} + \mathcal{I}_1^{c_3} + \mathcal{I}_2^{c_1} + \mathcal{I}_2^{c_2} \\ &= \frac{2\pi^2}{s^2} \frac{1}{\mathbf{k}(\mathbf{k}+\mathbf{k}_1)^2(\mathbf{k}+\mathbf{k}_3)^2} \left[1 - 1 - 1 + \Delta\right],\end{aligned} \tag{2.45}$$

corresponding respectively to the cuts of Fig. 2.5.

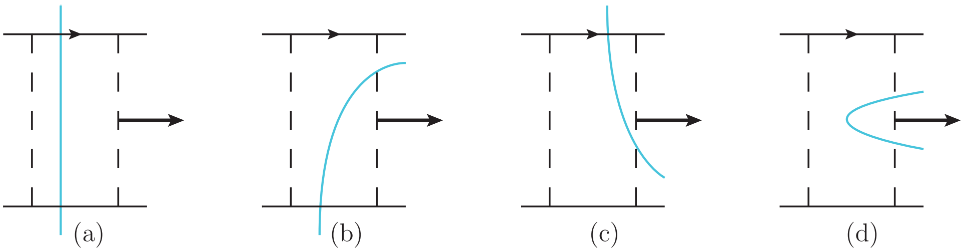

Figure 2.5: Cuts contributing to the imaginary part of the amplitude. Note that except for the last diagram, all contributions are equal to the usual cut of the first figure apart for the sign. One has respectively $\mathcal{I}_1^{c_1}$, $\mathcal{I}_1^{c_3}$, $\mathcal{I}_2^{c_1}$ and $\mathcal{I}_2^{c_2}$.

2.2 The Longitudinal Integral

One has now to evaluate the single-crossed and double-crossed diagrams. However, the calculation is left for Appendix B.2 where the reader will find all the details and we compile the results obtained from each diagram of Fig. 2.3 to draw the overall picture. In particular, one can note that contributions are identical apart for the sign and the final answer is

$$\begin{aligned}\mathcal{I} &= \mathcal{I}_{s_1 s_2} + \mathcal{I}_{s_1 u_2} + \mathcal{I}_{u_1 s_2} + \mathcal{I}_{u_1 u_2} \\ &= \frac{2\pi^2}{s^2} \frac{1}{(\mathbf{k}+\mathbf{k}_1)^2(\mathbf{k}+\mathbf{k}_3)^2\mathbf{k}^2} \left[(1-1-1+\Delta) + (1-\Delta) + (1-\Delta) + (1+\Delta)\right] \\ &= \frac{2\pi^2}{s^2} \frac{1}{(\mathbf{k}+\mathbf{k}_1)^2(\mathbf{k}+\mathbf{k}_3)^2\mathbf{k}^2} \times 2,\end{aligned} \tag{2.46}$$

that is equal to twice the usual contribution. It is interesting to look at the structure and at the cuts that actually contribute to the imaginary part of the amplitude.

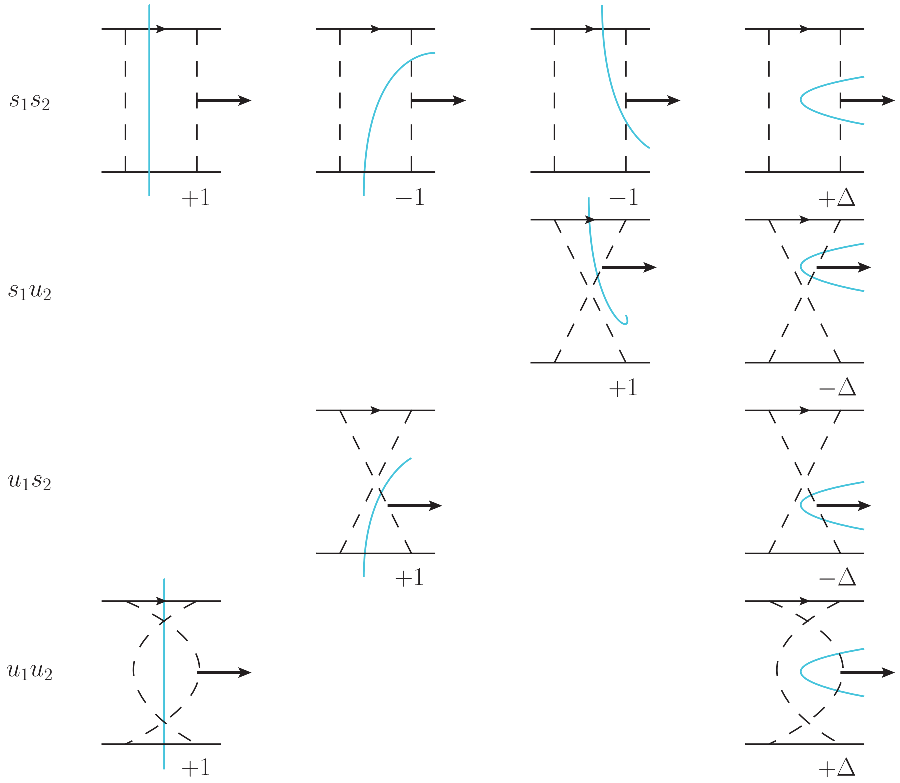

Figure 2.6: Non-zero contributions of cuts. The overall sum is equal to twice the usual cut.

From Fig. 2.6, one can directly note that after the sum, contributions that don't put simultaneously on-shell the two intermediate quarks cancel with the contribution of the same topology in the crossed diagram. This can be simply understood if one considers the two diagrams of the second column in Fig. 2.6 for which the only difference is the crossing of the bottom line that leads to the change $s_2 \to u_2$. Furthermore, one has the identity $s_2 + u_2 + t_2 = 0$ in the massless case, that becomes

$$s_2 \simeq -u_2, \tag{2.47}$$

in the limit of $|t| \ll s, u$ and explains the difference of sign. This general structure of the calculation is analysed in Sec. 2.3 and will be used to compute the longitudinal part of the integral in the two-gluon case. However, the perfect cancellation between some of the contributions calculated here only takes place if there are no other differences between the three diagrams. In particular, there was no colour factor.

Turning the Colour On

If one assumes that the produced particle is colourless and follows the notation of Fig. 2.7, the structure of the final result of Eq. (2.46), is modified to

$$\begin{aligned} C &= \Big[(1-1-1+\Delta)t^at^b \times t^at^b + (1-\Delta)t^at^b \times t^bt^a + (1-\Delta)t^bt^a \times t^at^b + (1+\Delta)t^bt^a \times t^bt^a\Big] \\ &= \Delta\Big[[t^a,t^b] \times [t^a,t^b]\Big] + \Big[\{t^a,t^b\} \times t^at^b - [t^a,t^b] \times t^at^b\Big] . \end{aligned} \tag{2.48}$$

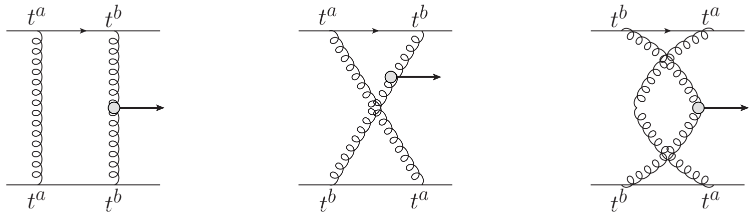

Figure 2.7: Indices of the colour factor.

Because we are interested in double pomeron exchange [78], we substitute

$$t^a t^b \to \frac{1}{2N}\delta^{ab}, \tag{2.49}$$

where N is the number of colours. Subsequently, the cancellation still holds for the contribution proportional to Δ and one is left with the colour factor

$$C = \{t^a, t^b\} \times t^a t^b = \frac{1}{2N^2}\delta^{ab}\delta^{ab} = \frac{N^2-1}{2N^2}. \tag{2.50}$$

Note that if the produced system is in a coloured state, the colour structure is non trivial and there are no cancellations among the diagrams.

2.3 The Overall Picture

In the previous sections, we have shown that the integral over the longitudinal part of the four-momentum has an imaginary part equal to twice the contribution of the usual cut and this because the others cancel each other. These cancellations between different diagrams can be understood in more details.

As explained in Sec. 2.2, one has

$$s_i \simeq -u_i, \tag{2.51}$$

but the effective change of sign can be seen from the fact that going from s_i to u_i only changes the sign of one propagator. As an example, the change in the kinematics when $s_2 \to u_2$ corresponds to the change of propagator

$$(q+k)^2 \to (q-k-k_1)^2, \tag{2.52}$$

so that

$$(1+z)ys - \mathbf{k}^2 \to -(y+y_1)(1-z-z_1)s - (\mathbf{k}+\mathbf{k}_1)^2. \tag{2.53}$$

In the case of contributions where only one of the intermediate quarks is on-shell, the orders of y and z are totally determined by the on-shell condition of the gluon cut. One has

$$(k+k_i)^2 = (z+z_i)(y+y_i)s - (\mathbf{k}+\mathbf{k}_i)^2 = 0, \tag{2.54}$$

for $i = 2 \pm 1$ using exactly the same kind of notation as in Sec. 2.1. Solving the equation in the multi-Regge-kinematics limit of Eq. (2.13) leads to the conditions

$$\begin{aligned} |z| &\ll 1, \\ y &\gg \mathbf{k}_i^2/s, \end{aligned} \tag{2.55}$$

and under those conditions, the change in the propagator simplifies to

$$ys \longrightarrow -ys. \tag{2.56}$$

From these considerations, one finds that the contribution of the $s_1 s_2$-diagram cancels that of the $s_1 u_2$ diagram, and the same for $s_1 s_2$ canceling $u_1 s_2$. This argument also defines the sign of the contribution proportional to Δ and the associated cancellations.

2.4 Two-Gluon Production

The structure of the calculation is exactly the same as in the one-particle production case if one considers a colourless final state. Hereafter, we shall concentrate on the two-gluon production for which the kinematics is defined in Fig. 2.8. Let us demonstrate that, in this case too, the amplitude depends only on the usual cut contribution and not on the “wrong” cuts that include only one intermediate-quark propagator.

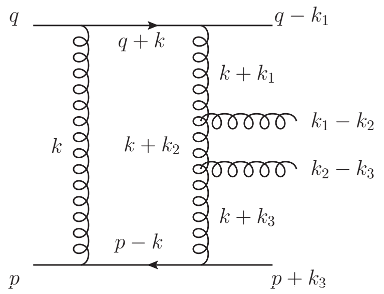

Figure 2.8: Kinematical conventions in the two-gluon exchange.

If two gluons are present in the final state, one should take into account all the contributions of Fig. 2.9 and consider three different situations: the first where only two gluons are attached to the upper line, the second where an additional gluon is attached outside the loop and the

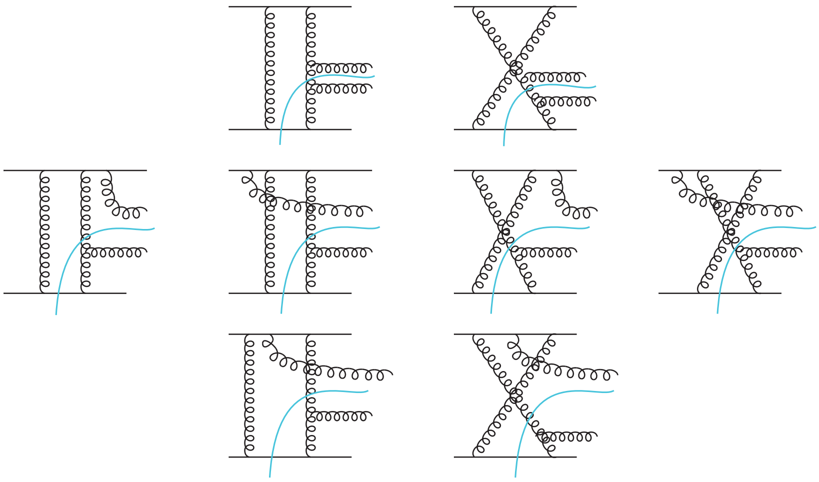

Figure 2.9: Diagrams contributing to two-gluon production but cut in the wrong way or giving a subleading contribution.

last where the additional gluon is attached inside the loop. In the former case, the lower part of the diagram remains unchanged from the crossing of the upper line and the only difference is then the propagator of the upper quark line. As previously, the two diagrams of the first row of Fig. 2.9 cancel. In the second case, *i.e.* with an extra gluon attached outside the loop, the values assigned to y and z don't change either and the crossing of the upper quark line only transforms the intermediate quark propagator from ys to $-ys$, leading to cancellations between all the diagrams of the second row. At last, one is left with diagrams where one of the final gluons is emitted from the intermediate quark line. In this particular case, because both quark propagators

$$\begin{aligned}(q+k)^2 &= y(1+z)s-\mathbf{k}^2 \simeq ys\\ (q-k_1+k_2+k)^2 &= (-y_1+y_2+y)(1-z_1-z_2+z)s-(\mathbf{k}+\mathbf{k}_2-\mathbf{k}_1)^2 \simeq ys,\end{aligned} \tag{2.57}$$

change sign after the crossing

$$\begin{aligned}(q-k-k_2)^2 &= -(y+y_2)(1-z_2-z)s-(\mathbf{k}+\mathbf{k}_2)^2 \simeq -ys,\\ (q-k_1-k)^2 &= -(y_1+y)(1-z_1-z)s-(\mathbf{k}+\mathbf{k}_1)^2 \simeq -ys,\end{aligned} \tag{2.58}$$

there is no cancellation between the usual and the crossed diagrams. Nevertheless, in the regime of multi-Regge kinematics one has two large additional propagators leading to an extra $1/\alpha s$ factor that makes their contribution suppressed at leading order.

The analysis of one- or two-gluon production in multi-Regge kinematics shows that for central production the contributions of the "wrong" cuts are canceled by the crossed diagrams or are subleading. Besides, the argument can be extended to any similar production in the same regime, one has only to compute the contributions from the usual cut in order to access the imaginary part of the amplitude. Usual cuts in Fig. 2.9 are suppressed because they lead to a forward jet, which is excluded by kinematical cuts.

Using the previous knowledge, we shall now compute the longitudinal part of the integral for the production of two gluons in the central region that constitutes the parton-level calculation for the production of quasi-elastic dijet. One has to consider the two diagrams of Fig. 2.10 and to compute the contribution of the cut that puts simultaneously on-shell the intermediate quarks. The momentum transferred from the first and second quarks are k_1 and $-k_3$ and we introduce the four-momenta of the two produced gluons,

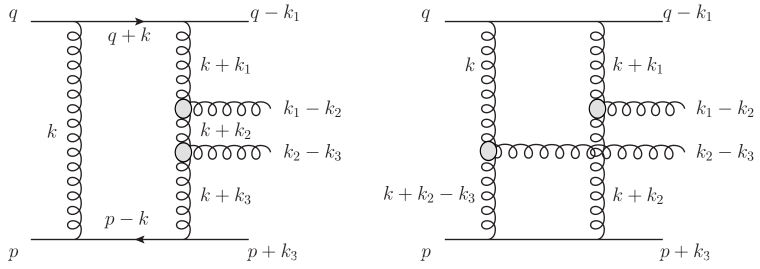

Figure 2.10: Contribution to the imaginary part of the amplitude at leading order for the two-gluon production.

$$\begin{aligned}(k_1-k_2)^\mu &= \alpha_1 p^\mu+\beta_1 q^\mu+(\mathbf{k}_1-\mathbf{k}_2)^\mu,\\ (k_2-k_3)^\mu &= \alpha_2 p^\mu+\beta_2 q^\mu+(\mathbf{k}_2-\mathbf{k}_3)^\mu.\end{aligned} \tag{2.59}$$

The amplitude is dominated by its imaginary part and the leading behavior of the cross section comes from the region where one has an ordering of the longitudinal momentum fractions

$$\frac{|\mathbf{k}_i^2|}{s} \ll \beta_2, \beta_1 \ll 1, \quad \frac{|\mathbf{k}_i^2|}{s} \ll \alpha_1, \alpha_2 \ll 1, \tag{2.60}$$

while transverse momenta are of the same order except for $\mathbf{k}_2^2$ that is large

$$|\mathbf{k}^2|, \; |\mathbf{k}_1^2| \;, |\mathbf{k}_3^2| \; < \; |\mathbf{k}_2^2| \ll s. \tag{2.61}$$

In addition, we work in the high-energy limit $s \gg |t|$ and in the quasi-elastic regime where the longitudinal momentum fractions transferred from the quarks are small to keep the initial particles intact. In our notation, this means $y_i, \; z_i \ll 1$.

The first step is to define y_i and z_i using the on-shell conditions of the final particles

$$\begin{aligned}
(k_1 - k_2)^2 &= \alpha_1\beta_1 s - (\mathbf{k}_1 - \mathbf{k}_2)^2 = 0 \\
&\to \alpha_1\beta_1 s = (\mathbf{k}_1 - \mathbf{k}_2)^2, \\
(k_2 - k_3)^2 &= \alpha_2\beta_2 s - (\mathbf{k}_2 - \mathbf{k}_3)^2 = 0 \\
&\to \alpha_2\beta_2 s = (\mathbf{k}_2 - \mathbf{k}_3)^2.
\end{aligned} \tag{2.62}$$

The same is done for the final quarks

$$\begin{aligned}
(q - k_1)^2 &= -y_1(1 - z_1)s - \mathbf{k}_1^2 = 0 \\
&\to y_1 = \frac{-\mathbf{k}_1^2}{(1 - z_1)s}, \\
(p + k_3)^2 &= z_3(1 + y_3)s - \mathbf{k}_3^2 = 0 \\
&\to z_3 = \frac{\mathbf{k}_3^2}{(1 + y_3)s}.
\end{aligned} \tag{2.63}$$

The last conditions also give information on the other longitudinal component considering the fact that

$$\begin{aligned}
y_2 &= y_1 - \alpha_1 \simeq -\alpha_1, \\
y_3 &= y_2 - \alpha_2 \simeq -\alpha_2, \\
z_1 &= z_2 + \beta_1 \simeq \beta_1, \\
z_2 &= z_3 + \beta_2 \simeq \beta_2.
\end{aligned} \tag{2.64}$$

We are now ready to evaluate the position of the poles coming from the different propagators to compute the integral over the longitudinal part of the first diagram of Fig. 2.10,

$$\mathcal{I}_1 = \int \frac{\mathrm{d}y \mathrm{d}z}{[(q+k)^2 + i\epsilon][(p-k)^2 + i\epsilon][(k+k_1)^2 + i\epsilon][(k+k_2)^2 + i\epsilon][(k+k_3)^2 + i\epsilon][k^2 + i\epsilon]}. \tag{2.65}$$

Using the Sudakov decomposition of the momenta, the denominators of the propagators become

$$
\begin{aligned}
P_1 &= (q+k)^2 + i\epsilon \\
&= y(1+z)s - \mathbf{k}^2 + i\epsilon, \\
P_2 &= (p-k)^2 + i\epsilon \\
&= -z(1-y)s - \mathbf{k}^2 + i\epsilon, \\
P_3 &= (k+k_1)^2 + i\epsilon \\
&= (y+y_1)(z+z_1)s - (\mathbf{k}+\mathbf{k}_1)^2 + i\epsilon, \\
P_4 &= (k+k_2)^2 + i\epsilon \\
&= (y+y_2)(z+z_2)s - (\mathbf{k}+\mathbf{k}_2)^2 + i\epsilon, \\
P_5 &= (k+k_3)^2 + i\epsilon \\
&= (y+y_3)(z+z_3)s - (\mathbf{k}+\mathbf{k}_3)^2 + i\epsilon, \\
P_6 &= k^2 + i\epsilon \\
&= yzs - \mathbf{k}^2 + i\epsilon,
\end{aligned}
\tag{2.66}
$$

and according to the preliminary discussion, the only contribution from the cuts is the one that puts on-shell propagators P_1 and P_2 in the region where $|z| \ll 1$. From the first propagator, one finds $y = \mathbf{k}^2/(1-|z|)s$ that is used in P_2 to compute the pole in z

$$
\begin{aligned}
P_2\Big|_{y=\frac{\mathbf{k}^2}{(1-|z|)s}} &= \left(1 - \frac{\mathbf{k}^2}{(1-|z|)s}\right)|z|s - \mathbf{k}^2 \\
&\simeq |z|s - \mathbf{k}^2 \\
&\to |z| = \frac{\mathbf{k}^2}{s}.
\end{aligned}
\tag{2.67}
$$

Considering both y and z values, one can compute the integral of Eq. (2.65) that is

$$
\mathcal{I}_1 = -\frac{2\pi^2}{s^2}\frac{1}{\mathbf{k}^2(\mathbf{k}+\mathbf{k}_1)^2(\mathbf{k}+\mathbf{k}_2)^2(\mathbf{k}+\mathbf{k}_3)^2}. \tag{2.68}
$$

The procedure is repeated to obtain the longitudinal integral of the second diagram of Fig. 2.10 and the only difference is from propagators P_2 and P_5 that become

$$
\begin{aligned}
P_2 &= (k+k_2-k_3)^2 + i\epsilon \\
&= (y+y_2-y_3)(z+z_2-z_3)s - (\mathbf{k}+\mathbf{k}_2-\mathbf{k}_3)^2 + i\epsilon \\
&= (y+\alpha_2)(z+\beta_2)s - (\mathbf{k}+\mathbf{k}_2-\mathbf{k}_3)^2 + i\epsilon, \\
P_5 &= (p-k-k_2+k_3)^2 + i\epsilon \\
&= -(1-y-y_2+y_3)(z+z_2-z_3)s - (\mathbf{k}+\mathbf{k}_2-\mathbf{k}_3)^2 + i\epsilon \\
&= -(1-y-\alpha_2)(z+\beta_2)s - (\mathbf{k}+\mathbf{k}_2-\mathbf{k}_3)^2 + i\epsilon.
\end{aligned}
\tag{2.69}
$$

using Eq. (2.64). The contributing poles are again those that correspond to the usual cut and put P_1 on-shell together with P_2. The integration region of $|z|$ is now between β_2 and 1 leading to

$$
\mathcal{I}_2 = -\frac{2\pi^2}{s^2}\frac{1}{\mathbf{k}^2(\mathbf{k}+\mathbf{k}_1)^2(\mathbf{k}+\mathbf{k}_2)^2(\mathbf{k}+\mathbf{k}_2-\mathbf{k}_3)^2}. \tag{2.70}
$$

The colour factors are different for the two diagrams and one can compute them using Eq. (2.49) and Fig. 2.11.

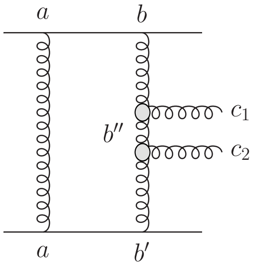

Figure 2.11: Indices of the colour factor.

Therefore, for the first diagram one can show that

$$C_1 = \left(t^a t^b \times t^a t^{b'}\right) f^{bc_1b''} f^{b''c_2b'} = \frac{-1}{4N}\delta^{c_1c_2}, \tag{2.71}$$

that corresponds to the emission of a coloured object at each three-gluon vertices and where N stands for the number of colour. For the second diagram

$$C_2 = \left(t^a t^b \times t^{a'} t^{b'}\right) f^{bc_1b'} f^{ac_2a'} = \frac{1}{4N}\delta^{c_1c_2}. \tag{2.72}$$

The opposite sign of the crossed diagram implies that its contribution decreases the dijet cross section. Taking into account that it is usually neglected, one can stress that the dijet cross section is an upper limit to the process.

We have calculated the integral on the longitudinal momentum of the imaginary part of the amplitude for the two gluons to a colour-singlet state. We have shown that the situation simplifies due to the fact that several contributions cancel each other and the final result reduces to two simple expressions that depend only on transverse momenta. Note that the second diagram has an additional large propagator $(\mathbf{k}+\mathbf{k}_2-\mathbf{k}_3)^2$ and because $\mathbf{k}_2^2$ is large in front of the other transverse momenta in the considered kinematics, this leads to the suppression of the second diagram with respect to the first[1]. Consequently, we shall focus on the first diagram only but the contribution of the second will be studied as a correction in the last chapter. The imaginary part of the amplitude of Eq. (2.2) becomes

$$\mathrm{Im}\,\mathcal{M} = \frac{g^4}{4\pi^2}\frac{\delta^{c_1c_2}}{4N^2}\int \frac{\mathrm{d}^2\mathbf{k}}{\mathbf{k}^2(\mathbf{k}+\mathbf{k}_1)^2(\mathbf{k}+\mathbf{k}_3)^2} \times a(g^*g^* \to gg). \tag{2.73}$$

2.5 Gluon Elastic Scattering

The final two-gluon state is produced by the elastic scattering of two gluons of momenta $k + k_1$ and $k + k_3$. The amplitude of the corresponding process $a(g^*g^* \to gg)$ is calculated in the Feynman gauge using the helicity amplitude method.

---

[1] This statement is developed in Appendix B.2 where we estimate analytically the two-gluon production in quark-quark scattering and the particular case of quasi-multi-Regge kinematics using standard Lipatov vertices.

We have defined

$$a(g^* g^* \to gg) = \sum_{\lambda_i} j^{(1)*}_{\lambda_1} j^{(2)*}_{\lambda_2} \mathcal{M}(g^*_{\lambda_1} g^*_{\lambda_2} \to g_{\lambda_3} g_{\lambda_4}), \tag{2.74}$$

where $\mathcal{M}(g^* g^* \to gg)$ corresponds to the amplitude of the hard subprocess of Fig 2.12 and the current j will be defined below. If one first considers the amplitude $q \to qg$, one has

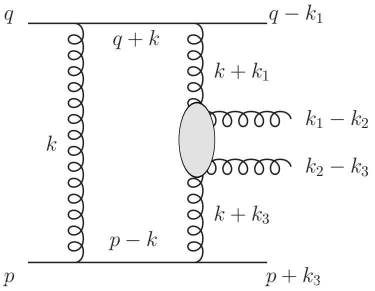

Figure 2.12: Leading diagram for the process $qq \to q + gg + q$ in the high-$\mathbf{k}_2^2$ regime. The central blob corresponds to the gluon-gluon scattering subprocess.

$$\begin{aligned} j^{(1)}_{\lambda_1} &= \bar{u}(q+k)\gamma . e^*_{\lambda_1} u(q - k_1), \\ j^{(2)}_{\lambda_2} &= \bar{u}(p-k)\gamma . e^*_{\lambda_2} u(p + k_3), \end{aligned} \tag{2.75}$$

as the imaginary part is calculated for the cut that puts the intermediate quarks propagators $q+k$ and $p-k$ on-shell. Now, we focus on the gluon scattering. Strictly speaking, the two colliding gluons are virtual. However, in our kinematics their off-shellness are equal to $-\mathbf{k}_1^2$ and $-\mathbf{k}_3^2$ that are much smaller, in modulus, than the hard scale of the subprocess $\mathbf{k}_2^2$. So, one can neglect the non-zero virtualities and approximate the amplitude by the scattering of two on-shell transversely polarized gluons and that corresponds to the sum of the four diagrams of Fig. 2.13. The Mandelstam invariants of the process can be written as a function of the Sudakov variables of the final gluons and yield

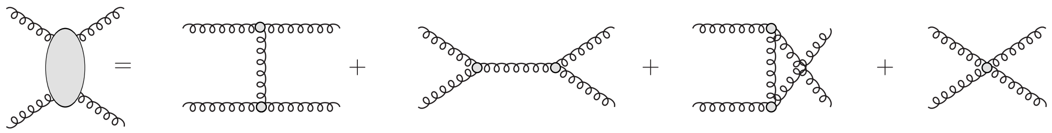

Figure 2.13: Two-gluon elastic scattering.

$$s_{gg} = M_{gg}^2 \simeq \mathbf{k}_2^2 \frac{(\beta_1 + \beta_2)^2}{\beta_1 \beta_2}, \quad t_{gg} \simeq -\mathbf{k}_2^2 \frac{\beta_1 + \beta_2}{\beta_1}, \quad u_{gg} \simeq -\mathbf{k}_2^2 \frac{\beta_1 + \beta_2}{\beta_2}. \tag{2.76}$$

The helicity amplitude for the tree level scattering of two gluons in a colour-singlet state in the center-of-mass frame is

$$\mathcal{M}(g_{\lambda_1} g_{\lambda_2} \to g_{\lambda_3} g_{\lambda_4}) = 2 g_h^2 \frac{N}{N^2 - 1} \delta^{ab} \delta^{c_1 c_2} \left(\frac{s_{gg}}{t_{gg}} + \frac{s_{gg}}{u_{gg}} \right) e^{i(\lambda_1 - \lambda_2)\phi} \mathcal{A}(\lambda_1 \lambda_2 \to \lambda_3 \lambda_4), \tag{2.77}$$

where g_h is the strong coupling constant and λ_i the helicities. The non-zero helicity amplitudes $\mathcal{A}(\lambda_1\lambda_2 \to \lambda_3\lambda_4)$ of the previous equation are

$$\begin{aligned}
\mathcal{A}(++ \to ++) &= \mathcal{A}(-- \to --) = 1, \\
\mathcal{A}(+- \to +-) &= \mathcal{A}(-+ \to -+) = \frac{u_{gg}^2}{s_{gg}^2}, \\
\mathcal{A}(+- \to -+) &= \mathcal{A}(-+ \to +-) = \frac{t_{gg}^2}{s_{gg}^2}.
\end{aligned} \tag{2.78}$$

Here, we denote by ϕ the azimuthal angle of the final two-gluon production plane with respect to the quantization axis that is arbitrary, taking into account that a change will be compensated by an opposite change in the current $j^{(i)}_{\lambda_i}$. One can align the axis of the gluon collision with the laboratory frame. This is because to go from the latter to the former, one has to perform a longitudinal boost to make the energy of the colliding gluons equal, a transverse boost to make the total momentum of the two-gluon system zero, and finally a rotation to align the z axis with the direction of the incoming gluons. If the longitudinal boost doesn't change ϕ, the transverse boost and the rotation at small angle have a negligible effect on the hard momentum k_2. Therefore, one can safely understand the angle of the final gluons production plane as the azimuthal angle in the laboratory frame. Their polarisation vectors can be chosen orthogonal to both $k + k_1$ and $k + k_3$ and, within our accuracy, they can be generically written as

$$e^\mu_\lambda = \mathbf{e}^\mu_\lambda + \frac{2}{s}\left(p^\mu \frac{\mathbf{e}_\lambda.(\mathbf{k}+\mathbf{k}_1)}{\beta_1+\beta_2} + q^\mu \frac{\mathbf{e}_\lambda.(\mathbf{k}+\mathbf{k}_3)}{\alpha_1+\alpha_2}\right), \tag{2.79}$$

where we use the standard definition of the polarization vector in the transverse plane

$$\mathbf{e}_\lambda = -\frac{1}{\sqrt{2}}(\lambda, i). \tag{2.80}$$

The incoming gluons have $\lambda = \lambda_1$ and $\lambda = -\lambda_2$ since they move in opposite longitudinal directions and one can now simplify Eq. (2.75) to

$$\begin{aligned}
j^{(1)*}_{\lambda_1} &\simeq 2\frac{\mathbf{e}^*_{\lambda_1}.(\mathbf{k}+\mathbf{k}_1)}{\beta_1+\beta_2} \\
&= -\frac{2}{\beta_1+\beta_2}\frac{\lambda_1}{\sqrt{2}}|\mathbf{k}+\mathbf{k}_1|e^{-i\lambda_1\phi_1}, \\
j^{(2)*}_{\lambda_2} &\simeq 2\frac{\mathbf{e}^*_{-\lambda_2}.(\mathbf{k}+\mathbf{k}_3)}{\alpha_1+\alpha_2} \\
&= \frac{2}{\alpha_1+\alpha_2}\frac{\lambda_2}{\sqrt{2}}|\mathbf{k}+\mathbf{k}_3|e^{i\lambda_2\phi_3},
\end{aligned} \tag{2.81}$$

where ϕ_1 and ϕ_3 are respectively the azimuthal angles of $\mathbf{k}+\mathbf{k}_1$ and $\mathbf{k}+\mathbf{k}_3$. To obtain the cross section, one has to take the square of the amplitude that is

$$\sum_f \sum_{\lambda_i,\lambda'_i} j^{(1)*}_{\lambda_1} j^{(2)*}_{\lambda_2} j^{(1')}_{\lambda'_1} j^{(2')}_{\lambda'_2} \mathcal{M}_{\lambda_1\lambda_2\to f}\mathcal{M}^*_{\lambda'_1\lambda'_2\to f}, \tag{2.82}$$

if f labels the polarization states of the final gluon system. The only non-trivial interference is between $\mathcal{M}_{+-\to f}$ and $\mathcal{M}_{-+\to f}$ for both $f = +-$ and $f = -+$ because such a term introduces an azimuthal dependence for high $|\mathbf{k}_2|$ via a factor $\exp(4i\phi)$. It contributes to the azimuthal correlations between the plane of the high transverse energy jets and that of the quark scattering.

However, after integration over ϕ, keeping the cross section differential in $\mathbf{k}_2$, this term vanishes and this allows one to consider only the diagonal contribution $\lambda'_i = \lambda_i$. The result is

$$\begin{aligned}
&\sum_f \sum_{\lambda_i} j^{(1)*}_{\lambda_1} j^{(2)*}_{\lambda_2} j^{(1')}_{\lambda_1} j^{(2')}_{\lambda_2} |\mathcal{M}_{\lambda_1\lambda_2\to f}|^2 \\
&= \sum_f \sum_{\lambda_i} 8 \frac{|\mathbf{k}+\mathbf{k}_1||\mathbf{k}+\mathbf{k}_3||\mathbf{k}'+\mathbf{k}_1||\mathbf{k}'+\mathbf{k}_3|}{(\beta_1+\beta_2)^2(\alpha_1+\alpha_2)^2} \frac{1}{4} e^{-i(\lambda_1\phi_1-\lambda_2\phi_3-\lambda_1\phi'_1+\lambda_2\phi'_3)} \mathcal{A}(\lambda_1\lambda_2 \to f).
\end{aligned} \tag{2.83}$$

We would like to present the result in a way that will be useful for the discussion of Chap. 6, so that we separate the case where the total helicity of the final gluon system $\lambda = \lambda_1 - \lambda_2$ is equal to 0 from the $\lambda = 2$ case. We denote the function depending on λ_i by $\mathcal{M}$ and one has respectively

$$|\mathcal{M}_0|^2 = \frac{1}{2}\left[|\mathcal{A}_{++\to++}|^2 + |\mathcal{A}_{--\to--}|^2\right] = 1, \tag{2.84}$$

$$|\mathcal{M}_2|^2 = \frac{1}{2}\left[|\mathcal{A}_{+-\to+-}|^2 + |\mathcal{A}_{+-\to-+}|^2 + |\mathcal{A}_{-+\to-+}|^2 + |\mathcal{A}_{-+\to+-}|^2\right] = \left(\frac{u^4_{gg}}{s^4_{gg}} + \frac{t^4_{gg}}{s^4_{gg}}\right).$$

The sum in Eq. (2.83) can be written, separating the two helicity cases,

$$\begin{aligned}
&\sum_f \sum_{\lambda_i} j^{(1)*}_{\lambda_1} j^{(2)*}_{\lambda_2} j^{(1')}_{\lambda_1} j^{(2')}_{\lambda_2} |\mathcal{M}_{\lambda_1\lambda_2\to f}|^2 \\
&= 8 \frac{|\mathbf{k}+\mathbf{k}_1||\mathbf{k}+\mathbf{k}_3||\mathbf{k}'+\mathbf{k}_1||\mathbf{k}'+\mathbf{k}_3|}{(\beta_1+\beta_2)^2(\alpha_1+\alpha_2)^2} \left(|\mathcal{M}_0|^2 \cos(\phi_1-\phi_3-\phi'_1+\phi'_3) + |\mathcal{M}_2|^2 \cos(\phi_1+\phi_3-\phi'_1-\phi'_3)\right) \\
&= 8 \frac{|\mathbf{k}+\mathbf{k}_1||\mathbf{k}+\mathbf{k}_3||\mathbf{k}'+\mathbf{k}_1||\mathbf{k}'+\mathbf{k}_3|}{(\beta_1+\beta_2)^2(\alpha_1+\alpha_2)^2} \left[\left(|\mathcal{M}_0|^2 + |\mathcal{M}_2|^2\right) \cos(\phi_1-\phi'_1)\cos(\phi_3-\phi'_3)\right. \\
&\qquad \left. + \left(|\mathcal{M}_0|^2 - |\mathcal{M}_2|^2\right) \sin(\phi_1-\phi'_1)\sin(\phi_3-\phi'_3)\right].
\end{aligned} \tag{2.85}$$

Using the relation

$$\cos(\phi_i - \phi'_j) = \frac{(\mathbf{k}+\mathbf{k}_i).(\mathbf{k}'+\mathbf{k}_j)}{|\mathbf{k}+\mathbf{k}_i|\,|\mathbf{k}'+\mathbf{k}_j|}, \tag{2.86}$$

one finds the cross section to be equal to

$$\begin{aligned}
&\sum_f \sum_{\lambda_i} j^{(1)*}_{\lambda_1} j^{(2)*}_{\lambda_2} j^{(1')}_{\lambda_1} j^{(2')}_{\lambda_2} |\mathcal{M}_{\lambda_1\lambda_2\to f}|^2 \\
&= \frac{8}{(\beta_1+\beta_2)^2(\alpha_1+\alpha_2)^2} \Big\{ \left(|\mathcal{M}_0|^2 + |\mathcal{M}_2|^2\right) \left[(\mathbf{k}+\mathbf{k}_1).(\mathbf{k}'+\mathbf{k}_1)\right] \left[(\mathbf{k}+\mathbf{k}_3).(\mathbf{k}'+\mathbf{k}_3)\right] \\
&\quad + \left(|\mathcal{M}_0|^2 - |\mathcal{M}_2|^2\right) \Big(\left[(\mathbf{k}+\mathbf{k}_1).(\mathbf{k}+\mathbf{k}_3)\right] \left[(\mathbf{k}'+\mathbf{k}_1).(\mathbf{k}'+\mathbf{k}_3)\right] \\
&\qquad - \left[(\mathbf{k}+\mathbf{k}_1).(\mathbf{k}'+\mathbf{k}_3)\right] \left[(\mathbf{k}'+\mathbf{k}_1).(\mathbf{k}+\mathbf{k}_3)\right] \Big) \Big\}.
\end{aligned} \tag{2.87}$$

An important remark is that during all the calculation we have kept an exact transverse kinematics. However, it is sometimes claimed [16] that a reasonable assumption is to take the limit

$$|\mathbf{k}_1|, |\mathbf{k}_3| \ll |\mathbf{k}|, |\mathbf{k}'|, \tag{2.88}$$

i.e to neglect the transverse momenta of the incoming gluons in front of those of the loop. In this particular case, the relations between the azimuthal angles are $\phi_3 \simeq \phi_1 + \pi$ and $\phi'_3 \simeq \phi'_1 + \pi$ and lead to a simplification of Eq. (2.87)

$$\begin{aligned}&\sum_f \sum_{\lambda_i} j^{(1)*}_{\lambda_1} j^{(2)*}_{\lambda_2} j^{(1')}_{\lambda_1} j^{(2')}_{\lambda_2} |\mathcal{M}_{\lambda_1\lambda_2\to f}|^2 \\ &= 8\frac{\mathbf{k}^2\mathbf{k}'^2}{(\beta_1+\beta_2)^2(\alpha_1+\alpha_2)^2}\left[|\mathcal{M}_0|^2 + |\mathcal{M}_2|^2\cos(2\phi-2\phi')\right],\end{aligned} \tag{2.89}$$

where ϕ and ϕ' are the azimuthal angles of k and k' respectively. After averaging over those angles, the $|\mathcal{M}_2|^2$ term vanishes and only the amplitude with a final state of zero helicity survives. Consequently, in this limit, one obtains the so-called $J_z = 0$ rule [16].

2.6 The Parton-Level Cross Section

One can now write the partonic differential cross section as an integral of the squared amplitude over a phase space factorized between light-cone and transverse degrees of freedom. The imaginary part of the amplitude is obtained from Eq. (2.74) and Eq. (2.87), using the identity

$$\frac{s_{gg}}{(\alpha_1+\alpha_2)(\beta_1+\beta_2)} = s. \tag{2.90}$$

One has

$$\mathrm{d}\sigma_{qq} = \frac{1}{16(2\pi)^8}\frac{g_h^4\, g^8}{(4\pi^4)}\, C\, \frac{\mathrm{d}\beta_1}{\beta_1}\frac{\mathrm{d}\beta_2}{\beta_2}\, \mathrm{d}^2\mathbf{k}_1\, \mathrm{d}^2\mathbf{k}_2\, \mathrm{d}^2\mathbf{k}_3 \times |\mathcal{M}|^2, \tag{2.91}$$

where factors, colour factor C and coupling constants are written explicitly in front, g is the coupling at the gluon-quark vertex while g_h is a hard coupling coming from the gluon-gluon collision, and

$$\begin{aligned}|\mathrm{Im}\mathcal{M}|^2 = \frac{1}{2}\left(\frac{1}{t_{gg}}+\frac{1}{u_{gg}}\right)^2 &\int \frac{\mathrm{d}^2\mathbf{k}}{\mathbf{k}^2(\mathbf{k}+\mathbf{k}_1)^2(\mathbf{k}+\mathbf{k}_3)^2}\frac{\mathrm{d}^2\mathbf{k}'}{\mathbf{k}'^2(\mathbf{k}'+\mathbf{k}_1)^2(\mathbf{k}'+\mathbf{k}_3)^2} \\ \times \Big\{ &\left(|\mathcal{M}_0|^2+|\mathcal{M}_2|^2\right)\left[(\mathbf{k}+\mathbf{k}_1).(\mathbf{k}'+\mathbf{k}_1)\right]\left[(\mathbf{k}+\mathbf{k}_3).(\mathbf{k}'+\mathbf{k}_3)\right] \\ + &\left(|\mathcal{M}_0|^2-|\mathcal{M}_2|^2\right)\Big(\left[(\mathbf{k}+\mathbf{k}_1).(\mathbf{k}+\mathbf{k}_3)\right]\left[(\mathbf{k}'+\mathbf{k}_1).(\mathbf{k}'+\mathbf{k}_3)\right] \\ &\qquad - \left[(\mathbf{k}+\mathbf{k}_1).(\mathbf{k}'+\mathbf{k}_3)\right]\left[(\mathbf{k}'+\mathbf{k}_1).(\mathbf{k}+\mathbf{k}_3)\right]\Big)\Big\}.\end{aligned} \tag{2.92}$$

Here we clearly separate the contribution of the two possible final helicity states in different terms, $\mathcal{M}_0$ for the 0 helicity state whereas the total helicity 2 term is $\mathcal{M}_2$.
If both final gluons are integrated over the whole available phase space, then an extra 1/2 factor should be included to take Bose statistics into account.

In the particular case of multi-Regge kinematics and with the help of some simple approximations, one can obtain an estimate of the partonic cross section analytically, see Appendix B.2. But in the general case of the production of two gluons with large transverse momentum and after the addition of soft and higher corrections coming in the next chapters, the result has to be obtained through a numerical integration over the variables β_1, β_2, $\mathbf{k}_1$, $\mathbf{k}_2$, $\mathbf{k}_3$, $\mathbf{k}$ and $\mathbf{k}'$.

2.7 Comments

The accuracy of some of the approximations found in the literature can be directly tested and the aim of the present section is to discuss those that can be taken at the parton level. The idea is to start with the reference curve of Fig. 1.12 and modify only the parton level part. The first point is the claim that the calculation is perturbative and the second, the importance of the $J_z = 0$ rule as well as the contribution of the diagram where one of the final partons is emitted from the screening gluon.

One of the main assumptions [16] is the perturbative nature of the calculation. The argument is based on the fact that the gluons involved in the loop have transverse momenta larger than 1 GeV but this assumption can be checked. In the plot of Fig. 2.14, we show the distributions of $\mathrm{d}\sigma/\mathrm{d}|\mathbf{k}|$ for the reference curve parametrisation at the TeVatron. One can directly see that the mean values are around 1 GeV. Although the distribution $\mathrm{d}\sigma/\mathrm{d}|\mathbf{k}|$ is not a physical observable, it is a useful quantity to test the assumptions used in the theoretical calculations. In addition, one can also choose to define the perturbative quantity σ_{pert} as the value of the cross section in which gluon-transverse momenta squared $\mathbf{k}^2$, $(\mathbf{k}+\mathbf{k}_1)^2$, $(\mathbf{k}+\mathbf{k}_3)^2$ are larger than 1 GeV^2 and compute the ratio $\sigma_{\mathrm{pert}}/\sigma$. This is done by cutting the momenta entering the gluon propagators and, for different jet transverse minimum energies, the result is given in Table 2.1. These small numbers are due to the fact that transverse momenta $\mathbf{k}_1$ and $\mathbf{k}_3$ are comparable to $\mathbf{k}$ in our model. Hence, they cannot be neglected and lead to three different cuts on the cross section that reduce it substantially[2].

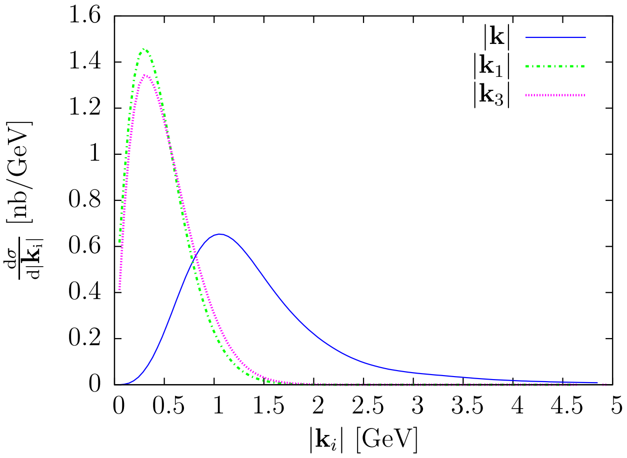

Figure 2.14: Distribution of the transverse momentum $|\mathbf{k}|$, $|\mathbf{k}_1|$, $|\mathbf{k}_3|$ for the reference curve at the TeVatron and $\mathrm{E}_T^{\mathrm{min}}$ >10 GeV. Note that even if it is not a physical observable it can be used to test properties of the theoretical calculation.

Experiment	$\mathbf{E}_T^{\mathrm{min}}$	$\sigma_{\mathrm{pert}}/\sigma$
CDF RunII	10 GeV	30%
CDF RunII	35 GeV	20%

Table 2.1: Ratio σ_{pert}/σ where σ_{pert} is the value of the cross section if gluon-transverse momenta squared $\mathbf{k}^2$, $(\mathbf{k}+\mathbf{k}_1)^2$, $(\mathbf{k}+\mathbf{k}_3)^2$ are larger than 1 GeV. Different experiments and jet transverse minimum energies are presented but in all cases the parametrisation is the one of the reference curve.

---

[2] This conclusion changes slightly with the implementation of the Sudakov form factor as explained in Chap. 4 but small momenta will keep contributing significantly to the cross section.

Note that as $E_T^{\min}$ increases the gluon loop gets softer. It can be explained by the fact that at fixed proton energy, the production of high-E_T jets requires larger longitudinal momentum transfer. So, the effect of the non-perturbative region of QCD is not negligible and under those conditions, it should be interesting to consider modifications of the gluon propagators to take into account the non-perturbative aspect of the gluon loop. This was already done in different quasi-elastic models [12, 15], however, it remains unclear how to take these modifications into account in a consistent and gauge invariant way as changes to the propagators also imply changes to the vertices.

If the momentum in the loop $\mathbf{k}$ is small, one can ask if neglecting $\mathbf{k}_i$ in front of $\mathbf{k}$ and $\mathbf{k}'$ is accurate. We show in Fig. 2.15.a the reference curve of Fig. 1.12 and the same curve if one neglects $\mathbf{k}_i$. The approximation is very rough, leading to a factor 2 with respect to the reference curve and to an overestimation of the cross section. Another current approximation is to keep only the term that gives the helicity-0 contribution in Eq. (2.91), this is what is called the $J_z = 0$ approximation. We confirm, as shown in Fig. 2.15.b, that the $\lambda = 0$ terms is dominant as noticed in [16], the $\lambda = 2$ term contributes only for 2-3% of the cross section. Nevertheless, we shall keep it in the following studies in order to be as complete as possible.

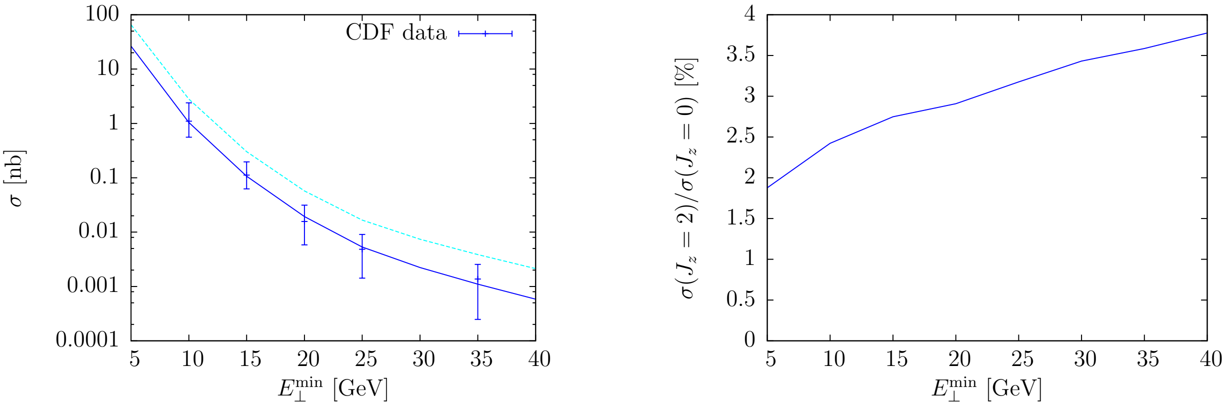

(a) (b)

Figure 2.15: (a) The effect of neglecting $\mathbf{k}_i$ in front of $\mathbf{k}$ and $\mathbf{k}'$. (b) Ratio between $\sigma(J_z = 2)$ and $\sigma(J_z = 0)$ as a function of the jet transverse minimum energy. $\sigma(J_z = 0)$ corresponds to the application of the J_z=0 rule.

Finally, there is the complicated question of the second diagram of Fig. 2.10. One knows that its contribution to the amplitude should be small as it contains one more hard propagator.

2.7.1 The Second Diagram

The calculation of the amplitude of the second diagram where the two gluons are emitted from different t-channel legs cannot be made in the same way as one doesn't have the $gg \to gg$ irreducible vertex. Nevertheless, it can be evaluated with the help of the Lipatov vertices [44, 79] in multi-Regge kinematics. We present here our result.

One has to start with the diagram of Fig. 2.16 and calculate

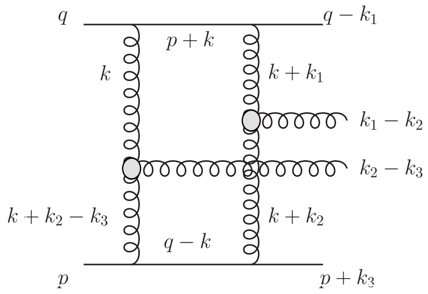

Figure 2.16: Kinematics of the diagram with final gluons emitted from different legs in the t-channel.

$$\begin{aligned} \mathrm{Im}\,\mathcal{M}_2 = s\frac{g_h^2 g^4}{(2\pi)^2}\frac{\delta^{c_1 c_2}}{4N}\int \frac{\mathrm{d}^2\mathbf{k}}{\mathbf{k}^2(\mathbf{k}+\mathbf{k}_1)^2(\mathbf{k}+\mathbf{k}_2)^2(\mathbf{k}+\mathbf{k}_2-\mathbf{k}_3)^2} \\ \times\, C_1^{\mu_1}\left(k+k_1,k+k_2\right) C_2^{\mu_2}\left(-k_1,-k-k_2+k_3\right)\, e^*_{\mu_1}(\lambda_3)e^*_{\mu_2}(\lambda_4). \end{aligned} \tag{2.93}$$

The main part is the evaluation of contractions of Lipatov vertices [44, 79] with the polarisation vectors $e^*_{\mu_1}(\lambda_3)e^*_{\mu_2}(\lambda_4)$, *e.g.* for the first vertex, between

$$C_1^{\mu_1}\left(k+k_1,k+k_2\right) = q^\mu\left(\beta_1 - 2\frac{(\mathbf{k}+\mathbf{k}_1)^2}{\alpha_1 s}\right) - p^\mu\left(\alpha_1 - 2\frac{(\mathbf{k}+\mathbf{k}_2)^2}{\beta_1 s}\right) - (2\mathbf{k}+\mathbf{k}1+\mathbf{k}_2)^\mu, \tag{2.94}$$

following the kinematics of Fig. 2.17, and

$$e^*_{\mu_1}(\lambda_3) = \frac{1}{\sqrt{2}}\begin{pmatrix} 0 \\ \lambda_3\cos(\theta) \\ -i \\ -\lambda_3\sin(\theta)\end{pmatrix}, \tag{2.95}$$

where λ_3 is the helicity of the emitted gluon and θ its polar angle in the center-of-mass frame of the collision. Obviously, this calculation is interesting in itself and the method is detailed in Appendix B.2.5, we directly present the results here. The first Lipatov vertex gives

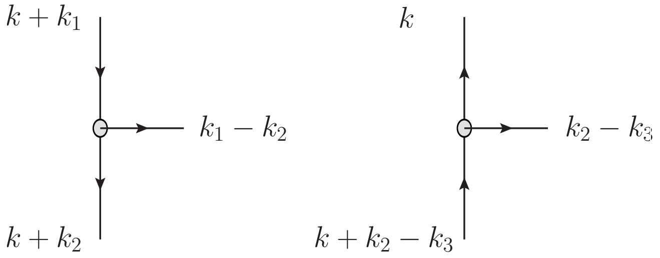

Figure 2.17: Kinematics of the Lipatov vertices.

$$C_1^{\mu_1}e^*_{\mu_1}(\lambda_3) = \sqrt{2}\frac{|\mathbf{k}+\mathbf{k}_1||\mathbf{k}+\mathbf{k}_2|}{|\mathbf{k}_1-\mathbf{k}_2|}\lambda_3 e^{-i\lambda_3\phi_{12}}, \tag{2.96}$$

while the second gives

$$C_2^{\mu_2} e^*_{\mu_2}(\lambda_4) = -\sqrt{2}\frac{|\mathbf{k}||\mathbf{k}+\mathbf{k}_2-\mathbf{k}_3|}{|\mathbf{k}_1-\mathbf{k}_2|}\lambda_4 e^{-i\lambda_4\phi_{23}}, \tag{2.97}$$

where ϕ_{ij} is the angle between the vectors. Using the above results, one can now compute the cross section by squaring the amplitude, so that

$$\begin{aligned}|\mathcal{M}_2|^2 = & \int \frac{\mathrm{d}^2\mathbf{k}}{\mathbf{k}^2(\mathbf{k}+\mathbf{k}_1)^2(\mathbf{k}+\mathbf{k}_2)^2(\mathbf{k}+\mathbf{k}_2-\mathbf{k}_3)^2}\frac{\mathrm{d}^2\mathbf{k}'}{\mathbf{k}'^2(\mathbf{k}'+\mathbf{k}_1)^2(\mathbf{k}'+\mathbf{k}_2)^2(\mathbf{k}'+\mathbf{k}_2-\mathbf{k}_3)^2}\\ &\times \frac{|\mathbf{k}+\mathbf{k}_1||\mathbf{k}+\mathbf{k}_2|}{|\mathbf{k}_1-\mathbf{k}_2|}\frac{|\mathbf{k}+\mathbf{k}_2||\mathbf{k}+\mathbf{k}_2-\mathbf{k}_3|}{|\mathbf{k}_1-\mathbf{k}_2|}\frac{|\mathbf{k}'+\mathbf{k}_1||\mathbf{k}'+\mathbf{k}_2|}{|\mathbf{k}_1-\mathbf{k}_2|}\frac{|\mathbf{k}'+\mathbf{k}_2||\mathbf{k}'+\mathbf{k}_2-\mathbf{k}_3|}{|\mathbf{k}_1-\mathbf{k}_2|}\\ &\times \sum_{\lambda_3\lambda_4}(-2\lambda_3\lambda_4)(-2\lambda'_3\lambda'_4)e^{-i\lambda_3\phi_{12}-i\lambda_4\phi_{23}}e^{i\lambda'_3\phi'_{12}+i\lambda'_4\phi'_{23}}.\end{aligned} \tag{2.98}$$

The main characteristics of the second diagram appears here, in the exponential factor. Since if the angles are identical then only the amplitudes with gluons of identical helicity $\lambda_3 = \lambda_4$ in the final state survive. Actually, in the limit of $\mathbf{k}_i \ll \mathbf{k}_2$, this condition is fulfilled and only processes with helicity 2 contribute to the cross section. Assuming that it is the dominant part, one can sum over the possible helicity states in the same spirit as what was done in the first diagram and one obtains

$$\begin{aligned}|\mathcal{M}_2|^2 = \frac{16}{|\mathbf{k}_1-\mathbf{k}_2|^4} & \int \frac{\mathrm{d}^2\mathbf{k}}{\mathbf{k}^2(\mathbf{k}+\mathbf{k}_1)^2(\mathbf{k}+\mathbf{k}_2)^2(\mathbf{k}+\mathbf{k}_2-\mathbf{k}_3)^2}\frac{\mathrm{d}^2\mathbf{k}'}{\mathbf{k}'^2(\mathbf{k}'+\mathbf{k}_1)^2(\mathbf{k}'+\mathbf{k}_2)^2(\mathbf{k}'+\mathbf{k}_2-\mathbf{k}_3)^2}\\ & \times \left[\mathrm{f_c}(\mathbf{k})\mathrm{f_c}(\mathbf{k}') + \mathrm{f_s}(\mathbf{k},\mathbf{k}')\right]\left[\mathrm{g_c}(\mathbf{k})\mathrm{g_c}(\mathbf{k}') + \mathrm{g_h}(\mathbf{k},\mathbf{k}')\right],\end{aligned} \tag{2.99}$$

where the functions are defined by

$$\begin{aligned}\mathrm{f_c}(\mathbf{k}) &= (\mathbf{k}+\mathbf{k}_1).(\mathbf{k}+\mathbf{k}_2),\\ \mathrm{g_c}(\mathbf{k}) &= \mathbf{k}.(\mathbf{k}+\mathbf{k}_2-\mathbf{k}_3),\end{aligned} \tag{2.100}$$

$$\begin{aligned}\mathrm{f_s}(\mathbf{k},\mathbf{k}') &= (\mathbf{k}+\mathbf{k}_1).(\mathbf{k}'+\mathbf{k}_1)(\mathbf{k}+\mathbf{k}_2).(\mathbf{k}'+\mathbf{k}_2) - (\mathbf{k}+\mathbf{k}_1).(\mathbf{k}'+\mathbf{k}_2)(\mathbf{k}+\mathbf{k}_2).(\mathbf{k}'+\mathbf{k}_1),\\ \mathrm{g_h}(\mathbf{k},\mathbf{k}') &= \mathbf{k}.\mathbf{k}'(\mathbf{k}+\mathbf{k}_2-\mathbf{k}_3).(\mathbf{k}'+\mathbf{k}_2-\mathbf{k}_3) - \mathbf{k}.(\mathbf{k}'+\mathbf{k}_2-\mathbf{k}_3)(\mathbf{k}+\mathbf{k}_2-\mathbf{k}_3).\mathbf{k}'.\end{aligned}$$

Finally, we gather all the coefficients in front and the differential cross section for the second diagram is

$$\mathrm{d}\sigma = \frac{g_h^4 g^8}{4\pi^4(2\pi)^8}\frac{N^2-1}{2N}\frac{1}{|\mathbf{k}_1-\mathbf{k}_2|^4}\frac{\mathrm{d}\beta_1}{\beta_1}\frac{\mathrm{d}\beta_2}{\beta_2}\mathrm{d}^2\mathbf{k}_1\mathrm{d}^2\mathbf{k}_3\mathrm{d}^2\mathbf{k}_2 \times |\mathcal{M}_2|^2. \tag{2.101}$$

Note that one could have evaluated the first diagram in the same way, *i.e.* by successive contractions of the active gluon momenta with the corresponding Lipatov vertices, and recover the final expression of Eq. (2.91) for the first amplitude.

The contribution to the cross section can now be evaluated numerically after the introduction of an impact factor to regulate the IR divergence. Without any other higher-order corrections that should decrease its importance, the second diagram accounts for 15% of the first diagram cross section with all corrections included and $\mathrm{E}_T^{\mathrm{min}}$ >10 GeV. In addition, the final dijet system is of helicity 2 and can be differentiated from the dominant contribution of the first diagram that has a total helicity 0. Consequently, the interference between the two diagrams is almost zero and will not be discussed here.

It is usually assumed that the extra gluon in the t-channel is needed only to screen the colour exchange and does not participate to the hard subprocess. Because of that, pomeron fusion is very similar to gluon fusion and the details of the final state of the hard interaction do not substantially change the calculation. In particular, one can change the hard subprocess without touching the rest of model. This also makes the calculation of the dijet quasi-elastic production similar to that of the Higgs boson quasi-elastic production and leads to the hope that the CDF data can be used to calibrate Higgs boson production.

This is where the lowest-order perturbative QCD calculation ends. The first correction that comes is the introduction of an impact factor that embeds the quarks into a proton to reproduce a typical collision at a hadron collider.

Chapter 3

The Impact Factor

The previous description of the dijet cross section considers only the parton-level amplitude where the final system is produced after the interaction of two quarks. Besides, the expression of Eq. (2.91) is singular when the exchanged gluons go on-shell, *i.e.* $\mathbf{k}^2$, $(\mathbf{k}+\mathbf{k}_1)^2$, $(\mathbf{k}+\mathbf{k}_3)^2$, $\mathbf{k}'^2$, $(\mathbf{k}'+\mathbf{k}_1)^2$, $(\mathbf{k}'+\mathbf{k}_3)^2 \to 0$. The following chapter presents two ways of embedding the parton-level gluon production into a proton-proton collision and takes care of the singularity by the introduction of an impact factor. The first section gives the general properties of this object. The second section develops a simple approach to the description of ultra-relativistic protons while Sec. 3.3 is devoted to the construction of an impact factor coming from unintegrated gluons density (UgD). Actually, the results of Chap. 2 have shown that the parton-level calculation is dominated by the non-perturbative region, *i.e.* the active and screening gluons can be very soft. Consequently, one has to carefully treat the soft part and this is one of the advantage of the present parametrisation that allows to consider it separately. Finally, both impact factors were built using parameters coming from data, a fit to the elastic cross section in the first case and to the gluons density in the second.

3.1 General Properties of Impact Factors

The hadron impact factor comes naturally from the fact that in a real process, the quarks between which the pomeron is exchanged are embedded into a hadron[1]. The impact factor Φ is the object that one should convolute with the parton level cross section to obtain the hadronic one and is pictured in Fig. 3.1. It is related to the partonic content of the proton and gives the probability amplitude of interaction between its constituents and the exchanged particles in the

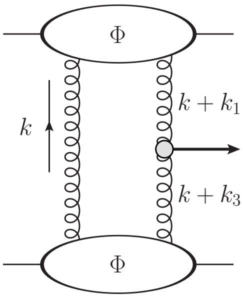

Figure 3.1: Gluon dijet production now embedded in proton-proton scattering.

---

[1] We consider here the general case. In the following we shall focus on proton-proton collisions that are typical of the LHC but it also applies for proton-antiproton collisions at the TeVatron.

t-channel. It also includes the expected energy behaviour of the cross section for this type of scattering.

Hadrons are colourless objects, so that if the gluon exchanged is very soft, its corresponding wavelength is too large to resolve the initial particle that appears colourless, without coloured constituent to couple with[2]. The argument can be expressed, according to [80, 81], as gluons with wavelength λ average the colour of the hadron, and hence a suppression proportional to r/λ must always be present when coupling to a colour singlet of size r. In two-gluon exchange, this property comes from the hadron impact factor $\Phi(\mathbf{k}_a, \mathbf{k}_b)$, which is such that

$$\Phi(0, \mathbf{k}_b) = 0 = \Phi(\mathbf{k}_a, 0), \tag{3.1}$$

where $\mathbf{k}_a$ and $\mathbf{k}_b$ are the transverse momenta of the two t-channel gluons. Consequently, the differential cross section for gluon dijet production of the previous chapter, now embedded in proton-proton scattering, is

$$\mathrm{d}\sigma = \mathrm{d}\sigma_{qq} \otimes \prod_{i=2\pm1} \Phi\left(\mathbf{k}, -(\mathbf{k}+\mathbf{k}_i)\right) \Phi\left(\mathbf{k}', -(\mathbf{k}'+\mathbf{k}_i)\right). \tag{3.2}$$

The impact factor has to be inside the loop integral over $\mathbf{k}$ and $\mathbf{k}'$. This first correction to the parton-level calculation also removes all infra-red singularities due to the fact that the impact factor goes to zero with the propagators. However, it has been argued that the divergence could be regularised via the Sudakov form factor [16], another correction discussed in Chap. 4. Very roughly, the Sudakov factor comes from virtual vertex corrections and exponentially suppresses the amplitude as the momentum in the loop becomes small. Thus it also makes the momentum integration infrared safe. One can see that it is not sufficient as the same diagram also contributes to the inclusive jet production which does not contain any Sudakov form factor but must be finite nevertheless. The source of the cancellation should be elsewhere, in the proton impact factor. It is why in the present work, the colour neutrality of the incoming hadrons is implemented separately from the Sudakov correction. This is different from the Durham model that defines the impact factor via a unintegrated gluon density that includes the Sudakov factor. Here, the idea is a little different as we do not use directly the unintegrated gluon density but an impact factor build in such a way that soft and hard emissions from the proton are treated in the same object. The impact factor is tuned to data to model the behavior of the proton and is supposed to include all corrections, and in this picture the Sudakov form factor is another piece of the calculation.

We present here two different manners to implement the impact factor in the calculation. The first one is a really simple impact factor that describes the proton in terms of the quark light-cone wave function. The second is based on a differentiation of usual parton distribution function and includes a dependence on the longitudinal momentum fraction lost by the proton.

3.2 Impact Factor from a Quark Model

An approach to the impact factor is to consider that an ultra-relativistic proton is made of 3 quarks to which the exchanged gluons couple. According to references [80] and [82], one can derive an impact factor in terms of the quark light-cone wavefunction (LCWF).

The first assumption is that the proton is dominated by a 3-quark Fock state. In this case, it was shown that the impact factor corresponding to two gluons of momenta $\mathbf{k}_a$ and $\mathbf{k}_b$ coupling to the proton is divided in the two diagrams of Fig. 3.2. The function $\mathcal{E}_1$ corresponds to the first

---

[2] This can be seen the other way around: a hadron cannot emit gluons with wavelength greater than its size.

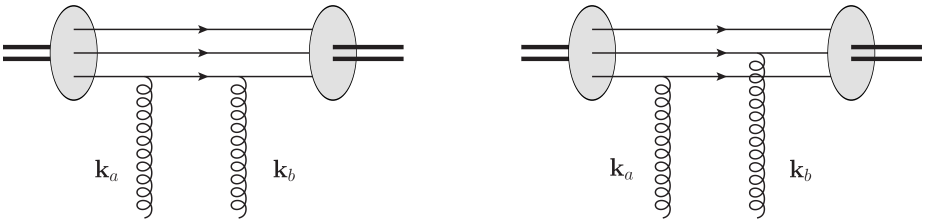

Figure 3.2: The two contributions to the LCWF impact factor.

one, where the two exchanged gluons are attached to the same quark and one can show that it is identical to the measured Dirac elastic form factor in $\gamma^* p$ scattering

$$\mathcal{E}_1\left(\mathbf{k}_a+\mathbf{k}_b\right)=F_1(t)=\frac{3.53-2.79t}{(3.53-t)(1-\frac{t}{0.71})^2}, \tag{3.3}$$

with $t=-\left(\mathbf{k}_a+\mathbf{k}_b\right)^2$. This fits the data [83] for $|t|$ smaller than 9 GeV^2. In order to build the complete impact factor, one has to add the contribution of the coupling of gluons to different quarks, $\mathcal{E}_2\left(\mathbf{k}_a,\mathbf{k}_b\right)$ which has the property

$$\mathcal{E}_2\left(\mathbf{k}_a,0\right)=F_1(-\mathbf{k}_a^2). \tag{3.4}$$

Hence, one can use a simple parametrization which takes into account the above statement,

$$\begin{aligned}\mathcal{E}_1\left(\mathbf{k}_a+\mathbf{k}_b\right)&=F_1\left[-(\mathbf{k}_a+\mathbf{k}_b)^2\right],\\ \mathcal{E}_2\left(\mathbf{k}_a,\mathbf{k}_b\right)&=F_1\left[-(\mathbf{k}_a^2+\mathbf{k}_b^2+c\,\mathbf{k}_a.\mathbf{k}_b)\right],\end{aligned} \tag{3.5}$$

where c is a free parameter that is of the order one in the proton case. The impact factor now reads

$$\Phi_{\mathrm{LCWF}}(\mathbf{k}_a,\mathbf{k}_b)=3\left[F_1\left(-(\mathbf{k}_a+\mathbf{k}_b)^2\right)-F_1\left(-(\mathbf{k}_a^2+\mathbf{k}_b^2+c\,\mathbf{k}_a.\mathbf{k}_b)\right)\right]. \tag{3.6}$$

This makes the dijet cross section finite. The factor 3 in front approximately gives the quark counting rule that says that hadronic cross sections are proportional to the number of valence quarks in the colliding particles.

The LCWF impact factor of Eq. (3.6) has no energy dependence but it can be easily introduced going back to the phenomenological description of pomeron exchange in the S-matrix formalism of Sec. 1.3.1. One can include the s behaviour of the cross section via a Regge factor [84]

$$R_i=\left(\frac{s}{s_i}\right)^{\alpha(t_i)}. \tag{3.7}$$

The Regge trajectory of the pomeron is $\alpha(t_i)$, s is the energy in the center-of-mass frame of the system and s_i, t_i with i=2 ± 1 are the Mandelstam invariants of the upper and lower part of the diagram as shown in Fig. 3.3.

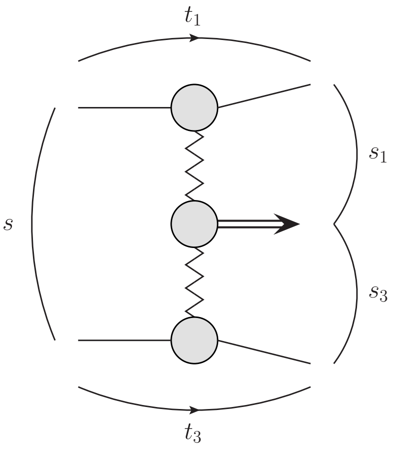

Figure 3.3: Decomposition of the main diagram in two parts according to [84]. Both subdiagrams have their own Mandelstam invariants s_i and t_i for i=2±1.

One has for the upper proton of the process of Fig. 2.10

$$\Phi^{p_1}_{\mathrm{LCWF}}(\mathbf{k}, -(\mathbf{k}+\mathbf{k}_1)) = 3\left(\frac{s}{s_1}\right)^{\alpha(t_1)}\left[F_1\left(-\mathbf{k}_1^2\right) - F_1\left(-(\mathbf{k}^2 + (\mathbf{k}+\mathbf{k}_1)^2 - c\,(\mathbf{k}+\mathbf{k}_1).\mathbf{k})\right)\right]. \tag{3.8}$$

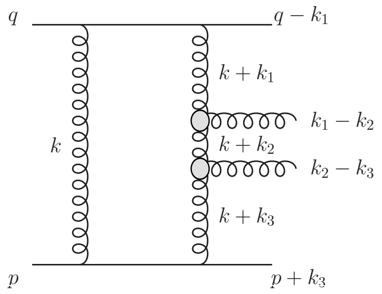

Figure 3.4: Kinematics of two-gluon production.

In the kinematics of Fig. 3.4, one can calculate s_1 and t_1 using the four-momentum of the centrally produced system

$$\begin{aligned} k_X^\mu &= (k_1 - k_2)^\mu + (k_2 - k_3)^\mu \\ &= (\alpha_1 + \alpha_2)p^\mu + (\beta_1 + \beta_2)q^\mu + (\mathbf{k}_1 - \mathbf{k}_3)^\mu, \end{aligned} \tag{3.9}$$

that leads to

$$\begin{aligned} s_1 &= (q - k_1 + k_X)^2 \\ &= (\beta_1 + \beta_2)s, \\ t_1 &= (q - q + k_1)^2 \\ &= -\mathbf{k}_1^2, \end{aligned} \tag{3.10}$$

in the large s limit. One can directly note that s_1 is proportional to the longitudinal momentum lost by the incoming hadrons and the same can be done for the bottom proton. Finally the coefficients c and the normalisation of the cross section can be fixed using soft data as explained in the next section.

3.2.1 Finding the Parameters of the Model

The previous model for the proton impact factor is also valid for other quasi-elastic or elastic processes. For instance, the elastic cross section calculation from the exchange of a pomeron modeled by two gluons, can be performed and compared to the data in order to fix the parameters.

The elastic cross section of Fig. 3.5, in the same framework and kinematics as the dijet production, is

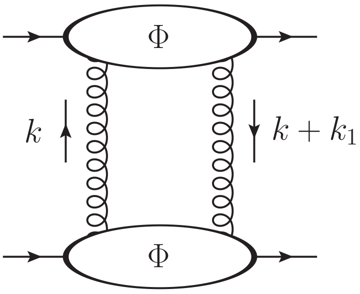

Figure 3.5: High-energy elastic cross section. The pomeron exchange is modeled by a two-gluon exchange in the same framework as the dijet production.

$$\begin{aligned}\sigma_{el} = g^8 \frac{4}{81\pi^2} \int \mathrm{d}^2\mathbf{k}_1 \int \frac{\mathrm{d}^2\mathbf{k}}{\mathbf{k}^2(\mathbf{k}+\mathbf{k}_1)^2}\, \Phi_{\mathrm{LCWF}}\left(\mathbf{k}, -(\mathbf{k}+\mathbf{k}_1)\right) \Phi_{\mathrm{LCWF}}\left(-\mathbf{k}, (\mathbf{k}+\mathbf{k}_1)\right) \\ \int \frac{\mathrm{d}^2\mathbf{k}'}{\mathbf{k}'^2(\mathbf{k}'+\mathbf{k}_1)^2}\, \Phi_{\mathrm{LCWF}}\left(\mathbf{k}', -(\mathbf{k}'+\mathbf{k}_1)\right) \Phi_{\mathrm{LCWF}}\left(-\mathbf{k}', (\mathbf{k}'+\mathbf{k}_1)\right),\end{aligned} \tag{3.11}$$

This result can be compared with available data on total and elastic cross sections, assuming that at high-energy those two are due to pomeron exchange only. Using the E710 result [85] leads to the values of the coefficient $c = 0.61$ and the normalisation is obtained through the use of an effective soft coupling $g = \sqrt{4\pi\alpha}$ with $\alpha = 0.88$. This value replaces g in Eq. (2.91). The authors of [82] obtain a fit to less than 10% and their results have been checked here. It was also shown that the curvature of the differential elastic cross section $\mathrm{d}\sigma/\mathrm{d}t$ within this model is too large, and implies the importance of the non-perturbative regime of QCD in the region of small $|t|$. The use of perturbative exchange is thus tentative at best to estimate the value of the parameters[3]. Another inconvenient of the method is that one had to postulate that the soft amplitude is dominated by the exchange of simple poles. Even if it is true at the TeVatron energy, one can have non-negligible corrections going to LHC that cannot be taken into account at this level.

The LCWF model is simple and possesses all needed ingredients, *i.e.* a dependence on the transverse momenta and on the energy in the center-of-mass frame. The problem of the curvature can be solved by introducing by hand a t-dependence, as it is done in the Durham model. However, it relies on non-perturbative cross sections to fix its input. It may be better to use an alternative model fitted to deep inelastic scattering (DIS) and photoproduction data, this is the idea behind unintegrated gluons density discussed in the next section.

---

[3] Note that the authors of [82] demonstrate that the introduction of non-perturbative effects through a modification of the gluons propagator as described in Sec. 1.3.3 improves the t-slope.

3.3 The Unintegrated Gluon Density

From the study of deep inelastic scattering at HERA, one can extract information about the parton content of the proton. In the standard approach, the gluon distribution depends only on longitudinal momentum fraction but we are looking for the emission of gluons with non-negligible transverse momenta. Moreover, in our case, the exchanged gluons can be very soft so that one could be interested to extend the description of the impact factor to the region where the DGLAP evolution breaks down. In the present section, we shall use the parametrisation of the impact factor described in [86] that solves these two issues and we present an impact factor that depends both on the longitudinal momentum lost by the proton and on the transverse momenta of the t-channel gluons.

The distribution of gluons inside an ultra-relativistic proton can be modeled for diagonal processes, *i.e* no momentum transfer, by replacing the Born-level impact factor of the quark model with an impact factor Φ_{UgD} based on the unintegrated gluon density $\mathcal{F}(x,\mathbf{k}^2)$ made of two parts. One drives the hard emission of gluons $\mathcal{F}^{\mathrm{Hard}}$ and the second the soft emisions $\mathcal{F}^{\mathrm{Soft}}$, in addition with a smooth interpolation between them. We start with the perturbative exchange, *i.e.* the emission of large transverse-momentum gluons. In this case, the gluon content of the proton is described by the usual gluon distribution and as we are looking for the dependence in the transverse momentum, the hard part of the impact factor comes from a direct differentiation of the gluon distribution [44, 45, 87]

$$\mathcal{F}^{H_1} = \frac{\partial\, xg(x,\mathbf{k}^2)}{\partial \log(\mathbf{k}^2)}. \tag{3.12}$$

6The gluon distribution function $g(x,\mathbf{k}^2)$ is extracted from fits to DIS data. This work has been done by the collaborations GRV [88], MRS [89] and CTEQ [90] and the fits are based on the DGLAP equation. The domain of validity of $\mathcal{F}^{\mathrm{Hard}}$ is for $\mathbf{k}^2 \geq \mathbf{k}_c^2$ with $\mathbf{k}_c^2 \simeq 0.9$ or 1.4 GeV^2 depending on the fit (see below). At small to moderate transverse momenta, one has to provide a model for the unintegrated gluon density (UgD). An educated guess, based on colour-dipole phenomenology of hard processes at small-x [91–93], suggests that the interaction of perturbative gluons is similar to the Yukawa screened flux of photon in a quark dipole, up to a colour factor and a coupling constant, so that

$$\mathcal{F}^{H_2} = \frac{N_c^2-1}{2}\frac{\alpha_s(\mathbf{k}^2)}{\pi}\left(\frac{\mathbf{k}^2}{\mathbf{k}^2+\mu_h^2}\right)^2 F_1(\mathbf{k}^2), \tag{3.13}$$

where N_c is the number of colours. The scale μ_h is related to the propagation length of gluons by $\mu_h = 1/R_h$. Because of confinement, perturbative gluons do not propagate at large distances and one can take $R_h \simeq 0.27$ fm according to lattice studies [94]. In this case, $F_1(\mathbf{k}^2)$ is the conventional quark dipole form factor

$$F_1(\mathbf{k}^2) = \frac{1}{\left(1+\frac{\mathbf{k}^2}{\Lambda^2}\right)^2}, \tag{3.14}$$

where Λ is a free parameter set to 1 GeV and the strong coupling constant is frozen at α_s=0.82 in the infra red [95, 96]. One can now define the hard part of the impact factor by matching the DGLAP fits with the above dipole picture at $\mathbf{k}_c$ and

$$\mathcal{F}^{\mathrm{Hard}} = \mathcal{F}^{H_2}\left(\mathbf{k}^2\right)\frac{\mathcal{F}^{H_1}\left(x,\mathbf{k}_c^2\right)}{\mathcal{F}^{H_2}\left(\mathbf{k}_c^2\right)}\theta\left(\mathbf{k}_c^2-\mathbf{k}^2\right) + \mathcal{F}^{H_1}\left(x,\mathbf{k}^2\right)\theta\left(\mathbf{k}^2-\mathbf{k}_c^2\right). \tag{3.15}$$

In the moderate transverse-momentum region, the hard impact factor shows consequently the same x-dependence as the DGLAP fit at $\mathbf{k}_c^2$ together with the $\mathbf{k}^2$-dependence of the dipole picture. The large-x behaviour is introduced via a purely phenomenological factor $(1-x)^5$.

In the soft region, *i.e.* at small $\mathbf{k}$, one has to deal with non-perturbative gluons interacting with large dipoles. The phenomenology of this soft exchange can be modeled in the spirit of the dipole picture of Eq. (3.13) at the tree-level

$$\mathcal{F}^{\text{Soft}} = a_{soft} \frac{N_c^2-1}{2} \frac{\alpha_s(\mathbf{k}^2)}{\pi} \left(\frac{\mathbf{k}^2}{\mathbf{k}^2+\mu_s^2} \right)^2 F_1(\mathbf{k}^2), \tag{3.16}$$

where a_{soft} is an adjustable parameter. The scale μ_s^2 is, as previously, related to the propagation length of gluons, but this time this is the propagation of non-perturbative gluons, so that $\mu_s^2 \ll \mu_h^2$ because $R_s^2 \gg R_h^2$. Finally, the unintegrated gluon density can be written

$$\mathcal{F}(x,\mathbf{k}^2) = \mathcal{F}^{\text{Soft}} \frac{\nu_s^2}{\mathbf{k}^2+\nu_s^2} + \mathcal{F}^{\text{Hard}} \frac{\mathbf{k}^2}{\mathbf{k}^2+\nu_h^2}, \tag{3.17}$$

with $\nu_s \simeq \mu_h$ that insures that the soft component decreases fast in the hard region $\mathbf{k}^2 > \mu_h^2$ but dominates in the soft one.

The above description of the unintegrated gluon density is a summary of reference [86] and we want to underline that this density was build in a phenomenological way, and hence is not unique. It depends on several assumptions and choices. Some of the parameters, R_h^2, $\mathbf{k}_c$ and the freezing of the strong coupling, are borrowed from the literature, but the others, a_{soft}, μ_s^2 and ν_h, were adjusted on available data from ZEUS [97–100], H1 [101–103], E665 [104] and NMC [105] in the ranges $0 \leq |\mathbf{k}^2| \leq 35$ GeV^2 and $x \leq 10^{-2}$. Actually, one has four different fits which give similar chi-square when fitting to the data and, in particular, the details of the non-perturbative region are different. All hard inputs are taken from LO GRV98 parton distributions apart for Fit-3 that comes from a functional form of $\mathcal{F}^{H_1}$. The main difference between the fits is in the parametrisation of the soft region for which the parameters were adjusted on data using different fitting techniques. As an example, we show in Fig. 3.6 the hard and soft parts of the Fit-1 unintegrated distribution as a function of $\mathbf{k}^2$ and for two values of x. One can directly note that both plots show a dip at the interface between the hard and soft component.

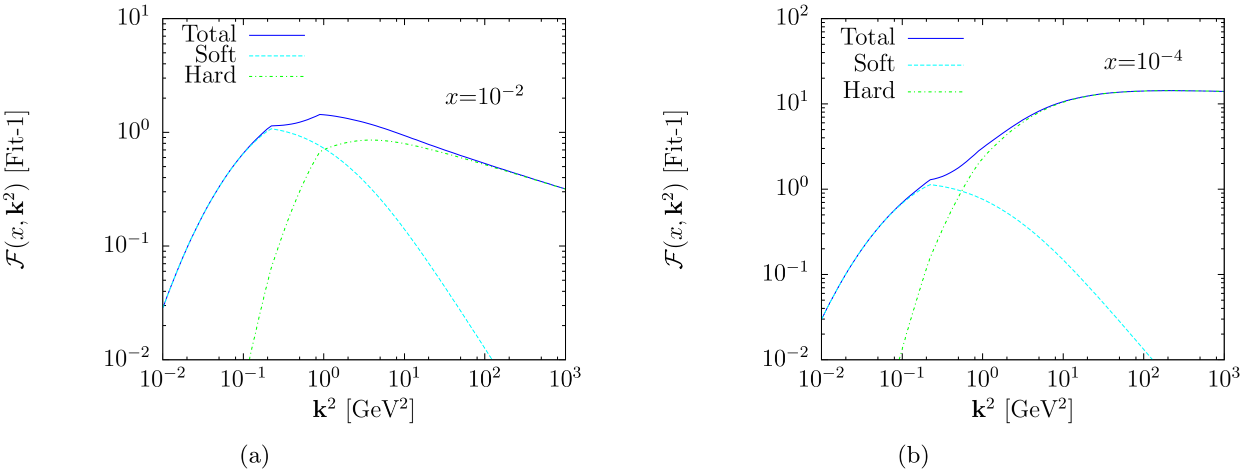

(a) (b)

Figure 3.6: Fit-1 parametrisation of the unintegrated gluon distribution as a function of $\mathbf{k}^2$ at fixed x. (a) x=10^{-2} and (b) x=10^{-4}. The plots present the different contributions $\mathcal{F}^{\text{Hard}}$, $\mathcal{F}^{\text{Soft}}$ and their sum.

This comes from the fact that the components are clearly separated but with a small extrapolation of the soft part into the hard part as well as of the hard into the soft. After integration over $\mathbf{k}^2$ one finds the correct description of F_{2p} in agreement with data.

The other fits have a similar behaviour despite the differences in the parametrisation of the soft region and are shown in Fig. 3.7, Fig. 3.8 and Fig. 3.9. The main remark is that the importance of the non-perturbative contribution in Fit-4 is extended to larger $\mathbf{k}^2$ in this case even if both parametrisations exhibit the same behavior at small and large $\mathbf{k}^2$.

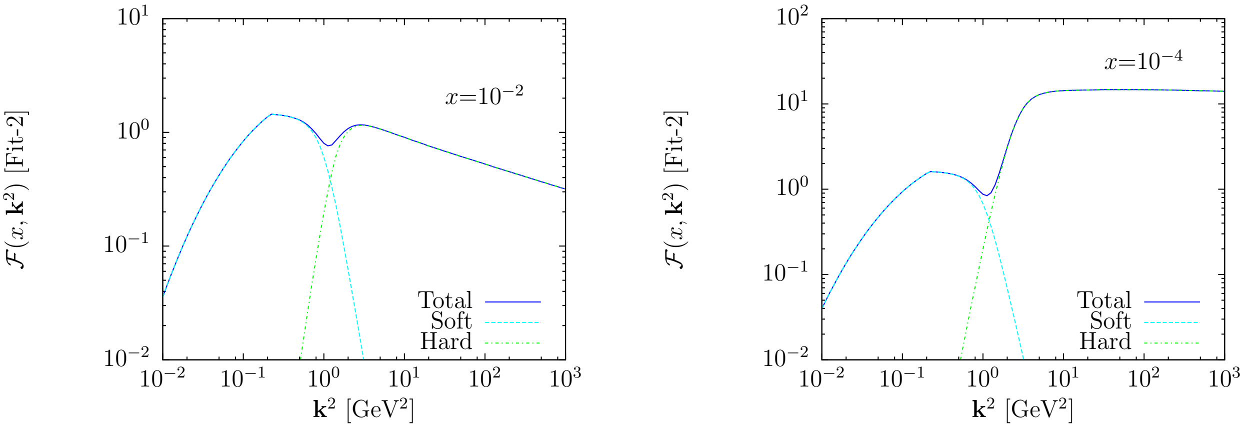

(a) (b)

Figure 3.7: Fit-2 parametrisation of the unintegrated gluon distribution as a function of $\mathbf{k}^2$ at fixed x: (a) x=10^{-2} and (b) x=10^{-4}. The plots present the different contributions $\mathcal{F}^{\text{Hard}}$, $\mathcal{F}^{\text{Soft}}$ and their sum.

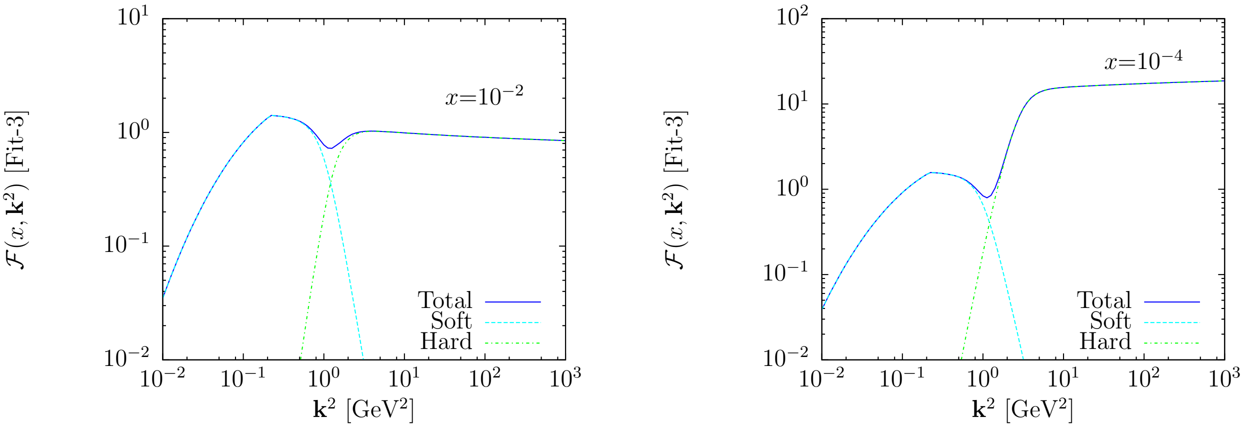

(a) (b)

Figure 3.8: Fit-3 parametrisation of the unintegrated gluon distribution as a function of $\mathbf{k}^2$ at fixed x: (a) x=10^{-2} and (b) x=10^{-4}. The plots present the different contributions $\mathcal{F}^{\text{Hard}}$, $\mathcal{F}^{\text{Soft}}$ and their sum.

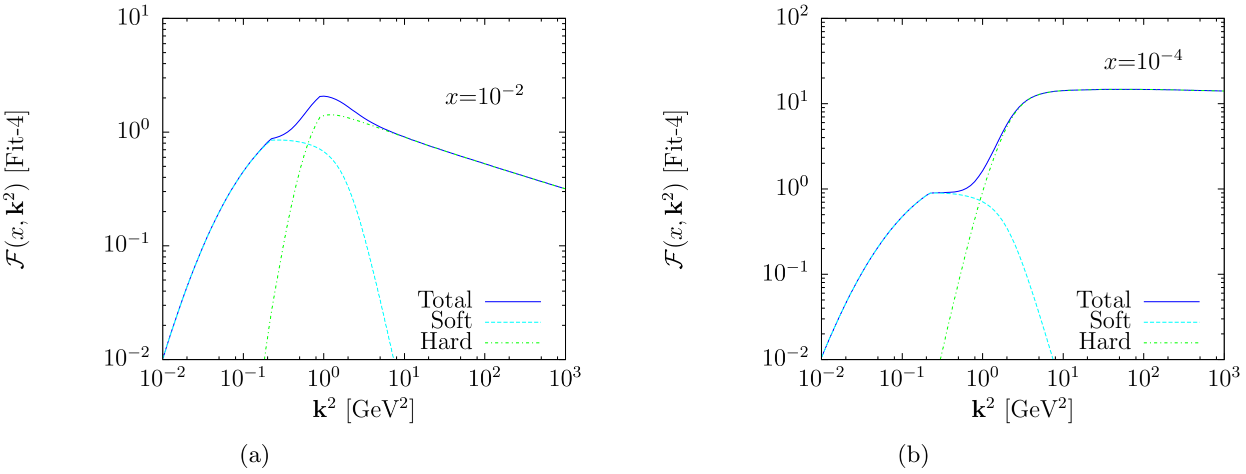

(a) (b)

Figure 3.9: Fit-4 parametrisation of the unintegrated gluon distribution as a function of $\mathbf{k}^2$ at fixed x: (a) x=10^{-2} and (b) x=10^{-4}. The plots present the different contributions $\mathcal{F}^{\text{Hard}}$, $\mathcal{F}^{\text{Soft}}$ and their sum.

3.3.1 Impact Factor from the Unintegrated Gluon Density

The above fits to the data allow to model the impact factor at non-zero momentum transfer and for different longitudinal momentum fractions. The kinematics used in the present description is shown in Fig. 3.10. In the studied case of quasi-elastic production, the two gluons have different longitudinal momentum fractions, the screening gluon can be very soft and one has $x_a \ll x_b$ as shown by the conditions (2.55) and (2.64).

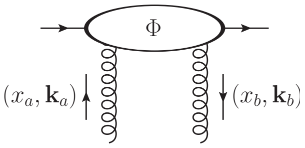

Figure 3.10: General picture of the kinematics used in the present description of the impact factor.

According to [106, 107] the skewed distribution can be related to the forward distribution by

$$\mathcal{F}_{\text{skewed}}\left(x_a \ll x_b, x_b, \mathbf{k}^2\right) = R_g\, \mathcal{F}\left(x_b, \mathbf{k}^2\right), \tag{3.18}$$

The skewness factor R_g can be effectively taken into account by rescalling the x at which the UgD is calculated. Assuming that $\mathcal{F}(x_b, \mathbf{k}^2) \propto x^{-\lambda}$ with λ the effective intercept, one has

$$R_g \left(\frac{1}{x}\right)^{\lambda} = \left(\frac{1}{c(\lambda)x}\right)^{\lambda}. \tag{3.19}$$

It appears that the factor $c(\lambda)$ has little dependance on the intercept and consequently one can choose to fix it at the mean value $< c(\lambda) >= 0.41$, so that

$$\mathcal{F}_{\text{skewed}}\left(x_a \ll x_b, x_b, \mathbf{k}^2\right) = \mathcal{F}\left(0.41\, x_b, \mathbf{k}^2\right). \tag{3.20}$$

The second problem is the non-zero transverse momentum transfer. This is introduced via a universal exponential factor constructed in such a way that it respects condition (3.1), includes the shrinkage and the t-dependence of the impact factor. The first condition is realised with the help of a prefactor $f(\mathbf{k}_a,\mathbf{k}_b)$ that goes to zero with one of its arguments and is equal to 1 if $\mathbf{k}_a=\mathbf{k}_b$. It can be choosen as

$$f(\mathbf{k}_a,\mathbf{k}_b)=\frac{2\mathbf{k}_a^2\mathbf{k}_b^2}{\mathbf{k}_a^4+\mathbf{k}_b^4}, \tag{3.21}$$

in addition with the prescription

$$\phi\left(x_a \ll x_b, x_b, \mathbf{k}_a, \mathbf{k}_b\right)=\frac{4\pi^2}{g^2}\frac{N_c^2-1}{2N_c}\mathcal{F}\left(0.41\,x_b, \left(\frac{\mathbf{k}_a+\mathbf{k}_b}{2}\right)^2\right) f(\mathbf{k}_a,\mathbf{k}_b), \tag{3.22}$$

that models the distribution of gluons inside an ultra-relativistic proton and in this prescription the soft coupling g is absorbed into the definition of $\mathcal{F}$.
The t-dependence is usually taken into account by an exponential. According to studies of diffractive vector meson production [86], one can take

$$\begin{aligned}\Phi &= \phi \times e^{-\frac{1}{2}B(x)|t|},\\ B &= B_0 + 2\alpha' \ln\frac{x_0}{x}.\end{aligned} \tag{3.23}$$

Here, $B_0 = 4$ GeV^{-2}, $\alpha' = 0.25$ GeV^{-2} and $x_0 = 3.4\ 10^{-4}$ are chosen to reproduce the correct $|t|$-slope of the cross section. The energy dependence is inspired by the Regge phenomenology of pomeron exchange of Sec. 1.3.1 and was tested on diffractive vector-meson production [108]. Using these values of the diffractive parameters, the logarithmic t-slope of the distribution is approximately equal to $B \simeq 4$ GeV^{-2}. This is significantly smaller than the slope in elastic proton-proton collision at the TeVatron energy, that is

$$\frac{\mathrm{d}\sigma_{pp}^{elastic}}{\mathrm{d}|t|} \propto e^{-2B_{el}|t|}, \tag{3.24}$$

where $B_{elastic} \simeq 8.5$ GeV^{-2}. The present choice of B is more natural than $B \simeq B_{el}$ since elastic scattering at the TeVatron probes the gluon distribution at very small x, of the order $x \sim 10^{-7}$, while in our process the energetic gluons carry only $\simeq 10^{-2}$ of the proton momentum. This choice is model-dependent and introduces an extra uncertainty into theoretical calculations of the quasi-elastic cross sections.

The complete UgD-based impact factor incorporates now all the ingredients requested and yields

$$\Phi_{\mathrm{UgD}}\left(x_a \ll x_b, x_b, \mathbf{k}_a, \mathbf{k}_b\right)=\frac{4\pi^2}{g^2}\frac{N_c^2-1}{2N_c}\mathcal{F}\left(0.41\,x_b, \left(\frac{\mathbf{k}_a+\mathbf{k}_b}{2}\right)^2\right)\times\frac{2\mathbf{k}_a^2\mathbf{k}_b^2}{\mathbf{k}_a^4+\mathbf{k}_b^4}e^{-\frac{1}{2}(B_0+2\alpha'\ln\frac{x_0}{x_b})|t|}. \tag{3.25}$$

This function replaces Φ_{LCWF}, as shown in Appendix A. After the considerations of Chap. 2 that have shown that an important part of the exchanged gluons are soft and that the calculation is sensitive to the details of the non-perturbative regime of QCD, one must note that the present impact factor is somewhat uncertain. One of its advantages is that it treats separately the soft and hard regimes and the parametrisation is just an attempt to describe phenomenologically the impact factor. Here, we want to underline that a good agrement of the fit to small, moderate and large transverse momentum is not trivial, and that below $x = 10^{-2}$ the accuracy is comparable to the one of the standard leading-order GRV fits.

3.4 Results and Conclusion

We have presented two possible parametrisations of the impact factor, based on a simple light-cone wave function or on the unintegrated gluon density. Both of them depend on the transverse momentum of the exchanged gluons and on the longitudinal fraction lost by the proton. We shall now define the variables in the particular kinematics of quasi-elastic production and show what are the effects of the choice of different parametrisations on the dijet quasi-elastic production.

The parton-level cross section calculation, embedded into proton-proton exchange is given by Eq. (3.2) and if one want to use Φ_{UgD}, the longitudinal fraction lost by the upper proton is the longitudinal fraction of k_1, given by

$$k_1^\mu = \frac{-\mathbf{k}_1^2}{(1-\beta_1)s} p^\mu + \left(\frac{\mathbf{k}_3}{(1-\alpha_2)s} + \beta_1 + \beta_2 \right) q^\mu + \mathbf{k}_1^\mu, \tag{3.26}$$

hence $x_b = \beta_1 + \beta_2$ in the kinematics of Sec. 2.4 and neglecting all terms of order $\mathcal{O}(1/s)$. It can also be taken directly from the four-momentum of the final system X of Eq. (3.9) since the transferred momentum $|t|$ is equal to $|t_1|$ as in Eq. (3.10). Consequently, the impact factor based on UgD of the upper proton is

$$\begin{aligned}\Phi^{p_1}_{\mathrm{UgD}}\left(z,(\beta_1+\beta_2),\mathbf{k},(\mathbf{k}+\mathbf{k}_1)\right) = \frac{4\pi^2}{g^2}\frac{N_c^2-1}{2N_c}\mathcal{F}\left(0.41(\beta_1+\beta_2), \left(\frac{\mathbf{k}+(\mathbf{k}+\mathbf{k}_1)}{2}\right)^2\right) \\ \times \frac{2\mathbf{k}^2(\mathbf{k}+\mathbf{k}_1)^2}{\mathbf{k}^4+(\mathbf{k}+\mathbf{k}_1)^4} e^{-\frac{1}{2}(B_0+2\alpha' \ln \frac{x_0}{\beta_1+\beta_2})|\mathbf{k}_1^2|}.\end{aligned} \tag{3.27}$$

In the case of the lower proton, one finds

$$\begin{aligned} x_b &= \alpha_1 + \alpha_2, \\ t_3 &= -\mathbf{k}_3^2. \end{aligned} \tag{3.28}$$

Fig. 3.11.a presents the reference curve for the two choices of impact factor.

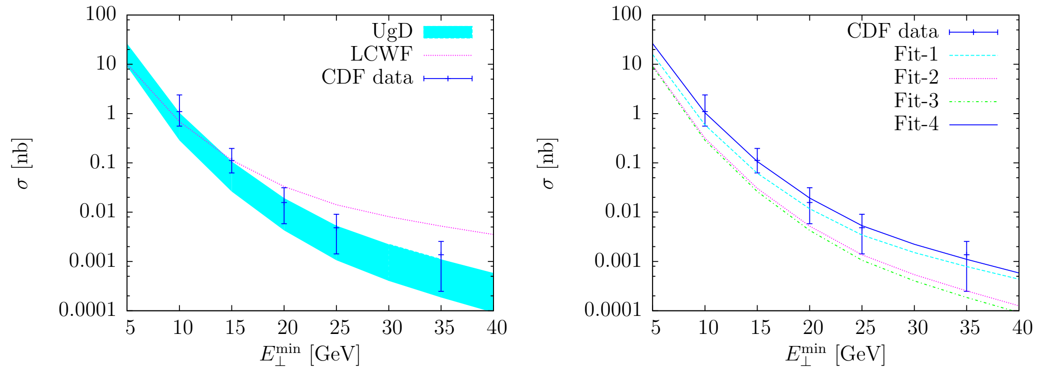

(a) (b)

Figure 3.11: Comparison of the impact factor. (a) LCWF stands for the light-cone-wave function impact factor and the band corresponds to the parametrisations of the unintegrated gluon density. (b) The four different fits of Φ_{UgD}.

Although both lead to an acceptable fit to the data, the curvature of Φ_{UgD} seems to be better. The band represents the four parametrisations of impact factor based on unintegrated gluon density that only differ by the description of the soft coulour-singlet exchange. A look at Fig. 3.11.b, that gives the results for the four different types of parametrisations, shows that the Fit-4 with the extended soft region gives the highest prediction.

The fact that one cannot fix the correct parametrisation of the impact factor using theoretical arguments introduces an uncertainty on the results. By comparing the different prescriptions, the present study shows that the choice of the impact factor amounts to an uncertainty of at least a factor 3 between the lowest and the highest curves.

Chapter 4

The Sudakov Form Factor

The central system produced in quasi-elastic processes comes from the scattering of two near-shell gluons and it is known that this kind of process has large logarithmic vertex corrections, which may be resummed to form the Sudakov form factor. One expects these corrections to lead to a substantial suppression of the cross section. This chapter describes different aspects of the Sudakov form factor and several comments are in order.
After the general definition, we shall discuss different open questions concerning the details of the Sudakov form factor as, in the dijet case, there exists no complete calculation to fix precisely the scales. Hence it brings large uncertainties on the final cross section. We shall start with the scales, then discuss the importance of the subleading logs and of the constant terms structure. We also explain how it is possible to evaluate the mean value of the loop momentum using the saddle point approximation and we shall confirm that the calculation is dominated by the non-perturbative region. We also briefly discuss the idea that non-standard diagrams may modify the final result for the quasi-elastic dijet cross section. All these pieces will be brought together in the last section that summarises the uncertainties and demonstrates that the Sudakov form factor is far from being under theoretical control.

4.1 General Definition of the Resummation

The present process is a typical case of the propagation of a gauge field from a long-distance configuration to a short-distance one, *i.e.* a soft scale to a hard scale. It was shown in [109, 110] that one expects large doubly logarithmic corrections from virtual diagrams such as those of Fig. 4.1. The Sudakov corrections have been evaluated in QCD [111] and for on-shell initial gluons, they diverge. However, in quasi-elastic processes, the initial gluons are slightly off-shell so that their virtualities provide a natural IR cut-off and the logarithms are large but finite. The present section gives the general properties of the Sudakov form factor and we shall try to explain how it can be calculated in QCD, the complete calculation is far beyond the scope of the thesis and hence, we just present the main lines[1].

One can consider the one-loop correction to the vertex shown in Fig. 4.1.b. This diagram includes an integral over the momentum in the loop, q, and in particular over both the fraction of light-cone momentum z and the transverse momentum $\mathbf{q}^2$. The integration builds up double logarithms in the kinematical region where the virtual emission is soft and sandwiched between a soft and a hard scale, respectively ℓ^2 and μ^2. As shown by Dokshitzer, Dyakonov and

---

[1] Sometimes, the Sudakov form factor is reworded using a Monte-Carlo language as the probability that the gluons in the t-channel do not emit extra partons. In this way, one has to subtract from unity the probability that the hard subprocess is accompanied by a certain number of secondary partons. However, we prefer to keep the original definition of the Sudakov form factor as a vertex correction.

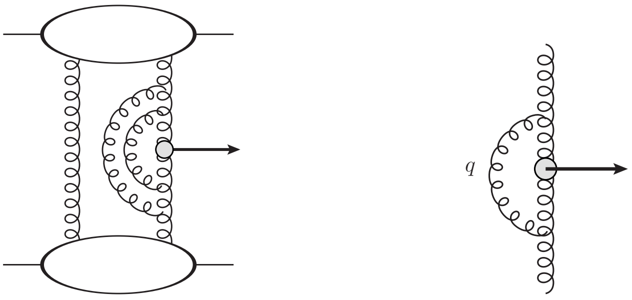

(a) (b)

Figure 4.1: (a) A higher-order diagram for quasi-elastic production that leads to large doubly logarithmic corrections in the Feynman gauge. (b) The Sudakov form factor viewed as virtual vertex corrections.

Troyan (DDT) [111], at higher order, the leading double logarithms exponentiate. The exponentiation is the QCD analog of the form factor discovered by Sudakov in QED. The main issue is that one is dealing here with loop momenta that lie in the non-perturbative region and it is then difficult to go beyond the leading-log approximation. However, DDT interestingly noticed that the log structure appears from equations that look like bremsshtrahlung emission with the same splitting function as those used in the DGLAP equation. Actually, if one looks at the cross section level, the logarithmic IR divergences of bremsshtrahlung diagrams are canceled by the divergences of virtual corrections, making the inclusive cross section finite, this is pictured in Fig. 4.2. Hence, the inclusive cancellation of the IR divergences leads to the conclusion that the log structure of virtual corrections is identical to that of real emissions, that can be calculated perturbatively in the DGLAP formalism. One can then write for the Sudakov form factor T the following expression [16, 17]

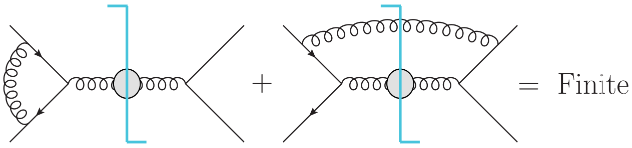

Figure 4.2: The logarithmic IR divergence of bremsshtrahlung diagrams is canceled by the divergence of virtual corrections, making the inclusive cross section finite. This suggests that the log structure of virtual corrections is identical to that of real emissions.

$$
\begin{aligned}
&T(\mu^2,\ell^2) = e^{-S(\mu^2,\ell^2)}, \\
&S(\mu^2,\ell^2) = \int_{\ell^2}^{\mu^2} \frac{\mathrm{d}\mathbf{q}^2}{2\pi}\frac{\alpha_s(\mathbf{q}^2)}{\mathbf{q}^2}\int_0^{1-\Delta}\mathrm{d}z\left[zP_{gg}+N_fP_{qg}\right],
\end{aligned}
\tag{4.1}
$$

that should be convoluted with the cross section of Eq. (3.2):

$$
\mathcal{M}(p_1p_2 \to p_1^* + gg + p_2^*) = \mathcal{M}_{qq} \otimes \Phi(p_1)\sqrt{T(\mu^2,\ell_1^2)}\ \Phi(p_2)\sqrt{T(\mu^2,\ell_2^2)}. \tag{4.2}
$$

Once again, we insist on the fact that the Sudakov form factor is a correction independent of the impact factor and is hence not introduced in a derivative as in models that uses simple parton distribution function for the proton. The first integral of Eq. (4.1) refers to the transverse momentum of the particle in the loop $\mathbf{q}^2$ and $\alpha_s(\mathbf{q}^2)$ is the strong coupling constant. The integration variable runs between ℓ_i^2 and μ^2, naturally related respectively to the soft and hard scales between which the colour gauge field is developed. So, ℓ_i is linked to the virtuality of the initial gluons $(\mathbf{k}+\mathbf{k}_i)^2$, depending on whether one deals with the upper or the lower part of the production diagram, that sets the scale from which an extra parton can be emitted, while μ is related to the hard transverse scale $\mathbf{k}_2$ of the hard subprocess. The problems attached to the definition of the scales is addressed in Sec. 4.2.1. The second integral is over the light-cone momentum z, Δ is a cut-off discussed below, N_f is the number of flavours and P_{gg}, P_{qg} are the unregularised splitting functions[2]. One has

$$\begin{aligned} P_{gg} &= 2N_c\left[\frac{z}{1-z}+\frac{1-z}{z}+z(1-z)\right], \\ P_{qg} &= \frac{1}{2}\left[z^2+(1-z)^2\right], \end{aligned} \tag{4.3}$$

where N_c is the number of colours. Note that the original prescription of DDT gives a slightly different result as discussed in Appendix B.3. The origin of the double-log is in the first term of P_{gg} since the other terms will only give simple logs and constant terms. Here, a second problem appears as the argument is that virtual logarithmic divergences of bremsshtrahlung diagrams are identical to the logarithmic divergences of the virtual diagram and it is known that those logs exponentiate, but the constant terms are not the same and nothing proves that they exponentiate. We leave this topic for Sec. 4.2.2 as the Sudakov correction is well defined in the regime where the logs are large and in particular when the double-log contribution is dominant. In order to obtain a quantitative idea of this factor one can work in the double log-approximation (DLA) of $S(\mu^2,\ell^2)$ that is computed by keeping only the term of interest after the integration over z,

$$S_{DLA}(\mu^2,\ell^2) = \frac{3}{\pi}\int_{\ell^2}^{\mu^2} \mathrm{d}^2\mathbf{q}\,\frac{\alpha_s(\mathbf{q}^2)}{\mathbf{q}^2}\log\left(\frac{1}{|\Delta|}\right). \tag{4.4}$$

All details of the integration over z can be found in Appendix B.3. For the purpose of the demonstration, one can fix the coupling constant to $\alpha_s(\mu^2)$ in Eq. (4.4) and evaluate the second integral that depends on the choice of Δ. First, pure DGLAP kinematics [111] leads to the cut-off $\Delta = \mathbf{q}^2/\mu^2$ and one obtains

$$S_{DLA}(\mu^2,\ell^2) = \frac{3\alpha_s(\mu^2)}{2\pi}\log^2\left(\frac{\mu^2}{\ell^2}\right). \tag{4.5}$$

However, it can be argued that the coherent effects lead to angular ordering in the successive splitting of the secondary partons [112–114]. This ordering introduces a more restrictive limit on the z integral, which becomes linear in $|\mathbf{q}|$ leading to $\Delta = |\mathbf{q}|/\mu$. This result is also obtained by the authors of [20, 112] who compute explicitly the next-to-leading-order (NLO) calculation of the relevant virtual corrections[3]. With this definition of the cut-off, one obtains a double-log result which is a factor of two smaller than Eq. (4.5)

$$S_{DLA}(\mu^2,\ell^2) = \frac{3\alpha_s(\mu^2)}{4\pi}\log^2\left(\frac{\mu^2}{\ell^2}\right). \tag{4.6}$$

---

[2] Note that the splitting function P_{gq} is not present as one deals only with gluons in the initial state.

[3] We don't want to enter into the details here, but one can note that, together with Eq. (4.1), it can also be derived from the CCFM equation [115, 116].

Numerically this change is very substantial as it can lead to a factor $\mathcal{O}(10)$ in the cross section. In the following, all results are produced with the latter definition of Δ.

All choices, scales, cut-off and approximations will be studied and their effects on the value of the quasi-elastic dijet cross section tested in the final section where we show how sensitive the Sudakov form factor is to those parameters.

4.2 Arbitrariness of the Sudakov Form Factor

From the point of view of the previous section, the Sudakov form factor seems to be under theoretical control. However, as it suppresses the cross section by a factor of the order of 100 to 1000, one can guess that we need to be very careful about its details. We would like to develop four topics, *i.e.* the choice of scales μ^2 and ℓ^2, the possibility to introduce a different upper scale in the transverse and longitudinal integrals, the importance of the log contributions versus the constant terms and the Sudakov form factor of non-standard diagrams.

4.2.1 Scales

At first sight, the Sudakov form factor depends on two scales that are the limits of the integral of Eq. (4.1). They are related to the soft and the hard scales of the process and we shall see that the suppression factor is very sensitive to a change in their values. The order of magnitude of both scales can be fixed from the kinematics but the theory doesn't provide the coefficient in the particular case of the two-gluon production.

As already mentioned, the lower limit ℓ^2 of the integral on transverse momentum must be of the order of the transverse momentum of the gluon that initiates the emission. In the present picture of the Sudakov form factor corresponding to virtual corrections at the vertex, this scale is obviously of the order of $(\mathbf{k}+\mathbf{k}_i)^2$ with $i = 2 \pm 1$. The status of the upper scale is a little bit more complicated due to the fact that in the standard discussion of the Sudakov form factors the hard point-like vertex is characterized by only one scale, that is the mass of the produced system m_X. In Monte Carlo language, this mass defines the phase space available for the secondary parton emission which needs to be suppressed. Consequently, the upper scale should be taken as $\mu = c\, m_X$ with c a constant of order 1 and this is true for a point-like vertex. Nevertheless, in the dijet case, we enter a new kinematical regime as the two gluons can have large invariant mass

$$m_{gg}^2 = s_{gg} = \frac{(\beta_2\mathbf{k}_1 + \beta_1\mathbf{k}_3 - (\beta_1+\beta_2)\mathbf{k}_2)^2}{\beta_1\beta_2}, \tag{4.7}$$

both via large transverse momenta for which $s_{gg} \simeq \mathbf{k}_2^2$ or via strong longitudinal ordering $s_{gg} \gg \mathbf{k}_2^2$. In Sec. 4.1, we have seen that a typical double-log-enhanced correction gets sizable logs only if there is a large transverse momentum or large virtuality $\mathbf{k}_2^2$ inside the effective vertex, or in other words, only if the effective vertex can be considered point-like. In this case, the flow of the transverse momentum $\mathbf{q}$ in the loop does not change the amplitude. On the contrary, if the vertex does not involve a sufficiently large scale, the momentum in the loop is enough to resolve the vertex and the transverse logarithm does not build up, leading to a complete change of the log structure of the amplitude. The two situations are pictured in Fig. 4.3, and one can reasonably guess that the upper scale of the transverse integral is somewhat uncertain, but must be of the order of $\mathbf{k}_2^2$ as it marks the limit beyond which the double-logs do not build up. With this discussion in mind, we anticipate a little on the second part of the thesis, devoted to Higgs boson quasi-elastic production.
According to [16, 17], one should have taken μ^2 related to the quantity s_{gg}. Actually, this is true

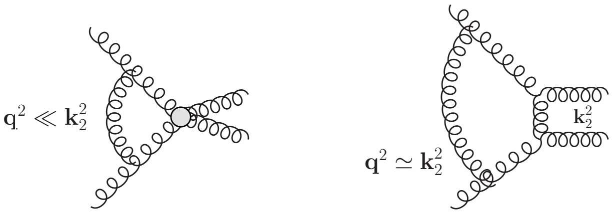

Figure 4.3: The two different kinematical regime for dijet production. Left: The effective point-like vertex $\mathbf{q}^2 \ll \mathbf{k}_2^2$. Right: The resolved vertex $\mathbf{q}^2 \simeq \mathbf{k}_2^2$.

in the case of Higgs boson quasi-elastic cross section as the hard vertex is effectively point-like. The transverse momenta and virtualities of the top quarks inside the loop are larger or similar to the Higgs boson mass, so that the only available hard scale is indeed this mass squared. In the dijet case, one cannot neglect the new kinematical regime $s_{gg} \gg \mathbf{k}_2^2$ and, in particular at TeVatron energy where $\mathbf{k}_2^2$ is of the order of the minimum transverse energy of the jet which can be as low as 10 GeV. Hence. according to the above discussion, we choose to fix the upper scale of the Sudakov form factor to

$$\mu^2 = \mathbf{k}_2^2/x, \tag{4.8}$$

where x is an integer used to study the variation of the cross section with the details of the Sudakov correction and thus the theoretical uncertainty on the numerical result.

The scale μ appears two times in Eq. 4.1, first as the upper limit of the transverse integral over $\mathbf{q}$ and second through the definition of Δ in the upper limit of the longitudinal integral over z. One can then suggest to introduce different upper limits dealing with the longitudinal and the transverse pieces. The latter should be naturally related to the previous definition of μ whereas the former, denoted ν, should be linked to $\sqrt{s_{gg}}$. For simplicity one can choose different transverse and longitudinal limits which become of the same order for purely transverse jets:

$$\mu^2 = \frac{\mathbf{k}_2^2}{x}, \quad \nu^2 = \frac{s_{gg}}{4x}. \tag{4.9}$$

The effect of the additional scale on the dijet cross section is shown in Fig. 4.4,

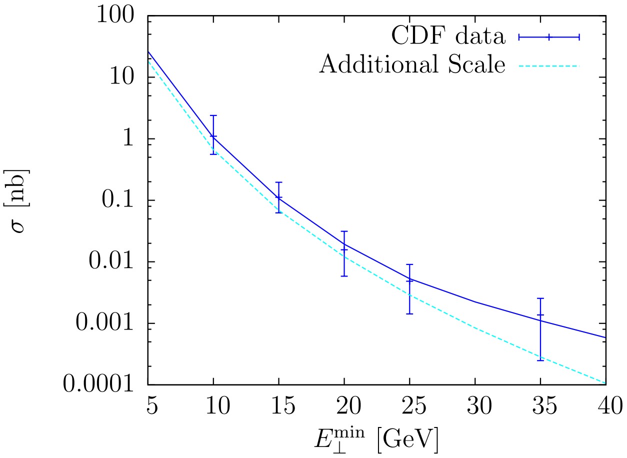

Figure 4.4: Effect of the additional scale on the dijet cross section. The central plain line is the reference curve of Fig. 1.12.

that presents on the same plot the two cases, the addition of the second scale changes the curvature in the high-mass region. Nevertheless, this change is small compared to the other sources of uncertainties and the error bars. The effect of the addition of a scale is not obvious but it can be seen from the DLA form of the Sudakov form factor. One can compute the function S_{DLA} of Eq. (4.4) but for $\Delta = |\mathbf{q}|/\nu$. It gives

$$\begin{aligned} S_{DLA}^{2scales} &\propto \int_{\ell^2}^{\mu^2} \frac{\mathrm{d}\mathbf{q}^2}{\mathbf{q}^2} \log \frac{\nu}{|\mathbf{q}|} \\ &= \log\left(\frac{\ell}{\mu}\right) \log\left(\frac{\ell\mu}{\nu^2}\right), \end{aligned} \tag{4.10}$$

after the calculation detailed in Appendix B.3.3. This expression has to be compared with the result of Eq. (4.6)

$$S_{DLA}(\mu^2, \ell^2) \propto \log^2\left(\frac{\mu^2}{\ell^2}\right), \tag{4.11}$$

and one can directly note that the dependence of $S(\mu^2, \ell^2)$ on the upper scale is strongly modified. Indeed, if μ starts increasing then one has now two opposite effects as $\log \frac{\ell\mu}{\nu^2}$ increases while $\log \frac{\ell}{\mu}$ decreases. As shown in Fig. 4.5.a and 4.5.b, the dependence in the 2-scale case is rather different and a change in μ has then a less dramatic effect on the final result and on the uncertainty that affects the calculation.

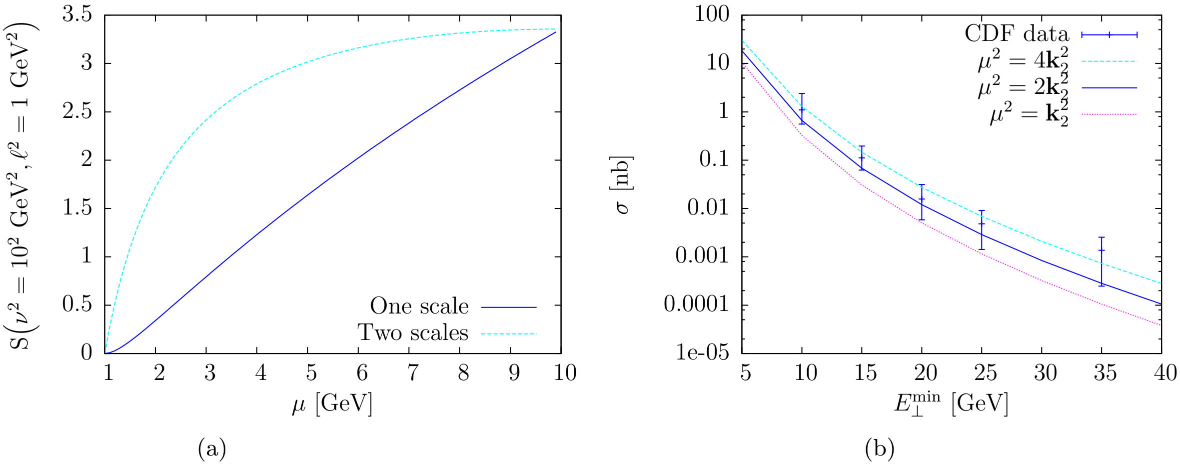

Figure 4.5: (a) Comparison of the dependence of the argument of the Sudakov form factor on the upper scale μ in the one-scale and two-scales cases. ν^2=100 GeV^2 and ℓ^2=1 GeV^2, *i.e.* typical values of the quasi-elastic production are fixed. (b) Effects of a change in the upper limit μ on the cross section in the 2-scale case.

4.2.2 The Logarithmic Contribution and the Constant Terms

The validity of the formulae used here is based on the assumption that the log contributions are dominant. However, the exact log contributions in the dijet case is not trivial and have not been fully calculated due to the additional difficulty described in the previous section. If the constant term contribution is small, one can trust the exponentiation but we shall show that it is not the case in the energy domain considered. Furthermore, we have assumed that the impact factor was similar to an integrated gluon density. In principle, the latter contains a Sudakov form factor inside the derivative of the gluon density. The derivation is performed in DIS but the regime considered here, with a spectator gluon, is quite different and we believe we should include it outside the impact factor.

One can choose to keep the Sudakov form factor of Eq. (4.1) and to test the dominance of the logs. The sign and hierarchy of the different contributions can be obtained by an analytic calculation in the approximation of fixed α_s. According to Appendix B.3, one has

$$S(\mu^2,\ell^2) \simeq \frac{\alpha_s}{2\pi}\left[6\log^2\frac{1}{\delta} + (-11 + \frac{2}{3}N_f)\log\frac{1}{\delta} + C\right], \tag{4.12}$$

where the term proportional to N_f is from P_{qg} and C gathers the non-leading log terms. This decomposes the argument of the Sudakov form factor in three terms

$$S(\mu^2,\ell^2) = \alpha_s\left[a\log^2\left(\frac{\mu^2}{\ell^2}\right) + b\log\left(\frac{\mu^2}{\ell^2}\right) + C\right], \tag{4.13}$$

namely, the double-log contribution, the single-log contribution and the constant term with a, b and C constant. In this approximation, the relative magnitude between the different terms is shown in Fig. 4.6 using $\Delta = |q|/\mu$ and for typical scales relevant for the CDF measurements.

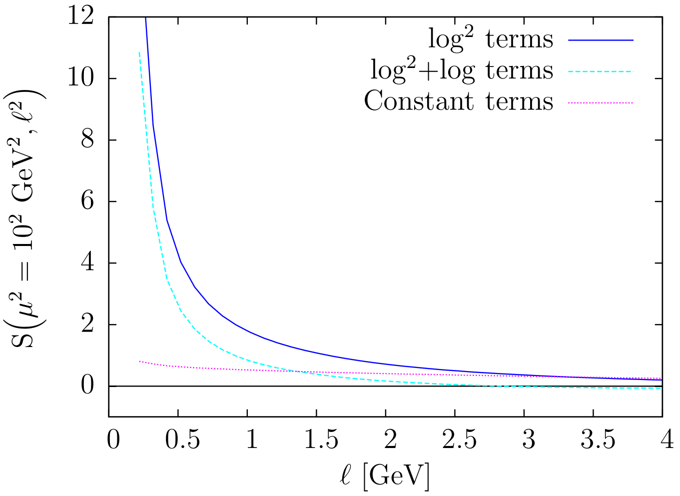

Figure 4.6: Contribution of the various terms entering the argument of the Sudakov form factor in the approximation of fixed strong coupling and for $\mu^2 = 10^2$ GeV^2.

We remind the reader that μ is related to the mass of the dijet system and that ℓ, the virtuality of the colliding gluons, is small.

In the case of a running coupling, one has to perform a numerical calculation and the contributions are shown in Fig. 4.7 where we label the terms as in the fixed coupling case. The first remark is that the picture is really different from what one expects, *i.e.* large double log contributions and small constant terms. The single-log contribution is negative and eventually leads to a change of sign of the argument $S(\mu^2,\ell^2)$ if one neglects the constant term[4]. As we explained in Sec. 4.1, the single-log contribution is not fully calculated in the dijet case and the fact that it is actually large makes the theoretical prediction particularly unstable. On top of this, one can also notice from Fig. 4.7 that the constant terms are numerically important, in

---

[4] Moreover, the negative contribution comes from P_{gg} and the positive one from P_{qg}.

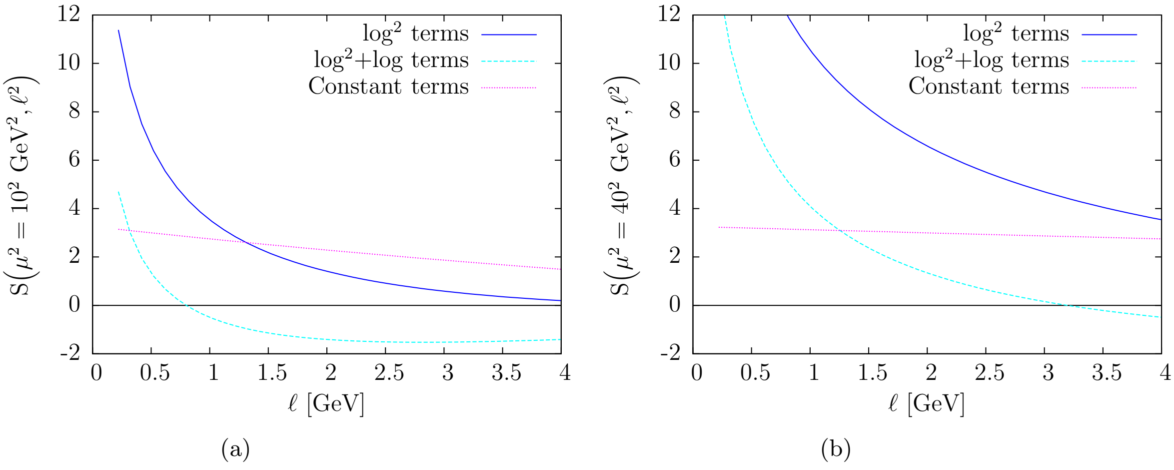

(a) (b)

Figure 4.7: Contribution of the various terms entering the argument of the Sudakov form factor. (a) $\mu^2 = 10^2$ GeV^2 and (b) $\mu^2 = 40^2$ GeV^2.

particular the logarithms are dominant only in the region $\ell \ll 0.5$ GeV for $\mu = 10$ GeV with a slight improvement if one takes $\mu = 40$ GeV. With a running coupling, the log terms are dominated by the constant contribution with the consequence that one can trust the perturbative formula of Eq. (4.1) only in the non-perturbative region. Taking into account that, in the dijet quasi-elastic production processes, the mean value of ℓ is around 1 GeV, one might have serious doubts about the validity of the Sudakov form factor in that context. In particular in the fixed running coupling approximation for which the suppression factor is underestimated in the small-ℓ region leading to important consequences on the final cross section.
We stress however that this result is model-dependent and as an example, we show in Fig. 4.8 the

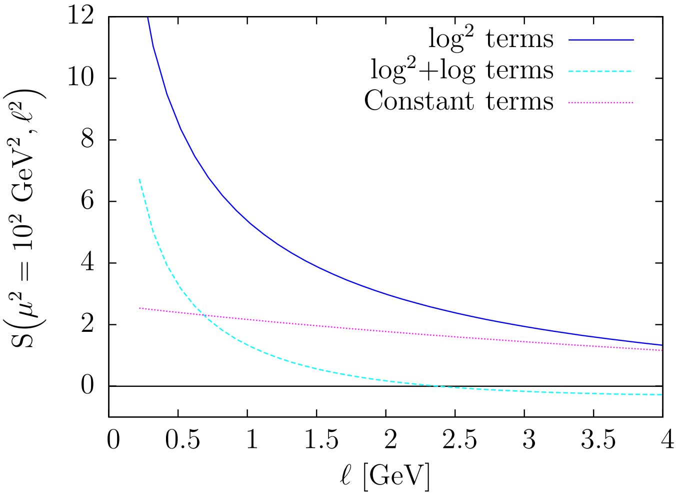

Figure 4.8: Contribution of the various term entering the argument of the Sudakov form factor using the prescription for the cut-off, $\Delta = \frac{|\mathbf{q}|}{|\mathbf{q}|+\mu}$.

same plot as the one of Fig. 4.7.a using this time the Durham prescription for the cut-off Δ [117]

$$\Delta = \frac{|\mathbf{q}|}{|\mathbf{q}| + \mu}, \tag{4.14}$$

that prevents the log contribution to go far below zero. One can also show that if we multiply the upper scale by two, an assumption that is theoretically reasonable, the double log + single log contribution becomes always positive.

We now address the question of the constant terms. The exponential form of the Sudakov form factor comes from the similarity of the log terms in the virtual and bremsshtrahlung diagrams, and it is known that the constant terms do not exponentiate. It is however assumed in most of the models that they are small. Consequently this introduces an additional uncertainty on the final result as the constant terms are not fixed by the theory and can vary. The effects of a simple change are shown in Fig. 4.9. It corresponds to the multiplication by a factor 2 or 1/2 of all terms of P_{gg} and P_{qg} that will not give a leading-log contribution after the integration over $\mathbf{q}$ in Eq. 4.1.

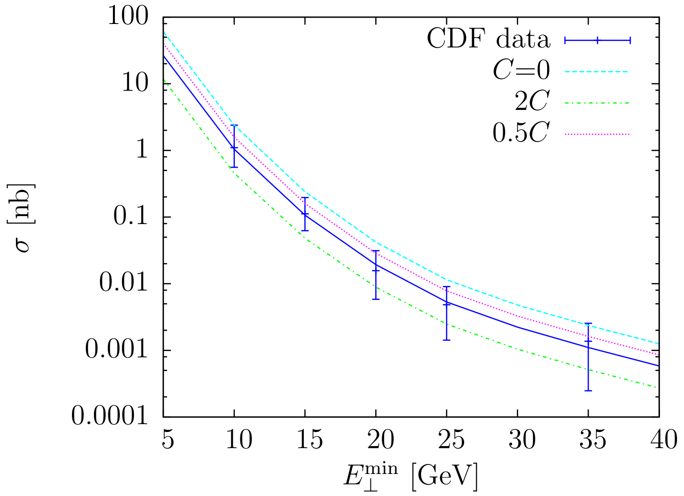

Figure 4.9: Effect of a change in the constant terms on the dijet cross section. It corresponds to the multiplication by a factor 2 or 1/2 of all terms in P_{gg} and P_{qg} that will not give a log contribution after the integration over $\mathbf{q}$ in Eq. 4.1.

The quasi-elastic dijet production cross section is plagued with a large theoretical uncertainty coming from the Sudakov form factor and moreover, a simple change in the prescription leads to a drastic change in the numerical result. Without tackling the question of the constant term, one can see that the single-log contribution to the Sudakov form factor cannot be neglected, and these corrections should be fully calculated in the dijet case. However the calculation is complex and up to now has only been performed completely in the case of a quark vertex [118–120].

4.2.3 Sensitivity to the Sudakov Parametrization

The Sudakov form factor $T(\mu^2, \ell^2)$ enters the loop integral as it depends on $\mathbf{k}$ via the lower scale ℓ. Because of that, it reshapes the region of momentum that contributes to the amplitude, *i.e.* the mean value and the distribution. Using the saddle point approximation, we discuss here the distribution over the transverse momentum of the screening gluon. Note that although the quantity $\mathbf{k}$ is not observable, one can use it in order to control the dynamics of the loop integration for theoretical purposes.

We want here to study the loop integral entering the dijet quasi-elastic cross section. Starting from Eq. (2.91), one can assume that the strongest dependence on $\mathbf{k}_1$ and $\mathbf{k}_3$ comes from the proton form factor so that, one can take $(\mathbf{k}+\mathbf{k}_1) \simeq (\mathbf{k}+\mathbf{k}_3) \simeq \mathbf{k}$ in the numerator. Neglecting the total helicity 2 amplitude, the integral is

$$\mathrm{d}\sigma_{qq} \propto \left| \int \frac{\mathrm{d}^2\mathbf{k}}{\mathbf{k}^6} \times \mathbf{k}^2 \times \Phi^2(\mathbf{k},-\mathbf{k}) e^{(\mathbf{k}_2^2,\mathbf{k}^2)} \right|^2 = |\mathcal{I}|^2, \tag{4.15}$$

where the impact factor plays the role of an IR cut-off. Without the Sudakov suppression, the integral is dominated by soft momenta due to the $\mathbf{k}^{-4}$ factor. With it, the weight of small momenta is suppressed and the dominant $\mathbf{k}$-region shifts towards harder scales. The corresponding mean value of $|\mathbf{k}|$ can be estimated using the saddle point approximation and according to [16, 17] is $|\mathbf{k}| \simeq 1-2$ GeV. It is sometimes claimed that this momentum is sufficiently hard to justify the applicability of pQCD in quasi-elastic calculation. However, we stress that one should be careful about this assumption. First, one has to agree with the fact that 1 GeV is indeed perturbative. Secondly, with two simple estimates, we show that the $|\mathbf{k}|$ shift depends strongly on the details of the Sudakov form factor.

We use the saddle point approximation to obtain the mean value of $\mathbf{k}$, so that we rewrite the integral $\mathcal{I}$ as a function of a more convenient notation

$$x \equiv \log\frac{\mathbf{k}^2}{\Lambda^2}, \quad x_2 \equiv \log\frac{\mathbf{k}_2^2}{\Lambda^2}, \tag{4.16}$$

with Λ a cut-off that can be chosen equal to Λ_{QCD}. One has now

$$\mathcal{I} = \frac{1}{\Lambda^4}\int e^{-[x-2\Phi(x)+S(x_2,x)]}\mathrm{d}x. \tag{4.17}$$

The global extremum x_0 of the argument $f(x) = x-2\Phi(x)+S(x_2,x)$ is the saddle point position, and can be obtained by calculating the zero of the derivative of $f(x)$. We first test the technique on the very simple case of the double-log approximation of the Sudakov form factor neglecting Φ, that is considered here as a cut-off. In the new variables, Eq. (4.6) is now

$$\begin{aligned} S_{DLA} &= \frac{3\alpha_s(\mathbf{k}_2^2)}{4\pi}\log^2\frac{\mathbf{k}_2^2}{\mathbf{k}^2} \\ &= \frac{3\alpha_s(\mathbf{k}_2^2)}{4\pi}\left[\log\frac{\mathbf{k}_2^2}{\Lambda^2} - \log\frac{\mathbf{k}^2}{\Lambda^2}\right]^2 \\ &= \frac{3}{x_2\beta_0}(x_2-x)^2, \end{aligned} \tag{4.18}$$

so that

$$f(x) = x + \frac{3}{x_2\beta_0}(x_2-x)^2, \tag{4.19}$$

with

$$\beta_0 = 11 - \frac{2}{3}N_f. \tag{4.20}$$

The last equality comes from the one-loop definition of the coupling constant α_s,

$$\alpha_s(\mathbf{k}_2^2) = \frac{12\pi}{(33-2N_f)}\frac{1}{\log\frac{\mathbf{k}_2^2}{\Lambda^2}} = \frac{12\pi}{(33-2N_f)x_2}. \tag{4.21}$$

One can now proceed to the evaluation of the saddle point position of $f(x)$ by taking the derivative

$$\begin{aligned} &\left.\frac{\mathrm{d}f(x)}{\mathrm{d}x}\right|_{x=x_0} = 0 \\ &\rightarrow x_0 = x_2\left(1-\frac{\beta_0}{6}\right) < 0. \end{aligned} \tag{4.22}$$

The fact that $x_0 = \log(\mathbf{k}_0^2/\Lambda^2)$ is always negative means that the integral is dominated by the small $\mathbf{k}^2$-region. Actually, if one takes typical TeVatron values $\mathbf{k}_2 \simeq 10$ GeV and $N_f = 4$, the mean $\mathbf{k}_0^2$ is 0.0025 GeV^2. Obviously, this is for a really simple Sudakov form factor. If instead one takes a running coupling, the picture is quite different. According to Appendix B.3.4 and in the same double log approximation, one has now

$$\begin{aligned} f(x) &= x + \frac{6}{\beta_0}\left(x_2 \log\frac{x_2}{x} - x_2 + x\right) \\ \rightarrow x_0 &= \frac{x_2}{1+\frac{\beta_0}{6}}, \end{aligned} \tag{4.23}$$

that gives $\mathbf{k}_0^2 \simeq 1$ GeV^2 for typical TeVatron values and the change from the previous result is substantial. The estimate of the suppression factor is

$$\begin{aligned} \mathcal{I} &\propto \int_0^\infty e^{-f(x)}\mathrm{d}x \\ &= \sqrt{\frac{2\pi}{-|f''(x_0)|}}e^{-f(x_0)}, \end{aligned} \tag{4.24}$$

by definition of the saddle-point approximation and in the present case, it gives

$$\mathcal{I} \propto e^{-\left[\frac{6x_2}{\beta_0}\log\left(1+\frac{\beta_0}{6}\right)\right]}, \tag{4.25}$$

which is about 0.008 for $\mathbf{k}_2 \simeq 10$ GeV. Numerically, one can obtain the saddle point position for more complex Sudakov form factor prescriptions without neglecting the impact factor. In Fig. 4.10.a, we show the function

$$f(x) = x - 2\Phi(x) + S(x_2, x), \tag{4.26}$$

for the impact and Sudakov form factors of the reference curve. For simplicity, the upper scale is fixed to typical TeVatron values $\mu = 10$ or 40 GeV and we take

$$x_2 = \log\frac{\mathbf{k}_2^2}{\Lambda} = \log\frac{\mu^2}{\Lambda}. \tag{4.27}$$

The second picture in Fig. 4.10 is the same function for different choices of impact factor and scales but still at $\mu = 10$ GeV. One can directly note that a change of a factor 2 in the scales doesn't modify the position of the saddle point, on the other hand, the type of the impact factor matters and can push the minimum to lower values of $\mathbf{k}$. This study is useful to obtain an idea of the mean value in the loop momentum but it doesn't include the true kinematics of the calculation. It nevertheless shows that the mean value of $\mathbf{k}$ is around 1 GeV or lower, that is clearly in the domain of soft momenta.

The severe change of the suppression factor with the prescription indicates the sensitivity of the calculation to the details of the Sudakov form factor. Depending on the assumptions used,

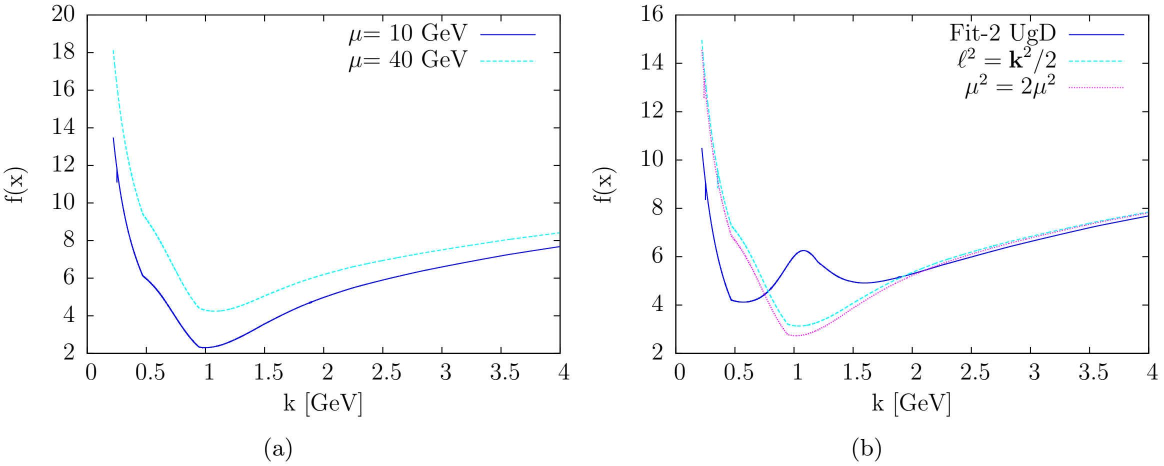

Figure 4.10: Function $f(x) = x - 2\Phi(x) + S(x_2, x))$. (a) For the impact and Sudakov form factor of the reference curve and for $\mu = 10$ GeV and $\mu = 40$ GeV. (b) Same function but for different parametrisation at $\mu = 10$ GeV.

the suppression can differ by one order of magnitude and the mean value of $\mathbf{k}$ can vary between 0.02 GeV and 1 GeV in the present simple approximations. One must conclude that claiming that the loop integral is perturbative is unjustified. In fact, this is not the end of the story as extra corrections are to be added as the gap-survival probability.

4.2.4 The Role of the Screening Gluon

In the two-gluon picture of quasi-elastic scattering, the first gluon leg is needed to screen colour and obtain a coulour-singlet exchange between initial hadrons. It is usually assumed that it does not participate to the hard subprocess. At lowest order, it is justified as the diagram of Fig. 4.11, with gluons emitted from different legs, is suppressed at large $\mathbf{k}_2$ because it contains one more

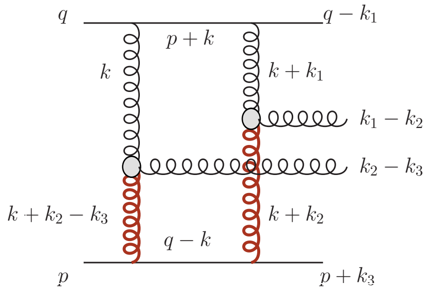

Figure 4.11: Lowest-order diagram with gluons emitted from different legs. The thick gluon lines represent hard propagators of the order $\mathbf{k}_2^2$.

hard gluon propagator. The diagram is of the order of $\log(\mathbf{k}_2^2)/\mathbf{k}_2^2$ at the Born level as shown in Chap. 2 and Appendix B.2.4. However, the virtual corrections of the Sudakov form factor are large for the first diagram but are different in the present case, so that, the contribution of this second diagram may matter.

In the standard picture, the final dijet system is emitted from only one gluon leg, the second is present only to screen the colour. Besides, standard BFKL soft exchanges of Fig. 4.12.a

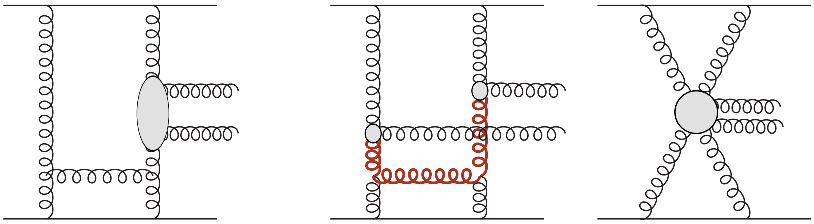
(a) (b) (c)

Figure 4.12: (a) In the case of the first diagram, standard BFKL soft exchanges can be reabsorbed in the evolution of the gluon density so that the screening gluon effectively decouples from the hard subprocess. The first order correction of (b) is only single-log enhanced. However at higher order, the hard momentum flow forms the effective irreducible $gggg \to gg$ vertex of (c) that is, for its part, double-log enhanced.

can be reabsorbed in the evolution of the gluon density so that the screening gluon effectively decouples from the hard subprocess. Nevertheless, in the case of the second diagram, the virtual corrections discussed in connection with the Sudakov form factor complicate the picture and lead to an nontrivial cross-talk between the t-channel gluons. The Sudakov form factor of the new diagram should modify the amplitude by

$$\mathrm{Im}\mathcal{M}_b \propto \frac{1}{\mathbf{k}_2^4} \int \frac{\mathrm{d}^2\mathbf{k}}{\mathbf{k}^4} e^{-S'(\mathbf{k}_2^2,\mathbf{k}^2)}, \tag{4.28}$$

if one only keeps the leading transverse momenta and where $e^{S'}$ is the new Sudakov factor. The correction at tree level is not double-log enhanced. One knows that double-log corrections build up from the longitudinal integral when z is small and in the presence of a hard scale at the vertex. The result of the integration is proportional to $\log(\mu^2/\ell^2)$ that depends on the fraction of momentum between the initial soft and the final hard scales. Consequently, if the scales are of the same order, *i.e.* in the considered case where the virtuality of the incoming parton is large $\mu^2 \simeq \ell^2$, then the log doesn't appear and the Sudakov form factor is at most single-log enhanced. The relevance of the argument can be demonstrated in the simpler case of QED calculation of [109, 110].

One can then go to higher orders and one must channel the hard transverse momentum as in Fig 4.12.c, the hard-momentum lines can be gathered in the irreducible four-gluons vertex $gggg \to g$. Now, one finds again the exact conditions for the double-log corrections to the vertex, *i.e.* the gluons entering the vertex are soft, and those contribution may be resummed leading to a novel type of Sudakov form factor. The virtual corrections discussed so far are interesting in themselves but they appear only at higher orders and we stress that the corrections to the tree-level result always lack one logarithm as they are of order $\alpha_s \log(\mathbf{k}_2^2) \left(\alpha_s \log^2(\mathbf{k}_2^2)\right)^n$. This is an indication that the corresponding Sudakov suppression is not as large as the one of the diagram where the final system is emitted from only one gluon leg, and it might be that

$$\begin{aligned} S'(\mathbf{k}_2^2,\mathbf{k}^2) &\ll S(\mathbf{k}_2^2,\mathbf{k}^2), \\ e^{-S'(\mathbf{k}_2^2,\mathbf{k}^2)} &\gg e^{-S(\mathbf{k}_2^2,\mathbf{k}^2)}. \end{aligned} \tag{4.29}$$

Looking back at Eq. (4.28), one can also note that it might happen that the second diagram is not as suppressed as it looks at the Born level, particularly if the mass of the final system, proportional to $\mathbf{k}_2^2$, is small.

Without a detailed calculation, one cannot say what this suppression factor is exactly and therefore if the contribution of the second diagram is effectively suppressed in the kinematical region of the CDF data for which the minimum jet transverse energy can be as small as 10 GeV. We have seen in Sec. 2.7.1 that without Sudakov form factor, the second diagram only accounts for 15% of the reference dijet cross section. Consequently, its contribution was neglected. However, if further calculations or data reduce the uncertainty below 10% then the contribution of the second diagram can have an impact. In particular, the negative sign of the correction would decrease the dijet cross section and require a re-tuning to the data. Moreover, as it is totally absent from the Higgs calculation, it would increase our estimate of the cross section.

4.3 Summary of the Uncertainties

In the present chapter, we have discussed the uncertainties coming from the addition of virtual corrections that can be large. We have identified two sources of uncertainty namely, the structure of the Sudakov form factor and the scale μ. Using the general formula of Eq. (4.2), we summarise here the main results in the particular case of dijet quasi-elastic production.

We have shown that theory is not able to fix the scales of the process precisely. Moreover, the calculation is sensitive to modest changes. The first question was about the expression of the cut-off Δ. In the literature, one finds the different definitions of Sec. 4.1 but recently, Coughlin and Forshaw computed the log corrections at NLO and they confirm in [20, 21] that the correct cut-off is $\Delta = |\mathbf{q}|/\mu$ which is the one used to produce the reference curve. The second important scale is the value of the lower limit ℓ related to the scale at which large logarithms start to be generated. The BFKL equation guarantees that below $\mathbf{k}^2$, the transverse integral only gives single logs in $s/\mathbf{k}^2$ that can be absorbed in the impact factor and consequently the lower scale should be $\mathbf{k}^2$. However, we argue that, as the Sudakov form factor is a vertex correction that involves partons emitted from the active gluons, the momentum in the transverse loop cannot be smaller than the transverse momentum of those active gluons. Hence, ℓ^2 should be proportional to the virtuality $(\mathbf{k}+\mathbf{k}_i)^2$ for $i = 2 \pm 1$ depending on whether one deals with the upper or the lower part of the production diagram. The effect on the numerical result of this assumption is shown in Fig. 4.13.a.

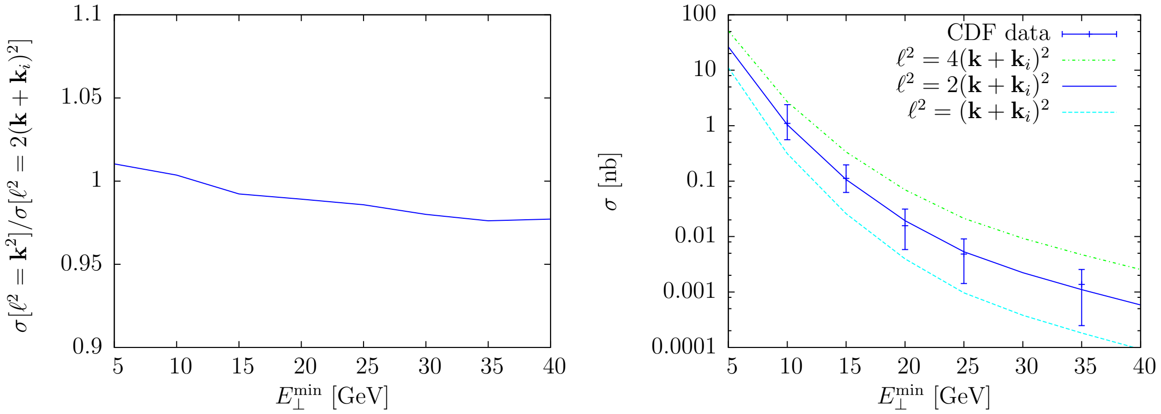

(a) (b)

Figure 4.13: (a) Ratio of the cross section with $\ell^2 = \mathbf{k}^2$ to that with $\ell^2 = 2(\mathbf{k}+\mathbf{k}_i)^2$. (b) Effect of a factor 2 in the lower limit of the Sudakov integral.

Besides, we insist on the fact that the log structure of the Sudakov form factor in the dijet case is not fully calculated and in order to study the effect of a change in this structure, *i.e.* the log and constant terms, one can choose to vary instead the upper and lower scales by

$$\begin{aligned} \mu^2 &= \mathbf{k}_2^2/x, \\ \ell^2 &= (\mathbf{k}+\mathbf{k}_i)^2/x' \quad i = 2 \pm 1, \end{aligned} \tag{4.30}$$

where x and x' are integers. It is equivalent to a change of the log structure of the Sudakov form factor and is used to study the theoretical uncertainty on the numerical result.

Note that from Fig. 4.13.b the lower scale in the reference curve is $2(\mathbf{k}+\mathbf{k}_i)^2$ and the same study can be made for the upper limit and we show in Fig. 4.14 the effect on the cross section of a change of a factor two in the scale μ^2 and note that the upper scale of the reference curve is $2\mu^2$. Finally, Fig. 4.15.a gives the mass distribution of the jet system compared with the CDF RunII data for $\mu^2 = 2\mathbf{k}_2^2$ and $\mu^2 = 0.62^2\, s_{gg}$, the scale in ExHume. One can directly note that the second distribution seems to fit perfectly the data but here one has to understand that the data are not true data but a model-dependent study of the dijet mass distribution using the prediction of the ExHume Monte-Carlo simulation [121]. Actually, the ExHume M_{jj} distribution is generated in different intervals of transverse minimum energy for the second jet[5], $E_\perp^{jet_2}$= 10-15 GeV, 15-20 GeV, 20-25 GeV, 25-35 GeV and above 35 GeV corresponding to i=1 to 5, then normalised to the cross section in this interval. After the sum

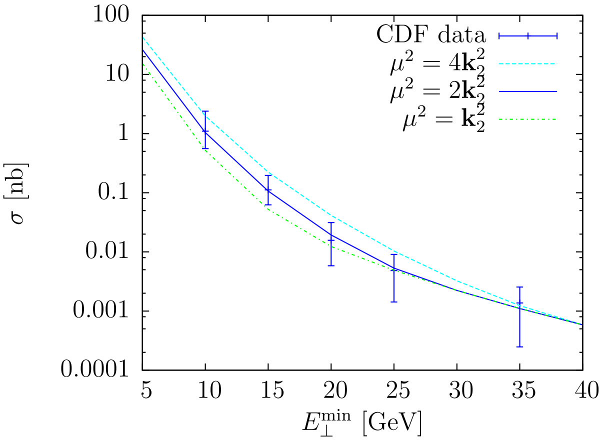

(a)

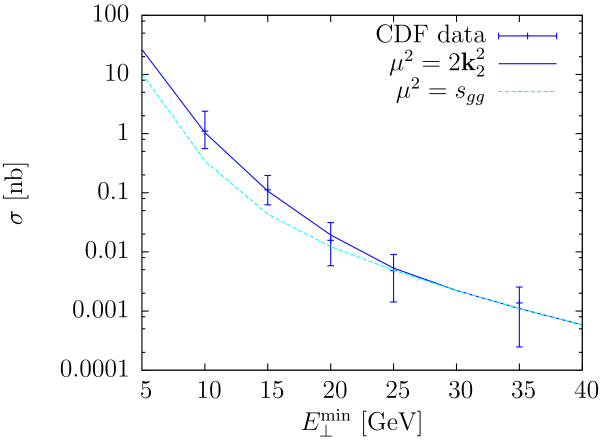

(b)

Figure 4.14: The effect of changing the scales of the Sudakov form factor with respect to the reference curve (in plain). (a) A factor 2 in the upper limit of the Sudakov loop and (b) the choice of s_{gg} for the upper limit.

$$\frac{\mathrm{d}\sigma}{\mathrm{d}M_{jj}} = \sum_{i=1}^{5} \frac{\mathrm{d}\sigma_i}{\mathrm{d}M_{jj}} \frac{\sigma_i^{\mathrm{data}}}{\sigma_i^{\mathrm{theory}}}, \tag{4.31}$$

one obtains the ExHume-based mass distribution for quasi-elastic dijet production. Consequently, one has to be careful about the accuracy of this test and true experimental data without theoretical bias would help to test the validity of our choice for the upper limit in the Sudakov

---

[5] Conventionally, the leading jet is the one with the largest transverse energy.

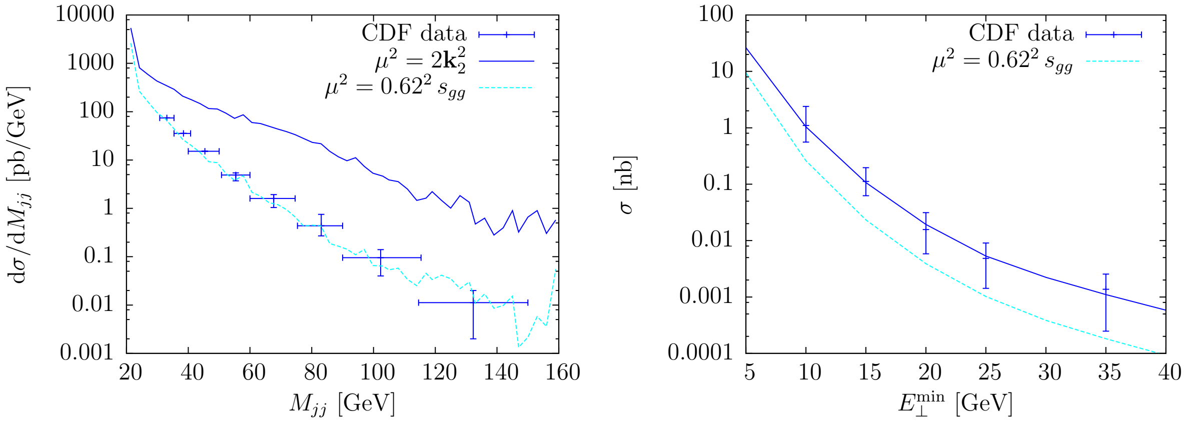

(a) (b)

Figure 4.15: Mass distribution of the jet system at $E_\perp^{\min} > 5$ GeV. Comparison of the parametrisation of the reference curve (a) with that for $\mu^2 = 0.62^2\, s_{gg}$, $\ell^2 = (\mathbf{k} + \mathbf{k}_i)^2$ and (b) corresponding $E_\perp$ distributions. Note that the data come directly from [57] without re-analysis.

integral. Furthermore, if one uses the exact transverse kinematics the $E_\perp$ distribution corresponding to the ExHume curve does not go through the data anymore, see Fig. 4.15.b.

Finally, we examine the various parametrisations discussed in Sec. 4.2.2. In Fig. 4.16, we compare

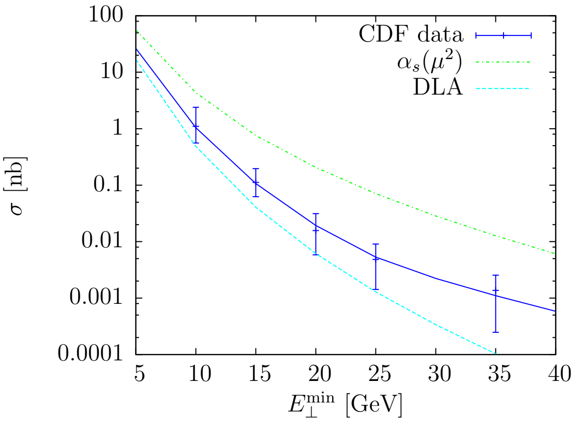

Figure 4.16: Effect of a change in the choice of the parametrisation discussed in Sec. 4.1. DLA stands for double-log approximation and $\alpha_s(\mu^2)$ corresponds to the option of fixed running coupling.

the double-log approximation (DLA) with the reference curve. Remember that the contribution of the single-log is negative so that its inclusion decreases the suppression but note that the curvature clearly shows that the double-log approximation cannot describe the data. In the same figure, we also show the effect of fixing the coupling constant α_s to the scale μ^2 and one can see that this leads to much larger changes than the inclusion of subleading logs and constant term.

Conclusion

The uncertainty coming from the Sudakov form factor can be evaluated in the following way: we first define the reference curve parametrisation and vary the different scales in a theoretically reasonable way. Once again, we stress that the reference curve is not a prediction but just an accurate parametrisation, summarised in Table 4.1, that produces a curve that goes through the CDF data. The uncertainty is evaluated using the variation due to a change from this parametrisation. We estimate the uncertainty coming from variations of the limits of integration to be about a factor 15 for the lower limit, and 6 for the upper one. Because one doesn't know what to do with the constant terms, we have decided to keep them as in other quasi-elastic models. Putting everything together leads to an uncertainty of a factor of at least 10 only for the Sudakov form factor that also constitutes the largest suppression factor to the cross section. In addition, the result is really sensitive to its parametrisation and this comes in part from the lack of knowledge concerning the Sudakov form factor in the dijet case. This should be improved by a detailed calculation. This suppression is fully calculated in the Higgs case as the vertex is effectively point-like simplifying the kinematics of the process, so that the uncertainty should be smaller in that case.

Parameter	**Reference Value**
μ^2	$2\mathbf{k}_2^2$
ℓ^2	$2(\mathbf{k}+\mathbf{k}_i)^2$
Δ	$\lvert\mathbf{q}\rvert/\mu$
α_s	Running
Sudakov exponentiation	$\log^2+\log$+constant

Table 4.1: Parameters of the reference curve.

Chapter 5

Additional Soft Corrections

In the previous chapters, we have described the main ingredients that compose the calculation of the quasi-elastic dijet cross section but one has also to deal with gap-survival probability and splash-out. The former comes from the fact that the hadron-level amplitude still has to be corrected for initial- and final-state interactions. These kinds of corrections are actually complicated to treat as they come from soft interactions that change the momenta of the protons and should be convoluted with the hard subprocess. The gap-survival probability can be estimated from a parametrisation of the elastic amplitude and one can find here a simple estimate that is then compared with the results from literature.

The correction due to splash-out is related to the way one compares the CDF data to the theoretical prediction. The final gluons produced through pomeron exchange hadronize into a bunch of particles collected in detectors and the jet is reconstructed during data analysis by a jet-finding cone algorithm. One thus misses some radiation outside the cone and consequently the energy measured at the jet level is smaller than the energy at the parton level. This loss of energy from partons to jets is the splash-out. In the second part of this chapter, we compare different prescriptions from the literature and present a method to improve the description of the splash-out developed on the basis of the present calculation.

5.1 Gap-Survival Probability

The concept of gap-survival probability was introduced by Bjorken a long time ago [1]. It is the estimate of the number of events that effectively present a rapidity gap in the final state, taking into account the fact that spectator partons, or multiple interactions which include particle production, might fill the gap produced at the parton level. The complete calculation of the gap-survival probability is far beyond the scope of this thesis, so that we shall only focus on the basics. For a recent review, one can refer to [122].

5.1.1 Definition and Method of Estimation

In order to understand the gap-survival probability, one must come back to Sec. 1.3.2 that presents quasi-elastic processes as the inclusion of a hard interaction into a multiple soft exchange. As the two processes occur at largely different scales, they do not interfere but the hard interaction changes the transverse momenta of the incoming hadrons. Consequently and in the eikonal approximation, the two amplitudes should be convoluted in transverse momentum space.

However, this convolution disappears if one works in impact parameter space where the probability of a quasi-elastic interaction at a given energy s, and for a transverse impact factor $\mathbf{b}$ is

$$|P_{QE}(\mathbf{b})|^2 = |H(\mathbf{b})|^2 |S(\mathbf{b})|^2, \tag{5.1}$$

where $|H(\mathbf{b})|^2$ is the probability of hard interaction, *i.e.* our cross section in impact parameter space and $|S(\mathbf{b})|^2$ is the probability for the two protons to go through each other. This second factor is the matrix element $|S(b)|^2 = |\langle pp|S|pp\rangle|^2$ that can be estimated from the expressions of the total and the elastic cross sections

$$S(\mathbf{b}) = 1 + ia_{el}(s, \mathbf{b}), \tag{5.2}$$

where 1 corresponds to the case of no interaction and where $a_{el}(s, \mathbf{b})$ is the elastic amplitude. The square $|S(\mathbf{b})|^2$, can be interpreted as the probability for no inelastic interactions between the two protons. After a multiplication by i, one has

$$|S(\mathbf{b})|^2 \propto |i - a_{el}(s, \mathbf{b})|^2. \tag{5.3}$$

Generically, the gap-survival probability tends to 1 at large impact parameter $\mathbf{b}$ and is suppressed at small $\mathbf{b}$. It becomes zero when the elastic amplitude is purely imaginary, $a_{el}(s, \mathbf{b}) = i$. This is referred to as the black disc limit (BDL) when the proton behaves as a black body, *i.e.* one half of the amplitude is elastic while the other is inelastic. In particular, current models agree that at the TeVatron, the elastic amplitude approaches the black disc limit and is hence dominated by its imaginary part.

However, to use the definition of Eq. (5.3) one has to know the elastic amplitude in impact-parameter space. Hence, if t is the transferred momentum such as $t = -\mathbf{\Delta}^2$, one obtains it by taking the Fourier transform $a_{el}(s, \mathbf{b})$ with

$$a_{el}(s, \mathbf{b}) = \frac{1}{2s} \int \frac{\mathrm{d}^2\mathbf{\Delta}}{(2\pi)^2}\, a_{el}(s, -\mathbf{\Delta}^2) e^{i\mathbf{\Delta}.\mathbf{b}}. \tag{5.4}$$

Note that the above convention leads to the expressions,

$$\begin{aligned} \sigma_{\text{tot}} &= 2 \int \mathrm{d}\mathbf{b}\, \mathrm{Im}\left(a_{el}(s, \mathbf{b})\right), \\ \sigma_{\text{el}} &= \int \mathrm{d}\mathbf{b}\, |a_{el}(s, \mathbf{b})|^2. \end{aligned} \tag{5.5}$$

So, starting with the definition of the differential cross section

$$\frac{\mathrm{d}\sigma_{el}}{\mathrm{d}t} = \frac{1}{16\pi s^2} |a_{el}(s, t)|^2, \tag{5.6}$$

one has

$$a_{el}(s, t) \simeq i \sqrt{16\pi s^2 \frac{\mathrm{d}\sigma_{el}}{\mathrm{d}t}}. \tag{5.7}$$

Consequently, an estimate of $a_{el}(s, t)$ can be extracted from the elastic cross section parametrised by the simplest fit to the CDF data [123], that gives

$$\frac{\mathrm{d}\sigma_{el}}{\mathrm{d}t} = N e^{(2B_{el}\, t)}, \tag{5.8}$$

with

$$\begin{aligned} N &= 334.6 \pm 18.8 \text{ mb GeV}^2, \\ 2B_{el} &= 16.98 \pm 0.24 \text{ GeV}^2. \end{aligned} \tag{5.9}$$

In fact, the amplitude $a_{el}(s, t)$ has a real and an imaginary parts and is usually written

$$a_{el}(s,t) = |a_{el}(s,t)| \frac{\rho(s,t)+i}{\sqrt{1+\rho(s,t)^2}}, \tag{5.10}$$

where ρ is the ratio of the real to imaginary parts of the forward elastic amplitude and one has $\rho \simeq 0.14 \pm 0069$ according to [124]. Hence, the contribution of the real part is small and, as the amplitude is close to the black disc limit for this range of energy, one can assume the amplitude to be purely imaginary and using Eq. (5.7) together with Eq. (5.4), compute the Fourier transform

$$a_{el}(s,\mathbf{b}) = \frac{i\sqrt{16\pi N}}{2} \int \frac{\mathrm{d}^2\mathbf{\Delta}}{(2\pi)^2}\, e^{-(B_{el}\mathbf{\Delta}^2)} e^{i\mathbf{\Delta}.\mathbf{b}}, \tag{5.11}$$

by completing the square to get

$$a_{el}(s,\mathbf{b}) = i\sqrt{\frac{N}{4\pi}} e^{\frac{-\mathbf{b}^2}{4B_{el}}} \frac{1}{B_{el}}, \tag{5.12}$$

and as expected

$$a_{el}(s,\mathbf{b}) \simeq i(0.974) e^{\frac{-\mathbf{b}^2}{4B_{el}}}, \tag{5.13}$$

is close to the black disc limit at $\mathbf{b} \simeq 0$. The corresponding gap-survival probability $|1-a_{el}(s,\mathbf{b})|^2$ is shown in Fig. 5.1.a and in fact if the cross section is really at short distance, the gap survival would be around $|S(\mathbf{b}=0)| \simeq 0.5\%$. Fortunately, the present result is obtained under the assumption of a purely imaginary amplitude but the real part is non-zero and consequently this estimate only gives a lower bound. Moreover, one can note that this real part would lead to a similar estimate and assuming it constant with t would provides then a upper bound. To get the real upper bound, one would have to consider also the E710 elastic data.

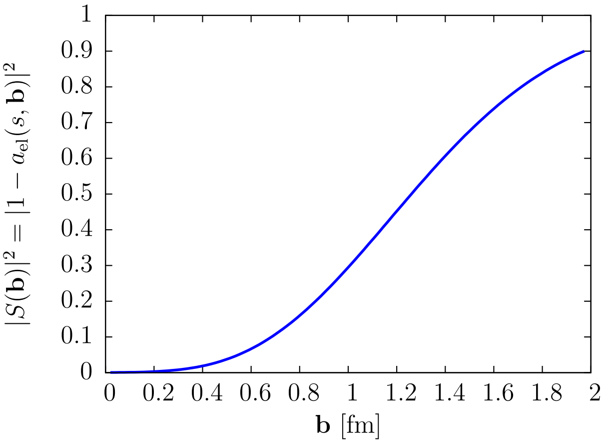

Figure 5.1: Gap-survival probability $|S(\mathbf{b})|^2 = |1 - a_{el}(s,\mathbf{b})|^2$ extracted from a fit to the elastic cross section at the TeVatron [123].

Going beyond the TeVatron energy to predict the gap-survival probability at the LHC is not the aim of this thesis but a simple test can be done. In the spirit of pomeron exchange in Regge theory, one can introduce a Regge factor to the elastic amplitude of Eq. (5.12) that thus yields

$$\begin{aligned} a_{el}(s,t) &= 4s\sqrt{N\pi}\, e^{-B_{el}t} \times \left(\frac{s}{s_{\text{TeV}}}\right)^{-(\alpha(0)+\alpha' t)} \\ &= 4s\left(\frac{s}{s_{\text{TeV}}}\right)^{\alpha(0)} \sqrt{N\pi}\, e^{-\left(B_{el}-\log\left(\frac{s}{s_{\text{TeV}}}\right)\alpha'\right)t} \\ \to a_{el}(s,\mathbf{b}) &= \left(\frac{s}{s_{\text{TeV}}}\right)^{\alpha(0)} \sqrt{\frac{N}{4\pi}}\, e^{\frac{-\mathbf{b}^2}{4\left(B_{el}-\log\left(\frac{s}{s_{\text{TeV}}}\right)\alpha'\right)}} \frac{1}{\left(B_{el}-\log\left(\frac{s}{s_{\text{TeV}}}\right)\alpha'\right)}, \end{aligned} \tag{5.14}$$

and provides the energy dependence of the amplitude and of the gap-survival probability. In the present case, one can note that we used s/s_{TeV} where s_{TeV} is the energy in the center-of-mass frame at the TeVatron, due to the fact that this factor is implicitly already included in the normalisation N of the TeVatron fit. The corresponding result at LHC with $\sqrt{s} = 14$ TeV is shown in Fig. 5.2 and one can note that in this very simple scheme, the elastic amplitude leads to the negativity of $1 + ia_{el}(s,\mathbf{b})$. It is not our purpose to solve this issue, but we stress that it is a pertinent way to point out the fact that gap survival is not yet under theoretical control. Of course, several more complex models exist in the literature, following the recent review of [125], one can note that most of them estimate the correction at the TeVatron to be from 5% to 15% and about a factor 2 lower at LHC.

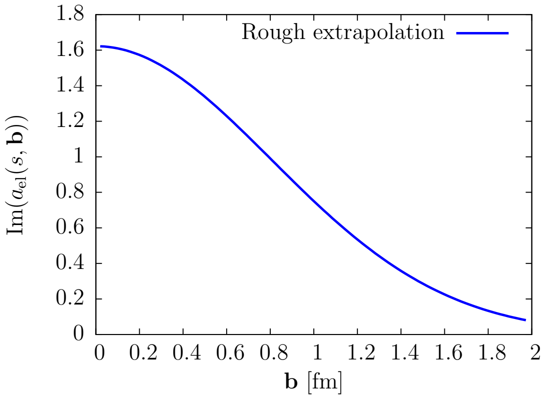

Figure 5.2: Extrapolation of the elastic amplitude at the LHC (14 TeV). As a_{el} can be larger than 1 in the presented simple scheme, it leads to a non-physical behavior of the gap survival.

The gap-survival probability used in the present work has to stay within this range but in view of the discrepancy between the different existing models, one can assume a factor 3 of uncertainty. A precise measurement of the real and imaginary parts of the elastic amplitude at the LHC may help to reduce this number. The present study of soft corrections coming from the rescatterings treats the gap-survival probability as a number that multiplies the amplitude, as do most of the existing calculations of quasi-elastic production. However, we would like to point out few problems coming from this picture.

5.1.2 Beyond the Gap

Indeed, it is true that in impact parameter space, the gap-survival probability factorises from the main calculation but it is not true in momentum space, where the quasi-elastic cross section is actually computed. Besides the problem of the convolution, there is also the question of the scale in $\mathbf{b}$ at which this correction has to be evaluated. Those questions are still open.

The conjugate variable to $\mathbf{b}$ is $\mathbf{k}_1 + \mathbf{k}_3$ that stands for the relative momentum of the incoming protons and is related to the transferred momenta. Most of the estimates in [125] assume that the t-dependence factorises, this makes the calculation of the gap survival S^2 quite simple and allows to write the quasi-elastic cross section

$$\mathcal{M}(p_1p_2 \rightarrow p_1^* + gg + p_2^*) = \sqrt{S^2}\,\mathcal{M}_{qq} \otimes \Phi(p_1)\sqrt{T(\mu^2, \ell_1^2)}\;\Phi(p_2)\sqrt{T(\mu^2, \ell_2^2)}. \tag{5.15}$$

However, this assumption also suggests that the momenta of the incoming particles stay unchanged after the hard interaction and furthermore, after any soft exchange. This is a very rough approximation even in quasi-elastic processes where the transferred momentum is small. In particular, some efforts have been made to keep an exact transverse kinematics in the present work so that the integrand depends explicitly on $\mathbf{k}_1$, $\mathbf{k}_3$. The correct way to implement the gap survival in the calculation should imply a convolution with the cross section in momentum space giving an additional integral over the impact parameter.
The second question to address is the scale. One has to know at which value of $\mathbf{b}$, the gap survival has to be taken and Eq. (5.1) suggests that the scale should be the same in the soft $|S(\mathbf{b})|$ and hard interaction $|H(\mathbf{b})|$. As $\mathbf{k}_1 + \mathbf{k}_3$ is a combination of soft momenta, one expects to have a very large suppression due to gap-survival probability which is small at small $\mathbf{b}$. However, the convolution with the hard amplitude shifts the mean value of the impact parameter to the long-distance region and this should lead to a smaller suppression of the cross section. It is then very unlikely that the rescattering corrections are given by this simple formalism and actually, one can guess that they probably have a smaller effect.

We stress that the implementation of the gap-survival probability should be improved in some way. Nevertheless, given the large uncertainties from gap survival itself and from the other pieces of the calculation, this may not be a crucial issue.

5.2 The Splash-Out

The problem is that data are presented as a function of the transverse energy of jets whereas one only has so far partons in the final state. In order to make experiment and theory speak to each other, one has to estimate the amount of energy lost when going from partons to jets and this effect is called the splash-out. The present section is devoted to the development of tools able to model this correction. The first part gives the definition followed by a description of the numerical method used to link the parton-level calculation to the jet-level cross section and finally, we present a short analysis leading to a new and more accurate parametrisation of the splash-out.

5.2.1 From Partons to Jets

To go from a parton to a jet, one has to follow a procedure in three steps. The first is obviously the generation of the partonic final state. In the present case, it corresponds to the four-momenta of the two final partons as shown in Fig. 5.3.a in the η/ϕ plane. The second is the hadronization of the final state that leads to the set of particles potentially seen in detectors and pictured by the green crosses of Fig. 5.3.b. The third is the reconstruction of jets via a cone algorithm that gathers all particles that are supposed to be from the same initial parton and gives the jet four-momentum and transverse energy as shown in Fig. 5.3.c. It can be directly noted from this simple example that some of the particles in the final state are not included in the reconstructed jet so that the transverse energy is modified by radiation outside the cone.

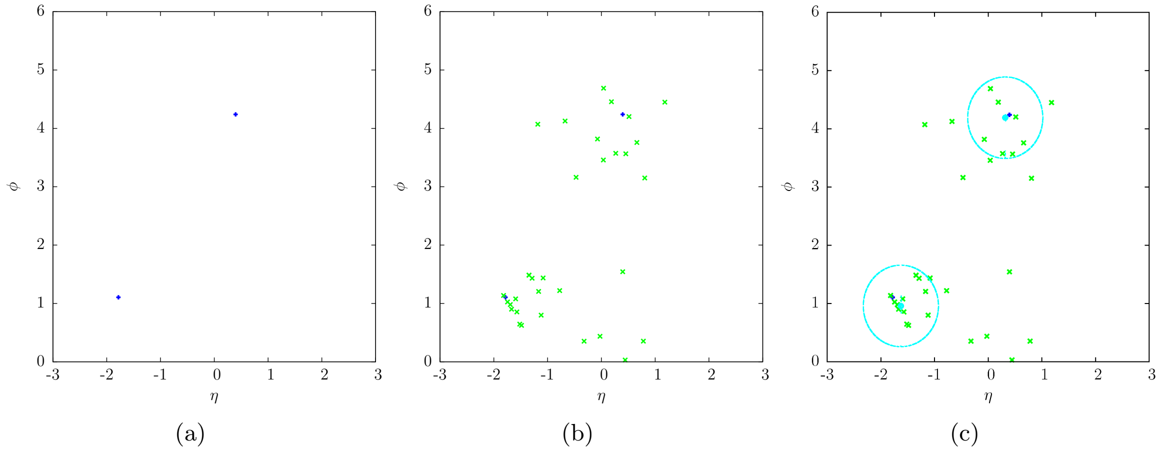

(a) (b) (c)

Figure 5.3: The η/ϕ space (a) at the parton level, (b) after hadronization by Pythia and (c) after the application of a cone algorithm. The jet is constituted by all the particles included in the circle and its center is the reconstructed parton.

This is what we called splash-out, a correction standing at the border between theoretical studies and experimental measurements.

There exist in the literature prescriptions for the splash-out. According to [22, 126], its structure is known and involves a constant shift in the transverse energy due to hadronization as well as a correction due to radiation. At the TeVatron, the corresponding shift has been estimated [127] from a Monte-Carlo study using the CDF cone algorithm with a radius R =0.7, to be

$$\text{Prescription A}: E_\perp^{\text{jet}} = (0.75 - 0.80)E_\perp^{\text{parton}}. \tag{5.16}$$

However, one can also consider a previous parametrisation [128] that gives

$$\text{Prescription B}: E_\perp^{\text{jet}} = E_\perp^{\text{parton}}\left[1 - \frac{1}{2}\alpha_s\left((E_\perp^{\text{parton}})^2\right)\right] - 1\ \text{GeV}. \tag{5.17}$$

The use of either of these prescriptions corresponds to the changes in the quasi-elastic dijet cross section shown in Fig. 5.4. One can see that for the energy range of the CDF data, the effect of splash-out is non-negligible and amounts to a correction of a factor 3 for $E_\perp^{\text{min}} > 10$ GeV. The various possibilities of Eq. (5.16) and Eq. (5.17) bring in an uncertainty of the order of 1.7 at 10 GeV to 4 at 35 GeV. In addition, these prescriptions have two drawbacks: first, splash-out should not be a simple shift in energy but rather a distribution in the energy of the jet as a function of the initial parton energy. Secondly, they are only usable at TeVatron energy and there exists no straightforward extrapolation to other experiments.

Hence, the idea is to link our code to a Monte-Carlo for hadronization and a jet-cone algorithm to perform the full simulation from partons to hadrons and not to be biased by the splash-out. However, the full procedure is time and CPU consuming, so that it quickly appears that one should instead use this tool to build a better parametrisation of the splash-out. Hence, we give here the steps of the method and first give an overview of the different necessary tools, *i.e* Pythia, Delphes and cone algorithms.

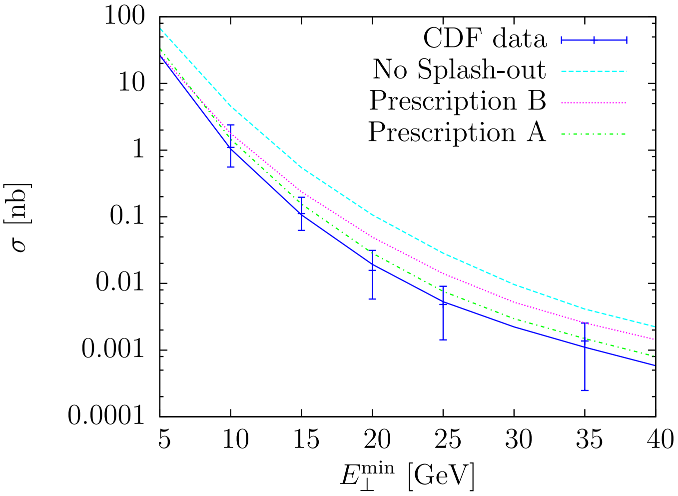

Figure 5.4: Suppression of the cross section for various splash-out prescriptions. For the reference curve, $E_\perp^{\text{jet}} = 0.75\, E_\perp^{\text{parton}}$ is used.

Hadronization and Smearing : Pythia and Delphes

Pythia is a program for the generation of high-energy physics events, *i.e.* for the description of collisions at high energy [129]. It models several physical processes from parton-level calculations to hard and soft interactions and contains parton distributions, initial and final-state parton showers, multiple interactions, fragmentation and decays. It is a large collection of formulae built since 1997 and Pythia has demonstrated its validity besides it being in continuous development. It is also used by most of the LHC collaborations to predict rates and cross sections of possible processes as it actually helps to choose the analysis strategies that should be used on real data providing studies of signal-to-background or detector regions of interest for a particular process. Pythia is also a perfect bridge between a theoretical study and the real event as it produces the missing steps between a parton-level calculation and the final state through all the complicated processes that occur when the partons become hadrons. Moreover, it is designed to allow the addition of user-defined processes, taking as an input the final state of user-defined events. Most of the time, it is used as a black box promoting partons to hadrons and, indeed, we used here version 6.4 with its default parameters, never touching the machinery cogwheel. The link between new processes and Pythia can easily be made thanks to the Les Houches Accord [130] that was made for passing information from a parton generator to a hadronizing Monte-Carlo. The method consists in the creation of a Les Houches Event File (LHEF or LHE) that contains all the information requested. The main part of this file is the event information that describes entirely the parton-level final state. This event part contains the ID, status and parent-child history of the event, *i.e.* all the particles that should be processed by Pythia:

- Particle ID according to the Particle Data Group convention.
- Particle status:

-1	Incoming particle
+1	Outgoing final-state particle
+2	Intermediate resonance

- A label referring to the mother particles.
- Colour flow, a label referring to where the colour of the particle comes from.
- Laboratory-frame momenta P_x, P_y, P_z, E and M in GeV.

- Invariant lifetime $c\tau$ and helicity, the last one could be set to 9 if helicity is unknown or non-necessary.

A more precise description of LHE files can be found in reference [131] and Appendix B.4.
After the hadronization by Pythia, one can perform an analysis of the result exactly as in the experimental case. This part is carried out by Delphes [132] that is a new tool for high-energy physics. It is a framework for the fast simulation of general-purpose experiments. It includes the smearing of the final particles, as well as the remaining protons of quasi-elastic interactions, a simulation of the detector responses and the possibility to picture the full final event using FROG [133]. At the beginning, Delphes was designed to describe the LHC detectors *e.g.* CMS including FP420. But now the program is driven by a card that allows a large spectrum of basic detector parameters, such as resolution or thresholds. This is the first time that such a tool is available to all, giving the possibility to perform the full chain of physics and analysis, from the direct generation of partons to a picture of the event in the detector.

Cone Algorithms

The role of cone algorithms is to cluster particles of the final state into jets and to relate the kinematical properties of these jets to the kinematical properties of initial partons [134]. It is made of a jet-finding algorithm and of a recombination scheme that combines the different momenta to obtain the jet four-momentum. The two parts are independent and can be different depending on the prescription but each cone algorithm has to satisfy a set of criteria defined during the Snowmass meeting of 1990 [135]. They have to be defined at each order of perturbation theory, infra-red and collinear safe, invariant under boost, order independent[1] and straightforwardly implemented. Based on these criteria, it is possible to develop several cone algorithms and indeed, there exists several prescriptions.
The CDF collaboration at the TeVatron RunII works with the CDF Midpoint algorithm [136] which they use for the analysis of quasi-elastic data. It chooses for seeds all particles in the final state with a transverse energy larger than some threshold, here $E_\perp = 100$ MeV, and each seed is enclosed into a cone of radius $R = 0.7$ in the η/ϕ plane, before it is used as a basis for the search of stable cones. The second step is to define the midpoint between all pairs of stable cones found in the first step and promote them to the status of seed. This part insures the infra-red safety of the algorithm.

Now that we have described all the tools, one has the option to run Pythia with a cone algorithm after the parton-level calculation to obtain the cross section, or one can use directly those tools to study the difference in energy between the parton and the reconstructed jet to find a parametrisation for the splash-out.

5.2.2 Simple Parametrisation of the Splash-Out

For a single parton in the final state, one has a bunch of particles in the detector and they have to be gathered to form the final jets. During this stage, a certain amount of energy is lost due to the fact that some particles created during the parton shower can escape from the cone and then the jet energy is smaller than the energy of the parton that gave birth to it. In particular, a given initial parton energy $E_\perp^{\text{gluon}}$ corresponds to a certain distribution of the reconstructed jet energy $E_\perp^{\text{jet}}$. Its distribution can be obtained by a systematic comparison of both energies and this may allow to derive the relation between $E_\perp^{\text{gluon}}$ and $E_\perp^{\text{jet}}$ and leads to a formula for the splash-out.

---

[1] The algorithm should behave equally at the parton, particle and detector level, *i.e.* be insensitive to hadronization and underlying events.

One can generate two partons in a colour-singlet state at $\phi = 0$ and $\eta = 2$. After hadronization by Pythia, the jets are reconstructed using the Midpoint jet cone algorithm for different initial parton transverse minimum energy. One has then the plots shown in Fig. 5.5.

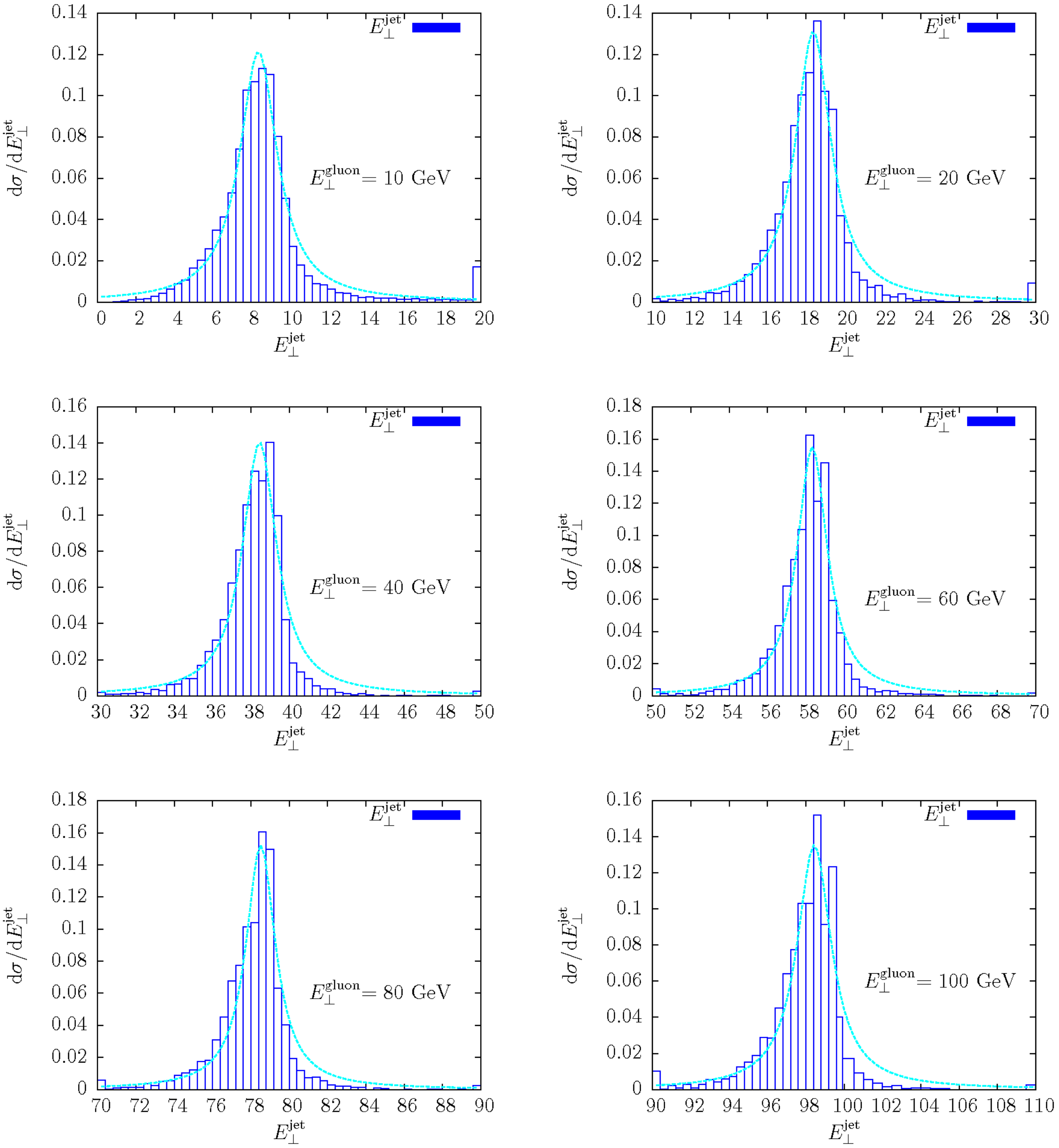

Figure 5.5: Distribution of the jet energy $E_\perp^{\text{jet}}$ for different initial gluon energies $E_\perp^{\text{gluon}}$. The solid line is the result of the fit (5.19).

The curves are Lorentzian so that, one can fit the distributions with the function

$$L\left(E_\perp^{\mathrm{jet}}, E_\perp^{\mathrm{gluon}}\right) = c\,\frac{1}{\left(E_\perp^{\mathrm{jet}} - b\,E_\perp^{\mathrm{gluon}}\right)^2 + \left(\frac{1}{2}a\right)^2}, \tag{5.18}$$

where a, b and c are parameters to be adjusted. Moreover, one can directly relate a to the scale parameter which specifies the width at half-maximum of the distribution while $b\,E_\perp^{\mathrm{gluon}}$ is the position of the maximum. Just looking at the graphs also shows that a is more or less identical in all distributions and that all maxima are shifted from $E_\perp^{\mathrm{gluon}}$ by the same quantity. A fit using MINUIT gives similar values for a and b in every region of transverse energy with average values

$$\begin{aligned} \bar{a} &= 2.08 \text{ GeV}, \\ \bar{b} &= 0.95. \end{aligned} \tag{5.19}$$

One can directly note from the value obtained for b that the argument of the function becomes

$$E_\perp^{\mathrm{jet}} - 0.9\,E_\perp^{\mathrm{gluon}}, \tag{5.20}$$

and the energy shift is not far from the one of Eq. (5.16). In addition, the Lorentz function is normalised to

$$\int_0^\infty L\left(E_\perp^{\mathrm{jet}}, E_\perp^{\mathrm{gluon}}\right) \mathrm{d}E_\perp^{\mathrm{jet}} = 1, \tag{5.21}$$

if N is the number of events and that leads to $c = \frac{a}{2\pi N}$. From Fig. 5.6 one can see that the shape of the distributions does not depend on the rapidity of the initial partons.

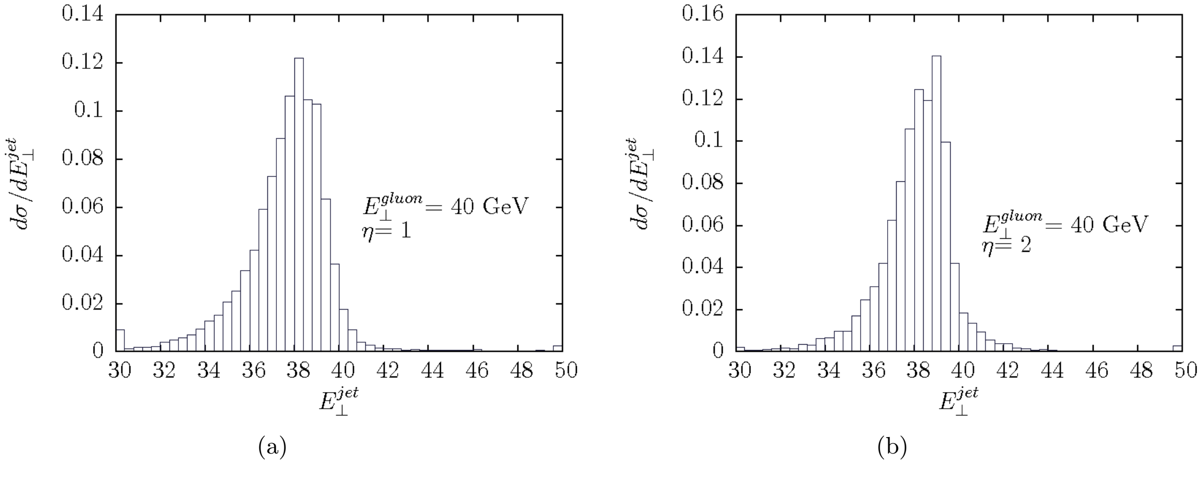

(a) (b)

Figure 5.6: Distribution of transverse energy of the jet $E_\perp^{\mathrm{jet}}$ for two different rapidities of the initial gluon.

Understanding the function $L\left(E_\perp^{\mathrm{jet}}, E_\perp^{\mathrm{gluon}}\right)$ as the probability to obtain a jet of energy $E_\perp^{\mathrm{jet}}$ from a parton of energy $E_\perp^{\mathrm{gluon}}$, one can now remove the heavy work done by Pythia and model the effect of splash-out by an additional integral

$$\mathrm{P}(E_\perp^{\mathrm{gluon}} \to E_\perp^{\mathrm{jet}}) = \int_0^\infty L\left(E_\perp^{\mathrm{jet}}, E_\perp^{\mathrm{gluon}}\right) \mathrm{d}E_\perp^{\mathrm{jet}}. \tag{5.22}$$

Note that due to the cuts on transverse energy, the lower bound of the integral is in fact $E_{\perp}^{\text{min}}$ while the upper is $E_{\perp}^{\text{gluon}}$ because the energy of the jet cannot be larger than the energy of the parton that gave birth to it.

This simple implementation of the splash-out is now ready to be used in quasi-elastic dijet production. Obviously, it is only useful for the TeVatron but the same study can be done for the LHC, *i.e.* for higher $E_{\perp}^{\text{gluon}}$ and if the values of a and b remain constant, one would have a function that gives the correction at all energies. Nevertheless, there is also the possibility to use directly the full analysis, *i.e* Pythia, cone algorithms and so one. This aim was achieved recently by the implementation of the calculation of dijet quasi-elastic production in a Monte Carlo dedicated to forward physics (FPMC) [137] from which one can find some results in the next chapter.

Chapter 6

Quasi-Elastic Dijet Results and Conclusion

In the previous chapters, we have covered all the elements of a model for the cross section of quasi-elastic two-gluon jet production. The general formula is now

$$\mathcal{M}(p_1p_2 \to p_1^* + gg + p_2^*) = \sqrt{S^2}\,\mathcal{M}_{qq} \otimes \Phi(p_1)\sqrt{T(\mu^2,\ell_1^2)}\ \Phi(p_2)\sqrt{T(\mu^2,\ell_2^2)}, \tag{6.1}$$

as announced in the introduction. We have seen that most of these elements are plagued by large uncertainties coming from a lack of knowledge of the theory or from the precision of the data. It is now time to summarise the different results and to use the CDF dijet data to narrow down the uncertainty. We shall start with a simple estimation of the bare cross section to understand the order of magnitude of the cross section. This will also be useful to control the numerical calculation that is done afterward. The numerical code that allows to model completely a quasi-elastic event, from the partonic interaction to the jet level, will be shortly described. We shall then give the predictions for the dijet cross section at the LHC.

6.1 Back-of-the-Envelope Calculation

The simple order-of-magnitude estimate of the cross section starts with the bare cross section at the hadronic level that includes only the parton level calculation and the impact factor.

Consider again the cross section of Eq. (2.91) and Eq. (3.2)

$$\mathrm{d}\sigma = \mathrm{d}\sigma_{qq} \otimes \prod_{i=2\pm1} \Phi\left(\mathbf{k}, -(\mathbf{k}+\mathbf{k}_i)\right) \Phi\left(\mathbf{k}', -(\mathbf{k}'+\mathbf{k}_i)\right), \tag{6.2}$$

with

$$\mathrm{d}\sigma_{qq} = \frac{1}{16(2\pi)^8}\frac{N^2-1}{N^2}\frac{g_h^4 g^8}{4\pi^4}\frac{\mathrm{d}\beta_1}{\beta_1}\frac{\mathrm{d}\beta_2}{\beta_2}\mathrm{d}^2\mathbf{k}_1\mathrm{d}^2\mathbf{k}_2\mathrm{d}^2\mathbf{k}_3 \times |\mathcal{M}|^2. \tag{6.3}$$

It can be simplified as follows. First, since the strongest dependence on $\mathbf{k}_1$ and $\mathbf{k}_3$ is in the impact factor, it seems reasonable to set $\mathbf{k}+\mathbf{k}_1 \simeq \mathbf{k} \simeq \mathbf{k}+\mathbf{k}_3$ in the other terms of the numerator. Furthermore, as the helicity-2 amplitude is small in front of the helicity 0 amplitude, one can neglect it and $|\mathcal{M}|^2$ simplifies to

$$\begin{aligned}|\mathcal{M}|^2 &\simeq \frac{1}{2}\left(\frac{1}{t_{gg}}+\frac{1}{u_{gg}}\right)^2 \int \mathrm{d}^2\mathbf{k}\mathrm{d}^2\mathbf{k}'\, \frac{\left[|\mathcal{M}_0|^2(\mathbf{k}.\mathbf{k}')^2 + |\mathcal{M}_0|^2\left(\mathbf{k}^2\mathbf{k}'^2 - (\mathbf{k}.\mathbf{k}')^2\right)\right]}{\mathbf{k}^2(\mathbf{k}+\mathbf{k}_1)^2(\mathbf{k}+\mathbf{k}_3)^2 \quad \mathbf{k}^2(\mathbf{k}'+\mathbf{k}_1)^2(\mathbf{k}'+\mathbf{k}_3)^2} \\ &= \frac{1}{2}\frac{1}{(\mathbf{k}_2^2)^2}\int \frac{\mathrm{d}^2\mathbf{k}}{(\mathbf{k}+\mathbf{k}_1)^2(\mathbf{k}+\mathbf{k}_3)^2}\frac{\mathrm{d}^2\mathbf{k}'}{(\mathbf{k}'+\mathbf{k}_1)^2(\mathbf{k}'+\mathbf{k}_3)^2},\end{aligned} \tag{6.4}$$

as $|\mathcal{M}_0|^2 = 1$ and

$$\frac{1}{t_{gg}} + \frac{1}{u_{gg}} = \frac{1}{\mathbf{k}_2^2}. \tag{6.5}$$

Now, one can change notation and write the longitudinal phase space as a function of two new variables

$$\begin{aligned} x &\equiv \frac{\beta_1}{\beta_2}, \quad x \in [1, x_{\text{max}}], \\ \beta &\equiv \sqrt{\beta_1 \beta_2}, \quad \beta \in [\beta_{\text{min}}, \beta_{\text{max}}], \end{aligned} \tag{6.6}$$

where the domain of integration in x comes from the ordering $\beta_1 > \beta_2$. The change of variable gives

$$\mathrm{d}x\mathrm{d}\beta = \begin{vmatrix} \frac{1}{\beta_2} & -\frac{x}{\beta_2} \\ \\ \frac{\beta}{2\beta_1} & \frac{\beta}{2\beta_2} \end{vmatrix} \mathrm{d}\beta_1 \mathrm{d}\beta_2, \tag{6.7}$$

where we used Eq. (6.6) and one has then

$$\frac{\mathrm{d}x}{x}\frac{\mathrm{d}\beta}{\beta} = \frac{\mathrm{d}\beta_1}{\beta_1}\frac{\mathrm{d}\beta_2}{\beta_2}. \tag{6.8}$$

The partonic cross section of Eq. (6.3) becomes

$$\begin{aligned} \mathrm{d}\sigma_{qq} = {} & \frac{1}{8\pi^6}\frac{N^2-1}{N^2}\frac{\alpha_s^2\alpha^4}{(\mathbf{k}_2^2)^2}\frac{\mathrm{d}\beta}{\beta}\frac{\mathrm{d}x}{x}\mathrm{d}^2\mathbf{k}_1\mathrm{d}^2\mathbf{k}_2\mathrm{d}^2\mathbf{k}_3 \\ & \times \int \frac{\mathrm{d}^2\mathbf{k}}{(\mathbf{k}+\mathbf{k}_1)^2(\mathbf{k}+\mathbf{k}_3)^2}\frac{\mathrm{d}^2\mathbf{k}'}{(\mathbf{k}'+\mathbf{k}_1)^2(\mathbf{k}'+\mathbf{k}_3)^2}, \end{aligned} \tag{6.9}$$

using the definition of the coupling $g^2 = 4\pi\alpha$. The hadronic cross section is obtained after multiplication with the impact factors, one for each proton in the process:

$$\begin{aligned} \mathrm{d}\sigma = {} & \frac{1}{8\pi^6}\frac{(N^2-1)}{N^2}\frac{\alpha_s^2\alpha^4}{(\mathbf{k}_2^2)^2}\frac{\mathrm{d}\beta}{\beta}\frac{\mathrm{d}x}{x}\mathrm{d}^2\mathbf{k}_1\mathrm{d}^2\mathbf{k}_2\mathrm{d}^2\mathbf{k}_3 \\ & \times \int \mathrm{d}^2\mathbf{k}\frac{\Phi\left(\mathbf{k}, -(\mathbf{k}+\mathbf{k}_1)\right)\Phi\left(-\mathbf{k}, (\mathbf{k}+\mathbf{k}_3)\right)}{(\mathbf{k}+\mathbf{k}_1)^2(\mathbf{k}+\mathbf{k}_3)^2}\mathrm{d}^2\mathbf{k}'\frac{\Phi\left(\mathbf{k}', -(\mathbf{k}'+\mathbf{k}_1)\right)\Phi\left(-\mathbf{k}', (\mathbf{k}'+\mathbf{k}_3)\right)}{(\mathbf{k}'+\mathbf{k}_1)^2(\mathbf{k}'+\mathbf{k}_3)^2}. \end{aligned} \tag{6.10}$$

To make an estimate of this, the dimensionless quantity

$$\langle\Phi^4\rangle = \frac{1}{\pi^4}\int \mathrm{d}^2\mathbf{k}_1\mathrm{d}^2\mathbf{k}_3\left[\int \mathrm{d}^2\mathbf{k}\frac{\Phi\left(\mathbf{k}, -(\mathbf{k}+\mathbf{k}_1)\right)\Phi\left(-\mathbf{k}, (\mathbf{k}+\mathbf{k}_3)\right)}{(\mathbf{k}+\mathbf{k}_1)^2(\mathbf{k}+\mathbf{k}_3)^2}\right]^2, \tag{6.11}$$

is introduced and the expression simplifies to

$$\mathrm{d}\sigma = \frac{1}{8\pi^2}\frac{(N^2-1)}{N^2}\alpha_s^2\alpha^4\int\frac{\mathrm{d}\beta}{\beta}\frac{\mathrm{d}x}{x}\int\frac{\mathrm{d}^2\mathbf{k}_2}{(\mathbf{k}_2^2)^2}\langle\Phi^4\rangle. \tag{6.12}$$

In the case of a simple impact factor that doesn't depend on the longitudinal fraction of momentum, the longitudinal integral over x and β reduces to integration over the whole phase space and one has

$$\begin{aligned} \mathrm{d}\sigma &= \frac{1}{8\pi^6}\frac{(N^2-1)}{N^2}\alpha_s^2\alpha^4 \int_{\beta_{\min}}^{\beta_{\max}} \frac{\mathrm{d}\beta}{\beta} \int_1^{x_{\max}} \frac{\mathrm{d}x}{x} \int \frac{\mathrm{d}^2\mathbf{k}_2}{(\mathbf{k}_2^2)^2}\langle\Phi^4\rangle \\ &= \frac{1}{8\pi^6}\frac{(N^2-1)}{N^2}\alpha_s^2\alpha^4 \left[\log\left(\frac{\beta_{\max}}{\beta_{\min}}\right)\log(x_{\max})\right] \int \frac{\mathrm{d}^2\mathbf{k}_2}{(\mathbf{k}_2^2)^2}\langle\Phi^4\rangle, \end{aligned} \tag{6.13}$$

while the last integral over $\mathbf{k}_2^2$, if $\mathbf{k}_2^2 > \mathbf{k}_{2,min}^2$, is

$$\begin{aligned} \int \frac{\mathrm{d}^2\mathbf{k}_2}{(\mathbf{k}_2^2)^2} &= \int_0^{2\pi}\int_{\mathbf{k}_{2,min}^2}^{s} \frac{\mathrm{d}\theta \mathrm{d}\mathbf{k}_2^2}{2}\frac{1}{(\mathbf{k}_2^2)^2} \\ &= -\pi\frac{1}{s} + \pi\frac{1}{\mathbf{k}_{2,min}^2} \\ &\simeq \pi\frac{1}{\mathbf{k}_{2,min}^2}, \end{aligned} \tag{6.14}$$

in the large-s limit. Hence, the cross section becomes

$$\mathrm{d}\sigma \simeq \frac{1}{9\pi}\alpha_s^2\alpha^4\frac{1}{\mathbf{k}_{2,min}^2}\left[\log\left(\frac{\beta_{\max}}{\beta_{\min}}\right)\log(x_{\max})\right]\langle\Phi^4\rangle, \tag{6.15}$$

and one needs to know the value of the different quantities. The limits on β and x are difficult to estimate in our kinematics but they can actually be extracted from their distributions in the numerical calculation and one obtains

$$\log\left(\frac{\beta_{\max}}{\beta_{\min}}\right)\log(x_{\max}) \simeq \mathcal{O}(30). \tag{6.16}$$

Now, the next step is the evaluation of $\langle\Phi^4\rangle$, which is an intrinsically soft quantity but can be related to the elastic cross section in the same approximation, that is

$$\sigma_{el} = \frac{4\alpha^4}{81\pi^2}\int \mathrm{d}^2\mathbf{k}_1\left[\int\frac{\mathrm{d}^2\mathbf{k}}{\mathbf{k}^2(\mathbf{k}+\mathbf{k}_1)^2}\times\Phi^2(\mathbf{k},-(\mathbf{k}+\mathbf{k}_1))\right]^2. \tag{6.17}$$

This expression is close to Eq. (6.11) and in particular, one can assume in both cases that the strongest $\mathbf{k}_1$ dependence comes from the exponential factor

$$\Phi \propto e^{-\frac{1}{2}B\,|t|}\,\mathrm{f}(\mathbf{k}). \tag{6.18}$$

Consequently, because here $|t| = \mathbf{k}_1^2$ and $\mathbf{k}_1^2$ is small, one has to compute

$$\begin{aligned} \sigma_{el} &\simeq \frac{4\alpha^4}{81\pi^2}\int \mathrm{d}^2\mathbf{k}_1\left[\int\frac{\mathrm{d}^2\mathbf{k}}{\mathbf{k}^4}\times e^{-B\mathbf{k}_1^2}\Phi^2(\mathbf{k},-\mathbf{k})\right]^2 \\ &= \frac{2\alpha^4}{81\pi^2}\frac{\pi}{B}\left[\int\frac{\mathrm{d}^2\mathbf{k}}{\mathbf{k}^4}\Phi^2(\mathbf{k},-\mathbf{k})\right]^2 \\ &= \frac{2\alpha^4}{81\pi B}\left[\int\frac{\mathrm{d}^2\mathbf{k}}{\mathbf{k}^4}\Phi^2(\mathbf{k},-\mathbf{k})\right]^2. \end{aligned} \tag{6.19}$$

Similar approximations lead to

$$
\begin{aligned}
\langle\Phi^4\rangle &\simeq \frac{1}{\pi^4}\int \mathrm{d}^2\mathbf{k}_1\mathrm{d}^2\mathbf{k}_3\left[\int \mathrm{d}^2\mathbf{k}\frac{e^{-\frac{1}{2}B\mathbf{k}_1^2}\Phi\left(\mathbf{k},-\mathbf{k}\right)e^{-\frac{1}{2}B\mathbf{k}_3^2}\Phi\left(-\mathbf{k},\mathbf{k}\right)}{\mathbf{k}^2\mathbf{k}^2}\right]^2 \\
&= \frac{1}{\pi^2B^2}\left[\int\frac{\mathrm{d}^2\mathbf{k}}{\mathbf{k}^4}\Phi^2(\mathbf{k},-\mathbf{k})\right]^2.
\end{aligned}
\tag{6.20}
$$

Hence, one has

$$\alpha^4\langle\Phi^4\rangle = \frac{81\sigma_{el}}{2\pi B}. \tag{6.21}$$

The elastic cross section at TeVatron energy is 19.7 mb [138] and the corresponding proton slope $B \sim 4$ GeV^2 leads to

$$\alpha^4\langle\Phi^4\rangle \simeq \mathcal{O}(60), \tag{6.22}$$

that itself leads to an estimation for the quasi-elastic dijet cross section at the hadronic level using Eq. (6.15) which is now

$$\mathrm{d}\sigma \simeq \frac{9\sigma_{el}}{2\pi^2B}\alpha_s^2\frac{1}{\mathbf{k}^2_{2,min}}\left[\log\left(\frac{\beta_{\max}}{\beta_{\min}}\right)\log(x_{\max})\right]. \tag{6.23}$$

For $|\mathbf{k}_{2,\mathrm{min}}| = 10$ GeV and $\alpha_s^2 = 0.04$, it gives roughly $\sigma \simeq 10$ μb.

By comparing this result with the CDF data for which the cross section is about 1 nb at $E_\perp^{\mathrm{min}} > 10$ GeV, one can directly note that it is three order of magnitude beyond. This indicates that the Sudakov suppression indeed plays a crucial role. In Sec. 4.2.3, we have estimated it to be of the order of 8.10^{-3} in the double-log approximation. If one adds the shift in $E_\perp^{\mathrm{min}}$ from the splash-out of Sec. 5.2 and the gap survival, it brings back our estimate of the cross section of about 10 nb in rough agreement with data.

6.2 Numerical Implementation

The calculation of the dijet quasi-elastic cross section cannot be done analytically if one wants to include all the corrections and preserve the exact transverse kinematics. In particular, one has to compute 11 different integrals. The choice was made to use a Monte-Carlo integration that is more or less the only way to perform this number of integrals in a finite time.

Hence, the integration over each variable is done by Vegas [139], a dedicated program for multi-dimensional integration. The idea behind the Monte-Carlo technique is to distribute randomly the n integration variables between their limits and compute the integrand at each of these random points. After that, a sum over the weighted averages is computed and from iteration to iteration, the increments size for each variables is adjusted to concentrate in the region where the integrand is the largest. Hence, Vegas changes the density of points, and the weight of the integrand, until the desired precision is reached. The main point is that the set of n points forms a distribution of the integration variables and if those variables are related to physical quantities, *i.e.* components of the four-momenta, rapidity, etc, one is left with a fully-defined high-energy event at each step.
The structure of the code is then simple, one starts with the parton-level calculation to which one adds the corrections to compute the cross section. Each step of Vegas defines a complete set of four-momenta for the final particles and then the numerical calculation behaves exactly as an event generator with all its possible advantages. Firstly there is the possibility to apply the

kinematical cuts of the CDF analysis to reproduce exactly the conditions of the measurement and consequently, to obtain a correct comparison between theory and data. Secondly, one can produce distributions over several quantities and this is useful to test the accuracy of the result as well as to control the numerical calculation. In addition, one has the possibility to interface the calculation with a hadronization code such as Pythia[1], jet algorithms or a full detector-response simulation.

In one picture, the structure of the code is represented in Fig. 6.1.

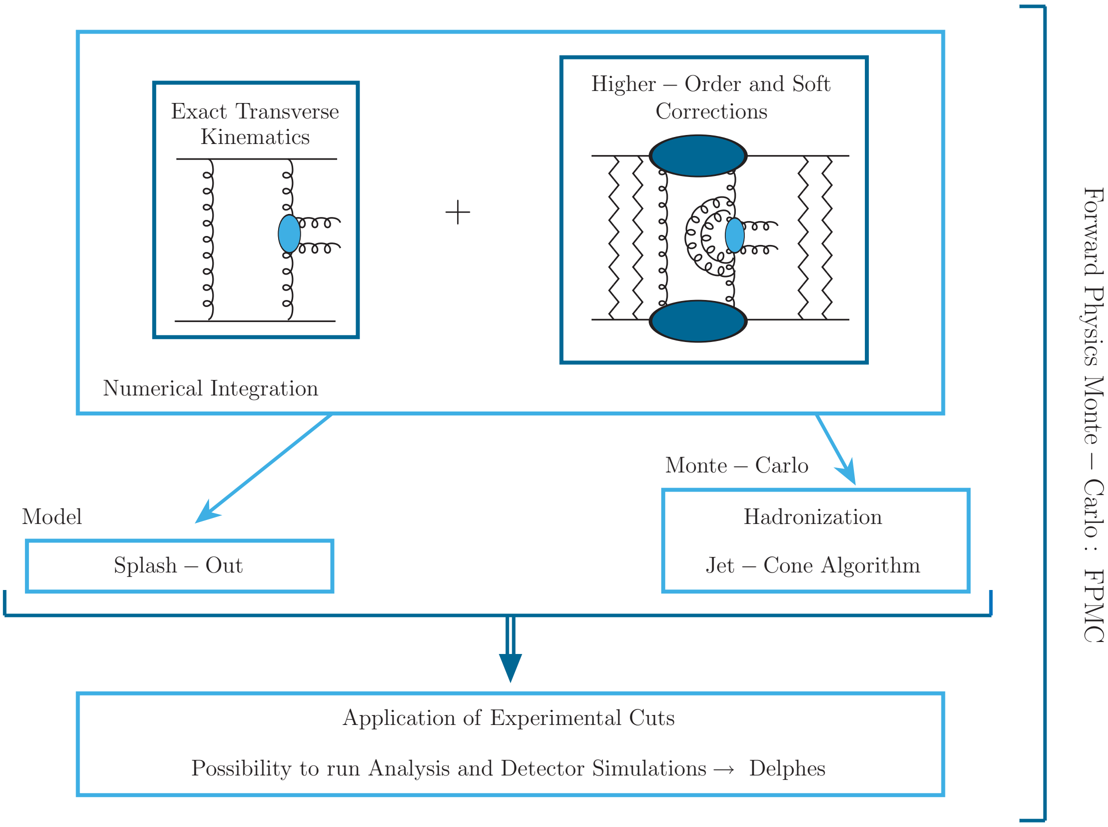

Figure 6.1: Structure of the code. The whole framework is implemented in FPMC, a Monte-Carlo for forward physics under the name of the CHIDe model.

6.3 Presentation of the Numerical Results

Traveling across the previous chapters has already introduced some of the main results and curves and, in particular, has demonstrated the sensitivity of the final answer to the different parameters of the calculation. Here, we would like to summarise those results and show how it is possible to use the CDF data to narrow down the uncertainties. Because the data are an essential part of this study, we shall start with a short description that will be followed by the presentation of our reference parametrisation and of the corresponding evaluation of the uncertainties.

---

[1] Note that in FPMC the hadronization is performed by HERWIG.

6.3.1 CDF Run II Data

Dijet quasi-elastic data were published in 2008 and are the result of 5 years of data taking during the Run II of the TeVatron $\bar{p}p$ collider. The energy in the center-of-mass frame was $\sqrt{s} = 1.96$ TeV and events were collected by the upgraded CDF II detector [57].

Quasi-elastic events are selected by requesting the presence of at least two jets with transverse energy $E_\perp^{\rm min} > 10$ GeV within the rapidity region $|\eta| < 2.5$. They are reconstructed with the CDF Midpoint algorithm using a cone radius of 0.7 in the η/ϕ space and the transverse energy $E_\perp$ of the jet is defined as the sum of the $E_\perp^i$ of the clustered calorimeter towers. One of the main difficulties is to extract the quasi-elastic signal from the other kinds of dijet productions, *i.e.* inclusive, single diffractive and non diffractive. The CDF detector only possesses Roman pot stations downstream in the antiproton direction and can only trigger final antiprotons. So, the strategy developed for the analysis is to look at the dijet mass fraction distribution of the full data sample with

$$R_{jj} = \frac{M_{jj}}{M_x}, \tag{6.24}$$

where M_{jj} is the mass of the dijet system and M_x the invariant mass of the sum of the four-momenta of all objects in the final state, proton and antiproton excluded. The idea is to measure the distribution and search for an excess of events at high R_{jj}, which exceeds the expectation of the POMWIG Monte-Carlo simulation [140] of dijet production in double pomeron exchange (DPE), which in fact doesn't simulate quasi-elastic processes. Obviously, the kind of event we are interested in is expected to have a mass fraction distribution peaked at large R_{jj} as the only two jets produced in the final state should carry, up to the splash-out correction, the total produced mass.

From the complete sample of dijet produced in double-pomeron exchange, the event has to pass a series of cuts that are chosen to enhance the quasi-elastic signal. There are four cuts, respectively on the transverse energy of the two jets, on their rapidity, on the size of the gap and on the momentum lost by the antiproton tagged in Roman pots. The values of the different cuts are given in Table 6.1 and one should note that they are not symmetric as only the antiproton longitudinal loss of momentum is measured. In addition, a third jet veto is applied that allows the presence of extra jets only if their energies are smaller than 5 GeV. The outcome for the dijet mass distribution of [57] shows an excess of events compared to the POMWIG prediction. This excess is well reproduced within the statistical uncertainties by the ExHume Monte-Carlo for quasi-elastic dijet production. POMWIG populates the low-R_{jj} region and ExHume events are at large R_{jj}, but this second distribution exhibits a long tail extending toward small-R_{jj} values due to gluon radiation. The issue is that one has to trust the Monte-Carlo simulation in order to extract the quasi-elastic data in the region of small dijet mass fraction and it introduces some uncertainties on the result. The CDF collaboration exploits the fact that the rapidity distribu-

Parameter	**Range**
$E_\perp^{\rm jet1,2}$	$> E_\perp^{\rm min}$
$\lvert\eta^{\rm jet1,2}\rvert$	< 2.5
$\lvert\eta_{\rm gap} \simeq \lvert\eta^{\rm p} - \eta^{\rm jj}\rvert$	>3.6
$(\alpha_1 + \alpha_2)$	$0.03 < (\alpha_1 + \alpha_2) < 0.08$
$E_\perp^{\rm ji>3}$	< 5 GeV

Table 6.1: Experimental cuts for CDF Run II data [57].

tion of inclusive dijet events is more symmetric around $\eta^{\mathrm{jet}1,2} = 0$ than the quasi-elastic one. Moreover, the cut on α introduces an asymmetry in the collision and boosts the dijet system toward negative rapidity values for quasi-elastic events only. These kinematical properties were used to improve the analysis. One can show the origin of this effect starting with the definition of the longitudinal momentum lost by the antiproton $(\alpha_1+\alpha_2)$, that in the kinematics of Chap. 2 is calculated from

$$\alpha_1 = \frac{(\mathbf{k}_1 - \mathbf{k}_2)^2}{\beta_1 s}, \quad \alpha_2 = \frac{(\mathbf{k}_2 - \mathbf{k}_3)^2}{\beta_2 s}, \tag{6.25}$$

and gives

$$\begin{aligned} \alpha_1 + \alpha_2 &= \frac{\beta_2(\mathbf{k}_1 - \mathbf{k}_2)^2 + \beta_1(\mathbf{k}_2 - \mathbf{k}_3)^2}{\beta_2\beta_1 s} \\ &\simeq \frac{(\beta_2 + \beta_1)\mathbf{k}_2^2}{\beta_2\beta_1 s} \\ &\simeq \frac{s_{gg}}{(\beta_1 + \beta_2)s}, \end{aligned} \tag{6.26}$$

using Eq. (2.76). One can evaluate the maximum and minimum of the longitudinal momentum lost by the proton $(\beta_1 + \beta_2)$ assuming that $s_{gg} \simeq 4E^2_{\mathrm{min},\perp}$ at the TeVatron energy of $\sqrt{s} = 1960$ GeV, to get

$$(\beta_1 + \beta_2)_{\mathrm{max}} \simeq \frac{s_{gg}}{s}\frac{1}{(\alpha_1 + \alpha_2)_{\mathrm{max}}} \simeq 0.0012. \tag{6.27}$$

Given the bounds of Table 6.1 one has $(\beta_1+\beta_2) < (\alpha_1+\alpha_2)$ and the rapidity of the dijet system

$$\eta_{jj} = \frac{1}{2}\log\left(\frac{\beta_1 + \beta_2}{\alpha_1 + \alpha_2}\right), \tag{6.28}$$

is negative. The data were then divided in the data sample A, for which at least one of the two leading jets has $\eta^{\mathrm{jet}1,2} < -0.5$ and contains most of the quasi-elastic events while data sample B with $\eta^{\mathrm{jet}1,2} > -0.5$ includes predominantly background.

We have shown the result of the CDF analysis in Fig. 1.12. We shall now tune the different parameters of our model to reproduce it. In order to compare the same quantities, we applied the same cuts as those of Table 6.1 and the accuracy of the result can be tested by producing some of the distributions shown in the CDF paper.

6.3.2 Choice of Parametrisation

Using those CDF measurements, one can choose among the different parametrisations of the dijet quasi-elastic cross section, one that gives a curve going through the data points. We stress that it is not a prediction but only an accurate parametrisation. From this particular curve, one can now study the effect of a change in the parametrisation and evaluate the theoretical uncertainties that affect the calculation. In addition, the reference parametrisation is the basis used to extrapolate our result to LHC energies or to predict the Higgs boson quasi-elastic cross section.

The available parameters come in the impact factor, the Sudakov form factor, the gap survival and the splash-out. Each ingredient was described in details and some prescriptions were ruled out either for theoretical reasons or for total incompatibility with the data. Consequently, the free parameters left are

- Impact factor: Type of the Φ_{UgD}, *i.e.* Fit: 1, 2, 3 or 4,
- Sudakov Form factor: Upper limit μ, Lower limit ℓ,
- Gap survival: $\langle S^2 \rangle$ between 5% and 15%,
- Splash-out: Three different prescriptions.

The complete parametrisation of the reference curve shown in Fig. 1.12 is given in Table 6.2 and is obtained after the application of the restrictions of Table 6.1. Without cuts, one has the curve of Fig. 6.2.a that is about 3.5 times bigger. Using FPMC[2], one can study more precisely the

Parameter	**Value**	**Reference**
- General		
Λ_{QCD}	0.20 GeV	
- Impact factor		
Φ_{UgD}	Fit-4	Sec. 3.3
- Sudakov form factor		
Exponentiation	$\log^2 + \log$+constant	Sec. 4.2.2
Δ	$\lvert\mathbf{q}\rvert/\mu$	angular ordering in Sec. 4.1
Coupling constant	Running with $\mathbf{k}_2^2$	
Upper scale	$\mu^2 = 2\mathbf{k}_2^2$	Sec. 4.2.1
Lower scale	$\ell^2 = 2(\mathbf{k}+\mathbf{k}_i)^2$	Sec. 4.2.1
- Gap-Survival Probability		
$\langle S^2 \rangle$	15%	Sec. 5.1
- Splash-Out		
$E_\perp^{\text{jet}}$	$0.75 E_\perp^{\text{parton}}$	Sec. 5.2

Table 6.2: Parameters of the reference curve of Fig. 1.12.

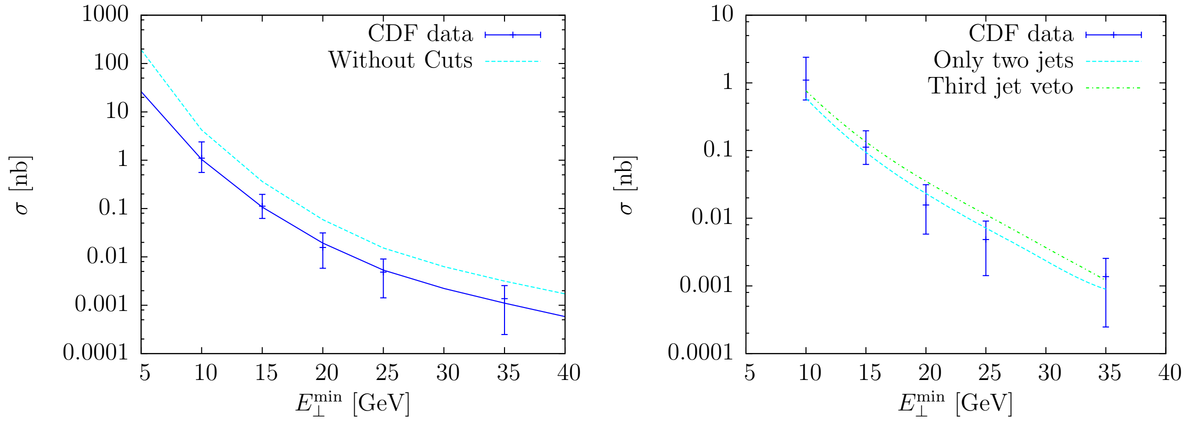

(a) (b)

Figure 6.2: The effect of CDF kinematical cuts. (a) The plain curve is again the reference and the higher curve is obtained by removing all cuts. (b) The effect of allowing only two leading jets in the final state or any number of additional jets if $E_\perp^{\text{jet}_{i>3}} < 5$ GeV. This last plot was obtained using FPMC with exactly the same parameters as for the reference curve.

effect of the experimental analysis and in particular of the third jet veto. In Fig. 6.2.b, one can note the importance of this additional constraint as the two curves show the difference between restricting the analysis to two jets or allowing for any number of extra jets with $E_\perp^{\mathrm{jet}_{i>3}} < 5$ GeV. This veto changes the cross section by a factor 0.8 and the application of the cone algorithm smoothes the curvature.

The question of other distributions is interesting as we can check the coherence of the model with the data. As an example, Fig. 6.3 shows two distributions similar to those of the CDF paper, namely the R_{jj} distribution and the mean jet-rapidity distribution. One can also have a look at the assumption of negative rapidity for the dijet system due to cuts used, and beside one can check the effect of the choice of the scale in the Sudakov form factor on this assumption. In the analysis, the rapidity space was divided into four regions, shown in Fig. 6.4, depending on the rapidity of the leading and second jet. According to ExHume, the region where both η_{j1} and η_{j2} are smaller than -0.5 is dominated by the quasi-elastic signal while the region with $\eta_{j1}, \eta_{j2} < -0.5$ contains few quasi-elastic events. One can evaluate the cross section in each of the four regions and compute the ratio between the two. For the reference parametrisation and $E_\perp^{\min}$ >10 GeV, one has

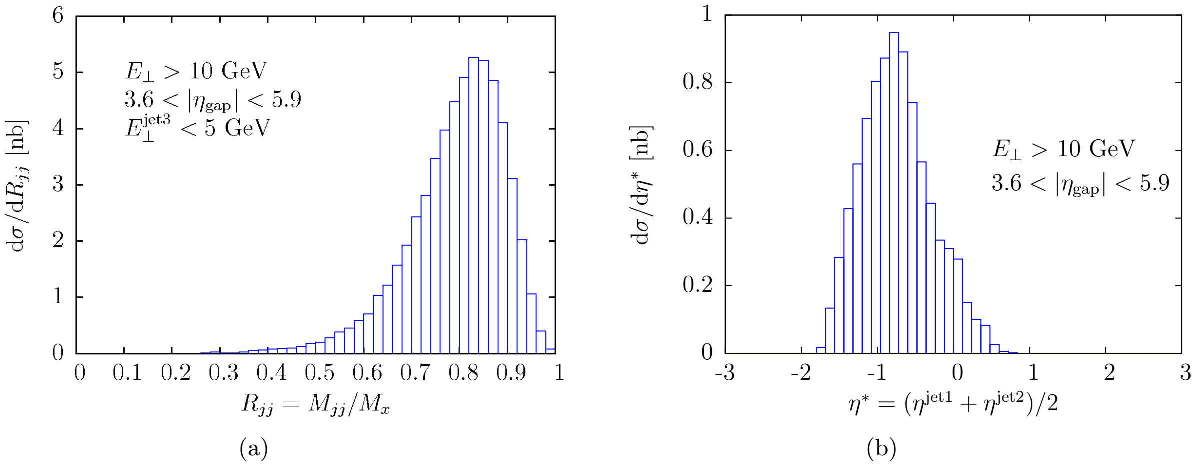

Figure 6.3: (a) Dijet mass fraction. (b) Mean jets rapidity distribution.

$$\frac{R_B}{R_A} = 0.65. \tag{6.29}$$

Here, let us remind the reader that the upper scale of the Sudakov form factor is $2\mathbf{k}_2^2$ whereas in ExHume it is $\mu = 0.62\sqrt{s_{gg}}$. In fact, using this very scale in our calculation together with parameters that fit the data, we obtain

$$\left.\frac{R_B}{R_A}\right|_{\mu=0.62\sqrt{s_{gg}}} = 0.45, \tag{6.30}$$

that is slighty different. Once again here, a more detail data analysis of this particularity and new results from LHC should help to settle the issue of the Sudakov form factor upper limit. The choice made for the parametrisation of the reference curve is not unique and one could have

---

[2] The parton-level calculation in FPMC is identical to the parton-level calculation in the code used for the thesis so that the two results are in agreement to better than 1%. The small difference is from the method of integration as one uses VEGAS while FPMC uses a traditional Monte-Carlo integration with a smaller precision.

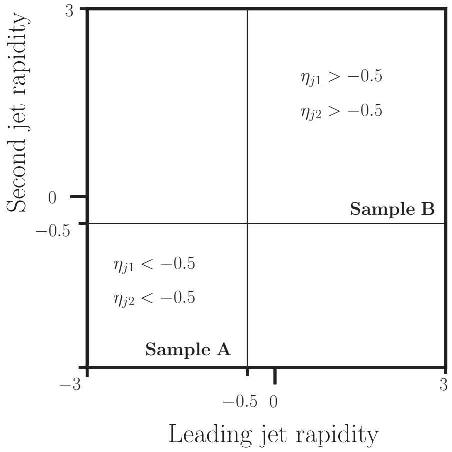

Figure 6.4: Division of the rapidity space in four different regions depending on the rapidity of the leading and second jet. According to ExHume, the region where both η_{j1} and η_{j2} are smaller than -0.5 is dominated by the quasi-elastic signal while the region with $\eta_{j1}, \eta_{j2} > -0.5$ contains few quasi-elastic events.

found another set of parameters that gives a curve in agreement with the data. By changing only the type of Φ_{UgD}, μ, ℓ and $\langle S^2 \rangle$, it is possible to obtain the curves of Fig. 6.5 that are

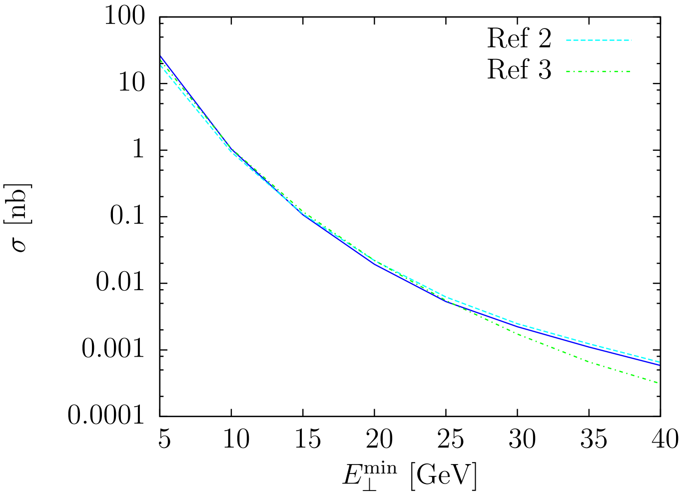

Figure 6.5: Two different sets of parameters that also give a curve in agreement with the data. The corresponding parametrisations can be found in Appendix B.5.

similar to the reference curve. One will see what happens to these curves after the extrapolation to LHC but we first summarise the uncertainties.

6.3.3 Uncertainties

The full uncertainty, based on the reasonable theoretical choices described in this thesis, is shown in Fig. 6.6.a. Restricting the model with the TeVatron data considerably reduces the uncertainty and one is left with the band of Fig. 6.6.b that is still affected by an uncertainty of 2 order of magnitude at high transverse energy.

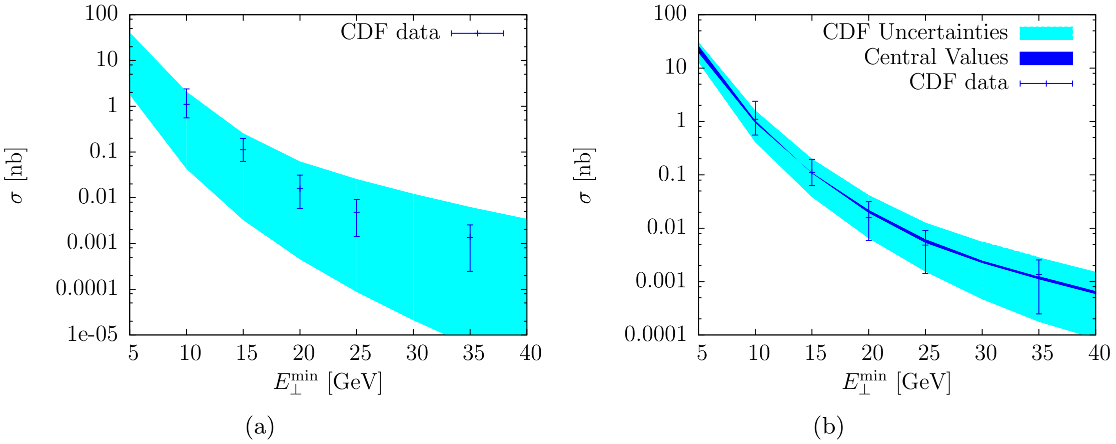

Figure 6.6: (a) Several reasonable parametrisations of ingredients for dijet quasi-elastic calculation and the resulting estimations of the cross section. (b) Restriction of the model using the TeVatron data. The different parametrisations are given in Appendix B.5.

Due to the choice of the intrinsic parameters, each ingredient of the calculation can change the final result, and those factors are summarised:

Ingredient	**Uncertainty**
Impact Factor	3
Sudakov form factor	10
Gap survival	3
Splash-out	1.5

Three remarks are in order and underline the fact that the evaluation of the total error is ambiguous. Firstly, a change in one parameter can be compensated by a change in another. Secondly, the sensitivity depends on the considered parameter, for instance the calculation is particularly sensitive to the parametrisation of the Sudakov form factor but only in the low-energy region. Taking that into account, we don't want to give a number that could be misinterpreted and conclude this section by saying that the uncertainty on the dijet quasi-elastic calculation is large.

6.4 Extrapolation to the LHC

The formulae derived for the dijet quasi-elastic cross section can be equally used to estimate the dijet cross section at the LHC.

The obvious change from the TeVatron to the LHC comes from the kinematical cuts as LHC detectors are different from those of the TeVatron. In particular, LHC detectors may have a better forward instrumentation, with the addition of the very forward detectors RP220 and FP420 in ATLAS and CMS, one might have the largest rapidity coverage ever. Specific cuts will be used to search for diffractive events and they are given in Table 6.3, assuming the presence of both RP220 and FP420. Note that without them, quasi-elastic events cannot be measured by proton tagging as final protons are outside the rapidity coverage of the central detector.

Parameter	**Range**
$\lvert\eta^{\text{jet1,2}}\rvert$	< 1
$(\alpha_1 + \alpha_2)$	$0.002 < (\alpha_1 + \alpha_2) < 0.2$
$(\beta_1 + \beta_2)$	$0.002 < (\beta_1 + \beta_2) < 0.2$

Table 6.3: Experimental cuts [72] for the LHC multi-purpose detectors ATLAS and CMS including the very forward detectors RP220 and FP420.

One also has to extrapolate the proton impact factor to LHC energies where the emitted gluons would have a smaller longitudinal fraction of momentum, which is easy as the impact factor built in Chap. 3 already includes a dependence in the center-of-mass frame energy. There is also the question of the gap-survival probability for which the extrapolation to LHC is model-dependent. For this estimate, we have decided to use the prescription

$$\langle S^2\rangle\Big|_{\text{LHC}} = \frac{1}{2}\langle S^2\rangle\Big|_{\text{TeVatron}}. \tag{6.31}$$

Note that this is just an assumption, in agreement with [122].

Our prediction for the dijet quasi-elastic cross section at LHC is shown in Fig. 6.7 for an energy in the center-of-mass frame of 10 TeV with and without cuts. We show the 10 TeV curves because due to technical issues the LHC shouldn't reach 14 TeV before 2012. We nevertheless give the prediction for $\sqrt{s}$=14 TeV and $\sqrt{s}$=7 TeV with cuts in Fig. 6.8.

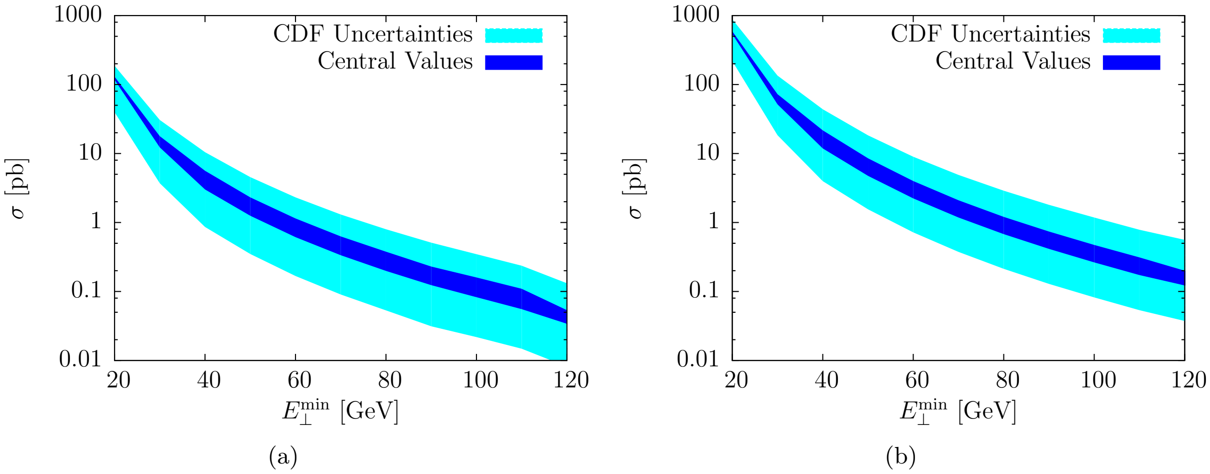

(a) (b)

Figure 6.7: (a) Dijet quasi-elastic cross section at the 10 TeV. The inner band corresponds to curves that reproduce the central values of the CDF data but slightly diverge at LHC energies, the outer band corresponds to the 1σ errors. (b) Same but without cuts.

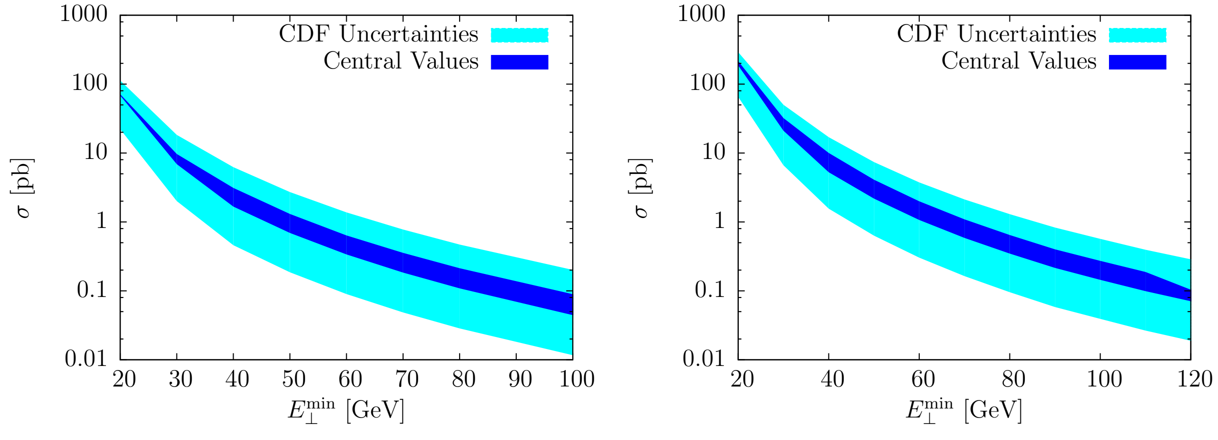

(a)

(b)

Figure 6.8: (a) Dijet quasi-elastic cross section at the 7 TeV and (b) dijet quasi-elastic cross section at the LHC (14 TeV). Both curves are obtained after the cuts of Table 6.3.

The results for the LHC tuned to the CDF data are unavoidably plagued by the same large uncertainties as those of the TeVatron and their range is indicated by the outer band. The inner band shows how different sets of parameters, tuned on the TeVatron data to reproduce the central values, diverge after extrapolation to the LHC. As for the TeVatron, one can check the importance of the non-perturbative region and the conclusion is confirmed that the gluon loop is still dominated by the soft region as shown in Table 6.4. One can also note an interesting feature of the calculation that makes the uncertainty on the upper limit in the Sudakov form factor vanish at large s and high $E_\perp^{\rm min}$. Fig. 6.9 illustrates the dominance of the Sudakov form factor double logs at large $E_\perp^{\rm min}$.

Experiment	$\mathbf{E}_T^{\rm min}$	$\sigma_{\rm pert}/\sigma$
LHC 14 TeV	50 GeV	55%
LHC 7 TeV	50 GeV	30%
LHC 10 TeV	50 GeV	45%
LHC 10 TeV	100 GeV	30%

Table 6.4: Ratio σ_{pert}/σ where σ_{pert} is the value of the cross section if all gluon transverse momenta are larger than 1 GeV. Different experiments and jet transverse minimum energies are presented but in all cases the parametrization is the one of the reference curve.

So, the data constrain the uncertainty at the LHC and allow for a better prediction of the quasi-elastic dijet cross section. However, the cross section presents the same characteristic as at the TeVatron, namely, a calculation dominated by the non-perturbative region and large uncertainties.

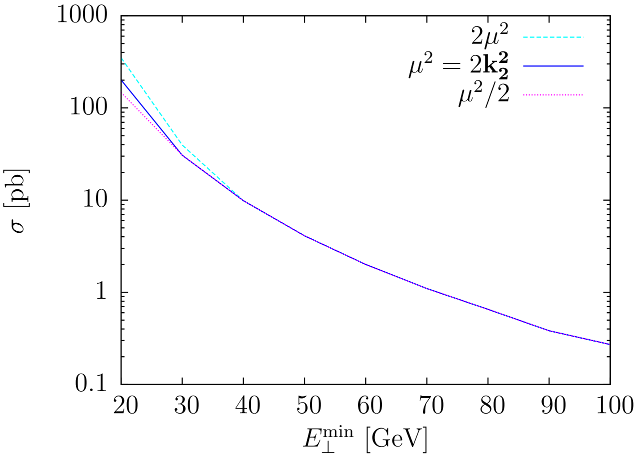

Figure 6.9: Results at the LHC for three different values of the upper limit in the Sudakov form factor: at large s and high $E_\perp^{\rm min}$ the uncertainty vanishes.

6.5 Conclusion

Our work was dedicated to the calculation of the dijet quasi-elastic cross section and to the evaluation of the theoretical uncertainties. We have described all the ingredients going into the calculation. In particular, we have kept an exact transverse kinematics and paid special attention to the higher-order corrections embodied by the introduction of the Sudakov form factor. We have shown that the result is plagued by large uncertainties that can be reduced using the recent CDF data.

The extrapolation to the LHC, for different possible energies, shows that the cross section is of the order of 2 pb at $\sqrt{s}$=10 TeV for jets of minimum transverse energy 50 GeV. Under the present assumptions, one then can be confident in the fact that quasi-elastic dijet should be seen. Note however that in the worst-case scenario, the gap survival is zero and quasi-elastic cross sections vanish, destroying in the same time the hope for all other high-mass quasi-elastic processes. Early dijet measurements at LHC are then crucial and the first data will give information on gap survival. If the cross section survives, then new measurements will help to narrow down the uncertainty.

Part II

Higgs Boson Quasi-Elastic Production

“How doth the little crocodile
Improve his shining tail,
And pour the waters of the Nile
On very golden scale!
How cheerfully he seems to grin,
How neatly spread his claws,
And welcome little fishes in
With gently smiling jaws!”

Alice’s Adventures in Wonderland,
Lewis Carrol

One of the interesting features of quasi-elastic production is that the structure of the calculation remains the same in all kinds of production. Consequently, the main idea of the thesis is to keep the parametrisations tuned to the CDF dijet data to predict the Higgs boson quasi-elastic cross section at the LHC. This choice is not innocent as the Higgs boson is the last particle of the Standard Model not yet detected experimentally, and without it, the theory is not complete. One can then guess that the Higgs boson hunt is one of the most exciting questions today. Up to now, the Higgs boson has escaped all its hunters although at LEP during the last runs, physicists have thought they had observed a signal for it but they had to make space for the building of LHC before any convincing evidence. A new machine is now ready to resume the search but, with the tremendous energy available, the Higgs boson signature may remain completely hidden in the background of old and new processes for a long time, and this is where quasi-elastic production may matter.

Quasi-elastic cross sections for the production of the Higgs boson or any other heavy particles are small. Nevertheless, those events have two very clear signatures, the rapidity gap and the remaining protons in the final state. Besides, with the appropriate detectors, it will be possible to reconstruct the mass of the centrally-produced system from the measurement of the missing mass of the final protons. Consequently, the clean signature is the key point that makes quasi-elastic production a competitive discovery channel at LHC energies. From the theoretical point of view, the situation is complicated as large uncertainties affect the calculation and the soft physics that enters the process is not fully under theoretical control. However, we have determined a set of parametrisations that reproduces the CDF data. Using the fact that the topology of the dijet diagram, shown schematically in Fig. 6.10.a, is the same as that of the Higgs diagram shown in Fig. 6.10.b, these parametrisations can be used to predict the Higgs boson production cross section.

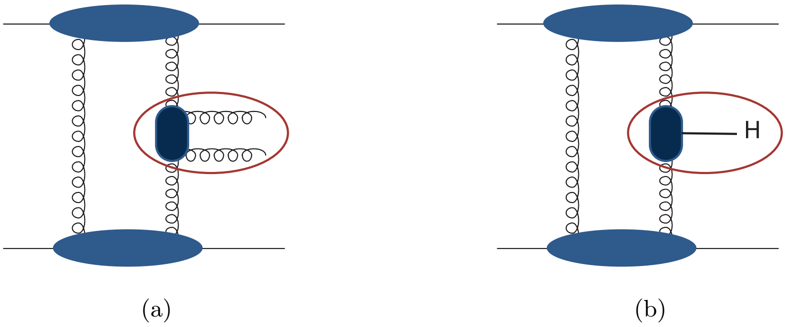

(a) (b)

Figure 6.10: Topology of the quasi-elastic production for (a) dijet and (b) Higgs boson. Apart from the hard subprocess, the topology is identical, so that the soft pieces.

In the first chapter, we shall briefly review the Higgs boson modes of production and present the Durham model which is the model closest to ours. In the second chapter, we discuss the calculation in the quasi-elastic regime but we focus only on the differences from the dijet calculation and on the effect of the parametrisation choices as the main ingredients were already described. Finally, we shall give a prediction for the Higgs boson quasi-elastic cross section at the LHC.

Chapter 7

Searching for the Higgs Boson

The search of the Higgs boson is an old quest but the idea of using the quasi-elastic channel for its discovery appeared 20 years ago [141]. It is now ready to be tested at the LHC using the current knowledge of the theoretical calculation and the possibility to use very forward detectors. Moreover, this kind of production is usually viewed as a golden channel due to the clear signature of the events. So, we show here why quasi-elastic Higgs boson production can be attractive from the experimental point of view.

7.1 Overview

At the LHC, the two dominant channels should be gluon and vector-boson fusion. In both cases, the final state is complicated and requests a careful analysis of the event in addition with powerful methods to tag the Higgs boson decay products to reconstruct its mass. Following [142, 143], we give here a brief summary of different inclusive cross sections and of their uncertainties.

7.1.1 Higgs-Boson Production in the Standard Model

The number of Higgs boson production mechanisms in the SM that lead to a sizable cross section and detectable final states is quite small. One has the production by gluon-gluon fusion [144], by WW and ZZ fusion [145], by associated production with W and Z bosons [146, 147], by associated production with $t\bar{t}$ [148–151] and representative Feynman diagrams are shown in Fig. 7.1.

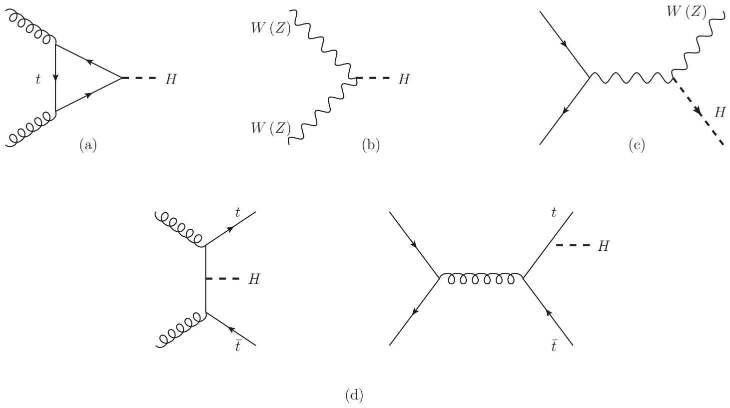

Figure 7.1: Representative diagrams of the main Higgs boson production mechanisms. (a) Gluon-gluon fusion, (b) vector boson fusion, (c) associated production with W and Z and (d) associated production with top pair quarks.

The corresponding cross sections as functions of the Higgs boson mass at $\sqrt{s}$=10 TeV are shown in Fig. 7.2 and one can directly note that gluon fusion is largely dominant in the whole considered mass range. The estimates for inclusive Higgs-boson cross sections at the LHC are from 10 pb up to 100 pb in the intermediate mass region for all modes of production combined and the main uncertainty is the knowledge of the gluon distribution at small x. According to [143], it is evaluated to be ±20% and the other source of error is the values of several input parameters as for example the top mass. Fortunately, corrections are now known for most of the processes and the parameters start to be more and more constrained due to precision measurements from LEP, the TeVatron and other experiments[1].

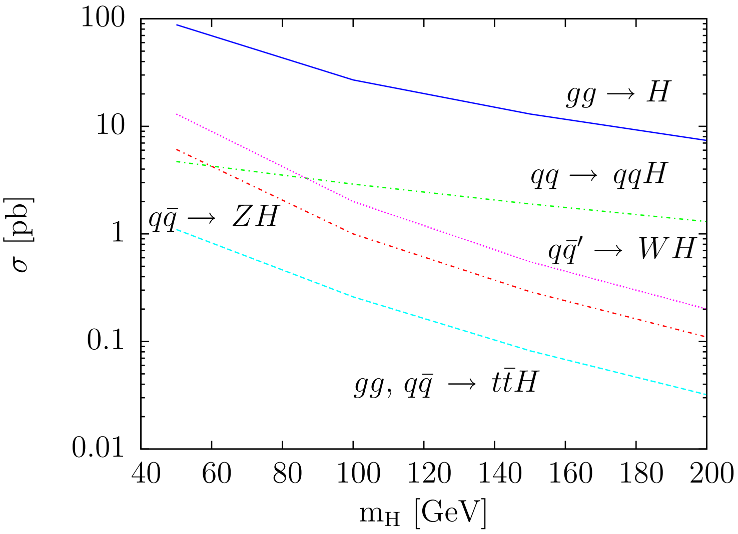

Figure 7.2: Total cross section for different production mechanisms at LHC 10 TeV. Adapted from [143].

The question to address is the possibility to reconstruct the Higgs boson from the particles observed in the detector. Actually, if one considers the LEP results [152] and the recent TeVatron data [153] that constrain the mass, the SM Higgs boson should have a mass beyond 114 GeV according to LEP and the TeVatron data excluded the mass region between 160 GeV and 170 GeV at the 95% confidence level[2]. Moreover, the few Higgs boson candidates observed at the end of the last run of the LEP collider [154] points to a light Higgs boson. In this case, as shown in Fig. 7.3 that presents the branching ratio of the SM Higgs boson as a function of its mass, the main decay channel is a pair of heavy quarks, $b\bar{b}$ and the observation of the resonance requests a good mass resolution in addition to a technique of flavour identification for the final jets. The background, constituted by processes with two b-jets in the final state is not small and according to reference [72], the signal-over-background ratio makes the dominant Higgs boson decay products almost invisible. In this domain of mass, it is hence easier to deal with associated productions that allow to trigger on the leptonic decay mode of the W or to look for rare decays, *i.e* purely leptonic or photonic final states, that have smaller branching fractions but recognizable signatures allowing for excellent mass resolution. All these scenarios were studied in great details by the LHC experiments and one should find in their technical reports [155, 156] the expectations as well as the evaluation of background not discussed here.

---

[1] A complete review of these as well as other processes in the Standard Model and beyond, can be found in [142].

[2] The region between 155 GeV and 180 GeV is also excluded but only at 65% confidence level.

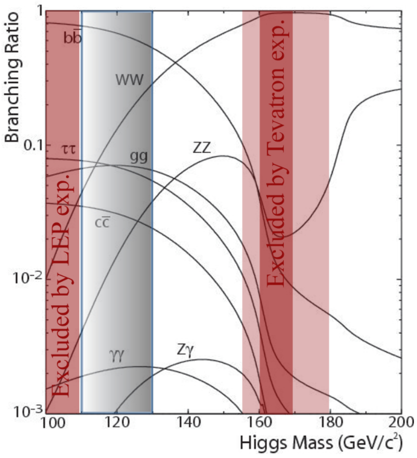

Figure 7.3: Branching ratio of the Higgs boson in the Standard Model as a function of the mass. Adapted from [138, 152, 153].

7.1.2 The Quasi-Elastic Mode

The issue is to track down the Higgs boson among the many particles produced in each collision. In comparison, quasi-elastic production has an unique and clear signature in addition to a high-quality mass reconstruction using the very forward detectors. The momenta of the two final protons may be measured very accurately in forward detectors and this leads to a simple estimate of the Higgs boson mass using the missing-mass technique described in Sec. 1.4.3 and Eq. (1.4). In the central region, the background is flat in rapidity and experimentalists should be able to separate the Higgs boson resonance peak with a ratio S/B of the order of 1 [72, 74]. The gap is also a typical and easily recognizable signature of this kind of production and all these properties point to a very clean channel of detection for the Higgs boson. Those advantages could be important in the Higgs boson hunt.

This challenge is big as the Higgs boson discovery (or its absence) will decide on the fate of high-energy physics. From the experimental point of view, quasi-elastic processes are competitive and provide a simple method of reconstruction if the dedicated forward detectors are built. From the theoretical point of view, the picture is complicated and this is mainly due to the uncertainties that are an obstacle to a precise prediction for the LHC. A lot of studies about quasi-elastic SM Higgs boson production have been made in the past and they have led to estimates that differ by several orders of magnitude. Those are summarised in Table 7.1. The

Reference	σ_{Higgs} **(fb)**	**Number of events** $\mathcal{L}$**=30 fb**$^{-1}$
Durham group [16, 17, 128]	1.4 - 3	90
Coughlin and Forshaw (KMR corrected) [20]	0.7 - 1.5	45
Bzdak [12, 13]	0.015	0.45
Soft Colour Interaction [8]	0.2	6
Saclay Hybrid Model [15]	1.1	33

Table 7.1: Several QCD calculations of the quasi-elastic cross section for a SM Higgs boson with a mass of 120 GeV at 14 TeV. The number of events at the LHC is calculated for an integrated luminosity equal to 30 fb^{-1}.

KMR model [16, 17, 128] from Durham is described in the next section while the Coughlin and Forshaw model [20] differs only by the limits used in the Sudakov form factor. The model used by Bzdak [12, 13] is based on the model for Higgs and dijet production by Bialas and Landshoff [84]. It includes the exchange of a pair of non-perturbative gluons, a dependence on the energy and the momentum transfer as well as a Sudakov form factor that gives the exclusive character of the process. After normalisation to the central inclusive production of dijet at the TeVatron, this model is consistent with the CDF data for double diffractive exclusive dijet production[3]. The soft colour interaction [8, 157] model is a Monte-Carlo method implemented in Pythia that allows additional soft interactions between the partons produced in the hard process or between the partons and the proton colour field. These interactions only change the colour configuration and lead to different hadronic final states. This is implemented by the introduction of a new parameter that accounts for the unknown non-perturbative dynamics phenomenologically determined from DIS data at the HERA collider. The particularity of this model is that it describes in the same framework diffractive and non-diffractive events where the formers are selected by the presence of a rapidity gap and a leading (anti)proton. The soft colour model is known to reproduce correctly the ratio of diffractive to non-diffractive events at the TeVatron, however, the value of the cross section is strongly sensitive to details in the model and in Pythia. Finally, the Saclay hybrid model is an exclusive model based on the exchange of an hybrid pomeron defined by a combination of one hard and one soft color exchange, the form of the soft and hard parts are fixed by the corresponding data or suitable parametrisations. Note that this model doesn't include a proper description of the impact factor, so that the normalisation is not fixed by the model. Nevertheless, it reproduces correctly the slope and properties of the dijet data.

7.2 The Durham Model

After the publication of the CDF dijet cross section, one model stayed, the one of Khoze, Martin and Ryskin or KMR model. We describe here its main lines, referring the reader to [16, 17, 158].

The cross section of the process represented schematically in Fig. 7.4, is assumed to factorize

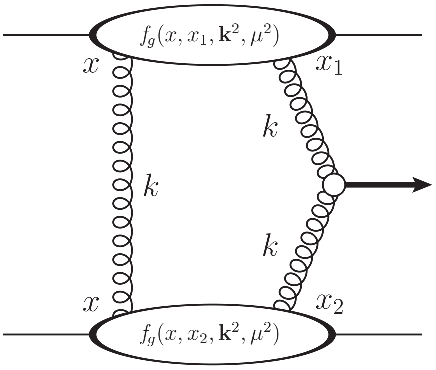

Figure 7.4: Schematic representation of the Higgs boson quasi-elastic amplitude.

between the effective luminosity $\mathcal{L}$ and the hard subprocess $\hat{\sigma}$, with

$$\sigma = \mathcal{L}\hat{\sigma}, \tag{7.1}$$

and in particular

---

[3] One should note that in 2005 the CDF Run II data weren't published.

$$\frac{\partial\sigma}{\partial s\partial y\partial\mathbf{P}^2\partial\mathbf{Q}^2} = S^2 e^{-B\left(\mathbf{P}^2+\mathbf{Q^2}\right)}\frac{\partial\mathcal{L}}{\partial s\partial y}\,\mathrm{d}\hat{\sigma}\left(gg\to H\right). \tag{7.2}$$

The different variables are the energy in the center-of-mass frame $\sqrt{s}$, the rapidity of the centrally produced system y and the transverse momenta of the final protons $\mathbf{P}$ and $\mathbf{Q}$. One can also recognise in turn the gap-survival probability S^2 and the logarithmic t-slope of the cross section $B = 4$ GeV^2, added by hand assuming that the dependence of the hard amplitude on final protons transverse momenta is small. The partonic cross section $\hat{\sigma}$ corresponds to the amplitude

$$\mathcal{M}(gg\to H) = \frac{1}{2}\frac{1}{N^2-1}\sum_{a,b}\sum_{\lambda_1,\lambda_2}\delta_{ab}\delta_{\lambda_1,\lambda_2}\mathcal{M}_{ab}^{\lambda_1,\lambda_2}(gg\to H). \tag{7.3}$$

The cross section to single-log accuracy is multiplied by a K factor of the order of 1.5, assumed to take into account next-to-leading-order corrections. The effective luminosity is given by

$$\frac{\partial\mathcal{L}}{\partial s\partial y} = \left(\frac{\pi}{(N_c^2-1)}\int\frac{\mathrm{d}\mathbf{k}^2}{\mathbf{k}^4}f_g\left(x,x_1,\mathbf{k}^2,\mu^2\right)f_g\left(x,x_2,\mathbf{k}^2,\mu^2\right)\right)^2. \tag{7.4}$$

The function f_g stands for the unintegrated skewed gluon density related to the conventional integrated gluon distribution function and taken here in the simplified form [117]

$$f_g\left(x,x_1,\mathbf{k}^2,\mu^2\right) = R_g\frac{\partial}{\partial\log\mathbf{k}^2}\left[\sqrt{T(\mathbf{k},\mu)}\,xg(x,\mathbf{k}^2)\right]. \tag{7.5}$$

The factor R_g accounts for the skeweness[4] and is found to be about 1.2 at the LHC energy of 14 TeV. One can note that the Sudakov form factor $T(\mathbf{k},\mu)$

$$T(\mathbf{k},\mu) = \exp\left[-\int_{\mathbf{k}^2}^{\mu^2}\frac{\mathrm{d}\mathbf{q}^2}{\mathbf{q}^2}\frac{\alpha_s\left(\mathbf{q}^2\right)}{2\pi}\int_0^{1-\Delta}\left(zP_{gg}+\sum_q P_{qg}(z)\right)\mathrm{d}z\right], \tag{7.6}$$

with $\mathbf{q}$ and z the transverse and longitudinal components of the additional emission, is here included in the differentiation. According to their next-to-leading order calculation [16, 17], the Durham group uses

$$\begin{aligned}\Delta &= \frac{\mathbf{q}}{\mathbf{q}+\mu},\\ \mu &= 0.62\,m_H.\end{aligned} \tag{7.7}$$

The definition of these two scales will be discussed below, following a recent re-evaluation by Coughlin and Forshaw [20]. In this model, it is the presence of the Sudakov form factor that makes the integration infra-red stable and it is claimed that consequently, perturbative QCD is applicable.

The Durham model has been developed for years and was the first to gather all the ingredients needed to reproduce the CDF data. It is one of the most complete models as it has been used to predict different types of quasi-elastic productions, from Higgs boson, dijet, $\gamma\gamma$, quark dijet, χ_c, … to supersymmetric particles, and as it gives results in agreement with the available data. It also investigates several aspects of the QCD calculation. One can note that our model is similar to the Durham model but differs from it in several ways presented in the following.

---

[4] The fact that $x \neq x_1$, $g(x,\mathbf{k}^2)$ is the gluon density $x = x_1$.

Chapter 8

Calculation

The basis of the calculation is the partonic subprocess $qq \to q+H+q$ and it corresponds exactly to the detailed calculation described in Sec. 2.1.2 for one-particle production in a colour-singlet exchange. Consequently, the reader will find here only the main lines of the Higgs calculation together with a new amplitude that will be described in details. In the first section, the effective vertex $gg \to H$ is evaluated, as well as the phase space available for the final Higgs boson. In the second section, one will find a brief description of the changes that have to be made in the higher-order corrections.

8.1 Higgs Boson Production at the Parton Level

As before, the parton-level calculation starts with the definition of the kinematics and variables used. As previously, we keep the exact transverse kinematics and we only compute here the diagram shown in Fig. 8.1. Note that the diagram in which the Higgs boson is emitted from the first gluon leg gives the same amplitude and one has to include a factor 2 to take it into account.

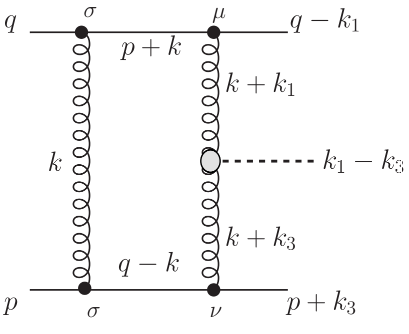

Figure 8.1: Kinematical conventions for the Higgs boson quasi-elastic production at the parton level.

First, one can assume that the initial quarks are massless with zero transverse momentum, their four-momenta are q^μ and p^μ with $s = 2p.q$. The momenta transferred from the quarks are k_1 and $-k_3$, respectively and the gluon momenta are written as functions of the incoming quarks momenta using a Sudakov decomposition. One has then

$$\begin{aligned} k_1^\mu &= \alpha_1 p^\mu + \beta_1 q^\mu + \mathbf{k}_1^\mu, \\ k_3^\mu &= \alpha_3 p^\mu + \beta_3 q^\mu + \mathbf{k}_3^\mu, \end{aligned} \tag{8.1}$$

where all transverse vectors are denoted in bold. The produced Higgs boson momentum is

$$k_H^\mu = (\alpha_1 - \alpha_3)p^\mu + (\beta_1 - \beta_3)q^\mu + (\mathbf{k}_1 - \mathbf{k}_3)^\mu. \tag{8.2}$$

In this description, the dominant kinematical region is where longitudinal components obey

$$1 \gg \alpha_i, \beta_i \gg \frac{|\mathbf{k}_i^2|}{s} \quad i = 1 \pm 3, \tag{8.3}$$

that corresponds to the quasi-elastic regime, with small momenta transferred from the initial particles. At lowest order, the amplitude reads

$$\mathcal{M} = g^4 C \int \mathrm{d}^2 k \frac{N^{\mu\nu}}{(k+k_1)^2 (k+k_3)^2 k^2} \times \mathcal{M}(gg \to H), \tag{8.4}$$

where g is the coupling constant between quarks and gluons, C=2/9 is the colour factor for the two-gluon exchange and $\mathcal{M}(gg \to H) = V_{\mu\nu}$ is the $gg \to H$ effective vertex. One can use the method developed in Sec. 2.1.2 to compute the longitudinal part of the integral and obtain

$$\mathcal{M} = g^4 \frac{C}{2(2\pi)^2 s} \int \mathrm{d}^2\mathbf{k} \frac{1}{(\mathbf{k}+\mathbf{k}_1)^2 (\mathbf{k}+\mathbf{k}_3)^2 \mathbf{k}^2} \times N^{\mu\nu} V_{\mu\nu}. \tag{8.5}$$

Now, the next difficulty is to evaluate the contraction of the vertex with the numerator and one first needs an expression for the effective vertex.

8.1.1 Higgs Boson Effective Vertex

In the Higgs case, the hard subprocess is the collision of two gluons that produce the Higgs boson via a triangle of quarks and it can be obtained by calculating the sum of the diagrams shown in Fig. 8.2. In the Standard Model, the coupling between the Higgs boson and quarks is proportional to the mass of the quarks so that the top contribution dominates and is the only one taken into account. The exact calculation was made in [14] and shows that the effective vertex can be written

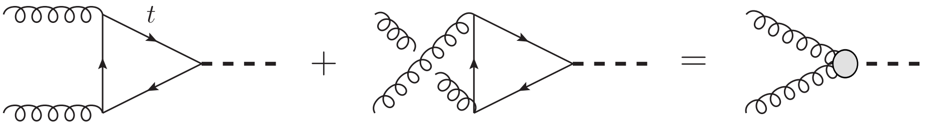

Figure 8.2: The gluon-gluon to Higgs boson hard subprocess. Because the coupling of the Higgs boson to quarks is proportional to their masses, the top quark contribution dominates.

$$\begin{aligned} V_{\mu\nu} = \delta^{ab} &\left[(k+k_1).(k+k_3)g^{\mu\nu} - (k+k_1)^\nu (k+k_3)^\mu\right] \frac{W_1}{m_H^2} \\ &+ \left[(k+k_1)^2 (k+k_3)^2 g^{\mu\nu} + (k+k_1)^\mu (k+k_3)^\nu (k+k_1).(k+k_3)\right. \\ &\left. -(k+k_1)^\mu (k+k_1)^\nu (k+k_3)^2 - (k+k_3)^\mu (k+k_3)^\nu (k+k_1)^2\right] \frac{W_2}{m_H^4}, \end{aligned} \tag{8.6}$$

where

$$W_1 = \frac{(\sqrt{2}G_f)^{1/2} g^2 m_H^2}{12\pi^2} N_1, \quad W_2 = \frac{(\sqrt{2}G_f)^{1/2} g^2 m_H^2}{12\pi^2} N_2. \tag{8.7}$$

Expressions for N_1 and N_2 come from the integration over the top loop in the specific kinematics of production within a rapidity gap, *i.e.* $(\mathbf{k}+\mathbf{k}_1)^2, (\mathbf{k}+\mathbf{k}_3)^2 \ll m_H^2$. Denoting $a \equiv m_H^2/m_t^2$, one has

$$N_1 = \frac{6}{a}\left[1 + \left(1 - \frac{4}{a}\right)\arctan^2\left(\sqrt{\frac{a}{4-a}}\right)\right]. \tag{8.8}$$

The calculation also demonstrates that the contribution of the W_2 term can be neglected. This comes from the fact that its tensor structure only gives contributions proportional to $(\mathbf{k}+\mathbf{k}_i)^2$ that are small in the considered kinematical regime. In addition, it was shown that $|N_2|^2$ is always 30% smaller than the $|N_1|^2$ for a Higgs boson mass below 1 TeV and consequently, this correction is negligible in front of the first term. This assumption will be discussed below and in Appendix C.1.

Using the Eikonal approximation and the indices as in Fig. 8.1, one can replace the upper (resp. lower) line of the diagram by $2p^\mu p^\sigma$ (resp. $2q_\sigma q_\nu$). The method [78] is valid whenever the gauge particle is soft and corresponds to taking the trace at the cross section level. Indeed, it can be shown, following the notation of Fig. 8.3, and computing the trace along the upper line, that is

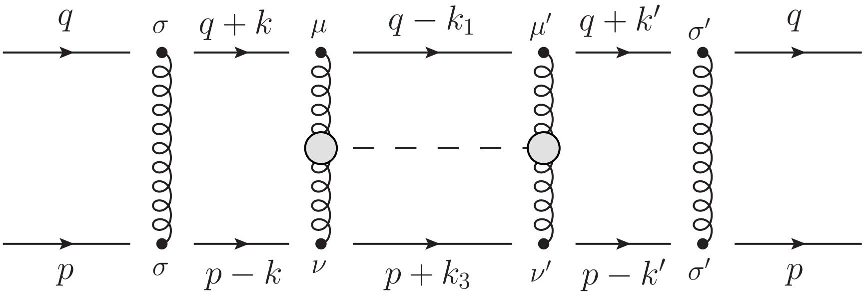

Figure 8.3: Square of the diagram contributing to the Higgs boson production with all momenta and indices.

$$\mathrm{Tr}_{\mathrm{U}} = \mathrm{Tr}\left(\not{q}\gamma^{\sigma'}(\not{q}+\not{k}')\gamma^{\mu'}(\not{q}-\not{k}_1)\gamma^{\mu}(\not{q}+\not{k})\gamma^{\sigma}\right). \tag{8.9}$$

In the present kinematics $k,\ k_1 \ll q$ and using the relation $\not{q}\gamma^\mu\not{p} = 2p^\mu\not{q}$, it becomes

$$\begin{aligned}\mathrm{Tr}_{\mathrm{U}} &= \mathrm{Tr}\left(\not{q}\gamma^{\sigma'}\not{q}\gamma^{\mu'}\not{q}\gamma^{\mu}\not{q}\gamma^{\sigma}\right)\\ &= (4q^{\sigma'}q^{\mu'})\,2q^{\mu}\,\mathrm{Tr}\,(\not{q}\gamma^{\sigma})\\ &= 2(4q^{\mu}q^{\sigma})(4q^{\mu'}q^{\sigma'}),\end{aligned} \tag{8.10}$$

divided by two after the average over spin. The same can be done with the bottom line for which one has

$$\mathrm{Tr}_{\mathrm{B}} = (4p^{\mu}p^{\sigma})(4p^{\mu'}p^{\sigma'}). \tag{8.11}$$

Using this trick at the amplitude level gives

$$\begin{aligned}N^{\mu\nu}V_{\mu\nu} &= (4q_\mu q_\sigma)\left[(k+k_1).(k+k_3)g^{\mu\nu} - (k+k_1)^\nu(k+k_3)^\mu\right](4p^\nu p^\sigma)\frac{W_1}{m_H^2}\\ &= \left[4s^2(k+k_1).(k+k_3)g^{\mu\nu} - 8s(k+k_1).p\,(k+k_3).q\right]\frac{W_1}{m_H^2},\end{aligned} \tag{8.12}$$

remembering that $p^\mu q_\mu = s/2$. Both four-vectors in Eq. (8.12) have a longitudinal and a transverse parts that can be written

$$\begin{aligned}(k+k_1)^\mu &= \frac{\alpha_1}{s}p^\mu + \beta_1 q^\mu + (\mathbf{k}+\mathbf{k}_1)^\mu,\\ (k+k_3)^\mu &= \alpha_3 p^\mu + \frac{\beta_3}{s}q^\mu + (\mathbf{k}+\mathbf{k}_3)^\mu.\end{aligned} \tag{8.13}$$

These definitions take into account the fact that the gluon $k+k_1$ (resp. $k+k_3$) is emitted from a quark moving in the q (resp. p) direction and hence, most of its longitudinal momentum is concentrated in this direction as shown in Appendix C.1. One can now come back to the evaluation of Eq. (8.12) that gives

$$\begin{aligned}N^{\mu\nu}V_{\mu\nu} &= \left[4s^2\left(\frac{\alpha_1\beta_3}{2s} + \beta_1\alpha_3\frac{s}{2} + (\mathbf{k}+\mathbf{k}_1).(\mathbf{k}+\mathbf{k}_3)\right) - 8s\left(\beta_1\frac{s}{2}\right)\left(\alpha_3\frac{s}{2}\right)\right]\frac{W_1}{m_H^2}\\ &= \left[2s\,\alpha_1\beta_3 + 4s^2(\mathbf{k}+\mathbf{k}_1).(\mathbf{k}+\mathbf{k}_3)\right]\frac{W_1}{m_H^2}\\ &\simeq \left[4s^2(\mathbf{k}+\mathbf{k}_1).(\mathbf{k}+\mathbf{k}_3)\right]\frac{W_1}{m_H^2},\end{aligned} \tag{8.14}$$

keeping only the term dominant in s. Practically, the same can be done for the second part of the vertex proportional to W_2, but we only give it in Appendix C.2 as it is negligible.

Finally, the amplitude (8.5) becomes

$$\mathcal{M} = 4sg^4\frac{C}{(2\pi)^2}\int \mathrm{d}^2\mathbf{k}\,\frac{[(\mathbf{k}+\mathbf{k}_1).(\mathbf{k}+\mathbf{k}_3)]}{(\mathbf{k}+\mathbf{k}_1)^2(\mathbf{k}+\mathbf{k}_3)^2\mathbf{k}^2}\frac{W_1}{m_H^2}, \tag{8.15}$$

and to obtain the cross section, one has to take the square and multiply by the phase space available for the final particle.

8.1.2 Phase Space

Calculating the phase space for the final state is not complicated by itself but as we want to keep the kinematics as exact as possible, it implies a little bit of algebra. The point here is to find the relation between the different components of the momenta and the Higgs boson mass.

The $p_1 + p_2 \to n$ particle phase space is given by

$$\mathrm{d}\Phi_n = (2\pi)^4\delta^4\left(p_1 + p_2 - \sum_{i=1}^{n} p_i\right)\prod_{i=1}^{n}\frac{\mathrm{d}^3p_i}{(2\pi)^3\,2E_i}, \tag{8.16}$$

and in the present case one has to evaluate

$$\begin{aligned}\mathrm{d}\Phi_3 = {}&(2\pi)^4\delta^4\left[p+q-(q-k_1)-k_H-(p+k_3)\right]\\ &\times\frac{\mathrm{d}^4k_1}{(2\pi)^3}\delta\left[(q-k_1)^2\right]\frac{\mathrm{d}^4k_H}{(2\pi)^3}\delta\left[k_H^2\right]\frac{\mathrm{d}^4k_3}{(2\pi)^3}\delta\left[(q+k_3)^2\right].\end{aligned} \tag{8.17}$$

First, each momentum is expressed in terms of its Sudakov variables using

$$\frac{\mathrm{d}^4k_i}{(2\pi)^3} = \frac{s}{2(2\pi)^3}\mathrm{d}\alpha_i\mathrm{d}\beta_i\mathrm{d}^2\mathbf{k}_i, \tag{8.18}$$

thus

$$\begin{aligned}
\mathrm{d}\Phi_3 = {} & (2\pi)^4\delta\left[1+\alpha_1-\alpha_H-(1+\alpha_3)\right]\delta\left[1-(1-\beta_1)-\beta_H-\beta_3\right]\delta^2\left[-\mathbf{k}_1+\mathbf{k}_H+\mathbf{k}_3\right] \\
& \times \frac{s}{2(2\pi)^3}\mathrm{d}\alpha_1\mathrm{d}\beta_1\mathrm{d}^2\mathbf{k}_1\delta\left[-\alpha_1(1-\beta_1)s-\mathbf{k}_1^2\right] \\
& \times \frac{s}{2(2\pi)^3}\mathrm{d}\alpha_H\mathrm{d}\beta_H\mathrm{d}^2\mathbf{k}_H\delta\left[\alpha_H\beta_H-\mathbf{k}_H^2-m_H^2\right] \\
& \times \frac{s}{2(2\pi)^3}\mathrm{d}\alpha_3\mathrm{d}\beta_3\mathrm{d}^2\mathbf{k}_3\delta\left[(1+\alpha_3)\beta_3-\mathbf{k}_3^2\right].
\end{aligned} \tag{8.19}$$

One can now solve successively the different δ-functions to find

$$\begin{aligned}
\mathrm{d}\Phi_3 = {} & \frac{s}{8(2\pi)^5}\frac{\mathrm{d}\beta_1}{(1-\beta_1)}\frac{\mathrm{d}\alpha_3}{(1+\alpha_3)}\mathrm{d}^2\mathbf{k}_1\mathrm{d}^2\mathbf{k}_3 \\
& \times\delta\left[-\left(\alpha_3+\frac{\mathbf{k}_1^2}{s(1-\beta_1)}\right)\left(\beta_1-\frac{\mathbf{k}_3^2}{s(1+\alpha_3)}\right)s+(\mathbf{k}_1-\mathbf{k}_3)^2-m_H^2\right].
\end{aligned} \tag{8.20}$$

The final delta function is used to put the Higgs boson on-shell and to perform the integral over α_3. In particular, the quadratic equation

$$-\left(\alpha_3+\frac{\mathbf{k}_1^2}{s(1-\beta_1)}\right)\left(\beta_1-\frac{\mathbf{k}_3^2}{s(1+\alpha_3)}\right)s+(\mathbf{k}_1-\mathbf{k}_3)^2-m_H^2=0, \tag{8.21}$$

has to be solved to obtain α_3 as a function of the Higgs boson mass. Rewriting it

$$\alpha_3^2\,s\beta_1+\alpha_3\left(s\beta_1-\mathbf{k}_3^2+\beta_1\frac{\mathbf{k}_1^2}{s(1-\beta_1)}-(\mathbf{k}_1-\mathbf{k}_3)^2+m_H^2\right)+\beta_1\frac{\mathbf{k}_1^2}{s(1-\beta_1)}-(\mathbf{k}_1-\mathbf{k}_3)^2+m_H^2=0, \tag{8.22}$$

one has two different solutions

$$\alpha_3'=\frac{-b+\sqrt{\Delta}}{s\beta_1}\text{ and }\alpha_3''=-\frac{b+\sqrt{\Delta}}{s\beta_1}, \tag{8.23}$$

with

$$\begin{aligned}
b &= s\beta_1-\mathbf{k}_3^2+\beta_1\frac{\mathbf{k}_1^2}{s(1-\beta_1)}-(\mathbf{k}_1-\mathbf{k}_3)^2+m_H^2, \\
\Delta &= s^2\beta_1^2-4s\beta_1\left(\beta_1\frac{\mathbf{k}_1^2}{s(1-\beta_1)}-(\mathbf{k}_1-\mathbf{k}_3)^2+m_H^2\right).
\end{aligned} \tag{8.24}$$

The correct solution corresponds to the choice of small[1] α_3. Then one can evaluate the order of both solutions by taking the large-s limit, that gives

$$\alpha_3'\simeq\frac{-\beta_1 s+\sqrt{\beta_1^2s^2}}{s\beta_1}=0\text{ and }\alpha_3''\simeq-\frac{\beta_1 s+\sqrt{\beta_1^2s^2}}{s\beta_1}=1. \tag{8.25}$$

Consequently, the first expression only is kept and one has $\alpha_3=\alpha_3'$. Note that taking directly the large s limit in Eq. (8.22) gives

$$\begin{aligned}
-\alpha_3\beta_1 s+(\mathbf{k}_1-\mathbf{k}_3)^2-m_H^2=0, \\
\to m_H^2\simeq\alpha_3\beta_1 s,
\end{aligned} \tag{8.26}$$

---

[1] Remember that the current kinematics requests $\alpha_3 \ll 1$.

using Eq. (8.3). It corresponds to the expected relation between the mass and the longitudinal momenta lost by the initial protons in quasi-elastic processes. Hence, the available phase space is

$$\mathrm{d}\Phi_3 = \frac{s}{8(2\pi)^5}\frac{\mathrm{d}\beta_1}{\beta_1(1-\beta_1)(1+\alpha_3)}\mathrm{d}^2\mathbf{k}_1\mathrm{d}^2\mathbf{k}_3. \tag{8.27}$$

The Higgs boson quasi-elastic cross section at the parton level can then be written

$$\begin{aligned}\mathrm{d}\sigma_{qq}^H &= \frac{2C^2g^8}{(2\pi)^9}\frac{\mathrm{d}\beta_1}{\beta_1(1-\beta_1)(1+\alpha_3)}\mathrm{d}^2\mathbf{k}_1\mathrm{d}^2\mathbf{k}_3 \\ &\times\int \mathrm{d}^2\mathbf{k}\mathrm{d}^2\mathbf{k}'\frac{(\mathbf{k}+\mathbf{k}_1).(\mathbf{k}+\mathbf{k}_3)}{\mathbf{k}^2(\mathbf{k}+\mathbf{k}_1)^2(\mathbf{k}+\mathbf{k}_3)^2}\frac{(\mathbf{k}'+\mathbf{k}_1).(\mathbf{k}'+\mathbf{k}_3)}{\mathbf{k}'^2(\mathbf{k}'+\mathbf{k}_1)^2(\mathbf{k}'+\mathbf{k}_3)^2}\frac{W_1^2}{m_H^4}.\end{aligned} \tag{8.28}$$

The expression is singular when the exchanged gluons go on-shell and this will be regulated by the introduction of the same impact factor as in the dijet case. The splash-out that models the energy lost from parton to hadron is not present in the Higgs boson calculation if one works with the Higgs boson in the final state and this reduces the uncertainty.

8.2 Higher-Order Corrections

With the lowest-order QCD amplitude, the end of the analytic calculation is reached and one has now to include higher-orders and soft corrections, namely the Sudakov form factor and the gap-survival probability. The main characteristic of quasi-elastic production is that those pieces are similar whatever the produced central system is and one can directly use the parametrisation of the dijet quasi-elastic calculation to predict the Higgs boson cross section. On the other hand, as these ingredients are similar, so are the uncertainties. However, it is not exactly the case as the Sudakov form factor is better defined here and in particular, there is no ambiguity on its lower scale that is given by the gluon virtuality. In addition, the CDF data constrain the dijet result and consequently constrain the Higgs boson cross section.

Given that the various ingredients were described in detail in the first part of the thesis, we shall underline only the differences and give the expressions used in the Higgs boson calculation when different from those in the dijet case.

In Sec. 4.1, we have shown that the upper scale in the Sudakov form factor should not be related to the mass of the system but to the jet transverse momentum. However, it is not the case in Higgs boson production where the vertex is effectively point-like due to the large mass of the top quark. The situation is simplified and some part of the Sudakov form factor can be estimated theoretically. The log structure of the suppression comes from an integration over the splitting functions and schematically, one has

$$S(\mu^2,\ell^2) = \alpha_s\left[a\log^2\left(\frac{\mu^2}{\ell^2}\right)+b\log\left(\frac{\mu^2}{\ell^2}\right)+c\right], \tag{8.29}$$

where ℓ^2 is proportional to the virtuality from which the evolution starts while μ^2 is related to the hard scale, for instance the mass squared of the Higgs boson. Actually, the ambiguity on the upper scale doesn't exist here as the transverse momenta and virtualities of the top quarks inside the loop are larger or similar to the Higgs boson mass. Hence, no additional soft gluons would be able to resolve the effective vertex that can be consequently considered point like. There is only one kinematical regime that builds the Sudakov logs and only one hard scale, *i.e.* the Higgs

boson mass.
A first calculation was performed by the Durham group[2] and to single-log accuracy [19]. They claimed that the complete one-loop result could be taken into account by adjusting the upper limit of the q-integration to $\mu = 0.62\, m_H$ and that the lower cut-off should be of the order of $\mathbf{k}^2$. A recent evaluation of the same correction was performed by Coughlin and Forshaw [20] who demonstrated explicitly that the values of the different scales are

$$\begin{aligned} \mu^2 &= m_H^2, \\ \ell^2 &= \mathbf{k}^2, \\ \Delta &= \frac{|\mathbf{q}|}{\mu}. \end{aligned} \tag{8.30}$$

These results come from a careful and explicit next-to-leading order calculation of the vertex corrections and in particular of the high- and low-$\mathbf{q}^2$ contributions. In particular, it appears that there are no large logarithm in the kinematical region where $\mathbf{q}^2$ is smaller than the transverse momentum in the loop $\mathbf{k}^2$, giving only single-logs and constant terms that are then claimed to be negligible. The main problem is that nobody knows what to do with those terms as they do not exponentiate and consequently, the Sudakov correction is only known to within a constant. In our model, one has the exact transverse kinematics and the momenta of active gluons are different from the loop momentum, hence we kept the choice of lower scale ℓ^2 to be equal to $(\mathbf{k}+\mathbf{k}_i)^2$. This actually corresponds to the momentum of the gluon to which the virtual emission is attached. To evaluate the uncertainty due to the constant term, we also keep the possibility to vary the lower scale by a factor x', *i.e* take ℓ^2/x' instead of ℓ^2. As explained in Sec. 4.2.2 this gives an idea of the effect of a change in the constant terms that are not proven to exponentiate and are a source of uncertainty (compare Fig. 4.9 and Fig. 4.13.b). This factor constitutes the main uncertainty coming from this part of the calculation as we shall see that a change of x' is not negligible in the final result.

---

[2] A very brief review of the model can be found in Sec. 7.2 or in the original references of the Durham group.

Chapter 9

Estimation of the Higgs-Boson Quasi-elastic Cross Section

The CDF data have provided a good opportunity to reduce the uncertainties that affect this family of process. The different parametrisations obtained in the first part of the thesis can now be used to constrain our prediction of the Higgs quasi-elastic cross section at the LHC.

The comparison between different parametrisations of the model and data have led to a selection of parameters that reproduced reasonably the measurements and theoretical uncertainties are now constrained by the experimental uncertainties. The free parameters are

- Φ-type : the label of the impact factor,
- x' : the factor on the lower scale in the Sudakov form factor,
- S^2 : the value of the gap-survival probability.

In the dijet calculation, particular combinations of them lead to curves within the CDF error-bars and the resulting band of theoretical possibilities constitutes the uncertainty on the calculation. This was shown in Fig. 6.6.b for which the parametrisations are given in Appendix B.5. Note that the upper scale of the Sudakov form factor μ is now fixed to m_H and is not a free parameter anymore.

9.1 Results

One can use these parametrisations to make a prediction of the Higgs boson quasi-elastic cross section at the TeVatron ($\sqrt{s}$=1960 GeV), and at the LHC for different energies, *i.e.* $\sqrt{s}$=14 TeV, 10 TeV and 7 TeV. In each case, one has to consider specific cuts that are, or will be, used in the search for such events and given in Table 9.1.

Cuts	**TeVatron** [57]	**LHC** [72]
$\lvert\alpha_3\rvert$	[0.03,0.08]	[0.002,0.2]
β_1	-	[0.002,0.2]
$\lvert y_X\rvert$	[-2.5,2.5]	< 1
Gap size	> 3.6	-

Table 9.1: Experimental cuts for the TeVatron and the LHC. The second column includes the joint acceptances of both RP220 and FP420.

At the TeVatron, one directly finds that the cross section is of the order of 30 attobarn for the reference curve and m$_H$=120 GeV. This makes the Higgs boson within a gap impossible to observe during the current run. Nevertheless, at the LHC the cross section becomes of the order of a few femtobarns and, in Fig. 9.1.b, we give this cross section for $\sqrt{s}$= 10 TeV as a function of the Higgs-boson mass.

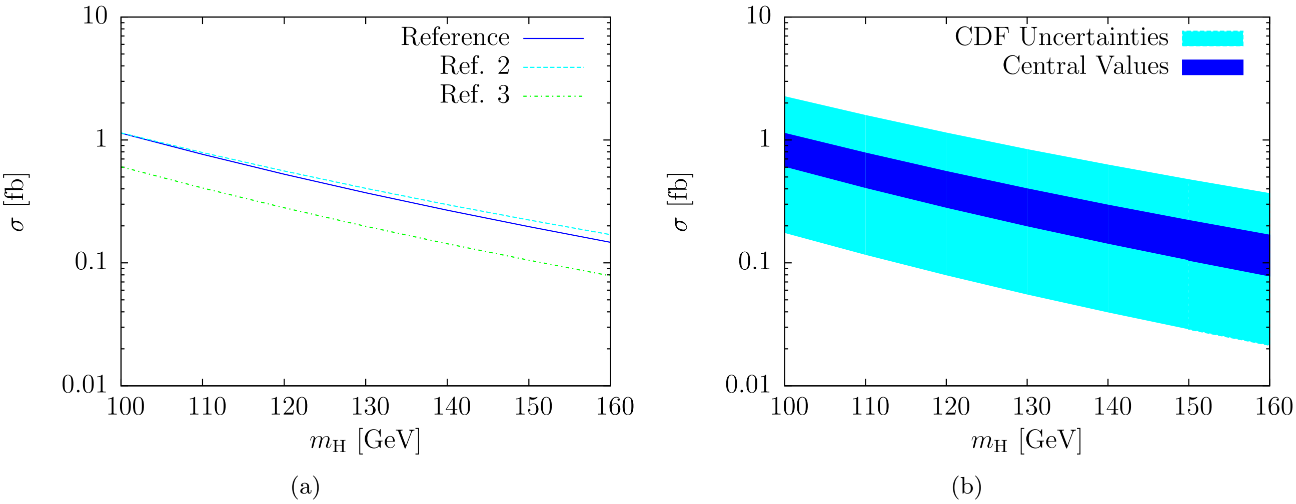

Figure 9.1: (a) Three identical curves at TeVatron energy but that spread at the LHC. They constitute the central uncertainty band of (b) the Higgs boson quasi-elastic cross section at 10 TeV.

The larger band comes from the CDF error bars, the parameters Φ-type, x' and S^2 corresponding to curves going through the 1 σ error bars of CDF are kept to produce the curves as explained in the beginning of this chapter. The uncertainty is of one order of magnitude. In the plot of Fig. 9.1.a, one can find the three parametrisations that give identical curves for the dijet at the TeVatron. The effect at the LHC is a divergence of results, mainly due to the type of impact factor and the dark blue band of predictions corresponds to the reference curves of (a), the central values. Without any cuts, one has the plot shown in Fig. 9.2. If the energy in the center-of-mass frame reaches 14 TeV, one has the predicted cross section with cuts in Fig. 9.3.a and one can observe that at m_H=120 GeV, the cross section goes from 0.5 fb to 2 fb. However, up to now the LHC runs with two beams of 3.5 TeV each, so that $\sqrt{s}$= 7 TeV, that give the smaller cross section shown in Fig. 9.3.b.

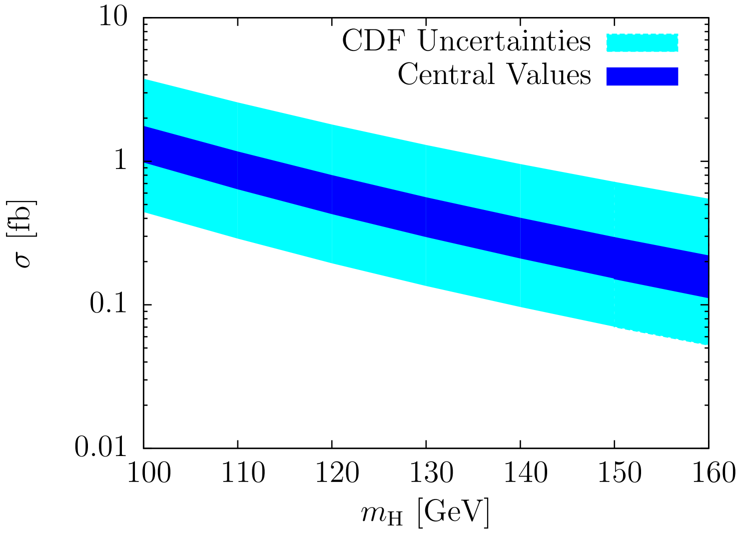

Figure 9.2: Higgs boson quasi-elastic cross section at 10 TeV, no cuts.

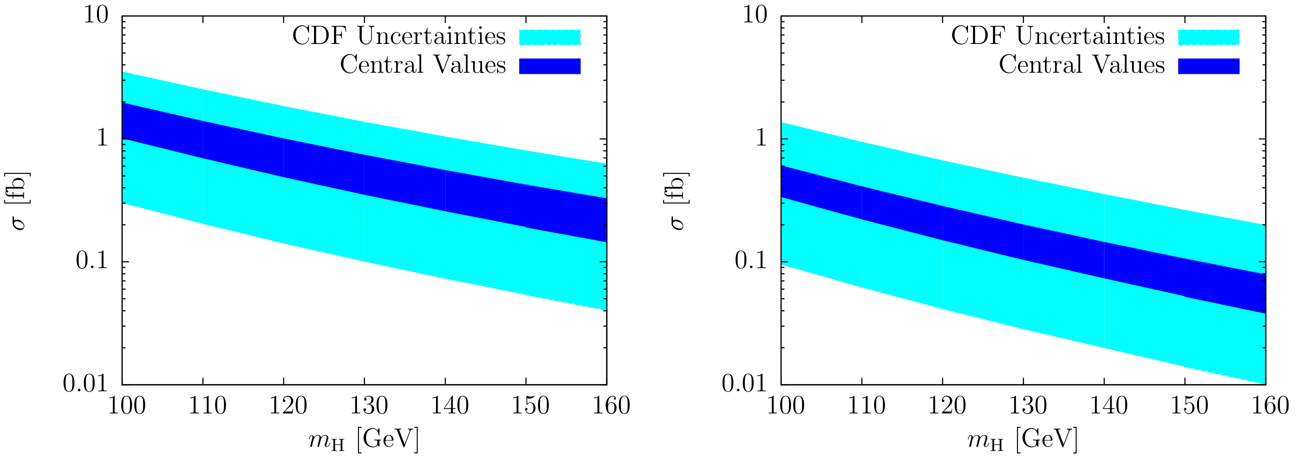

(a)

(b)

Figure 9.3: Higgs boson quasi-elastic cross section at the LHC. (a) 14 TeV and (b) 7 TeV.

This result can be compared with the KMR prediction for the central production of a Higgs boson in pp collision. In Fig. 9.4, we show the result found in [16] as well as the band obtained

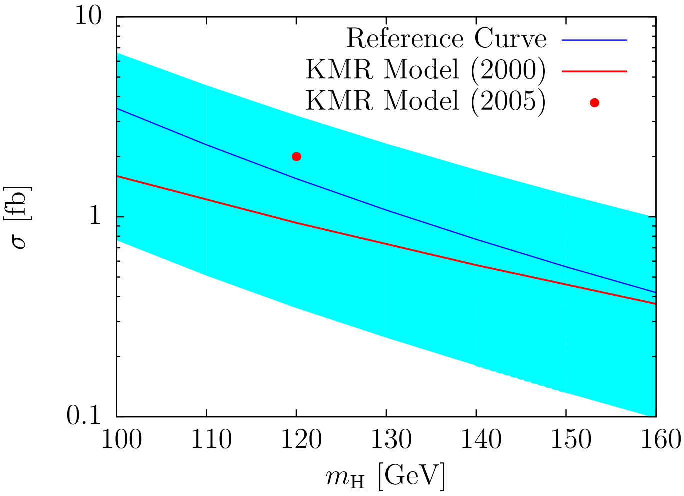

Figure 9.4: Higgs boson quasi-elastic cross section at 14 TeV without any cuts and the KMR prediction with the K factor, see Sec. 7.2, set to 1 for the same process [16]. The dot corresponds to a more recent prediction from KMR found in [128].

in our model for $\sqrt{s}$ =14 TeV without cuts. One can note that our model is consistent with the Durham model even if our study of the dijet data allows for larger cross section, up to 3.2 fb at m_H=120 GeV. In particular, the curvature is different as expected with the use of the impact factor described in Chap. 3 and this make the cross section for a light Higgs boson larger than the Durham prediction.

In all plots, we have considered the possibility to use both FP420 and RP220 to tag final protons but if only FP420 is built the kinematical cuts are more restrictive leading to a smaller acceptance of events and consequently to a smaller cross section. In particular, one should observe a rapid fall down at large masses. To illustrate this point, Fig. 9.5 shows two curves corresponding to the set of cuts of Table. 9.2 found in the literature relative to FP420 [72, 159]. For masses larger

Cuts	**LHC** [72]	**LHC** [159]
$\lvert\alpha_3\rvert$	[0.002,0.02]	[0.005,0.018]
β_1	[0.002,0.02]	[0.004,0.014]
$\lvert y_X\rvert$	< 1	< 0.06

Table 9.2: Experimental cuts for LHC including only FP420.

than 150 GeV, the cross section vanishes quickly but the phenomenon is purely due to cuts. Actually, the relation between the mass of the centrally produced system and the longitudinal transferred momentum fractions, α_3 and β_1, gives roughly

$$\alpha_3 \simeq \frac{m_H^2}{s\beta_1}. \tag{9.1}$$

Considering a Higgs boson with a mass of 200 GeV in a process where the energy in the center-of-mass frame is 10 TeV, the only possible values for $|\alpha_3|$ lay between 0.02 and 0.2 are outside

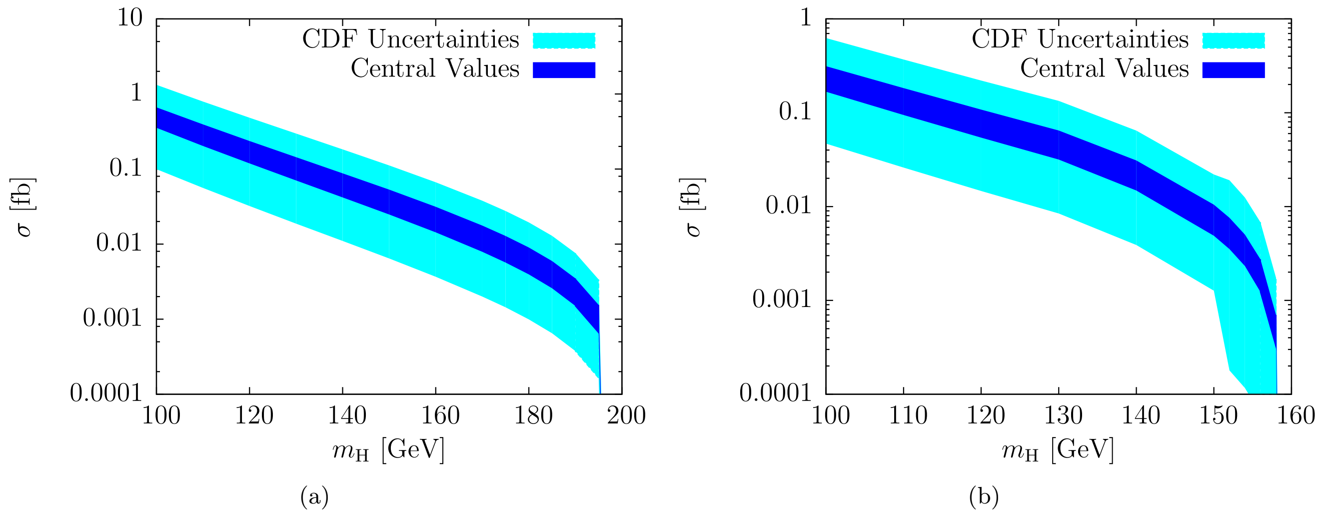

Figure 9.5: (a) Higgs boson quasi-elastic cross section at 10 TeV using FP420 only and (b) the same but for a more restrictive set of cuts [72].

the range of FP420. Consequently, the event is not selected and the cross section tends to zero, except if one uses in addition RP220 to tag the final protons. Obviously, this effect disappears for higher energy. One can also consider an even more restrictive set of cuts taken from typical values used in Monte-Carlo studies and shown in the third column of Table 9.2 [159]. The result is shown in Fig. 9.5.b. The effect of cuts is important and cannot be neglected. For the central curve they amount to a factor 2 between Fig. 9.5.a and Fig. 9.5.b at $m_H = 120$ GeV.
The cross section properties are similar to those in the dijet case as the non-perturbative region is still important: for the reference curve at 10 TeV and $m_H = 120$ GeV, only 44% of the cross section[1] comes from momenta in the loop greater than 1 GeV.

9.2 Strategy Analysis of Early Data

One of the remaining question is how early LHC measurements could constrain the different parameters. Assuming that quasi-elastic dijet cross section is measured with a given precision, one can define an analysis strategy to discard parametrisations that are not in the error bars at both TeVatron and LHC. Several comments are in order.

If an estimation of the gap survival can be done independently of the dijet or the Higgs boson cross section, one has then three free parameters, *i.e* the type of impact factor and the two scales in the Sudakov form factor. The upper scale is not an issue, as for jets with high-transverse energy, the uncertainty disappears so that one is left with the lower scale and the type of impact factor. For each impact factor, two values of the lower scale give curves at the limit of the error at the TeVatron and, after extrapolation to the LHC, one can check whether they correspond to the data. Note that it is not possible to fix independently these two parameters that have to be fixed together.
The precision on the new result depends completely on the precision of the LHC dijet data and on the level of accuracy reached. In Chap. 4 and Sec. 4.2.4, we have seen that there exist higher order diagrams that involve the screening gluon in the dijet case but are not present in the Higgs calculation. One has found that they amount to at least 15% of the quasi-elastic

---

[1] This number is obtained using the same method as the one described in Sec. 2.7, all gluon-transverse momenta are cut below 1 GeV.

cross section and their contributions were neglected. However, this made the dijet quasi-elastic process topologically identical to the Higgs boson one but if the LHC measurements achieved precision of this order, the contribution of those diagrams would start to matter as well as the many small details of the calculation that then might be settled.

9.3 Summary

First of all, the Higgs quasi-elastic production calculation is completely similar to that of dijet quasi-elastic production apart from the hard subprocess. Moreover, the situation is less complicated as the vertex is effectively point-like allowing at the same time an evaluation of the Sudakov corrections. The upper scale in the suppression factor is fixed by the theory and the uncertainty on the final result is reduced. From the parton level calculation, one can build the full Higgs boson quasi-elastic cross section that contains both the impact factor and the Sudakov form factor. The only additional soft correction is the gap survival, for which we keep the prescription used in the dijet case. The parametrisations are also kept from our previous study, in particular the four different curves that gives the band of Fig. 6.6.b.
We have found that if the Higgs boson has a mass of 120 GeV, the quasi-elastic cross section at the LHC, assuming the presence of the RP220 and FP420 forward detector, is below 2 fb. The uncertainties are large, of one order of magnitude, and the largest ones come from the extrapolation of the proton impact factor and of the gap-survival probability to LHC energy. This shows the importance to have a measurement of quasi-elastic dijet at the beginning of the LHC runs.

Conclusion

We have proposed a new model of quasi-elastic production that is similar to the Durham model, but differs from it in the implementation and the details of the different ingredients.
The calculation was divided in five ingredients, the analytic calculation at the parton level, the impact factor, the Sudakov form factor, the gap-survival probability and the splash-out. Each was studied separately and the sources of uncertainty were carefully evaluated. In particular, the recent CDF measurement of the quasi-elastic dijet cross section at the TeVatron was used to narrow down the total uncertainty evaluated to be a factor 10 up or down, with no theoretically preferred curve. The actual computing power allowed us to perform a calculation beyond the usual approximations found in the literature and to evaluate their effects on the final result.

Efforts were made to keep an exact transverse kinematics all along and in all ingredients of the calculation. Considering that it changes the cross section by a factor two, this can be a crucial point. The second is the importance of the non-perturbative region as about 60% of the dijet cross section comes from a region where gluon momenta are smaller than 1 GeV^2. This underlines the importance of an impact factor which takes the non-perturbative region into account. The two models for the impact factor presented here were build for this purpose, the LCWF impact factor relies on non-perturbative cross sections to fix its input and the unintegrated gluon density models soft exchanges in addition to the usual differentiation of gluon distribution function. Both behave in accordance with what is expected from the proton wave function. The vertex corrections, *i.e* the Sudakov form factor, is one of the main sources of uncertainty even if a recent NLO calculation sets its structure and upper scale in the Higgs boson case. We have shown that the upper scale should be the hard transverse momentum in the vertex instead of the mass of the centrally produced system in the dijet case. Finally, in the case of partons in the final state, there is the question of the loss of energy when reconstructing the jets. We have proposed a new parametrisation of the splash-out based on a Monte-Carlo study that matches the transverse energy of the partons to the transverse energy of the jets in an accurate way. The next step was to compare the model with the CDF data and this allowed us to select a set of reasonable theoretical parametrisations. Those parametrisations were then used to extrapolate our result to the LHC and to make a prediction for the Higgs boson quasi-elastic production.

The extrapolation to the LHC showed that quasi-elastic dijet should be seen with a sufficient rate to be measured by detectors such as RP220 and FP420. Nevertheless, this requests the knowledge of the impact factor and of gap survival at larger energies. The energy dependence was already included in the spirit of Regge theory but one knows that unitarisation effects will be important when going from the TeV scale to the LHC energy. The inclusion of multi-pomeron exchanges, materialised by the gap-survival probability, will be more complicated. In particular, it is usually assumed that one can write the process as a product of the gap survival with the hard amplitude. It is not the case here where the t-dependence is included directly in the cross section.
The prediction for the Standard Model Higgs boson quasi-elastic cross section was straightforward. Using the parametrisations selected, the Higgs boson cross section was found to be

between 0.2 and 2 femtobarns for a Higgs boson of mass 120 GeV and $\sqrt{s} = 10$ TeV considering the kinematical cuts of RP220 and FP420. Our result is consistent with the Durham calculation but the previous study of the dijet cross section and the CDF data gave parametrisations that allow a cross section two times bigger for the Higgs boson quasi-elastic cross section. The uncertainty is estimated to be of one order of magnitude and the result raises the same issues as the dijet calculation: the importance of the non-perturbative region and the uncertainty coming from the corrections. Clearly, this emphasises the importance of new quasi-elastic data.

Let us now come to the prospects. The first urgent question is the gap-survival probability at the LHC. In the worst-case scenario, it is almost zero and then the field of high-mass quasi-elastic processes is dead at LHC. The uncertainty could be narrowed down with new data *e.g.* on dijet. As all calculations of quasi-elastic cross sections follow the same scheme, the best approach should be to compare systematically the model with data for different quasi-elastic productions. Di-quark, di-photon, χ_c (that has no Sudakov form factor) should be implemented in the same way and compared with data. Hence, one can believe that measurements at the LHC, including the rapidity distribution, the mass distribution as well as transverse energy, will be a very important task that will help to clarify many of the issues raised in the thesis.

One should note that this work is now beginning in FPMC, a Monte-Carlo dedicated to Forward Physics which gathers different models and production mechanisms in the same framework. In particular, the model presented in this thesis was recently implemented under the name of CHIDe model. It should allow to have a general view of quasi-elastic production from the parton level to the detector analysis and to compare directly the predictions to the data.

So she sat on, with closed eyes, and half believed herself in Wonderland, though she knew she had but to open them again, and all would change to dull reality – the grass would be only rustling in the wind, and the pool rippling to the waving of the reeds – the rattling teacups would change to tinkling sheep-bells, and the Queen's shrill cries to the voice of the shepherd boy – and the sneeze of the baby, the shriek of the Gryphon, and all the other queer noises, would change (she knew) to the confused clamour of the busy farm-yard – while the lowing of the cattle in the distance would take the place of the Mock Turtle's heavy sobs.

Lastly, she pictured to herself how this same little sister of hers would, in the after-time, be herself a grown woman; and how she would keep, through all her riper years, the simple and loving heart of her childhood: and how she would gather about her other little children, and make *their* eyes bright and eager with many a strange tale, perhaps even with the dream of Wonderland of long ago: and how she would feel with all their simple sorrows, and find a pleasure in all their simple joys, remembering her own child-life, and the happy summer days.

THE END

Alice's Adventures in Wonderland,
Lewis Carrol

Appendix A

Master Formulae and FORTRAN code

In this appendix, we write the complete expression for the cross section in the case of quasi-elastic production of dijet and the different functions implemented in the FORTRAN codes that were used to produce the results of the thesis. All programs has the same structure:

1. Inputs.
2. A common part with the definitions of variables and vectors.
3. The formula for the cross section including the amplitude, the impact factor, the Sudakov form factor, the gap survival probability and the splash-out.
4. Output and histograms.

A.1 Dijet Production

Coefficients and phase space:

$$\begin{aligned}
&\mathrm{factps} = \frac{81}{2}\frac{1}{16(2\pi)^8\beta_1\,\beta_2},\\
&\mathrm{gq} = \sqrt{4\pi\,0.88},\\
&\mathrm{gg} = \sqrt{4\pi\,\mathrm{as(sgg)}},\\
&\mathrm{fact} = gg^4\,gq^8\,\frac{0.3894^6}{4\pi^4},\\
&\mathrm{Cf} = \frac{N_c^2-1}{N_c^2},
\end{aligned} \tag{A.1}$$

$$\boxed{\sigma\text{=fact*factps*}S^2\text{*}\big[\sigma_{qq}(\alpha_1,\,\alpha_2,\,\beta_1,\,\beta_2,\,\mathbf{k}_1,\,\mathbf{k}_2,\,\mathbf{k}_3,\,\mathbf{k},\,\mathbf{k}')\big]}$$

The gap survival probability S^2 is a number and the function σ_{qq} is integrated over α_1, α_2, β_1, β_2, $\mathbf{k}_1$, $\mathbf{k}_2$, $\mathbf{k}_3$, $\mathbf{k}$, $\mathbf{k}'$. It is defined by

$$\sigma_{qq} = \frac{\mathrm{Num}}{\mathrm{Deno}} \times \Phi \times \mathrm{Suda}\Phi. \tag{A.2}$$

The numerator is

$$\text{Num} = \frac{1}{2}\,(I2 + J2)(I1 + J1) + \frac{1}{2}(I2 - J2)(I1 - J1), \tag{A.3}$$

with

$$\begin{aligned} I1 &= \frac{1}{2}\left(1 + \frac{u_{gg}^4}{s_{gg}^4} + \frac{t_{gg}^4}{s_{gg}^4}\right)\left(\frac{1}{t_{gg}} + \frac{1}{u_{gg}}\right)^2, \\ J1 &= \frac{1}{2}\left(1 - \frac{u_{gg}^4}{s_{gg}^4} - \frac{t_{gg}^4}{s_{gg}^4}\right)\left(\frac{1}{t_{gg}} + \frac{1}{u_{gg}}\right)^2, \end{aligned} \tag{A.4}$$

and

$$I2 = \left[(\mathbf{k} + \mathbf{k}_1).(\mathbf{k}' + \mathbf{k}_1)\right]\left[(\mathbf{k} + \mathbf{k}_3).(\mathbf{k}' + \mathbf{k}_3)\right], \tag{A.5}$$

$$J2 = \left[(\mathbf{k} + \mathbf{k}_1).(\mathbf{k} + \mathbf{k}_3)\right]\left[(\mathbf{k}' + \mathbf{k}_1).(\mathbf{k}' + \mathbf{k}_3)\right] - \left[(\mathbf{k} + \mathbf{k}_1).(\mathbf{k}' + \mathbf{k}_3)\right]\left[(\mathbf{k}' + \mathbf{k}_1).(\mathbf{k} + \mathbf{k}_3)\right]. \tag{A.6}$$

The Mandelstam invariants are defined in Eq. (2.76). The denominator is

$$\text{Deno} = \mathbf{k}^2(\mathbf{k} + \mathbf{k}_1)^2(\mathbf{k} + \mathbf{k}_3)^2\mathbf{k}'^2(\mathbf{k}' + \mathbf{k}_1)^2(\mathbf{k}' + \mathbf{k}_3)^2. \tag{A.7}$$

We have implemented two models for the impact factor Φ: the LCWF impact factor (see Sec. 3.2) and the unintegrated gluon density UgD (see Sec. 3.3). Both include four pieces corresponding to the two-colliding protons and their complex conjugates

$$\Phi = \Phi^{p_1}\,\Phi^{p_2} \times \Phi^{p_1'}\,\Phi^{p_2'}. \tag{A.8}$$

In the former case, one has

$$\begin{aligned} \Phi^{p_1} &= 3\left(\frac{s}{s_1}\right)^{\alpha(t_1)}\left[F_1\left(-\mathbf{k}_1^2\right) - F_1\left(-(\mathbf{k}^2 + (\mathbf{k} + \mathbf{k}_1)^2 - c\,(\mathbf{k} + \mathbf{k}_1).\mathbf{k})\right)\right], \\ \Phi^{p_2} &= 3\left(\frac{s}{s_3}\right)^{\alpha(t_3)}\left[F_1\left(-\mathbf{k}_3^2\right) - F_1\left(-(\mathbf{k}^2 + (\mathbf{k} + \mathbf{k}_3)^2 - c\,(\mathbf{k} + \mathbf{k}_1).\mathbf{k})\right)\right], \\ \Phi^{p_1'} &= 3\left(\frac{s}{s_1'}\right)^{\alpha(t_1')}\left[F_1\left(-\mathbf{k}_1^2\right) - F_1\left(-(\mathbf{k}'^2 + (\mathbf{k}' + \mathbf{k}_1)^2 - c\,(\mathbf{k}' + \mathbf{k}_1).\mathbf{k}')\right)\right], \\ \Phi^{p_2'} &= 3\left(\frac{s}{s_3'}\right)^{\alpha(t_3')}\left[F_1\left(-\mathbf{k}_3^2\right) - F_1\left(-(\mathbf{k}'^2 + (\mathbf{k}' + \mathbf{k}_3)^2 - c\,(\mathbf{k}' + \mathbf{k}_1).\mathbf{k}')\right)\right]. \end{aligned} \tag{A.9}$$

One can calculate s_i and t_i using the four-momentum of the centrally produced system as shown in Eq. (3.10) and

$$F1(p) = \frac{3.53 + 2.79\,p}{(3.53 + p)(1 + \frac{p}{0.71})^2}. \tag{A.10}$$

In the case of the unintegrated gluon density, the impact factors are

$$\begin{aligned}
\Phi^{p_1} &= \frac{4\pi^2}{g^2}\frac{N_c^2-1}{2N_c}\mathcal{F}\left(0.41(\beta_1+\beta_2), \left(\frac{\mathbf{k}+(\mathbf{k}+\mathbf{k}_1)}{2}\right)^2\right) \\
&\quad\times \frac{2\mathbf{k}^2(\mathbf{k}+\mathbf{k}_1)^2}{\mathbf{k}^4+(\mathbf{k}+\mathbf{k}_1)^4}\, e^{-\frac{1}{2}(B_0+2\alpha'\ln\frac{x_0}{\beta_1+\beta_2})|\mathbf{k}_1^2|}, \\
\Phi^{p_2} &= \frac{4\pi^2}{g^2}\frac{N_c^2-1}{2N_c}\mathcal{F}\left(0.41(\alpha_1+\alpha_2), \left(\frac{\mathbf{k}+(\mathbf{k}+\mathbf{k}_3)}{2}\right)^2\right) \\
&\quad\times \frac{2\mathbf{k}^2(\mathbf{k}+\mathbf{k}_3)^2}{\mathbf{k}^4+(\mathbf{k}+\mathbf{k}_3)^4}\, e^{-\frac{1}{2}(B_0+2\alpha'\ln\frac{x_0}{\alpha_1+\alpha_2})|\mathbf{k}_3^2|}, \\
\Phi^{p_1'} &= \frac{4\pi^2}{g^2}\frac{N_c^2-1}{2N_c}\mathcal{F}\left(0.41(\beta_1+\beta_2), \left(\frac{\mathbf{k}'+(\mathbf{k}'+\mathbf{k}_1)}{2}\right)^2\right) \\
&\quad\times \frac{2\mathbf{k}'^2(\mathbf{k}'+\mathbf{k}_1)^2}{\mathbf{k}'^4+(\mathbf{k}'+\mathbf{k}_1)^4}\, e^{-\frac{1}{2}(B_0+2\alpha'\ln\frac{x_0}{\beta_1+\beta_2})|\mathbf{k}_1^2|}, \\
\Phi^{p_2'} &= \frac{4\pi^2}{g^2}\frac{N_c^2-1}{2N_c}\mathcal{F}\left(0.41(\alpha_1+\alpha_2), \left(\frac{\mathbf{k}'+(\mathbf{k}'+\mathbf{k}_3)}{2}\right)^2\right) \\
&\quad\times \frac{2\mathbf{k}'^2(\mathbf{k}'+\mathbf{k}_3)^2}{\mathbf{k}'^4+(\mathbf{k}'+\mathbf{k}_3)^4}\, e^{-\frac{1}{2}(B_0+2\alpha'\ln\frac{x_0}{\alpha_1+\alpha_2})|\mathbf{k}_3^2|}.
\end{aligned} \tag{A.11}$$

The Sudakov form factor described in Chap. 4 is introduced in the same way

$$\mathrm{Suda}\Phi = \mathrm{Suda}\Phi^{p_1}\,\mathrm{Suda}\Phi^{p_2} \times \mathrm{Suda}\Phi^{p_1'}\,\mathrm{Suda}\Phi^{p_2'}, \tag{A.12}$$

where SudaΦ is a function of two scales μ and ℓ

$$\mathrm{Suda}\Phi[\mu,\ell] = \sqrt{e^{-\int_{\ell^2}^{\mu^2}\frac{\mathrm{d}\mathbf{q}^2}{2\pi}\frac{\alpha_s(\mathbf{q}^2)}{\mathbf{q}^2}\int_0^{1-\Delta}\mathrm{d}z\left[zP_{gg}+N_fP_{qg}\right]}}. \tag{A.13}$$

One has for the different Sudakov corrections in our model

$$\begin{aligned}
&\mathrm{Suda}\Phi^{p_1}\left[\mathbf{k}_2^2,(\mathbf{k}+\mathbf{k}_1)^2\right]\,\mathrm{Suda}\Phi^{p_2}\left[\mathbf{k}_2^2,(\mathbf{k}+\mathbf{k}_3)^2\right] \\
&\quad\times \mathrm{Suda}\Phi^{p_1'}\left[\mathbf{k}_2^2,(\mathbf{k}'+\mathbf{k}_1)^2\right]\,\mathrm{Suda}\Phi^{p_2'}\left[\mathbf{k}_2^2,(\mathbf{k}'+\mathbf{k}_3)^2\right].
\end{aligned} \tag{A.14}$$

All these ingredients formed the final quasi-elastic dijet cross section.

Appendix B

Dijet Quasi-Elastic Cross Section: Details of the Calculation

In the present Appendix, we detail some of the calculations of the dijet quasi-elastic production cross section.

B.1 Integration by Residue

Most of the integrals of the present work are performed using the residue theorem. The method of integration comes from the Cauchy theorem on a closed curve.

Residue theorem 1. *If $f(z)$ is an analytic and uniform function inside and on a closed contour $\mathcal{C}$ expect at a finite number of singularities z_1,..., z_n inside $\mathcal{C}$, then*

$$\oint_{\mathcal{C}} f(z)dz = 2i\pi \sum_{i=1}^{n} Res_{z_i}[f(z)],$$

with $Res_{z_i}[f(z)]$ the residue of $f(z)$ at the pole z_i.

The definition of the residue depends of the multiplicity of the pole and one has for a

1. simple pole: $Res_{z_i}[f(z)] = \lim_{z\to z_i}(z - z_i)f(z)$.
2. pole of order α: $Res_{z_i}[f(z)] = \frac{1}{(n-1)!}\lim_{z\to z_i}\frac{d^{\alpha-1}}{dz^{\alpha-1}}(z - z_i)^{\alpha}f(z)$.

In practice, one integrates along a closed contour in a the half-complex plane that should be similar to the one shown in Fig. B.1. The integral along the whole contour is divided in integrals

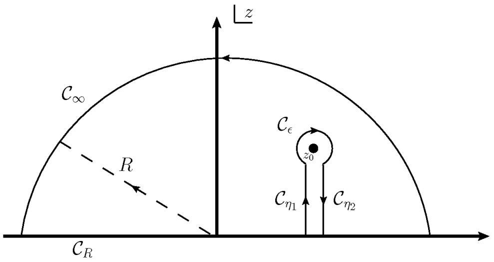

Figure B.1: Closed contour.

on its different parts,

$$\oint_{\mathcal{C}} f(z)dz = \int_{\mathcal{C}_\infty} f(z)dz + \int_{\mathcal{C}_\epsilon} f(z)dz + \int_{\mathcal{C}_{\eta 1}} f(z)dz + \int_{\mathcal{C}_{\eta 2}} f(z)dz + \int_{\mathcal{C}_R} f(z)dz = 0, \qquad \text{(B.1)}$$

where $\mathcal{C}_\infty$ is the large half semicircle and $\mathcal{C}_\epsilon$ the little one around the pole. The contribution of $\mathcal{C}_{\eta 1}$ and $\mathcal{C}_{\eta 2}$ are exactly the same but with opposite signs and their contributions cancel. The integration on $\mathcal{C}_R$ is equivalent to the principal part of an integration along the real axis,

$$\mathrm{p}\int_{-\infty}^{\infty} \frac{f(z)}{z - z_i} dx = \lim_{\epsilon \to 0} \left[\int_{-\infty}^{z_i - \epsilon} + \int_{z_i + \epsilon}^{\infty} \right] \frac{f(z)}{z - z_i} dz. \qquad \text{(B.2)}$$

Finally, one has to compute integrals along $\mathcal{C}_\infty$ and $\mathcal{C}_\epsilon$. Usually, the contribution of the former is zero if $f(z)$ tends to zero fast enough at infinity. One can use the Estimation lemma to prove this:

Estimation lemma 1. *If* $\mathcal{C}$ *is an arc of center* z_i *and of radius* R *intercepted by an oriented angle* β*, if* $f(z)$ *is a continuous function in the closed sector* $|z - z_i| \geq R_0$ *and such as*

$$\lim_{z \to \infty} (z - z_i) f(z) = L,$$

with $L \in \mathbb{C}$*. Then*

$$\lim_{R \to \infty} \int_{\mathcal{C}_\infty} f(z) = iL\beta.$$

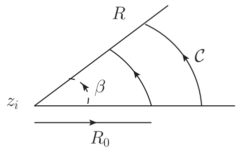

The limit is zero if the function $f(z)$ decreases faster than $1/z$.

B.2 Lowest-Order Two-Gluon Production in Quasi-Multi-Regge Kinematics

Here, we detail some of the calculations of Chap. 2, *i.e.* calculations of the parton-level cross section for two-gluon production in the quasi-multi-Regge-kinematics limit.

B.2.1 s_1u_2 and u_1s_2 Diagrams

There are two types of single-crossed diagrams as shown in Fig. B.2, both of them differ from the s_1s_2 diagram by only one propagator and their contributions are evaluated in the same way as in Sec. 2.1.2.

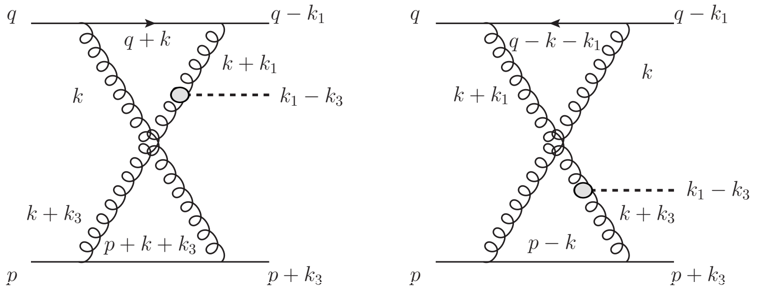

Figure B.2: Single-crossed diagram: (a) s_1u_2 diagram and (b) u_1s_2 diagram.

We start with the position of the poles of diagram s_1u_2, the only difference from the s-diagram is propagator P_2 that becomes

$$\begin{aligned}P_2 &= (p+k+k_3)^2 + i\epsilon \\ &= (1+y+y_3)(z+z_3)s - (\mathbf{k}+\mathbf{k}_3)^2 + i\epsilon,\end{aligned} \tag{B.3}$$

that changes sign at

$$y_{P_2} = \frac{(\mathbf{k}+\mathbf{k}_3)^2 - i\epsilon}{(z+z_3)s} - 1 - y_3. \tag{B.4}$$

The relative position of the different y poles is hence modified as shown in Fig. B.3 and accordingly, it is convenient to write the longitudinal integral as

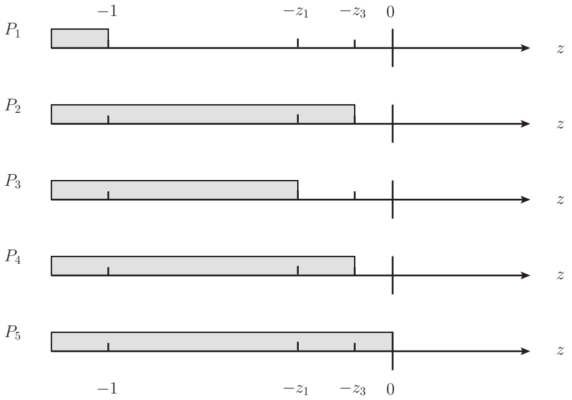

Figure B.3: Single-crossed diagram s_1u_2: Positions of the y poles of the different propagators as functions of z. The shaded regions correspond to poles above the real axis while the unshaded ones to poles below the real axis.

$$\begin{aligned}\mathcal{I}_{s_1u_2} &= \int_{-1}^{-z_3} \mathrm{d}z \int \mathrm{d}y(-2\pi i)\delta\left[y(1+z)s - \mathbf{k}^2\right]\frac{1}{P_2P_3P_4P_5} \\ &+ \int_{-z_1}^{-z_3} \mathrm{d}z \int \mathrm{d}y(-2\pi i)\delta\left[(y+y_1)(z+z_1)s - (\mathbf{k}+\mathbf{k}_1)^2\right]\frac{1}{P_1P_2P_4P_5} \\ &+ \int_{-z_3}^{0} \mathrm{d}z \int \mathrm{d}y(-2\pi i)\delta\left[yzs - \mathbf{k}^2\right]\frac{1}{P_1P_2P_3P_4}.\end{aligned} \tag{B.5}$$

One can directly note that, once again, the variable z is negative in all the regions of interest and we shall use $-|z|$ instead of z. We come now to the calculation of the integrals.

Contribution s_1u_2

The first term is similar to the first term of the s_1s_2 integral and reads

$$\begin{aligned}\mathcal{I}_{su}^{c_1} &= \int_{-1}^{-z_3} \mathrm{d}z \int \mathrm{d}y(-2\pi i)\delta\left[y(1+z)s - \mathbf{k}^2\right]\frac{1}{P_2P_3P_4P_5} \\ &= \int_{-1}^{-z_3} \mathrm{d}z \frac{(-2\pi i)}{(1-|z|)s}\frac{1}{P_2P_3P_4P_5}\Big|_{y=\frac{\mathbf{k}^2}{(1-|z|)s}}.\end{aligned} \tag{B.6}$$

Among the remaining propagators, we only have to check the contribution of P_2 and P_4 to compute the z integral. The new propagator at the pole $y = \mathbf{k}^2/(1-|z|)s$ is

$$P_2\Big|_{y=\frac{\mathbf{k}^2}{(1-|z|)s}} = \left(1+\frac{\mathbf{k}^2}{(1-|z|)s}-\alpha\right)\left(\frac{\mathbf{k}_3^2}{(1-\alpha)s}-|z|\right)-(\mathbf{k}+\mathbf{k}_3)^2 \quad < 0, \tag{B.7}$$

and cannot be put on shell together with P_1. One is left with the contribution of P_4 as in the previous subsection and we compute

$$\begin{aligned}
\mathcal{I}^{c_1}_{su} &= \int_{-1}^{-z_3} \mathrm{d}z \frac{(-2\pi i)}{s}\frac{(-i\pi)}{\alpha s}\delta\left[|z|-\frac{(\mathbf{k}+\mathbf{k}_3)^2}{\alpha s}\right]\frac{1}{(p+k+k_3)^2(k+k_1)^2k^2}\Big|_{y=\frac{\mathbf{k}^2}{(1-|z|)s}} \\
&\simeq \frac{-2\pi^2}{(1-|z|)\alpha s^2}\frac{\alpha}{[-(\mathbf{k}+\mathbf{k}_3)^2]}\frac{1}{[-(\mathbf{k}+\mathbf{k}_1)^2]}\frac{(1-|z|)}{[-\mathbf{k}^2]} \\
&\simeq \frac{2\pi^2}{s^2}\frac{1}{(\mathbf{k}+\mathbf{k}_3)^2(\mathbf{k}+\mathbf{k}_1)^2\mathbf{k}^2},
\end{aligned} \tag{B.8}$$

in the small $|z|$ limit. Again, the result is equal, apart for the sign, to the usual cut contribution. The second term of Eq. (B.5) is now evaluated and one has to compute

$$\mathcal{I}^{c_2}_{su} = \int_{-z_1}^{-z_3} \mathrm{d}z \int \mathrm{d}y \frac{(-2\pi i)}{(\beta-|z|)s}\delta\left[y-\frac{\mathbf{k}_1^2}{(1-\beta)s}-\frac{(\mathbf{k}+\mathbf{k}_1)^2}{(\beta-|z|)s}\right]\frac{1}{P_1P_2P_4P_5}. \tag{B.9}$$

We first check the different propagators at the pole, detailing only the new one:

$$\begin{aligned}
P_5:&\quad k^2<0 \\
P_4:&\quad (k+k_3)^2<0 \\
P_1:&\quad (q+k)^2>0
\end{aligned} \tag{B.10}$$

$$P_2: \quad (p+k+k_3)^2 = \left(1+\frac{(\mathbf{k}+\mathbf{k}_1)^2}{(\beta-|z|)s}+\frac{\mathbf{k}_1^2}{(1-\alpha)s}-\alpha\right)\left(\frac{(\mathbf{k}_3^2}{(1-\alpha)s}-|z|\right)s-(\mathbf{k}+\mathbf{k}_3)^2<0.$$

As expected in the massless case, there is no contribution. However, in the massive case and along the same lines as before, the contribution yields

$$\mathcal{I}^{c_2}_{su} = \frac{-2\pi^2}{s^2}\frac{1}{(\mathbf{k}+\mathbf{k}_3)^2(\mathbf{k}+\mathbf{k}_1)^2\mathbf{k}^2}\times\Delta. \tag{B.11}$$

The quantity is the same but opposite in sign to the one of the s_1s_2 integral due to the crossing argument developed in Sec. 2.3.
Finally, we compute the third integral

$$\mathcal{I}^{c_3}_{su} = \int_{-z_3}^{0} \mathrm{d}z \int \frac{(-2\pi i)}{|z|s}\delta\left[-y-\frac{\mathbf{k}^2}{|z|s}\right]\frac{1}{P_1P_2P_3P_4}. \tag{B.12}$$

After evaluation of the four propagators at the pole, one can show that they are all negative definite. Any of them can be put on-shell together with P_5, giving no contribution. Actually, this is obvious taking into account the fact that if one cuts the diagram through the two-gluon legs, these gluons correspond to real particles and consequently to positive energies not allowed in the present kinematics.

B.2.2 Single-Crossed Diagram u_1s_2

The single-crossed diagram u_1s_2 is the second diagram of Fig. B.2. The above arguments can be repeated with only one change from the s_1s_2 diagram: P_1 now becomes

$$\begin{aligned} P_1 &= (q-k-k_1)^2 + i\epsilon \\ &= -(y+y_1)(1-z-z_1)s - (\mathbf{k}+\mathbf{k}_1)^2 + i\epsilon \\ \to y_{P_1} &= \frac{-(\mathbf{k}+\mathbf{k}_1)^2 + i\epsilon}{(1-z-z_1)s} - y_1. \end{aligned} \tag{B.13}$$

The position of the poles is shown in Fig. B.4, and one has to compute

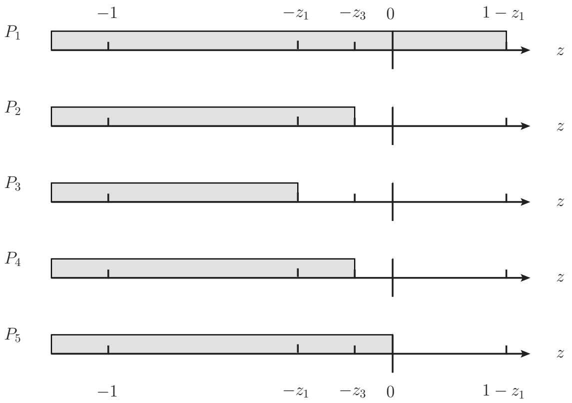

Figure B.4: Single-crossed diagram $u_1 s_2$: Positions of the y poles of the different propagators as functions of z. The shaded regions correspond to poles above the real axis while the unshaded ones to poles below the real axis.

$$\begin{aligned} \mathcal{I}_{u_1 s_2} &= \int_{-z_3}^{1-z_1} \mathrm{d}z \int \mathrm{d}y(-2\pi i)\delta\left[-(y+y_1)(1-z-z_1)s - (\mathbf{k}+\mathbf{k}_1)^2\right] \frac{1}{P_2P_3P_4P_5} \\ &+ \int_{-z_1}^{-z_3} \mathrm{d}z \int \mathrm{d}y(-2\pi i)\delta\left[(y+y_1)(z+z_1)s - (\mathbf{k}+\mathbf{k}_1)^2\right] \frac{1}{P_1P_2P_4P_5} \\ &+ \int_{-z_3}^{0} \mathrm{d}z \int \mathrm{d}y(-2\pi i)\delta\left[yzs - \mathbf{k}^2\right] \frac{1}{P_1P_2P_3P_4}. \end{aligned} \tag{B.14}$$

The last term is exactly the same as in the $s_1 u_2$ case so that one can directly check that the result is zero due to kinematical arguments. The second term is similar to the second term of Eq. (B.5) apart for the new propagator and one can then write the result

$$\mathcal{I}_{us}^{c_2} = \frac{-2\pi^2}{s^2} \frac{1}{(\mathbf{k}+\mathbf{k}_3)^2(\mathbf{k}+\mathbf{k}_1)^2\mathbf{k}^2} \times \Delta. \tag{B.15}$$

The first term is

$$\mathcal{I}_{us}^{c_1} = \int_{-z_3}^{1-z_1} \mathrm{d}z \frac{(-2\pi i)}{(1-z-\beta)s} \frac{1}{P_2P_3P_4P_5}\bigg|_{y=\frac{(\mathbf{k}+\mathbf{k}_1)^2}{(1-z-\beta)s} - \frac{\mathbf{k}_1^2}{(1-\beta)s}}. \tag{B.16}$$

Looking at the other propagators, only P_4 can give a contribution considering that it changes sign at $z = (\mathbf{k}+\mathbf{k}_3)^2/\alpha s$. This leads to

$$\mathcal{I}_{us}^{c_1} = \frac{2\pi^2}{s^2} \frac{1}{(\mathbf{k}+\mathbf{k}_3)^2(\mathbf{k}+\mathbf{k}_1)^2\mathbf{k}^2}. \tag{B.17}$$

Summary of Diagrams s_1u_2 and u_1s_2

The result for the two single-crossed diagrams is

$$\begin{aligned}\mathcal{I}_{s_1u_2}+\mathcal{I}_{u_2s_1}&=\mathcal{I}^{c_1}_{su}+\mathcal{I}^{c_2}_{su}+\mathcal{I}^{c_1}_{us}+\mathcal{I}^{c_2}_{us}\\&=\frac{2\pi^2}{s^2}\frac{1}{\mathbf{k}(\mathbf{k}+\mathbf{k}_1)^2(\mathbf{k}+\mathbf{k}_3)^2}\left[1-\Delta+1-\Delta\right].\end{aligned}\tag{B.18}$$

B.2.3 u_1u_2 Diagram

Now, we proceed to the evaluation of the double-crossed diagram, *i.e* the diagram where both quark lines are crossed. As previously, we focus on the longitudinal integral only. The five propagators of Fig. 2.3.c are

$$\begin{aligned}P_1&=(q-k-k_1)^2+i\epsilon\\&=-(y+y_1)(1-z-z_1)s-(\mathbf{k}+\mathbf{k}_1)^2+i\epsilon\\&\to y_{P_1}=\frac{-(\mathbf{k}+\mathbf{k}_1)^2+i\epsilon}{(1-z-z_1)s}-y_1,\\P_2&=(p+k+k_3)^2+i\epsilon\\&=(1+y+y_3)(z+z_3)s-(\mathbf{k}+\mathbf{k}_3)^2+i\epsilon\\&\to y_{P_2}=\frac{(\mathbf{k}+\mathbf{k}_3)^2-i\epsilon}{(z+z_3)s}-1-y_3,\\P_3&=(k+k_1)^2+i\epsilon\\&=(y+y_1)(z+z_1)s-(\mathbf{k}+\mathbf{k}_1)^2+i\epsilon\\&\to y_{P_3}=\frac{(\mathbf{k}+\mathbf{k}_1)^2-i\epsilon}{(z+z_1)s}-y_1,\\P_4&=(k+k_3)^2+i\epsilon\\&=(y+y_3)(z+z_3)s-(\mathbf{k}+\mathbf{k}_3)^2+i\epsilon\\&\to y_{P_4}=\frac{(\mathbf{k}+\mathbf{k}_3)^2-i\epsilon}{(z+z_3)s}-y_3,\\P_5&=k^2+i\epsilon\\&=yzs-\mathbf{k}^2+i\epsilon\\&\to y_{P_5}=\frac{\mathbf{k}^2-i\epsilon}{zs},\end{aligned}\tag{B.19}$$

and the position of their y poles are shown in Fig. B.5. The integration can be divided into three regions and one has

$$\begin{aligned}\mathcal{I}_{u_1u_2}=&\int_{-z_3}^{1-z_1}\mathrm{d}z\int\mathrm{d}y(-2\pi i)\delta\left[-(y+y_1)(1-z-z_1)s-(\mathbf{k}+\mathbf{k}_1)^2\right]\frac{1}{P_2P_3P_4P_5}\\&+\int_{-z_1}^{-z_3}\mathrm{d}z\int\mathrm{d}y(-2\pi i)\delta\left[(y+y_1)(z+z_1)s-(\mathbf{k}+\mathbf{k}_1)^2\right]\frac{1}{P_1P_2P_4P_5}\\&+\int_{-z_3}^{0}\mathrm{d}z\int\mathrm{d}y(-2\pi i)\delta\left[yzs-\mathbf{k}^2\right]\frac{1}{P_1P_2P_3P_4}.\end{aligned}\tag{B.20}$$

For the first term of Eq. (B.20), one has to compute

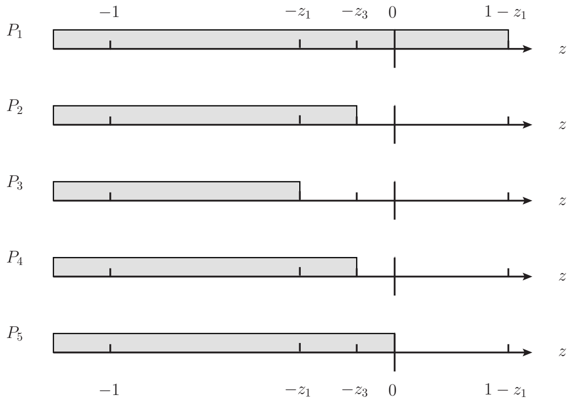

Figure B.5: Double-crossed diagram u_1s_2: Positions of the y poles of the different propagators as functions of z. The shaded regions correspond to poles above the real axis while the unshaded ones to poles below the real axis.

$$\begin{aligned}\mathcal{I}^{c_1} &= \int_{-z_3}^{1-z_1} \mathrm{d}z \int \mathrm{d}y \frac{(-2\pi i)}{(1-z-\beta)s} \delta\left[-y + \frac{\mathbf{k}_1^2}{(1-\beta)s} - \frac{(\mathbf{k}+\mathbf{k}_1)^2}{(1-z-\beta)}\right] \frac{1}{P_2P_3P_4P_5} \\ &= \int_{-z_3}^{1-z_1} \mathrm{d}z \frac{(-2\pi i)}{(1-z-\beta)s} \frac{1}{(p+k+k_3)^2(k+k_1)^2(k+k_3)^2k^2}\Bigg|_{y=\frac{-(\mathbf{k}+\mathbf{k}_1)^2}{(1-\beta-z)s}+\frac{\mathbf{k}_1^2}{(1-\beta)s}} .\end{aligned} \tag{B.21}$$

One only has to check propagators P_2 and P_4 due to the fact that P_5 and P_3 are negative at $y = y_{P_1}$. Propagators P_4 becomes

$$(k+k_3)^2\Big|_{y=y_{P_1}} = \left(\frac{-(\mathbf{k}+\mathbf{k}_1)^2}{(1-\beta-z)s} + \frac{\mathbf{k}_1^2}{(1-\beta)s} - \alpha\right)\left(z + \frac{\mathbf{k}_3^2}{(1-\alpha)s}\right)s - (\mathbf{k}+\mathbf{k}_3)^2 \quad < 0, \tag{B.22}$$

but P_2 is

$$(p+k+k_3)^2\Big|_{y=y_{P_1}} \simeq zs - (\mathbf{k}+\mathbf{k}_3)^2, \tag{B.23}$$

that has a pole at $z = (\mathbf{k}+\mathbf{k}_3)/s$ and can be used to compute the z integral. Therefore, substituting the value of z and y into the remaining propagators yields

$$\begin{aligned}\mathcal{I}^{c_1} &\simeq \frac{-2\pi^2}{s^2} \frac{1}{[-(\mathbf{k}+\mathbf{k}_1)^2]\,[-(\mathbf{k}+\mathbf{k}_3)^2]\,[-\mathbf{k}^2]} \\ &\simeq \frac{2\pi^2}{s^2} \frac{1}{(\mathbf{k}+\mathbf{k}_1)^2(\mathbf{k}+\mathbf{k}_3)^2\mathbf{k}^2} .\end{aligned} \tag{B.24}$$

The second term of Eq. (B.20) takes propagator P_3 on-shell. Due to kinematics, P_1 and P_5 are negative definite and there is no contribution in the massless case. If the produced particle is massive, one obtains

$$\mathcal{I}^{c_2} \simeq \frac{2\pi^2}{s^2} \frac{1}{(\mathbf{k}+\mathbf{k}_1)^2(\mathbf{k}+\mathbf{k}_3)^2\mathbf{k}^2} \times \Delta, \tag{B.25}$$

with the same sign as in the s_1s_2 diagram calculation according to the argument developed in Sec. 2.3.

The third term gives no contribution since the on-shellness of propagator P_5 is incompatible with any other on-shell condition in the considered kinematics.

Summary of Diagram u_1u_2

Putting together all the results of the u_1u_2 diagram gives

$$\begin{aligned}\mathcal{I}_{u_1u_2} &= \mathcal{I}^{c_1} + \mathcal{I}^{c_2} \\ &= \frac{2\pi^2}{s^2}\frac{1}{(\mathbf{k}+\mathbf{k}_1)^2(\mathbf{k}+\mathbf{k}_3)^2\mathbf{k}^2}\left[1+\Delta\right].\end{aligned} \tag{B.26}$$

B.2.4 Comparison of the Two Main Diagrams

Consider the production of a colour-singlet two-gluon state in a qq collision. The only requirement is that the two-gluon system be separated in rapidity from the quarks and that there be no overall colour flow in the t-channel. Hence, the kinematics and all simplifications discussed in Sec. 2.1 and Sec. 2.1.2 still hold, and one is left with the two generic diagrams shown in Fig. B.6. From the BFKL point of view, one deals here with two-gluon production in quasi-multi-Regge kinematics and the imaginary part of the amplitude can be written

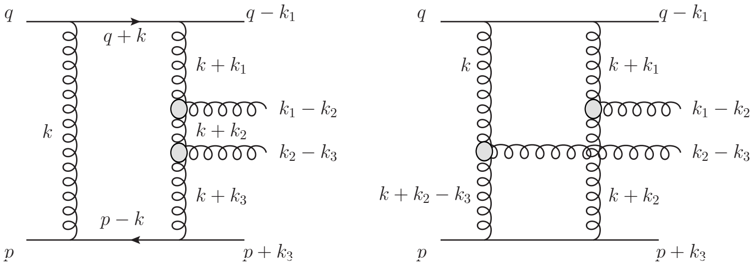

Figure B.6: Contribution to the imaginary part of the amplitude at leading order for the two-gluons production.

$$\begin{aligned}\mathrm{Im}\mathcal{M} = \mathrm{Im}\mathcal{M}_a + \mathrm{Im}\mathcal{M}_b = s\frac{g_s^2 g^6}{2\pi^2}\frac{\delta^{c_1c_2}}{4N}\int \mathrm{d}^2\mathbf{k} \quad e^{(1)*}_{\mu_1}e^{(2)*}_{\mu_2} \\ \times\left[\frac{C^{\mu_1}(k+k_1,k+k_2)C^{\mu_2}(k+k_2,k+k_3)}{\mathbf{k}^2(\mathbf{k}+\mathbf{k}_1)^2(\mathbf{k}+\mathbf{k}_2)^2(\mathbf{k}+\mathbf{k}_3)^2} - \frac{C^{\mu_1}(k+k_1,k+k_2)C^{\mu_2}(-k,-k-k_2+k_3)}{\mathbf{k}^2(\mathbf{k}+\mathbf{k}_1)^2(\mathbf{k}+\mathbf{k}_2)^2(\mathbf{k}-\mathbf{k}_2+\mathbf{k}_3)^2}\right].\end{aligned} \tag{B.27}$$

Here $C^{\mu_i}(p_1,p_2)$ is the Lipatov effective vertex [160]

$$C^{\mu_1}(k+k_1,k+k_2) = p^{\mu_1}\left(\alpha_1 - 2\frac{(\mathbf{k}+\mathbf{k}_2)^2}{\beta_1 s}\right) - q^{\mu_1}\left(\beta_1 - 2\frac{(\mathbf{k}+\mathbf{k}_1)^2}{\alpha_1 s}\right) + (2\mathbf{k}+\mathbf{k}_1+\mathbf{k}_2)^{\mu_1}. \tag{B.28}$$

When $|\mathbf{k}_2| \gg |\mathbf{k}_1|, |\mathbf{k}_3|$, one recovers from Eq. (B.27) the amplitude (2.74) described in the main text. The two terms describe the respective contributions of the two diagrams and let us estimate how the contribution of the second diagram compares with that of the first one in the case of large $\mathbf{k}_2^2$ and, for simplicity, for $\beta_1 \gg \beta_2$. The square of the first diagram is

$$\begin{aligned}|\mathrm{Im}\mathcal{M}_a|^2 \propto & \int \frac{\mathrm{d}^2\mathbf{k}}{\mathbf{k}^2(\mathbf{k}+\mathbf{k}_2)^2}\frac{\mathrm{d}^2\mathbf{k}'}{\mathbf{k}'^2(\mathbf{k}'+\mathbf{k}_2)^2} \\ & \times \frac{-2}{(\mathbf{k}+\mathbf{k}_1)^2(\mathbf{k}'+\mathbf{k}_1)^2}\left[\frac{(\mathbf{k}+\mathbf{k}_1)^2(\mathbf{k}'+\mathbf{k}_2)^2+(\mathbf{k}+\mathbf{k}_2)^2(\mathbf{k}'+\mathbf{k}_1)^2}{(\mathbf{k}_1-\mathbf{k}_2)^2}-(\mathbf{k}-\mathbf{k}')^2\right] \\ & \times \frac{-2}{(\mathbf{k}+\mathbf{k}_3)^2(\mathbf{k}'+\mathbf{k}_3)^2}\left[\frac{(\mathbf{k}+\mathbf{k}_3)^2(\mathbf{k}'+\mathbf{k}_2)^2+(\mathbf{k}+\mathbf{k}_2)^2(\mathbf{k}'+\mathbf{k}_3)^2}{(\mathbf{k}_3-\mathbf{k}_2)^2}-(\mathbf{k}-\mathbf{k}')^2\right] \\ & \simeq \frac{16}{(\mathbf{k}_2^2)^2}\int\frac{\mathrm{d}^2\mathbf{k}}{\mathbf{k}^2}\frac{\mathrm{d}^2\mathbf{k}'}{\mathbf{k}'^2}\frac{(\mathbf{k}+\mathbf{k}_1).(\mathbf{k}'+\mathbf{k}_1)}{(\mathbf{k}+\mathbf{k}_1)^2(\mathbf{k}'+\mathbf{k}_1)^2}\frac{(\mathbf{k}+\mathbf{k}_3).(\mathbf{k}'+\mathbf{k}_3)}{(\mathbf{k}+\mathbf{k}_3)^2(\mathbf{k}'+\mathbf{k}_3)^2}.\end{aligned} \tag{B.29}$$

For nearly forward scattering, $|\mathbf{k}_1|, |\mathbf{k}_3| \ll |\mathbf{k}|, |\mathbf{k}'|$, the estimate simplifies to

$$|\mathrm{Im}\mathcal{M}_a|^2 \propto \frac{1}{(\mathbf{k}_2^2)^2}\int\frac{\mathrm{d}^2\mathbf{k}}{(\mathbf{k}^2)^2}\frac{\mathrm{d}^2\mathbf{k}'}{(\mathbf{k}'^2)^2} \quad\rightarrow\quad |\mathrm{Im}\mathcal{M}_a| \propto \frac{1}{\mathbf{k}_2^2}\int\frac{\mathrm{d}^2\mathbf{k}}{(\mathbf{k}^2)^2}. \tag{B.30}$$

A similar calculation for the second diagram gives

$$\begin{aligned}|\mathrm{Im}\mathcal{M}_b|^2 \propto & \int \frac{\mathrm{d}^2\mathbf{k}}{\mathbf{k}^2(\mathbf{k}+\mathbf{k}_2)^2}\frac{\mathrm{d}^2\mathbf{k}'}{\mathbf{k}'^2(\mathbf{k}'+\mathbf{k}_2)^2} \\ & \times \frac{-2}{(\mathbf{k}+\mathbf{k}_1)^2(\mathbf{k}'+\mathbf{k}_1)^2}\left[\frac{(\mathbf{k}+\mathbf{k}_1)^2(\mathbf{k}'+\mathbf{k}_2)^2+(\mathbf{k}+\mathbf{k}_2)^2(\mathbf{k}'+\mathbf{k}_1)^2}{(\mathbf{k}_1-\mathbf{k}_2)^2}-(\mathbf{k}-\mathbf{k}')^2\right] \\ & \times \frac{-2}{(\mathbf{k}+\mathbf{k}_2-\mathbf{k}_3)^2(\mathbf{k}'+\mathbf{k}_2-\mathbf{k}_3)^2}\left[\frac{(\mathbf{k}+\mathbf{k}_2-\mathbf{k}_3)^2\mathbf{k}'^2+\mathbf{k}^2(\mathbf{k}'+\mathbf{k}_2-\mathbf{k}_3)^2}{(\mathbf{k}_3-\mathbf{k}_2)^2}-(\mathbf{k}-\mathbf{k}')^2\right] \\ & \simeq \frac{16}{(\mathbf{k}_2^2)^2}\int\frac{\mathrm{d}^2\mathbf{k}}{\mathbf{k}^2}\frac{\mathrm{d}^2\mathbf{k}'}{\mathbf{k}'^2}\frac{(\mathbf{k}+\mathbf{k}_1).(\mathbf{k}'+\mathbf{k}_1)}{(\mathbf{k}+\mathbf{k}_1)^2(\mathbf{k}'+\mathbf{k}_1)^2}\frac{\mathbf{k}.\mathbf{k}'}{(\mathbf{k}_2^2)^2},\end{aligned} \tag{B.31}$$

which in the same limit becomes

$$|\mathrm{Im}\mathcal{M}_b|^2 \propto \frac{1}{(\mathbf{k}_2^2)^4}\int\frac{\mathrm{d}^2\mathbf{k}}{(\mathbf{k}^2)^2}\frac{\mathrm{d}^2\mathbf{k}'}{(\mathbf{k}'^2)^2} \quad\rightarrow\quad |\mathrm{Im}\mathcal{M}_b| \propto \frac{1}{(\mathbf{k}_2^2)^2}\int\frac{\mathrm{d}^2\mathbf{k}}{(\mathbf{k}^2)^2}. \tag{B.32}$$

Thus, the second diagram is not only suppressed with respect to Eq. (B.30) by an extra power of $\mathbf{k}_2^2$, but also enhanced by an extra logarithm.

B.2.5 The Second Diagram

We give here some details on the calculation of the diagram where the final gluon system is emitted from different t-channel gluon legs. As explained in Sec. 2.7.1, we use the Lipatov vertices and we work in the center-of-mass frame of the colliding gluons. One has to calculate

$$\begin{aligned}\mathrm{Im}\mathcal{M}_s = & \, s\frac{g_s^2 g^4}{(2\pi)^2}\frac{\delta^{c_1c_2}}{4N}\int\frac{\mathrm{d}^2\mathbf{k}}{\mathbf{k}^2(\mathbf{k}+\mathbf{k}_1)^2(\mathbf{k}+\mathbf{k}_2)^2(\mathbf{k}+\mathbf{k}_2-\mathbf{k}_3)^2} \\ & \times C_1^{\mu_1}(k+k_1, k+k_2)\, C_2^{\mu_2}(-k_1, -k-k_2+k_3)\,.e^*_{\mu_1}(\lambda_3)e^*_{\mu_2}(\lambda_4).\end{aligned} \tag{B.33}$$

B.2.6 Kinematics

The main part of the calculation is the evaluation of the contraction of the Lipatov vertices with the polarisation vectors $e^*_{\mu_1}(\lambda_3)e^*_{\mu_2}(\lambda_4)$. These vectors are written in the center-of-mass frame of the final gluons but the Lipatov vertices depend on two opposite light-cone vectors q^μ and p^μ. Thus, one has to calculate the contraction in a specific frame. We perform a longitudinal boost so that the energies of the two colliding gluons are identical. Then

$$\begin{aligned} q^\mu &= \frac{q_+}{\sqrt{2}}(1,0,0,1), \\ p^\mu &= \frac{p_-}{\sqrt{2}}(1,0,0,-1), \\ s &= 2\,p^\mu q_\mu = 2\,p^- q_+ . \end{aligned} \tag{B.34}$$

The new frame is defined by the center-of-mass frame of the collision with energy

$$\begin{aligned} E &= (\beta_1+\beta_2)\frac{q_+}{\sqrt{2}} \\ &= (\alpha_1+\alpha_2)\frac{p_-}{\sqrt{2}}, \end{aligned} \tag{B.35}$$

from the usual definition of β_i and α_i and the kinematics shown of Fig. B.7. As usual, one can consider $\mathbf{k}_2^2 \gg \mathbf{k}_i^2$ and let us remind the reader of two relations coming from the on-shellness of the final gluons $(k_1-k_2)^2 = 0 = (k_2-k_3)^2$ that gives

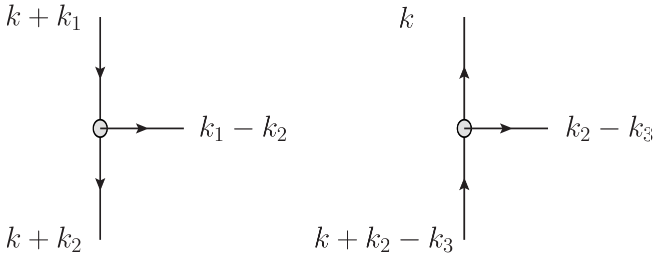

Figure B.7: Kinematics.

$$\beta_1\alpha_1 \simeq \beta_2\alpha_2 \simeq \frac{(\mathbf{k}_1-\mathbf{k}_2)^2}{s}, \qquad \frac{\alpha_1}{\alpha_1+\alpha_2} = \frac{\beta_2}{\beta_1+\beta_2}. \tag{B.36}$$

One can identify the xz plane with the scattering plane and the final gluons in this specific frame have four-momenta

$$\begin{aligned} (k_1-k_2)^\mu &= \beta_1 q^\mu + \alpha_1 p^\mu + (k_1-k_2)^\mu \\ &= E\frac{\beta_1}{\beta_1+\beta_2}(1,0,0,1) + E\frac{\alpha_1}{\alpha_1+\alpha_2}(1,0,0,-1) - (\mathbf{k}_1-\mathbf{k}_2) \\ &= \left(E, -(\mathbf{k}_1-\mathbf{k}_2), E\,\frac{\beta_1-\beta_2}{\beta_1+\beta_2}\right), \\ (k_2-k_3)^\mu &= \beta_2 q^\mu + \alpha_2 p^\mu + (k_2-k_3)^\mu \\ &= E\frac{\beta_2}{\beta_1+\beta_2}(1,0,0,1) + E\frac{\alpha_2}{\alpha_1+\alpha_2}(1,0,0,-1) + (\mathbf{k}_2-\mathbf{k}_3) \\ &= \left(E, (\mathbf{k}_2-\mathbf{k}_3), E\,\frac{\beta_1-\beta_2}{\beta_1+\beta_2}\right). \end{aligned} \tag{B.37}$$

In the center-of-mass frame of the produced gluons one can write

$$\begin{aligned}(k_1-k_2)^\mu &= E\,(1,\sin\theta_1,0,\cos\theta_1)\,,\\ (k_2-k_3)^\mu &= E\,(1,-\sin\theta_2,0,-\cos\theta_2)\,,\end{aligned} \tag{B.38}$$

as the two gluons are almost back-to-back with $\theta_1 \simeq \theta_2 \simeq \theta$. One can identify the component of Eq. (B.37) and Eq. (B.38) to obtain

$$\begin{aligned}E\sin\theta &= (\mathbf{k}_1-\mathbf{k}_2)^2,\\ \cos\theta &= \frac{\beta_1-\beta_2}{\beta_1+\beta_2}.\end{aligned} \tag{B.39}$$

Using

$$\frac{q_+}{p_-} = \frac{\alpha_1+\alpha_2}{\beta_1+\beta_2}, \tag{B.40}$$

one finds

$$\begin{aligned}\sin^2\theta &= \frac{(\mathbf{k}_1-\mathbf{k}_2)^2}{E^2}\\ &= \frac{\alpha_1\beta_1 s}{\mathbf{q}^2(\beta_1+\beta_2)}\\ &= \frac{4\beta_1\beta_2}{(\beta_1+\beta_2)^2}\\ \rightarrow \sin\theta &= \frac{2\sqrt{\beta_1\beta_2}}{\beta_1+\beta_2}.\end{aligned} \tag{B.41}$$

With these relations, one can now compute the contraction of the two Lipatov vertices with their respective polarisation vectors.

B.2.7 Contraction with the First Lipatov Vertex

The first Lipatov vertex only depends on the longitudinal component of the final gluon and has the form

$$C_1^{\mu_1}(k+k_1,k+k_2) = q^{\mu_1}\left(\beta_1 - 2\frac{(\mathbf{k}+\mathbf{k}_1)^2}{\alpha_1 s}\right) - p^{\mu_1}\left(\alpha_1 - 2\frac{(\mathbf{k}+\mathbf{k}_2)^2}{\beta_1 s}\right) - (2\mathbf{k}+\mathbf{k}_1+\mathbf{k}_2)^{\mu_1}, \tag{B.42}$$

that can be written in our specific frame in terms of its components

$$C_1 = (C_0, -(2\mathbf{k}+\mathbf{k}_1+\mathbf{k}_2)_x, -(2\mathbf{k}+\mathbf{k}_1+\mathbf{k}_2)_y, C_z)\,, \tag{B.43}$$

where

$$\begin{aligned}C_0 &= \frac{q^+}{\sqrt{2}}\left(\beta_1 - 2\frac{(\mathbf{k}+\mathbf{k}_1)^2}{\alpha_1 s}\right) - \frac{p^+}{\sqrt{2}}\left(\alpha_1 - 2\frac{(\mathbf{k}+\mathbf{k}_2)^2}{\beta_1 s}\right)\\ &= \frac{E}{\beta_1+\beta_2}\left(\beta_1 - 2\frac{(\mathbf{k}+\mathbf{k}_1)^2}{\alpha_1 s}\right) - \frac{E}{\alpha_1+\alpha_2}\left(\alpha_1 - 2\frac{(\mathbf{k}+\mathbf{k}_2)^2}{\beta_1 s}\right)\\ &= \frac{E}{\beta_1+\beta_2}\left(\beta_1 - 2(\mathbf{k}+\mathbf{k}_1)^2\frac{\beta_1}{(\mathbf{k}_1-\mathbf{k}_2)^2}\right) - \frac{E}{\alpha_1+\alpha_2}\left(\alpha_1 - 2(\mathbf{k}+\mathbf{k}_2)^2\frac{\alpha_1}{(\mathbf{k}_1-\mathbf{k}_2)^2}\right),\end{aligned} \tag{B.44}$$

using the on-shell condition $\beta_1 s = (\mathbf{k}_1 - \mathbf{k}_2)^2/\alpha_1$. After a little bit of algebra with the help of the relations (B.39) and (B.41), one finds

$$\begin{aligned} C_0 &= E\left[\cos\theta + (1-\cos\theta)\frac{(\mathbf{k}+\mathbf{k}_2)^2}{(\mathbf{k}_1-\mathbf{k}_2)^2} - (1+\cos\theta)\frac{(\mathbf{k}+\mathbf{k}_1)^2}{(\mathbf{k}_1-\mathbf{k}_2)^2}\right], \\ C_z &= E\left[1 - (1+\cos\theta)\frac{(\mathbf{k}+\mathbf{k}_1)^2}{(\mathbf{k}_1-\mathbf{k}_2)^2} - (1-\cos\theta)\frac{(\mathbf{k}+\mathbf{k}_2)^2}{(\mathbf{k}_1-\mathbf{k}_2)^2}\right]. \end{aligned} \tag{B.45}$$

Now, one can define the polarisation vector of the produced gluon with helicity λ_3 as

$$e^\mu(\lambda_3) = -\frac{1}{\sqrt{2}}\left(0, \lambda_3\cos\theta, i, -\lambda_3\sin\theta\right), \tag{B.46}$$

and check that

$$e^\mu(\lambda_3)(k_1-k_2)_\mu = \frac{E}{\sqrt{2}}\lambda_3\cos\theta\sin\theta - \frac{E}{\sqrt{2}}\lambda_3\cos\theta\sin\theta = 0. \tag{B.47}$$

Therefore, the contraction of the above polarisation vector with the Lipatov vertex is

$$\begin{aligned} C_1^{\mu_1} e^*_{\mu_1}(\lambda_3) &= (C_0, -(2\mathbf{k}+\mathbf{k}_1+\mathbf{k}_2)_x, -(2\mathbf{k}+\mathbf{k}_1+\mathbf{k}_2)_y, C_z)\,\frac{1}{\sqrt{2}}\begin{pmatrix} 0 \\ \lambda_3\cos(\theta) \\ -i \\ -\lambda_3\sin(\theta)\end{pmatrix} \\ &= \frac{1}{\sqrt{2}}\big[0 - \lambda_3\cos\theta(2\mathbf{k}+\mathbf{k}_1+\mathbf{k}_2)_x + i(2\mathbf{k}+\mathbf{k}_1+\mathbf{k}_2)_y \\ &\quad -E\lambda_3\sin\theta\left(1-(1+\cos\theta)\frac{(\mathbf{k}+\mathbf{k}_1)^2}{(\mathbf{k}_1-\mathbf{k}_2)^2} - (1-\cos\theta)\frac{(\mathbf{k}+\mathbf{k}_2)^2}{(\mathbf{k}_1-\mathbf{k}_2)^2}\right)\bigg] \\ &= \frac{1}{\sqrt{2}}\big[-\lambda_3\cos\theta(2\mathbf{k}+\mathbf{k}_1+\mathbf{k}_2)_x + i(2\mathbf{k}+\mathbf{k}_1+\mathbf{k}_2)_y \\ &\quad -\lambda_3|\mathbf{k}_1-\mathbf{k}_2|\theta\left(1-(1+\cos\theta)\frac{(\mathbf{k}+\mathbf{k}_1)^2}{(\mathbf{k}_1-\mathbf{k}_2)^2} - (1-\cos\theta)\frac{(\mathbf{k}+\mathbf{k}_2)^2}{(\mathbf{k}_1-\mathbf{k}_2)^2}\right)\bigg]. \end{aligned} \tag{B.48}$$

One can choose to define the x axis as the direction of the first produced gluon, so that for any four-vector a, its x component is defined as

$$a_x = \mathbf{a}\frac{\mathbf{k}_1-\mathbf{k}_2}{|\mathbf{k}_1-\mathbf{k}_2|}. \tag{B.49}$$

Hence, in Eq. (B.48), one has

$$\begin{aligned} (2\mathbf{k}+\mathbf{k1}+\mathbf{k}_2)_x &= \left[(\mathbf{k}+\mathbf{k}_1)+(\mathbf{k}+\mathbf{k}_2)\right]\frac{\mathbf{k}_1-\mathbf{k}_2}{|\mathbf{k}_1-\mathbf{k}_2|} \\ &= \left[(\mathbf{k}+\mathbf{k}_1)+(\mathbf{k}+\mathbf{k}_2)\right]\frac{(\mathbf{k}+\mathbf{k}_1)-(\mathbf{k}+\mathbf{k}_2)}{|(\mathbf{k}+\mathbf{k}_1)-(\mathbf{k}+\mathbf{k}_2)|} \\ &= \frac{(\mathbf{k}+\mathbf{k}_1)^2-(\mathbf{k}+\mathbf{k}_2)^2}{|(\mathbf{k}+\mathbf{k}_1)-(\mathbf{k}+\mathbf{k}_2)|}. \end{aligned} \tag{B.50}$$

The y component can also be calculated

$$\begin{aligned} \left[(\mathbf{k}+\mathbf{k}_1)+(\mathbf{k}+\mathbf{k}_2)\right]_y^2 &= |(\mathbf{k}+\mathbf{k}_1)+(\mathbf{k}+\mathbf{k}_2)|^2 - \left[(\mathbf{k}+\mathbf{k}_1)+(\mathbf{k}+\mathbf{k}_2)\right]_x, \\ \to \left[(\mathbf{k}+\mathbf{k}_1)+(\mathbf{k}+\mathbf{k}_2)\right]_y &= 2\frac{\sqrt{(\mathbf{k}+\mathbf{k}_1)^2(\mathbf{k}+\mathbf{k}_2)^2-(\mathbf{k}+\mathbf{k}_1).(\mathbf{k}+\mathbf{k}_2)}}{|(\mathbf{k}+\mathbf{k}_1)-(\mathbf{k}+\mathbf{k}_2)|}, \end{aligned} \tag{B.51}$$

and if one decomposes the scalar product using

$$(\mathbf{k}+\mathbf{k}_1).(\mathbf{k}+\mathbf{k}_2) = |\mathbf{k}+\mathbf{k}_1||\mathbf{k}+\mathbf{k}_2|\,\cos\psi_{12}, \tag{B.52}$$

where $\psi_{12} = \psi_1 - \psi_2$ is the angle between the two vectors in the transverse plane, the component reads

$$\begin{aligned}[(\mathbf{k}+\mathbf{k}_1)+(\mathbf{k}+\mathbf{k}_2)]_y^2 &= |\mathbf{k}+\mathbf{k}_1|^2 - (\mathbf{k}+\mathbf{k}_1)_x^2 \\ &= 4\frac{|\mathbf{k}+\mathbf{k}_1|^2|\mathbf{k}+\mathbf{k}_2|^2}{|(\mathbf{k}+\mathbf{k}_1)-(\mathbf{k}+\mathbf{k}_2)|^2}\,\sin^2\psi_{12}.\end{aligned} \tag{B.53}$$

The different angles are shown in Fig. B.8 and now one can complete the contraction, back to Eq. (B.48), using the definition of the x and y components

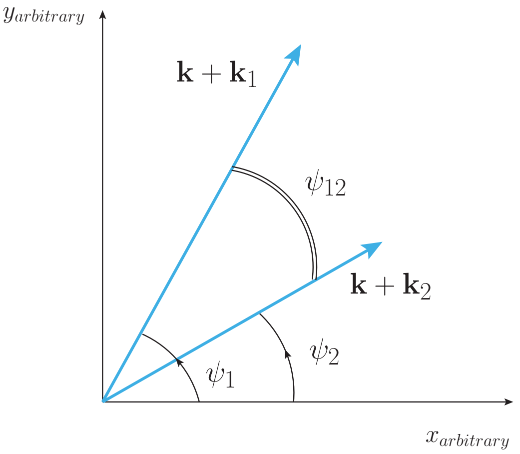

Figure B.8: Definition of the angles in the arbitrary system of axis.

$$\begin{aligned}C_1^{\mu_1}e^*_{\mu_1}(\lambda_3) &= \frac{1}{\sqrt{2}}\left[i((\mathbf{k}+\mathbf{k}_1)+(\mathbf{k}+\mathbf{k}_2))_y - \lambda_3|(\mathbf{k}+\mathbf{k}_1)-(\mathbf{k}+\mathbf{k}_2)| + \lambda_3\frac{(\mathbf{k}+\mathbf{k}_1)^2+(\mathbf{k}+\mathbf{k}_2)^2}{[(\mathbf{k}+\mathbf{k}_1)-(\mathbf{k}+\mathbf{k}_2)]}\right] \\ &= \frac{1}{\sqrt{2}}\left[i((\mathbf{k}+\mathbf{k}_1)+(\mathbf{k}+\mathbf{k}_2))_y + \lambda_3\frac{(\mathbf{k}+\mathbf{k}_1).(\mathbf{k}+\mathbf{k}_2)}{|(\mathbf{k}+\mathbf{k}_1)-(\mathbf{k}+\mathbf{k}_2)|}\right] \\ &= \sqrt{2}\frac{|\mathbf{k}+\mathbf{k}_1||\mathbf{k}+\mathbf{k}_2|}{|(\mathbf{k}+\mathbf{k}_1)-(\mathbf{k}+\mathbf{k}_2)|}\left(\lambda_3\cos\psi_{12} - i\sin\psi_{12}\right).\end{aligned} \tag{B.54}$$

Taking into account that the helicity has only two possible values, $\lambda_3 = \pm 1$, one can write the final result as

$$C_1^{\mu_1}e^*_{\mu_1}(\lambda_3) = \sqrt{2}\frac{|\mathbf{k}+\mathbf{k}_1||\mathbf{k}+\mathbf{k}_2|}{|\mathbf{k}_1-\mathbf{k}_2|}\lambda_3 e^{-i\lambda_3\psi_{12}}. \tag{B.55}$$

Actually, the same calculation can be done for the second Lipatov vertex of Fig. B.7 and one finds

$$C_2^{\mu_2}e^*_{\mu_2}(\lambda_4) = -\sqrt{2}\frac{|\mathbf{k}||\mathbf{k}+\mathbf{k}_2-\mathbf{k}_3|}{|\mathbf{k}_1-\mathbf{k}_2|}\lambda_4 e^{-i\lambda_4\psi_{23}}. \tag{B.56}$$

B.3 Sudakov Form Factor

We develop here some of the calculations of Chap. 4 that is devoted to the Sudakov form factor. The first section describes the original Dokshitzer, Diakonov and Troian or DDT prescription [111] and the second, the Durham parametrisation of the Sudakov form factor in the Monte-Carlo picture [16]. One can note that they only differ by the way they regularise the splitting function P_{gg}. For simplicity, the analytic calculation is done at fixed coupling constant, nevertheless, the final results of the whole thesis are obtained numerically with a running coupling. The present computation is just an approximation used in order to have a better view of the different contributions to the Sudakov form factor.

B.3.1 The DDT Prescription

The DDT calculation of the Sudakov form factor makes use of a regularised splitting function in the argument of the exponential. One has thus to compute

$$\begin{aligned} S_{DDT}(\mu^2, \ell^2) &= \frac{\alpha_s}{2\pi} \int_{\ell^2}^{\mu^2} \frac{\mathrm{d}\mathbf{q}^2}{\mathbf{q}^2} \int_0^1 \mathrm{d}z \left[z P_{gg} + N_f P_{qg} \right], \\ P_{gg} &= 2N_c \left[\frac{z}{1-z+\Delta} + \frac{1-z}{z} + z(1-z) \right], \\ P_{qg} &= \frac{1}{2} \left[z^2 + (1-z)^2 \right], \end{aligned} \tag{B.57}$$

where $N_c = 3$ is the number of colours and N_f the number of flavours. The integral over the second splitting function P_{qg} is straightforward, and one gets

$$N_f \int_0^1 P_{qg}\, \mathrm{d}z = \frac{N_f}{2} \int_0^1 \mathrm{d}z \left[z^2 + (1-z)^2 \right] = \frac{1}{3} N_f, \tag{B.58}$$

while the first term gives

$$\begin{aligned} 6 \int_0^1 z P_{gg}\, \mathrm{d}z &= 6 \int_0^1 \mathrm{d}z \left[1 - z + z^2 - z^3 \right] + 6 \int_0^1 \mathrm{d}z \frac{z^2}{1-z+\Delta} \\ &= \frac{7}{2} + \left[6(1+\Delta)^2 \log\left(\frac{1+\Delta}{\Delta} \right) - 9 - 6\Delta \right] \\ &= -\frac{11}{2} - 6\Delta + 6(1+\Delta)^2 \left[\log(1+\Delta) - \log(\Delta) \right], \end{aligned} \tag{B.59}$$

with the help of

$$\int \frac{x^2}{ax+b} \mathrm{d}x = \frac{1}{a^3} \left[\frac{1}{2}(ax+b)^2 - 2b(ax+b) + b^2 \log|ax+b| \right]. \tag{B.60}$$

To obtain the second integral, one can use $\Delta = |\mathbf{q}|/\mu$ with the change of variable

$$\int_{\ell^2}^{\mu^2} \frac{\mathrm{d}\mathbf{q}^2}{\mathbf{q}^2} \to 2 \int_\delta^1 \frac{\mathrm{d}\Delta}{\Delta}, \tag{B.61}$$

where $\delta = \ell^2/\mu^2$. The terms that do not include logs can be calculated directly and give

$$\begin{aligned} \mathcal{I}_1 &= 2 \int_\delta^1 \frac{\mathrm{d}\Delta}{\Delta} \left[\frac{-11}{2} + \frac{1}{3} N_f - 6\Delta \right] \\ &= \left(-11 + \frac{2}{3} N_f \right) \log \frac{1}{\delta} - 12 + 12\delta. \end{aligned} \tag{B.62}$$

The rest of the integral is

$$\mathcal{I}_2 = 12\left[\int_\delta^1 \frac{\mathrm{d}\Delta}{\Delta}(1+\Delta)^2\log(1+\Delta) - \int_\delta^1 \frac{\mathrm{d}\Delta}{\Delta}(1+\Delta)^2\log\Delta\right], \tag{B.63}$$

and can be calculated using the first-order Taylor expansion of the logarithm $\log(1+\Delta) \simeq \Delta$ as well as

$$\int \Delta\log\Delta\mathrm{d}\Delta = \frac{1}{2}\left(\Delta^2\log\Delta - \frac{\Delta^2}{2}\right), \tag{B.64}$$

that is a good approximation as there is no large Δ involved. The final result for $\mathcal{I}_2$ is

$$\mathcal{I}_2 = 6\log^2\frac{1}{\delta} - 6\delta(4+\delta)\log\frac{1}{\delta} - 4\delta^3 - 15\delta^2 - 36\delta + 55. \tag{B.65}$$

Because δ is small, one can neglect all terms proportional to it and, finally, the double- and single-log contributions to the Sudakov form factor are

$$S_{DDT}(\mu^2,\ell^2) \simeq \frac{\alpha_s}{2\pi}\left[6\log^2\frac{1}{\delta} + (-11+\frac{2}{3}N_f)\log\frac{1}{\delta}\right]. \tag{B.66}$$

All other contributions constitute the constant term

$$c_{DDT} = -6\delta(4+\delta)\log\frac{1}{\delta} - 4\delta^3 - 15\delta^2 - 24\delta + 43. \tag{B.67}$$

One can note that the single-log term comes in part from P_{gg} and in part from P_{qg} and that the two contributions are opposite in sign.

B.3.2 The Cut-Off Prescription

The definition of the Sudakov form factor makes use of the unregularised splitting function in the argument of the exponential. The divergence is removed by the addition of a cut-off to the upper limit of the longitudinal integral. One has to compute

$$\begin{aligned} S_{CO}(\mu^2,\ell^2) &= \frac{\alpha_s}{2\pi}\int_{\ell^2}^{\mu^2}\frac{\mathrm{d}\mathbf{q}^2}{\mathbf{q}^2}\int_0^{1-\Delta}\mathrm{d}z\,[zP_{gg} + N_f P_{qg}], \\ P_{gg} &= 6\left[\frac{z}{1-z} + \frac{1-z}{z} + z(1-z)\right], \\ P_{qg} &= \frac{1}{2}\left[z^2 + (1-z)^2\right]. \end{aligned} \tag{B.68}$$

Following the same line as in the DDT case, the first integral gives

$$\begin{aligned} \int_0^{1-\Delta} zP_{gg}\,\mathrm{d}z &= -\frac{11}{2} + 12\Delta - 9\Delta^2 + 4\Delta^3 - \frac{3}{2}\Delta^4 - 6\log\Delta, \\ N_f\int_0^{1-\Delta} P_{qg}\,\mathrm{d}z &= \frac{1}{2}N_f\left[\frac{2}{3} - \Delta + \Delta^2 - \frac{1}{3}\Delta^3\right]. \end{aligned} \tag{B.69}$$

After the change of variable and the integration over Δ, the dominant log contributions are identical to those of the DDT prescription

$$S_{CO}(\mu^2,\ell^2) \simeq \frac{\alpha_s}{2\pi}\left[6\log^2\frac{1}{\delta} + (-11+\frac{2}{3}N_f)\log\frac{1}{\delta}\right], \tag{B.70}$$

but the constant terms are slightly different

$$c_{CO} = \frac{1}{6}\left(\frac{203}{2} - \frac{13}{3}N_f\right) + \delta\left(N_f - 24\right) + \delta^2\left(9 - \frac{N_f}{2}\right) + \frac{2}{3}\delta^3\left(\frac{N_f}{3} - 4\right) + \frac{3}{4}\delta^4. \tag{B.71}$$

The two different prescriptions are presented in Fig. B.9 and clearly show the importance of the constant terms.

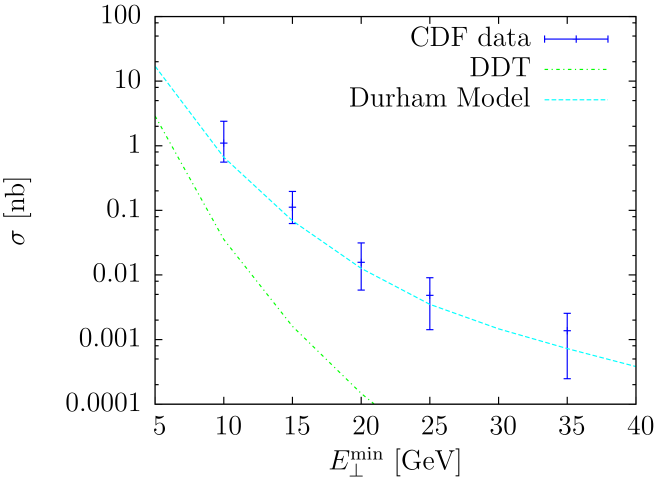

Figure B.9: Comparison of the DDT and cut-off prescriptions for the Sudakov form factor using the parametrisation of the reference curve in Table 6.2.

B.3.3 The Sudakov Form Factor with Two Scales

The leading double-log behaviour (DLA) of the Sudakov form factor can be computed analytically for a fixed coupling constant. In the same approximation, one can also estimate the leading term after introduction of different scales to drive the transverse and longitudinal parts of the integral.

We work in the second prescription that reads

$$S_{DLA} \propto \int_{\ell^2}^{\mu^2} \frac{\mathrm{d}\mathbf{q}^2}{\mathbf{q}^2} \log\frac{1}{\Delta}. \tag{B.72}$$

Instead of $\Delta = |\mathbf{q}|/\mu$, the second scale ν is introduced in the cut-off on the longitudinal integral via $\Delta = |\mathbf{q}|/\nu$ and then

$$\begin{aligned} S_{DLA} &\propto \int_{\ell^2}^{\mu^2} \frac{\mathrm{d}\mathbf{q}^2}{\mathbf{q}^2} \log\frac{\nu}{|\mathbf{q}|} \\ &= 2\int_{\ell}^{\mu} \frac{\mathrm{d}\mathbf{q}}{|\mathbf{q}|}\left(\log\frac{\nu}{\mu} - \log\frac{\mu}{|\mathbf{q}|}\right) \\ &= 2\left[\log\frac{\mu}{\ell}\log\frac{\nu}{\mu} + \frac{1}{2}\log^2\frac{\ell}{\mu}\right], \end{aligned} \tag{B.73}$$

using an integration by parts. Now, after a little bit of algebra one finds

$$\begin{aligned}
S_{DLA} &\propto 2\log\frac{\mu}{\ell}\log\frac{\nu}{\mu}+\log^2\frac{\ell}{\mu} \\
&= 2\left(\log\mu-\log\ell\right)\left(\log\nu-\log\mu\right)+\left(\log\ell-\log\mu\right)^2 \\
&= \log^2\frac{\ell}{\nu}-\log^2\frac{\mu}{\nu}.
\end{aligned} \tag{B.74}$$

It can be interesting to express the last result as only one log term

$$\begin{aligned}
S_{DLA} &\propto 2\log\frac{\mu}{\ell}\log\frac{\nu}{\mu}+\log^2\frac{\ell}{\mu} \\
&= \log^2\frac{\ell}{\mu}+2\log\frac{\ell}{\mu}\log\frac{\mu}{\nu} \\
&= \log\frac{\ell}{\mu}\left(\log\frac{\ell}{\mu}+\log\frac{\mu^2}{\nu^2}\right) \\
&= \log\frac{\ell}{\mu}\log\frac{\ell\mu}{\nu^2}.
\end{aligned} \tag{B.75}$$

From this last result, one sees that if ν increases, then S_{DLA} decreases and the Sudakov form factor

$$T(\mu^2,\ell^2)=e^{-S}, \tag{B.76}$$

increases. On the contrary, if the first scale μ starts increasing then one has two opposite effects, $\log\frac{\ell\mu}{\nu^2}$ increases while $\log\frac{\ell}{\mu}$ decreases so that the effect of a change in μ is suppressed.

B.3.4 Estimation of the Sudakov Suppression

We estimate here the Sudakov suppression in the case of a running coupling constant, using the saddle point approximation.

One starts with Eq. (4.4)

$$S_{DLA}(\mu^2,\ell^2)=\frac{3}{\pi}\int_{\ell^2}^{\mu^2}\frac{\mathrm{d}^2\mathbf{q}}{\mathbf{q}^2}\,\alpha_s(\mathbf{q}^2)\log\left(\frac{1}{|\Delta|}\right). \tag{B.77}$$

Remembering the definition $\Delta=|\mathbf{q}|/\mu$ and using Eq. (4.21) for $\alpha_s(\mathbf{q}^2)$, the integral becomes

$$\begin{aligned}
S_{DLA} &= \frac{3}{\pi}\int_{\ell^2}^{\mu^2}\frac{\mathrm{d}^2\mathbf{q}}{\mathbf{q}^2}\,\frac{12\pi}{(33-2N_f)\log\frac{\mathbf{q}^2}{\Lambda_{QCD}^2}}\,\frac{1}{2}\log\left(\frac{\mu^2}{\mathbf{q}^2}\right) \\
&= \frac{3}{2\pi}\int_{\ell^2}^{\mu^2}\frac{\mathrm{d}^2\mathbf{q}}{\mathbf{q}^2}\,\frac{12\pi}{(33-2N_f)\log\frac{\mathbf{q}^2}{\Lambda_{QCD}^2}}\left(\log\frac{\mu^2}{\Lambda_{QCD}^2}+\log\frac{\Lambda_{QCD}^2}{\mathbf{q}^2}\right).
\end{aligned} \tag{B.78}$$

One can then switch to a more convenient notation that is

$$x=\log\frac{\ell^2}{\Lambda_{QCD}^2},\quad x_2=\log\frac{\mu^2}{\Lambda_{QCD}^2}, \tag{B.79}$$

and perform a change of variable from $\log(\mathbf{q}^2/\Lambda_{QCD}^2)$ to y, to compute

$$\begin{aligned} S_{DLA} &= \frac{6}{\beta_0}\int_x^{x_2}\frac{\mathrm{d}y}{y}(x_2-y) \\ &= \frac{6}{\beta_0}\left(x_2\log\frac{x_2}{x}-x_2+x\right), \end{aligned} \tag{B.80}$$

where again

$$\beta_0 = 11-\frac{2}{3}N_f. \tag{B.81}$$

Now, one can estimate the integral

$$\mathcal{I} = \frac{1}{\Lambda^4}\int e^{-[x-S(x_2,x)]}\mathrm{d}x, \tag{B.82}$$

using the saddle-point approximation. If $f(x) = x+\frac{6}{\beta_0}\left(x_2\log\frac{x_2}{x}-x_2+x\right)$, the saddle point x_0 is given by

$$\begin{aligned} \left.\frac{\mathrm{d}f(x)}{\mathrm{d}x}\right|_{x=x_0} &= 0, \\ \rightarrow x_0 &= \frac{x_2}{1+\frac{\beta_0}{6}}, \end{aligned} \tag{B.83}$$

and one can use

$$\int_0^\infty e^{-f(x)}\mathrm{d}x \simeq \sqrt{\frac{2\pi}{-|f''(x_0)|}}e^{-f(x_0)}, \tag{B.84}$$

to compute the order of magnitude of the suppression due to this Sudakov form factor. First, one can compute $f(x_0)$:

$$\begin{aligned} f(x_0) &= \frac{x_2}{1+\frac{\beta_0}{6}}+\frac{6x_2}{\beta_0}\left[\log\left(1+\frac{\beta_0}{6}\right)-1+\frac{1}{1+\frac{\beta_0}{6}}\right] \\ &= x_2\left[\frac{\beta_0-6(1+\frac{\beta_0}{6})+6}{\beta_0(1+\frac{\beta_0}{6})}+\frac{6}{\beta_0}\log\left(1+\frac{\beta_0}{6}\right)\right] \\ &= \frac{6x_2}{\beta_0}\log\left(1+\frac{\beta_0}{6}\right), \end{aligned} \tag{B.85}$$

and the second derivative of the same function at $x = x_0$ gives

$$\begin{aligned} \left.\frac{\mathrm{d}^2f(x)}{\mathrm{d}^2x}\right|_{x=x_0} &= \left.\frac{\mathrm{d}}{\mathrm{d}x}\left[1+\frac{6}{\beta_0}\left(1-\frac{x_2}{x}\right)\right]\right|_{x=x_0} \\ &= -\left.\frac{6}{\beta_0}\frac{x_2}{x^2}\right|_{x=x_0} \\ &= -\frac{6}{\beta_0}\frac{\left(1+\frac{\beta_0}{6}\right)^2}{x_2}. \end{aligned} \tag{B.86}$$

Finally, one gets

$$\mathcal{I} = \frac{1}{\Lambda_{QCD}^4}\sqrt{\frac{2\pi\,\beta_0x_2}{6\left(1+\frac{\beta_0}{6}\right)^2}}e^{-\left[\frac{6x_2}{\beta_0}\log\left(1+\frac{\beta_0}{6}\right)\right]}. \tag{B.87}$$

B.4 Model of the Splash-Out: LHE files

We already have a code for the dijet cross section at the parton level, so that one only needs to modify it in such a way that the final state, *i.e.* gluons and protons four-momenta, can be taken as a Pythia entry. This is easily done using the Les Houches Accord for user-defined processes [130] that was made for passing information from a parton-level generator to any kind of hadronization Monte-Carlo, in the present case Pythia. The Les Houches Event File (LHEF or LHE) [131] that contains all the information requested and the basic list of ingredients that have to appear in the file are

Beam information: An initial line that contains all generic information that only appears once, such as the particle ID according to the Particle Data Group [138], the energy of the beam, the cross section, a label defined by the user and some additional switches, if necessary.

After this general information, one comes to the events generated at the parton level. An LHE file contains one or several events and each event is embedded between headers <event>. The requested event information is described in the following.

Parameters: The number of particles in the event and the possibility for the user to define his own values for coupling constants and scales. These values will be used by Pythia.

Event: Contains the ID, status and parent-child history of the process, this means all the particles that should be processed by Pythia. In sequence:

- Particle ID according to the Particle Data Group convention.
- Particle status:

-1	Incoming particle
+1	Outgoing final-state particle
+2	Intermediate resonance

- A label referring to the mothers of the present particles.
- A label referring to where the colour of the particle comes from. This can be viewed as a numbering of the different colour lines in the $N_C \to \infty$ limit and, to avoid confusion, the colour labels are usually larger than 500.
- Laboratory-frame momentum P_x, P_y, P_z, E and M in GeV.
- Lifetime τ and helicity, the last one could be set to 9 if helicity is unknown or non-necessary.

As an example, for one of our diagrams shown in Fig. B.10, the event part of the corresponding LHE is

```
<init>
            2212   -2212   0.98000000E+03   0.98000000E+03
</init>
<event>
   1        2212    -1
   2       -2212    -1
   3        2212     1
   4       -2212     1
   5          21     1         1            501        503
   6          21     1         2            503        501
</event>
```

where between the headers <event>, one finds in turn: a label, the PID of the particle (proton: 2212, antiproton: -2212, gluon: 21), its status, the label of its mother particle, its colour and anticolour label. In the example, the final gluon system is in a colour-singlet state.

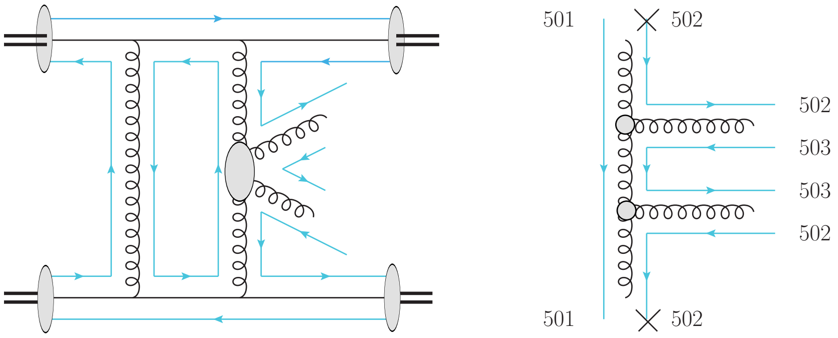

Figure B.10: Colour flow pictured by the plain-coloured lines labeled using the LHE convention. The final gluons are in a colour-singlet state.

B.5 Parametrisation of the Curves

In this section, we explicitly give the parametrisation of the different curves presented in Chap. 6 and in particular in Sec. 6.3.3 for Fig. 6.6.a and Fig. 6.5. The gap-survival probability is given at the TeVatron and parameters not mentioned here are identical to those of the reference curve, hence to those of Table 6.2.

Parameter	**Upper**	**Lower**
Φ_{UgD}	Type-4	Type-1
Upper scale	$\mu^2 = 2\mathbf{k}_2^2$	$\mu^2 = \mathbf{k}_2^2$
Lower scale	$\ell^2 = 4(\mathbf{k}+\mathbf{k}_i)^2$	$\ell^2 = (\mathbf{k}+\mathbf{k}_i)^2$
$\langle S^2\rangle$	9%	16%
$E_\perp^{\text{jet}}$	$0.75\ E_\perp^{\text{parton}}$	$0.8\ E_\perp^{\text{parton}}$

Table B.1: Parameters of the upper and lower curves in Fig. 6.6.

Parameter	**Ref. 2**	**Ref. 3**
Φ_{UgD}	Type-2	Type-4
Upper scale	$\mu^2 = 2\mathbf{k}_2^2$	$\mu^2 = \mathbf{k}_2^2$
Lower scale	$\ell^2 = 4(\mathbf{k}+\mathbf{k}_i)^2$	$\ell^2 = 2(\mathbf{k}+\mathbf{k}_i)^2$
$\langle S^2\rangle$	11%	8%
$E_\perp^{\text{jet}}$	$0.8\ E_\perp^{\text{parton}}$	$0.75\ E_\perp^{\text{parton}}$

Table B.2: Parameters of the labeled Ref. 2 and Ref. 3 curves in Fig. 6.5.

Appendix C

Higgs Boson Quasi-Elastic Cross Section: Details of the Calculation

In this Appendix, we detail some of the calculations related to the introduction of an effective vertex $gg \to H$ in two-gluon exchange. The first section presents the evaluation of the order of magnitude of the different momentum components of the colliding gluons and the second, the contribution of the term proportional to W_2 to the cross section.

C.1 Some Kinematics

The different momenta k_1, k_3 and k can be projected on the four-momenta of the initial quarks using a Sudakov decomposition

$$\begin{aligned} k_1^\mu &= \alpha_1 p^\mu + \beta_1 q^\mu + \mathbf{k}_1^\mu, \\ k_3^\mu &= \alpha_3 p^\mu + \beta_3 q^\mu + \mathbf{k}_3^\mu, \\ k^\mu &= \alpha_k p^\mu + \beta_k q^\mu + \mathbf{k}^\mu. \end{aligned} \tag{C.1}$$

The aim is to evaluate the order of magnitude of α_i and β_i. One can first use the on-shell conditions for final quarks that yield

$$\begin{aligned} (q-k_1)^2 &= 0 \\ &\qquad \to \alpha_1 = \frac{-\mathbf{k}_1^2}{(1-\beta_1)s}, \\ (p+k_3)^2 &= 0 \\ &\qquad \to \beta_3 = \frac{\mathbf{k}_3^2}{(1+\alpha_3)s}. \end{aligned} \tag{C.2}$$

In addition,

$$\begin{aligned} (k_1-k_3)^2 &= (\alpha_1-\alpha_3)(\beta_1-\beta_3)s + (\mathbf{k}_1-\mathbf{k}_3)^2 \\ &= \left(\frac{-\mathbf{k}_1^2}{(1-\beta_1)s} - \alpha_3\right)\left(\beta_1 - \frac{\mathbf{k}_3^2}{(1+\alpha_3)s}\right) s + (\mathbf{k}_1-\mathbf{k}_3)^2 \\ &\simeq -\alpha_3\beta_1 s + (\mathbf{k}_1-\mathbf{k}_3)^2, \end{aligned} \tag{C.3}$$

and finally the on-shellness of the Higgs boson $(k_1 - k_3)^2 = m_H^2$ gives

$$\begin{aligned} m_H^2 &= -\alpha_3\beta_1 s + (\mathbf{k}_1 - \mathbf{k}_3)^2, \\ \rightarrow \alpha_3 &\simeq \frac{-m_H^2}{\beta_1 s}. \end{aligned} \tag{C.4}$$

The last equality is obtained in the multi-Regge kinematical limit where $\alpha_i\beta_i s \gg |\mathbf{k}_i|^2$. Now, one is left with the components of k that are evaluated using the cuts that put the intermediate quarks on-shell

$$\begin{aligned} (q+k)^2 &= 0 \\ &\rightarrow y_k = \frac{\mathbf{k}^2}{(1+z_k)s}, \\ (p-k)^2 &= 0 \\ &\rightarrow z_k = \frac{-\mathbf{k}^2}{(1-\alpha_k)s}, \end{aligned} \tag{C.5}$$

that are both $\mathcal{O}\left(\frac{1}{s}\right)$. Hence, one has as announced

$$\begin{aligned} (k+k_1)^\mu &= (y_k + \alpha_1)p^\mu + (z_k + \beta_1)q^\mu + (\mathbf{k} + \mathbf{k}_1)^\mu \\ &= \left(\frac{\mathbf{k}^2}{(1+z_k)s} - \frac{\mathbf{k}_1^2}{(1-\beta_1)s}\right)p^\mu + \left(\frac{-\mathbf{k}^2}{(1-\alpha_k)s} + \beta_1\right)q^\mu + (\mathbf{k}+\mathbf{k}_1)^\mu \\ &\simeq \mathcal{O}\left(\frac{1}{s}\right)p^\mu + \beta_1 q^\mu + (\mathbf{k}+\mathbf{k}_1)^\mu, \end{aligned} \tag{C.6}$$

C.2 Contribution of W_2

According to [14], the $gg \rightarrow H$ effective vertex is

$$\begin{aligned} V^{\mu\nu} &= \delta^{ab}\left[(k+k_1).(k+k_3)g^{\mu\nu} - (k+k_1)^\nu(k+k_3)^\mu\right]\frac{W_1}{m_H^2} \\ &+ \big[(k+k_1)^2(k+k_3)^2 g^{\mu\nu} + (k+k_1)^\mu(k+k_3)^\nu(k+k_1).(k+k_3) \\ &-(k+k_1)^\mu(k+k_1)^\nu(k+k_3)^2 - (k+k_3)^\mu(k+k_3)^\nu(k+k_1)^2\big]\frac{W_2}{m_H^4}, \end{aligned} \tag{C.7}$$

where

$$W_1 = \frac{(\sqrt{2}G_f)^{1/2}g^2m_H^2}{12\pi^2}N_1, \quad W_2 = \frac{(\sqrt{2}G_f)^{1/2}g^2m_H^2}{12\pi^2}N_2. \tag{C.8}$$

The expressions for N_1 and N_2 come from the integration over the top loop in the specific kinematics of production in a rapidity gap, *i.e.* $(\mathbf{k}+\mathbf{k}_1)^2, (\mathbf{k}+\mathbf{k}_3)^2 \ll m_H^2$. Denoting $a \equiv m_H^2/m_t^2$, one has

$$N_1 = \frac{6}{a}\left[1 + \left(1 - \frac{4}{a}\right)\arctan^2\left(\sqrt{\frac{a}{4-a}}\right)\right], \tag{C.9}$$

and

$$N_2 = \frac{-12}{a}\left[5-\left(1+\frac{4}{a}\right)\left(\text{arctanh}\sqrt{\frac{a}{(4-a)}}\right)^2 - \frac{4}{\sqrt{\frac{a}{4-a}}}\left(\text{arctanh}\sqrt{\frac{a}{4-a}}\right)\right]. \qquad \text{(C.10)}$$

The calculation also demonstrated that the contribution of the W_2 term can be neglected and this comes from the fact that the tensor structure will always give contributions proportional to $(\mathbf{k}+\mathbf{k}_i)^2$ that are much smaller than s in the considered kinematical regime. Moreover, it was shown that $|N_2|^2$ is always 30% smaller than the $|N_1|^2$ for Higgs boson mass below 1 TeV and consequently, this correction is negligible in front of the first term. Nevertheless, in order to control the theoretical uncertainty on the calculation, one can evaluate its contribution.
One has to compute

$$\begin{aligned}
N^\mu_\nu V^\nu_\mu\Big|_2 &= (4q^\mu q^\sigma)\left[(k+k_1)^2(k+k_3)^2 g^{\mu\nu} + (k+k_1)^\mu(k+k_3)^\nu(k+k_1).(k+k_3)\right.\\
&\quad \left. -(k+k_1)^\mu(k+k_1)^\nu(k+k_3)^2 - (k+k_3)^\mu(k+k_3)^\nu(k+k_1)^2\right](4p^\mu p^\sigma)\frac{W_2}{m_H^4}\\
&= 8s\left[(k+k_1)^2(k+k_3)^2\frac{s}{2} + (k+k_1).q(k+k_3).q(k+k_1).(k+k_3)\right.\\
&\quad \left. -(k+k_1).q\,(k+k_1).p\,(k+k_3)^2 - (k+k_3).q\,(k+k_3).p\,(k+k_1)^2\right]\frac{W_2}{m_H^4},
\end{aligned} \qquad \text{(C.11)}$$

using $p^\mu q_\mu = s/2$. As previously, one can define

$$\begin{aligned}
(k+k_1)^\mu &= \frac{\alpha_1}{s}p^\mu + \beta_1 q^\mu + (\mathbf{k}+\mathbf{k}_1)^\mu,\\
(k+k_3)^\mu &= \alpha_3 p^\mu + \frac{\beta_3}{s}q^\mu + (\mathbf{k}+\mathbf{k}_3)^\mu,
\end{aligned} \qquad \text{(C.12)}$$

and compute the different scalar products necessary to evaluate Eq. (C.11). One finds

$$\begin{aligned}
(k+k_1).(k+k_3) &= \alpha_1\beta_3\frac{1}{2s} + \alpha_3\beta_1\frac{s}{2} + (\mathbf{k}+\mathbf{k}_1)(\mathbf{k}+\mathbf{k}_3),\\
(k+k_1)^2 &= \alpha_1\beta_1 + \mathbf{k}_1^2,\\
(k+k_3)^2 &= \alpha_3\beta_3 + \mathbf{k}_3^2,\\
(k+k_1).p &= \beta_1\frac{s}{2},\\
(k+k_1).q &= \frac{1}{2}\alpha_1,\\
(k+k_3).p &= \frac{1}{2}\beta_3,\\
(k+k_3).p &= \alpha_3\frac{s}{2}.
\end{aligned} \qquad \text{(C.13)}$$

So that

$$\begin{aligned}
N^\mu_\nu V^\mu_\nu\Big|_2 &= 8s\left[(k+k_1)^2(k+k_3)^2\frac{s}{2} + \frac{\alpha_1}{4}\beta_3(k+k_1)(k+k_3) - \alpha_1\beta_1\frac{s}{4}(k+k_3)^2 - \beta_3\alpha_3\frac{s}{2}(k+k_1)^2\right]\frac{W_2}{m_H^4}\\
&= \left[s^2\left(\alpha_1\beta_1\alpha_3\beta_3 + 2\alpha_1\beta_1(\mathbf{k}+\mathbf{k}_3)^2 + 2\alpha_3\beta_3(\mathbf{k}+\mathbf{k}_1)^2 + 4(\mathbf{k}+\mathbf{k}_1)^2(\mathbf{k}+\mathbf{k}_3)^2\right)\right.\\
&\quad \left. +2\alpha_1^2\beta_3^2 + 4s\alpha_1\beta_3(\mathbf{k}+\mathbf{k}_1)(\mathbf{k}+\mathbf{k}_3)\right]\frac{W_2}{m_H^4}\\
&\simeq s^2\left[\alpha_1\beta_1\alpha_3\beta_3 + 2\alpha_1\beta_1(\mathbf{k}+\mathbf{k}_3)^2 + 2\alpha_3\beta_3(\mathbf{k}+\mathbf{k}_1)^2 + 4(\mathbf{k}+\mathbf{k}_1)^2(\mathbf{k}+\mathbf{k}_3)^2\right]\frac{W_2}{m_H^4} + \mathcal{O}(s).
\end{aligned}$$

$$\text{(C.14)}$$

Bibliography

[1] J. D. Bjorken, *Rapidity gaps and jets as a new physics signature in very high-energy hadron hadron collisions*, Phys. Rev. **D47** (1993) 101–113.

[2] M. L. Good and W. D. Walker, *Diffraction disssociation of beam particles*, Phys. Rev. **120** (1960) 1857–1860.

[3] D. Kharzeev and E. Levin, *Soft double-diffractive Higgs production at hadron colliders*, Phys. Rev. **D63** (2001) 073004. [arXiv:hep-ph/0005.311].

[4] B. Cox, J. R. Forshaw and B. Heinemann, *Double diffractive Higgs and di-photon production at the Tevatron and LHC*, Phys. Lett. **B540** (2002) 263–268. [arXiv:hep-ph/0110.173].

[5] M. Boonekamp, R. B. Peschanski and C. Royon, *Inclusive Higgs boson and dijet production via double pomeron exchange*, Phys. Rev. Lett. **87** (2001) 251806. [arXiv:hep-ph/0107.113].

[6] M. Boonekamp, R. B. Peschanski and C. Royon, *Sensitivity to the standard model Higgs boson in exclusive double diffraction*, Phys. Lett. **B598** (2004) 243–251. [arXiv:hep-ph/0406.061].

[7] N. Timneanu, R. Enberg and G. Ingelman, *Diffractive Higgs production: Soft colour interactions perspective*, Acta Phys. Polon. **B33** (2002) 3479–3484. [arXiv:hep-ph/0206.147].

[8] R. Enberg, G. Ingelman, A. Kissavos and N. Timneanu, *Diffractive Higgs boson production at the Tevatron and LHC*, Phys. Rev. Lett. **89** (2002) 081801. [arXiv:hep-ph/0203.267].

[9] R. Enberg, G. Ingelman and N. Timneanu, *Diffractive Higgs and prompt photons at hadron colliders*, Phys. Rev. **D67** (2003) 011301. [arXiv:hep-ph/0210.408].

[10] R. B. Appleby and J. R. Forshaw, *Diffractive dijet production*, Phys. Lett. **B541** (2002) 108–114. [arXiv:hep-ph/0111.077].

[11] R. J. M. Covolan and M. S. Soares, *Diffractive production of dijets by double Pomeron exchange processes*, Phys. Rev. **D67** (2003) 077504. [arXiv:hep-ph/0305.186].

[12] A. Bzdak, *Production of gluon jets in p p collisions by double pomeron exchange in the Landshoff-Nachtmann model*, Acta Phys. Polon. **B35** (2004) 1733–1746. [arXiv:hep-ph/0404.153].

[13] A. Bzdak, *Exclusive Higgs and dijet production by double pomeron exchange. The CDF upper limits*, Phys. Lett. **B615** (2005) 240–246. [arXiv:hep-ph/0504.086].

[14] J.-R. Cudell and O. F. Hernandez, *Particle Production in a Hadron Collider Rapidity Gap: The Higgs Case*, Nucl. Phys. **B471** (1996) 471–502. [arXiv:hep-ph/9511.252].

[15] R. Peschanski, M. Rangel and C. Royon, *Hybrid Pomeron Model of exclusive central diffractive production*, Acta Phys. Polon. **B40** (2009) 2323–2344. [arXiv:hep-ph/0808.1691].

[16] V. A. Khoze, A. D. Martin and M. G. Ryskin, *Can the Higgs be seen in rapidity gap events at the Tevatron or the LHC?*, Eur. Phys. J. **C14** (2000) 525–534. [arXiv:hep-ph/0002.072].

[17] V. A. Khoze, A. D. Martin and M. G. Ryskin, *Double-diffractive processes in high-resolution missing- mass experiments at the Tevatron*, Eur. Phys. J. **C19** (2001) 477–483. [arXiv:hep-ph/0011.393].

[18] I. P. Ivanov and N. N. Nikolaev, *Anatomy of the differential gluon structure function of the proton from the experimental data on* $F_2(p)(x, Q^2)$, Phys. Rev. **D65** (2002) 054004. [arXiv:hep-ph/0004.206].

[19] A. B. Kaidalov, V. A. Khoze, A. D. Martin and M. G. Ryskin, *Extending the study of the Higgs sector at the LHC by proton tagging*, Eur. Phys. J. **C33** (2004) 261–271. [arXiv:hep-ph/0311.023].

[20] T. D. Coughlin and J. R. Forshaw, *Central Exclusive Production in QCD*, JHEP **01** (2010) 121. [arXiv:hep-ph/0912.3280].

[21] T. D. Coughlin, *Central Exclusive Production*, Ph.D. thesis, University of Manchester (2010).

[22] M. Dasgupta, L. Magnea and G. P. Salam, *Non-perturbative QCD effects in jets at hadron colliders*, JHEP **02** (2008) 055. [arXiv:hep-ph/0712.3014].

[23] J. R. Cudell, A. Dechambre, O. F. Hernandez and I. P. Ivanov, *Central exclusive production of dijets at hadronic colliders*, Eur. Phys. J. **C61** (2009) 369–390. [arXiv:hep-ph/0807.0600].

[24] J. R. Cudell, A. Dechambre, O. F. Hernandez and I. P. Ivanov, *Higgs Quasi-elastic Production at Hadronic Colliders* In preparation.

[25] S. P. Denisov *et al.*, *Total cross-sections of pi+, K+ and p on protons and deuterons in the momentum range 15-GeV/c to 60-GeV/c*, Phys. Lett. **B36** (1971) 415–421.

[26] W. Heisenberg, *Mesonenerzeugung als Stosswellenproblem*, Z. Phys. **133** (1952) 65.

[27] I. Y. Pomeranchuk, *Equality between the Interaction Cross Sections of High-Energy Nucleons and Antinucleons*, Zh. Eksp. Teor. Fiz. **34** (1958) 725. [Sov.Phys.JETP 7 499 (1958)].

[28] T. Regge, *Introduction to complex orbital momenta*, Nuovo Cim. **14** (1959) 951.

[29] G. F. Chew and S. C. Frautschi, *Principle of equivalence for all strongly interacting particles within the S-matrix framework*, Phys. Rev. Lett. **7** (1961) 394–397.

[30] V. N. Gribov, *Partial waves with complex orbital angular momenta and the asymptotic behavior of the scattering amplitude*, Sov. Phys. JETP **14** (1962) 1395.

[31] H. Fritzsch, M. Gell-Mann and H. Leutwyler, *Advantages of the Color Octet Gluon Picture*, Phys. Lett. **B47** (1973) 365–368.

[32] M. Gell-Mann, *A Schematic Model of Baryons and Mesons*, Phys. Lett. **8** (1964) 214–215.

[33] J. C. Collins, D. E. Soper and G. Sterman, *Factorization of Hard Processes in QCD*, Adv. Ser. Direct. High Energy Phys. **5** (1988) 1–91. [arXiv:hep-ph/0409.313].

[34] M. Derrick *et al.*, *Observation of events with a large rapidity gap in deep inelastic scattering at HERA*, Phys. Lett. **B315** (1993) 481–493.

[35] A. Donnachie and P. V. Landshoff, *Elastic Scattering and Diffraction Dissociation*, Nucl. Phys. **B244** (1984) 322.

[36] G. Ingelman and P. E. Schlein, *Jet Structure in High Mass Diffractive Scattering*, Phys. Lett. **B152** (1985) 256.

[37] R. Bonino *et al.*, *Evidence for Transverse Jets in High Mass Diffraction*, Phys. Lett. **B211** (1988) 239.

[38] F. Abe *et al.*, *Observation of rapidity gaps in* $\bar{p}p$ *collisions at 1.8 TeV*, Phys. Rev. Lett. **74** (1995) 855–859.

[39] *TOTEM cross section: Elastic scattering and diffraction dissociation at the LHC* CERN-LHCC-97-49.

[40] J. Barone and E. Predazzi, *High-Energy Particle Diffraction* (Springer, Verlag Berlin Heidelberg New York, 2002).

[41] S. Abatzis *et al.*, *Observation of a narrow scalar meson at 1450-MeV in the reaction p* $p \to p(f)\ (\pi^+\pi - \pi^+\pi^-)p(s)$ *at 450-GeV/c using the CERN Omega Spectrometer*, Phys. Lett. **B324** (1994) 509–514.

[42] A. Donnachie and P. V. Landshoff, *Total cross-sections*, Phys. Lett. **B296** (1992) 227–232. [arXiv:hep-ph/9209.205].

[43] J. R. Cudell, A. Lengyel and E. Martynov, *The Soft and the hard pomerons in hadron elastic scattering at small* t, Phys. Rev. **D73** (2006) 034008. [arXiv:hep-ph/0511.073].

[44] E. A. Kuraev, L. N. Lipatov and V. S. Fadin, *Multi - Reggeon Processes in the Yang-Mills Theory*, Sov. Phys. JETP **44** (1976) 443–450.

[45] I. I. Balitsky and L. N. Lipatov, *The Pomeranchuk Singularity in Quantum Chromodynamics*, Sov. J. Nucl. Phys. **28** (1978) 822–829.

[46] V. S. Fadin, *BFKL resummation*, Nucl. Phys. **A666** (2000) 155–164.

[47] V. S. Fadin, *Non-forward BFKL at next-to-leading approximation*, Nucl. Phys. Proc. Suppl. **99A** (2001) 204–212. [arXiv:hep-ph/0101.003].

[48] P. V. Landshoff and O. Nachtmann, *Vacuum Structure and Diffraction Scattering*, Z. Phys. **C35** (1987) 405.

[49] A. Donnachie and P. V. Landshoff, *Gluon Condensate and Pomeron Structure*, Nucl. Phys. **B311** (1989) 509.

[50] F. E. Low, *A Model of the Bare Pomeron*, Phys. Rev. **D12** (1975) 163–173.

[51] S. Nussinov, *Colored Quark Version of Some Hadronic Puzzles*, Phys. Rev. Lett. **34** (1975) 1286–1289.

[52] J. R. Cudell, *A short course on Quantum Chromodynamics* (Gand, 2004). `http://qcd.theo.phys.ulg.ac.be/cudell/QCD/index.html`

[53] M. E. Peskin and D. V. Schroeder, *An Introduction to quantum field theory.* Reading, USA: Addison-Wesley (1995) 842 p.

[54] V. N. Gribov, *Quantization of non-Abelian gauge theories*, Nucl. Phys. **B139** (1978) 1.

[55] A. Dechambre, *Aspects of Diffractive Physics, Introduction of Non-perturbative aspects.* Master's thesis, Université de Liège.
`http://www.theo.phys.ulg.ac.be/wiki/index.php`

[56] P. T. Lukens, *The CDF IIb detector: Technical design report* FERMILAB-TM-2198.

[57] T. Aaltonen *et al.*, *Observation of Exclusive Dijet Production at the Fermilab Tevatron* $p^{-}\bar{p}$ *Collider*, Phys. Rev. **D77** (2008) 052004. [arXiv:hep-ex/0712.0604].

[58] V. M. Abazov *et al.*, *The Upgraded D0 Detector*, Nucl. Instrum. Meth. **A565** (2006) 463–537. [arXiv:physics/0507.191].

[59] C. Ochando, *Search for the Higgs boson in the ZH→ $\nu\nu$ bb channel*, Ph.D. thesis, Université Paris XI Orsay (2008). FERMILAB-THESIS-2008-78.

[60] Official web sites.
`http://www-cdf.fnal.gov/,http://www-d0.fnal.gov/`

[61] R. Assmann *et al.*, *Beam parameters and machine performance to be reached in 2010* .
`http://lhc-commissioning.web.cern.ch/lhc-commissioning/`

[62] LHC commissioning Web Pages.
`http://lhc-commissioning.web.cern.ch/lhc-commissioning/`

[63] Official web sites.
`http://atlas.ch/,http://cms.web.cern.ch/cms/index.html`

[64] Official web sites.
`http://aliceinfo.cern.ch/,http://lhcb-public.web.cern.ch/lhcb/`

[65] Private record.

[66] O. S. Bruning, (Ed.) *et al.*, *LHC design report. Vol. I: The LHC main ring* CERN-2004-003-V-1.

[67] X. Rouby, *Measurements of photon induced processes in CMS and forward proton detection at the LHC*, Ph.D. thesis, Université Catholique de Louvain.

[68] D. G. d'Enterria, *Forward Physics at the LHC* [arXiv:hep-ex/0708.0551].

[69] C. Joram, A. Braem and H. Stenzel, *Basic considerations on the overlap detectors of the ATLAS ALFA system* ATL-LUM-PUB-2007-002.

[70] V. Berardi *et al.*, *TOTEM: Technical design report. Total cross section, elastic scattering and diffraction dissociation at the Large Hadron Collider at CERN* CERN-LHCC-2004-002.

[71] Thanks to Xavier Rouby for the picture.

[72] M. G. Albrow *et al.*, *The FP420 R&D Project: Higgs and New Physics with forward protons at the LHC*, JINST **4** (2009) T10001. [arXiv:hep-ex/0806.0302].

[73] H. Abramowicz and A. Caldwell, *HERA collider physics*, Rev. Mod. Phys. **71** (1999) 1275–1410. [arXiv:hep-ex/9903.037].

[74] M. G. Albrow and A. Rostovtsev, *Searching for the Higgs at hadron colliders using the missing mass method* [arXiv:hep-ph/0009.336].

[75] R. E. Cutkosky, *Singularities and discontinuities of Feynman amplitudes*, J. Math. Phys. **1** (1960) 429–433.

[76] I. T. Drummond, P. V. Landshoff and W. J. Zakrzewski, *The two-reggeon/particle coupling*, Nucl. Phys. **B11** (1969) 383–405.

[77] I. T. Drummond, P. V. Landshoff and W. J. Zakrzewski, *Signature in production amplitudes*, Phys. Lett. **B28** (1969) 676–678.

[78] J. R. Forshaw and D. A. Ross, *Quantum chromodynamics and the pomeron*, vol. 9 (Cambridge Lect. Notes Phys., 1997).

[79] L. N. Lipatov, *Reggeization of the Vector Meson and the Vacuum Singularity in Nonabelian Gauge Theories*, Sov. J. Nucl. Phys. **23** (1976) 338–345.

[80] J. F. Gunion and D. E. Soper, *Quark Counting and Hadron Size Effects for Total Cross-Sections*, Phys. Rev. **D15** (1977) 2617–2621.

[81] H. Cheng and T. T. Wu, *Expanding Protons: Scattering at High-energies.* Cambridge, USA: MIT-Pr. (1987) 285p.

[82] J. R. Cudell and B. U. Nguyen, *A Consistent next-to-leading order QCD calculation of hadronic diffractive scattering*, Nucl. Phys. **B420** (1994) 669–694. [arXiv:hep-ph/9310.298].

[83] P. N. Kirk *et al.*, *Elastic electron - Proton Scattering at Large Four Momentum Transfer*, Phys. Rev. **D8** (1973) 63–91.

[84] A. Bialas and P. V. Landshoff, *Higgs production in p p collisions by double pomeron exchange*, Phys. Lett. **B256** (1991) 540–546.

[85] S. Sadr *et al.*, *Anti-p p collisions at* $s^{(1/2)}$ *= 1.8-TeV: rho, sigma(t) and B* Prepared for International Conference on Elastic and Diffractive Scattering (5th Blois Workshop), Providence, RI, 8-12 Jun 1993.

[86] I. P. Ivanov and N. N. Nikolaev, *Diffractive vector meson production in k(t)-factorization approach*, Acta Phys. Polon. **B33** (2002) 3517–3522. [arXiv:hep-ph/0206.298].

[87] V. S. Fadin, E. A. Kuraev and L. N. Lipatov, *On the Pomeranchuk Singularity in Asymptotically Free Theories*, Phys. Lett. **B60** (1975) 50–52.

[88] M. Gluck, E. Reya and A. Vogt, *Dynamical parton distributions revisited*, Eur. Phys. J. **C5** (1998) 461–470. [arXiv:hep-ph/9806.404].

[89] A. D. Martin, R. G. Roberts, W. J. Stirling and R. S. Thorne, *Scheme dependence, leading order and higher twist studies of MRST partons*, Phys. Lett. **B443** (1998) 301–307. [arXiv:hep-ph/9808.371].

[90] H. L. Lai and W. K. Tung, *Charm production and parton distributions*, Z. Phys. **C74** (1997) 463–468. [arXiv:hep-ph/9701.256].

[91] N. N. Nikolaev and B. G. Zakharov, *BFKL evolution and universal structure function at very small x*, Phys. Lett. **B327** (1994) 157–165. [arXiv:hep-ph/9401.312].

[92] N. N. Nikolaev, B. G. Zakharov and V. R. Zoller, *The BFKL-Regge phenomenology of deep inelastic scattering*, JETP Lett. **66** (1997) 138–143. [arXiv:hep-ph/9707.463].

[93] N. N. Nikolaev, J. Speth and V. R. Zoller, *The color dipole BFKL-Regge expansion: From DIS on protons to pions to rise of hadronic cross sections*, Phys. Lett. **B473** (2000) 157–166. [arXiv:hep-ph/9911.433].

[94] E. Meggiolaro, *Field strength correlators in QCD: New fits to the lattice data*, Phys. Lett. **B451** (1999) 414–421. [arXiv:hep-ph/9807.567].

[95] V. Gribov, *QCD at large and short distances (annotated version)*, Eur. Phys. J. **C10** (1999) 71–90. [arXiv:hep-ph/9807.224].

[96] Y. L. Dokshitzer, G. Marchesini and B. R. Webber, *Non-perturbative effects in the energy-energy correlation*, JHEP **07** (1999) 012. [arXiv:hep-ph/9905.339].

[97] M. Derrick *et al.*, *Measurement of the F_2 structure function in deep inelastic e+ p scattering using 1994 data from the ZEUS detector at HERA*, Z. Phys. **C72** (1996) 399–424. [arXiv:hep-ex/9607.002].

[98] J. Breitweg *et al.*, *ZEUS results on the measurement and phenomenology of F_2 at low x and low Q^2*, Eur. Phys. J. **C7** (1999) 609–630. [arXiv:hep-ex/9809.005].

[99] J. Breitweg *et al.*, *Measurement of the proton structure function F_2 at very low Q^2 at HERA*, Phys. Lett. **B487** (2000) 53–73. [arXiv:hep-ex/0005.018].

[100] S. Chekanov *et al.*, *Measurement of the neutral current cross section and F_2 structure function for deep inelastic e+ p scattering at HERA*, Eur. Phys. J. **C21** (2001) 443–471. [arXiv:hep-ex/0105.090].

[101] S. Aid *et al.*, *A Measurement and QCD Analysis of the Proton Structure Function $F_2(x, Q^2)$ at HERA*, Nucl. Phys. **B470** (1996) 3–40. [arXiv:hep-ex/9603.004].

[102] C. Adloff *et al.*, *A measurement of the proton structure function $F_2(x, Q^2)$ at low-x and low Q^2 at HERA*, Nucl. Phys. **B497** (1997) 3–30. [arXiv:hep-ex/9703.012].

[103] C. Adloff *et al.*, *Deep-inelastic inclusive e p scattering at low x and a determination of alpha(s)*, Eur. Phys. J. **C21** (2001) 33–61. [arXiv:hep-ex/0012.053].

[104] M. R. Adams *et al.*, *Proton and deuteron structure functions in muon scattering at 470-GeV*, Phys. Rev. **D54** (1996) 3006–3056.

[105] M. Arneodo *et al.*, *Measurement of the proton and deuteron structure functions, $F_2(p)$ and $F_2(d)$, and of the ratio sigma(L)/sigma(T)*, Nucl. Phys. **B483** (1997) 3–43. [arXiv:hep-ph/9610.231].

[106] A. V. Radyushkin, *Symmetries and structure of skewed and double distributions*, Phys. Lett. **B449** (1999) 81–88. [arXiv:hep-ph/9810.466].

[107] A. G. Shuvaev, K. J. Golec-Biernat, A. D. Martin and M. G. Ryskin, *Off-diagonal distributions fixed by diagonal partons at small x and xi*, Phys. Rev. **D60** (1999) 014015. [arXiv:hep-ph/9902.410].

[108] I. P. Ivanov, N. N. Nikolaev and A. A. Savin, *Diffractive vector meson production at HERA: From soft to hard QCD*, Phys. Part. Nucl. **37** (2006) 1–85. [arXiv:hep-ph/0501.034].

[109] V. V. Sudakov, *Vertex parts at very high-energies in quantum electrodynamics*, Sov. Phys. JETP **3** (1956) 65–71.

[110] N. N. Bogolyubov and D. V. Shirkov, *Introduction to the theory of quantized fields*, Intersci. Monogr. Phys. Astron. **3** (1959) 1–720.

[111] Y. L. Dokshitzer, D. Diakonov and S. I. Troian, *Hard Processes in Quantum Chromodynamics*, Phys. Rept. **58** (1980) 269–395.

[112] M. Ciafaloni, *Coherence Effects in Initial Jets at Small q^2 / s*, Nucl. Phys. **B296** (1988) 49.

[113] S. Catani, F. Fiorani and G. Marchesini, *Small x Behavior of Initial State Radiation in Perturbative QCD*, Nucl. Phys. **B336** (1990) 18.

[114] S. Catani, F. Fiorani and G. Marchesini, *QCD Coherence in Initial State Radiation*, Phys. Lett. **B234** (1990) 339.

[115] M. A. Kimber, A. D. Martin and M. G. Ryskin, *Unintegrated parton distributions*, Phys. Rev. **D63** (2001) 114027. [arXiv:hep-ph/0101.348].

[116] M. A. Kimber, J. Kwiecinski, A. D. Martin and A. M. Stasto, *The unintegrated gluon distribution from the CCFM equation*, Phys. Rev. **D62** (2000) 094006. [arXiv:hep-ph/0006.184].

[117] A. D. Martin and M. G. Ryskin, *Unintegrated generalised parton distributions*, Phys. Rev. **D64** (2001) 094017. [arXiv:hep-ph/0107.149].

[118] J. C. Collins, *Sudakov form factors*, Adv. Ser. Direct. High Energy Phys. **5** (1989) 573–614. [arXiv:hep-ph/0312.336].

[119] A. Sen, *Asymptotic Behavior of the Sudakov Form-Factor in QCD*, Phys. Rev. **D24** (1981) 3281.

[120] G. P. Korchemsky, *Sudakov Form-Factor in QCD*, Phys. Lett. **B220** (1989) 629.

[121] J. Monk and A. Pilkington, *ExHuME: A Monte Carlo event generator for exclusive diffraction*, Comput. Phys. Commun. **175** (2006) 232–239. [arXiv:hep-ph/0502.077].

[122] L. Frankfurt, C. E. Hyde, M. Strikman and C. Weiss, *Generalized parton distributions and rapidity gap survival in exclusive diffractive pp scattering*, Phys. Rev. **D75** (2007) 054009. [arXiv:hep-ph/0608.271].

[123] F. Abe *et al.*, *Measurement of small angle $\bar{p}p$ elastic scattering at $\sqrt{s} = 546$ GeV and 1800 GeV*, Phys. Rev. **D50** (1994) 5518–5534.

[124] N. A. Amos *et al.*, *Measurement of ρ, the ratio of the real to imaginary part of the $\bar{p}p$ forward elastic scattering amplitude, at $\sqrt{s}$ = 1.8-TeV*, Phys. Rev. Lett. **68** (1992) 2433–2436.

[125] A. Achilli *et al.*, *Total cross-section and rapidity gap survival probability at the LHC through an eikonal with soft gluon resummation*, Phys. Lett. **B659** (2008) 137–143. [arXiv:hep-ph/0708.3626].

[126] J. M. Campbell, J. W. Huston and W. J. Stirling, *Hard Interactions of Quarks and Gluons: A Primer for LHC Physics*, Rept. Prog. Phys. **70** (2007) 89. [arXiv:hep-ph/0611.148].

[127] V. A. Khoze, A. D. Martin and M. G. Ryskin, *New Physics with Tagged Forward Protons at the LHC*, Frascati Phys. Ser. **44** (2007) 147–160. K. Therashi's result, mentioned in, [arXiv:hep-ph/0705.2314].

[128] V. A. Khoze, A. B. Kaidalov, A. D. Martin, M. G. Ryskin and W. J. Stirling, *Diffractive processes as a tool for searching for new physics* [arXiv:hep-ph/0507.040].

[129] T. Sjostrand, S. Mrenna and P. Z. Skands, *PYTHIA 6.4 Physics and Manual*, JHEP **05** (2006) 026. [arXiv:hep-ph/0603.175].

[130] J. Alwall *et al.*, *A standard format for Les Houches event files*, Comput. Phys. Commun. **176** (2007) 300–304. [arXiv:hep-ph/0609.017].

[131] E. Boos *et al.*, *Generic user process interface for event generators* [arXiv:hep-ph/0109.068].

[132] S. Ovyn, X. Rouby and V. Lemaitre, *Delphes, a framework for fast simulation of a generic collider experiment* [arXiv:hep-ph/0903.2225].

[133] L. Quertenmont and V. Roberfroid, *FROG: The Fast and Realistic OPENGL Displayer* [arXiv:hep-ex/0901.2718].

[134] G. Soyez, *Lectures: QCD for LHC* (UCL, Belgique, 2008). `http://www.theo.phys.ulg.ac.be/~soyez/lectures/plan.html`

[135] J. E. Huth *et al.*, *Toward a standardization of jet definitions* Presented at Summer Study on High Energy Physics, Reaearch Directions for the Decade, Snowmass, CO, Jun 25 - Jul 13, 1990.

[136] G. C. Blazey *et al.*, *Run II jet physics* [arXiv:hep-ex/0005.012].

[137] *FPMC* In preparation.

[138] C. Amsler *et al.*, *Review of particle physics*, Phys. Lett. **B667** (2008) 1.

[139] G. P. Lepage, *VEGAS: An adaptative multidimensional integration program* CLNS-80/447.

[140] B. E. Cox and J. R. Forshaw, *POMWIG: HERWIG for diffractive interactions*, Comput. Phys. Commun. **144** (2002) 104–110. [arXiv:hep-ph/0010.303].

[141] A. Schafer, O. Nachtmann and R. Schopf, *Production of Higgs particles in diffractive hadron hadron collisions*, Phys. Lett. **B249** (1990) 331–335.

[142] J. F. Gunion, H. E. Haber, G. L. Kane and S. Dawson, *The Higgs Hunter's Guide.* SCIPP-89/13.

[143] Z. Kunszt, S. Moretti and W. J. Stirling, *Higgs production at the LHC: An update on cross sections and branching ratios*, Z. Phys. **C74** (1997) 479–491. [arXiv:hep-ph/9611.397].

[144] H. M. Georgi, S. L. Glashow, M. E. Machacek and D. V. Nanopoulos, *Higgs Bosons from Two Gluon Annihilation in Proton Proton Collisions*, Phys. Rev. Lett. **40** (1978) 692.

[145] R. N. Cahn and S. Dawson, *Production of Very Massive Higgs Bosons*, Phys. Lett. **B136** (1984) 196.

[146] S. L. Glashow, D. V. Nanopoulos and A. Yildiz, *Associated Production of Higgs Bosons and Z Particles*, Phys. Rev. **D18** (1978) 1724–1727.

[147] Z. Kunszt, Z. Trocsanyi and W. J. Stirling, *Clear signal of intermediate mass Higgs boson production at LHC and SSC*, Phys. Lett. **B271** (1991) 247–255.

[148] Z. Kunszt, *Associated Production of Heavy Higgs Boson with Top Quarks*, Nucl. Phys. **B247** (1984) 339.

[149] W. J. Marciano and F. E. Paige, *Associated production of Higgs bosons with t anti-t pairs*, Phys. Rev. Lett. **66** (1991) 2433–2435.

[150] J. F. Gunion, H. E. Haber, F. E. Paige, W.-K. Tung and S. S. D. Willenbrock, *Neutral and Charged Higgs Detection: Heavy Quark Fusion, Top Quark Mass Dependence and Rare Decays*, Nucl. Phys. **B294** (1987) 621.

[151] D. A. Dicus and S. Willenbrock, *Higgs Boson Production from Heavy Quark Fusion*, Phys. Rev. **D39** (1989) 751.

[152] M. Acciarri *et al.*, *Search for Standard Model Higgs boson in* e^+e^- *interactions at* $S^{(1/2)}$ *= 189-GeV*, Phys. Lett. **B461** (1999) 376–386. [arXiv:hep-ex/9909.004].

[153] *Combined CDF and D0 Upper Limits on Standard Model Higgs- Boson Production with 2.1 - 5.4 fb-1 of Data* [arXiv:hep-ex/0911.3930].

[154] R. Barate *et al.*, *Search for the standard model Higgs boson at LEP*, Phys. Lett. **B565** (2003) 61–75. [arXiv:hep-ex/0306.033].

[155] *ATLAS detector and physics performance. Technical design report. Vol. 2* CERN-LHCC-99-15.

[156] G. L. Bayatian *et al.*, *CMS technical design report, volume II: Physics performance*, J. Phys. **G34** (2007) 995–1579.

[157] R. Enberg, G. Ingelman and N. Timneanu, *Soft color interactions and diffractive hard scattering at the Tevatron*, Phys. Rev. **D64** (2001) 114015. [arXiv:hep-ph/0106.246].

[158] V. A. Khoze, A. D. Martin and M. G. Ryskin, *Higgs or dijet production in double rapidity gap events* [arXiv:hep-ph/0006.005].

[159] B. E. Cox, F. K. Loebinger and A. D. Pilkington, *Detecting Higgs bosons in the* $b\bar{b}$ *decay channel using forward proton tagging at the LHC*, JHEP **10** (2007) 090. [arXiv:hep-ph:0709.3035].

[160] V. S. Fadin and L. N. Lipatov, *High-Energy Production of Gluons in a QuasimultiRegge Kinematics*, JETP Lett. **49** (1989) 352.